

Polymer Optical Waveguide Link Design for High-Speed and High-Density On-Board Interconnects

March 2012

A thesis submitted in partial fulfilment of the requirements for the degree of
Doctor of Philosophy in Engineering



Keio University

Graduate School of Science and Technology
School of Integrated Design Engineering

Hsu, Hsiang-Han

CONTENTS

TABLE OF CONTENTS	i
LIST OF FIGURES	iv
LIST OF TABLES	ix
ABSTRACT	xi
1. INTRODUCTION	1
1.1 SHORT RANGE OPTICAL INTERCONNECTION	3
1.2 ISSUES AND CHALLENGES	6
1.3 DISSERTATION OVERVIEW	9
REFERENCES	11
2. MODELING WITH RAY OPTICS	14
2.1 RAY TRAJECTORIES FOR GI CORES	15
2.1.1 Ray equations for a GI core	15
2.1.2 Classification of rays and ray trajectories	18
2.1.3 Ray equations for a rectangular GI core	25
2.2 RAY TRAJECTORIES FOR SI CORES	27
2.3 LAUNCHING CONDITION	30
2.4 SCATTERING EFFECT IN CORE AREA	33
2.5 ROUGH CORE/CLADDING BOUNDARY	39
2.5.1 Random rough surface	41
2.5.2 Moving average method	42
2.5.3 Kirchhoff approximation	42
REFERENCE	46
3. MODELING WITH WAVE OPTICS	47
3.1 MODAL SOLUTION BY SERIES EXPANSION METHOD	48
3.2 BEAM PROPAGATION METHOD	52
3.2.1 Implementation by finite difference method	54
3.2.2 Transparent boundary condition	56
3.3 RADIATION FIELD FROM WAVEGUIDE	59
3.4 MIE SCATTERING	60
3.5 COMPARISON OF SCATTERED FAR FIELD PATTERN	65

3.5.1	Partial wave decomposition for Gaussian beam	65
3.5.2	The coincidence between BPM and Mie scattering	68
	REFERENCE	75

4. APPLICATIONS 76

4.1	CROSSTALK ANALYSIS FOR CO-POLYMER WAVEGUIDES	77
4.1.1	Waveguide fabrication and characterization	78
4.1.2	Loss and crosstalk measurement	83
4.1.3	Calculated NFP for high scattered waveguides	86
4.1.4	Calculated crosstalk for high scattered waveguides	88
4.1.5	Calculated loss for high scattered waveguides	89
4.1.6	Conclusion	93
4.2	CROSSTALK ANALYSIS FOR W-SHAPED WAVEGUIDES	94
4.2.1	Waveguide fabrication and characterization	95
4.2.2	Near field pattern and propagation loss	98
4.2.3	Refractive index profile and inter-channel crosstalk	100
4.2.4	Inter-channel crosstalk in short length waveguides	103
4.2.5	Theoretical analysis of inter-channel crosstalk	104
4.2.6	Calculation results	108
4.2.7	Conclusion	112
4.3	OPTICAL LINK ANALYSIS WITH RAY OPTICS	112
4.3.1	Modeling layout	115
4.3.2	Theoretical calculation	117
4.3.3	Calculation results	120
4.3.4	Discussion	123
4.3.5	Conclusion	126
4.4	OPTICAL LINK ANALYSIS WITH WAVE OPTICS	131
4.4.1	Connection loss evaluation of GI-PPOW based optical link	131
4.4.2	Connection loss evaluation of fiber based optical link	135
4.4.3	Theoretical modeling	137
4.4.4	Scattering effect	139
4.4.5	Calculation results	140
4.4.6	Conclusion	145
4.5	THE OPTIMIZATION OF WAVEGUIDE DESIGN	146
4.5.1	Connection loss with various core shapes	148
4.5.2	Connection loss with various NAs of SI cores	149
4.5.3	Connection loss with various core sizes	151
4.5.4	Connection loss with imperfection within cores	154

4.5.5 Conclusion	156
REFERENCE	157
5. SUMMARY	159
APPENDIX A SAMPLE CODES FOR RAY TRAJECTORY IN A RECTANGULAR GI MEDIA	161
AKNOWLEDGEMENT	166

LIST OF FIGURES

1.1	The single layer PPOW fabricated by IBM Research - Zurich has 35 μm core size and 62.5 μm pitch [17].	6
2.1	Schematic representation of a ray path in GI medium.	16
2.2	Ray path in a parabolic profile fiber [3].	16
2.3	Calculated ray path for parabolic index profile described by Eq. (2-4) with different initial conditions (a) three dimensional view and (b) two dimensional view. In this calculation, $n_{co} = 1.507$, $n_{cl} = 1.492$, and core size is 50 μm . The starting point is (30, 0, 0).	19
2.4	The configuration of tunneling ray in a GI circular core.	21
2.5	The exponential decay of transmission coefficient (T_{tun}) of tunneling ray. In this calculation, $n_{co} = 1.507$, $n_{cl} = 1.492$, and core size is 50 μm .	21
2.6	An example of refracting ray with a starting point (30, 0, 0) and $\theta_z = 7^\circ$. The cross points are mutually symmetric points according the line OP .	26
2.7	Examples of ray path for rectangular shape GI media. The launching point in all the cases is the same, and other parameters are shown above of each figure.	26
2.8	Ray trajectories in an SI circular core (a) 3D view and (b) top view. The launching point is (30, 0, 0), $n_{co} = 1.507$, $n_{cl} = 1.492$, and $\theta_z = 3^\circ$.	28
2.9	The configuration of tunneling ray in an SI circular core.	29
2.10	A single ray is launched at the exit of light source.	31
2.11	Multiple rays injected into the core. (a) 200 bound rays generated by the Monte-Carlo method. (b) Angle (θ_z) distribution of the 200 rays in (a).	32
2.12	(a) The small light spot is enlarged by the scattering effect. (b) Simulated angle distribution according to Eq. (2-22) with $\theta_z = 10^\circ$ and $\sigma = 3$ (1000 examples). (c) An example for the calculation.	35
2.13	The same launching position (a) without and (b) with scattering effect considered. In this calculation, the launching point is (30, 0, 0), $n_{co} = 1.507$, $n_{cl} = 1.492$, and $\theta_z = 3^\circ$.	37
2.14	The biased launch with a Gaussian distributed field: (a) no offset, (b) 10 μm offset, and (c) 20 μm offset. The $n_{co} = 1.507$, $n_{cl} = 1.492$, and core size is 50 μm .	38
2.15	The concept of a ray scattered by rough core/cladding boundary.	40
2.16	Random rough surface and its mean plane [6].	41
2.17	Random rough surface generated by moving average method. In this	43

calculation, $\sigma_x = 0.4 \mu\text{m}$, $\lambda_x = 0.3 \mu\text{m}$, $\sigma_y = 0.25 \mu\text{m}$, $\lambda_y = 0.6 \mu\text{m}$.

2.18	Scattering geometry for plane wave incident [6].	43
2.19	The calculated scattered pattern based on Eq. 2-27. In both cases, $x = -5 \sim 5 \mu\text{m}$. (a) $\theta_i = 70^\circ$ is fixed. (b) $\sigma = 0.1 \mu\text{m}$ is fixed.	45
3.1	The layout of a rectangular dielectric waveguide core embedded in a homogeneous media.	49
3.2	Examples of modes calculated from series expansion method with corresponding effective indices. Each of figures represents the amplitude of a modal field within core area. (a) Bound modes with $n_{eff} > 1.492$. (b) Leaky modes with $n_{eff} < 1.492$. (c) The color map applied to the above figures.	51
3.3	Flow chart of FD-BPM in two dimension condition.	57
3.4	Output profile calculated by three dimensional FD-BPM (a) launching field in a (b) GI waveguide (c) SI waveguide.	58
3.5	Coordinate system for waveguide output and far field plane.	60
3.6	Coordinate geometry for and Mie scattering.	61
3.7	Scattered pattern with corresponding (a) polarization state (particle diameter is $10 \mu\text{m}$) and (b) particle diameters (incident light is S polarized). Both cases are calculated under $m = 1$, $n_{med} = 1.5$, $\lambda = 0.85 \mu\text{m}$ and in logarithm scale.	64
3.8	Comparison of output pattern between a typical Gaussian profile broadened in a uniform media and calculated by FD-BPM.	69
3.9	(a) The particle with index of 1 is centered at $z = 10 \mu\text{m}$, where the two white curves beside the particle represent estimated width of the Gaussian beam. (b) The far field profile based on formulations introduced in Sec. 3.5.1.	71
3.10	Intensity profile by FD-BPM at (a) $20 \mu\text{m}$ (b) $60 \mu\text{m}$.	72
	Intensity profile by FD-BPM at (c) $200 \mu\text{m}$ (d) $1000 \mu\text{m}$.	73
	(e) The intensity profile of a Gaussian beam scattered by a circular particle.	74
4.1	The molecule of (a) poly methyl methacrylate (PMMA) (b) poly benzyl methacrylate (PBzMA) (c) diphenyl sulphide (DPS).	79
4.2	The GI PPOW with 20-wt.% BzMA for core material. (a) Cross section image, and (b) the waveguide is launched by a white light source.	80
4.3	(a) The white light interference fringes and (b) the measured refractive index profile along the white dash line in Fig. 4.3(a)	82
4.4	The measured spectrum with corresponding waveguide length for loss	84

measurement.	
4.5 The measured intensity map for crosstalk measurement	84
4.6 The calculated NFP under offset launching conditions (a) without and (b) with scattering effect. The offset distance from left to right is 10, 20, 30 and 40 μm . In this simulation $p = 10\%$, $N_s = 5$ and $\theta_m = 20$ is applied. The white circle surround the calculated NFP is the assumed core-cladding boundary.	87
4.7 The calculated NFP for (a) launching condition (b) without and (c) with scattering effect included for a GI multi-channel waveguide. In this simulation, the parameters are identical as single channel case.	90
4.8 The scattering probability p dominates the scattering loss and shows the unexpected propagation length dependence.	91
4.9 (a) The loss value (in dB/cm) for the center channel. (b) The crosstalk value (in dB) for the right channel and (c) left channel.	92
4.10 Fabrication process of W-shaped refractive index profile PPOW.	95
4.11 (a) W-shaped and (b) previously obtained GI-PPOW illuminated by a Halogen-Tungsten lump	97
4.12 Near-field patterns of GI PPOW (a) when the core center and (b) cladding are launched and W-shaped PPOW (c) when the core center and (d) cladding are launched.	97
4.13 Propagation loss of SI, GI, and W-shaped PPOW.	98
4.14 The interference fringe patters (top) and its corresponding refractive index profile (bottom) of (a) GI (b) W-shaped profile with 3.66 wt. % BzMA PPOW.	101
4.15 Experimental setup for inter-channel crosstalk measurement.	101
4.16 Output intensity when one of the cores (second from the left) in waveguides is launched via (a) SMF probe (RML condition) and (b) MMF probe (near OML condition). The concentration of BzMA for W-shaped profile PPOW here is 10 wt. %.	101
4.17 (a) The measured refractive index profile of W-shaped profile PPOW with 10 wt. % BzMA in cladding. In the right side are the calculated ray trajectories with different incident angles. (b) The theoretical modeling of refractive index profile according to Eq. (1).	104
4.18 The launching condition for the simulation. We apply the same condition as the experimental setup in which the second core from the left side is launched by an MMF (50 μm in diameter).	106
4.19 Calculated NFP and propagation loss with corresponding output end (1 cm to 5 cm) for various refractive index of cladding under very lossy condition: (a) 1.492 (GI), 0.56 dB/cm (b) 1.495 (3.66 wt. %), 0.58 dB/cm (c) 1.499 (10 wt. %), 0.60 dB/cm (d) 1.502 (15 wt. %), 0.60	109

	dB/cm.	
4.20	Calculated results by ray trace simulation: (a) Output intensity from the launched core. (b) Output intensity from the whole cladding. (c) Crosstalk value (XT) to the left-edge core. (d) Crosstalk value to the third core from the left edge.	109
4.21	Calculated NFP and propagation loss of W-shaped PPOWs with various refractive index of cladding compared to that of GI PPOW: (a) 1.492 (GI), 0.26 dB/cm (b) 1.495 (3.66 wt. %), 0.26 dB/cm (c) 1.499 (10 wt. %), 0.27 dB/cm (d) 1.502 (15 wt. %), 0.26 dB/cm.	110
4.22	Calculated results by ray trace simulation (a) Output intensity from the launched core. (b) Output intensity from the whole cladding. (c) Crosstalk value (XT) to the left-edge core. (d) Crosstalk value to the third core from the left edge.	110
4.23	Modeling layout of this calculation.	113
4.24	(a) VCSEL output pattern after SMF. (b) Multi-core GI or SI PPOW ($n_{co} = 1.581$, $n_{cl} = 1.541$, $NA = 0.35$). (c) MMF ($n_{co} = 1.4525$, $n_{cl} = 1.43866$, $NA = 0.2$). (d) Photo diode.	113
4.25	$NA(r)$ of MMF for this calculation.	114
4.26	Centered launching condition in this calculation. A ray originates from a virtual point inside VCSEL. The ray is reflected by uniform medium ($n = 1.5$).	116
4.27	Number of rays is 1000 and total intensity is 432.69. (a) NFP of VCSEL exit (S1) (b) NFP of the waveguide entrance (S2) (c) angle distribution of rays in (a). (d) Angle distribution of rays in (b).	116
4.28	Refractive index profile for (a) SI (b) GI waveguides.	117
4.29	Calculated scattered field with roughness around 0.1 μm .	118
4.30	The relation between incident and scattered rays.	118
4.31	NFP for end 2, 3 and 4. (a) SIWG (b) SIWGr (c) GIWG (d) GIWGr. From top to down of terminal II and IV corresponds to 1 to 5 cm. All of the calculated NFPs are shown with the same thermal color table (maximum value = 1).	121
4.32	Intensity distribution of rays for (a) TxSIWG (b) TxSIWGr (c) TxGIWG (d) TxGIWGr. From top to down corresponds to 1 to 5 cm. Here, $n_{co} = 1.581$ and $n_{cl} = 1.541$.	122
4.33	Intensity distribution of rays right after MMF for (a) TxSIWG (b) TxSIWGr (c) TxGIWG (d) TxGIWGr. Here, $n_{co} = 1.4525$ and $n_{cl} = 1.4387$.	122
4.34	Intensity distribution of rays for (a) RxSIWG (b) RxSIWGr (c) RxGIWG (d) RxGIWGr. From top to down corresponds to 1 to 5 cm.	123

Here, $n_{co} = 1.581$ and $n_{cl} = 1.541$.

- 4.35 Numerical results of optical link with SIWG-MMF-SIWG configuration without rough core/cladding boundary. There is almost no loss in both Tx and Rx parts. 127
- 4.36 Numerical results of optical link with SIWG-MMF-SIWG configuration with rough core/cladding boundary. The loss is 0.173 dB/cm and 0.218 dB/cm for TxSIWGr and RxSIWGr, respectively. 128
- 4.37 Numerical results of optical link with GIWG-MMF-GIWG configuration without rough core/cladding boundary. There is almost no loss in WGTx and 0.03 dB/cm loss in WGRx parts. 129
- 4.38 Numerical results of optical link with GIWG-MMF-GIWG configuration with rough core/cladding boundary. There is almost no loss in WGTx and 0.041 dB/cm loss in WGRx parts. 130
- 4.39 The PMMA based GI-PPOW with square shape cores fabricated using the preform method. (a) The waveguide is attached on a glass plate. (b) cross section and (c) top view image of the waveguide. (d) interference fringes show the graded index profile in the core area. 132
- 4.40 Experimental setup of the optical link. 133
- 4.41 For convenience, we designate nine ends (1 to 9) to show the optical properties when the light propagates from VCSEL to the power meter. The corresponding measured NFP are also shown for the ends 1, 3, 5, 7, and 9. 133
- 4.42 Evaluation of alignment tolerance between GI-GI-GI and SI-GI-SI connection. The corresponding NFPs without offset for end 1, 3, and 5 are also listed. 136
- 4.43 (a) The modal field applied in the simulation and (b) measured output modal field from SMF. 138
- 4.44 (a) The scatterers are randomly distributed in the launched core with 100 μm space along propagation (z) direction. (b) Projection on the x - y plane of 1000 scatterers within the core area where scatterers are randomly placed as Gaussian distribution. 139
- 4.45 The calculated NFPs of the perfect condition: (a) NFP of end 3, (b) NFP of end 5, (c) NFP of end 7, and (d) NFP of end 9. 141
- 4.46 The calculated NFPs of the second consideration: (a) NFP of end 3, (b) NFP of end 5, (c) NFP of end 7, and (d) NFP of end 9. 141
- 4.47 The calculated NFPs of the third consideration: (a) NFP of end 3, (b) NFP of end 5, (c) NFP of end 7, and (d) NFP of end 9. 143
- 4.48 The calculated NFPs of the fourth consideration: (a) NFP of end 3, (b) NFP of end 5, (c) NFP of end 7, and (d) NFP of end 9. 143
- 4.49 Three kinds cores considered in Sec. 4.5.1 and their physical dimensions. 147

(a) Circular core, (b) Square core. (c) Trapezoidal core.

- | | | |
|------|---|-----|
| 4.50 | The total losses with corresponding core shapes and refractive index profiles. The meaning of ends (2), (3), (5), (7), and (9) in abscissa refer to Fig. 4.41. | 147 |
| 4.51 | The total loss for corresponding ends of (a) 50 μm and (b) 40 μm in diameter SI core waveguide based optical link. The meaning of ends (2), (3), (5), (7), and (9) in abscissa refer to Fig. 4.41. | 150 |
| 4.52 | The total loss for corresponding core size of (a) SI and (b) GI waveguide based optical link. The NA is 0.21 here. The meaning of ends (2), (3), (5), (7), and (9) in abscissa refer to Fig. 4.41. | 153 |
| 4.53 | The total loss for corresponding core size of (a) SI and (b) GI waveguide based optical link. In this case scattering effect is involved. The meaning of ends (2), (3), (5), (7), and (9) in abscissa refer to Fig. 4.41. | 155 |

LIST OF TABLES

1.1	OSI model for communication system	2
1.2	Server physical interconnection hierarchy	3
1.3	Summarized works in this dissertation	11
2.1	Classification of rays and corresponding calculated ray paths	24
3.1	Parameters applied in Fig. 3.2	52
3.2	Parameters applied in Sec. 3.5.2	70
4.1	Measurement results of the waveguides	86
4.2	Crosstalk value and refractive index with corresponding concentration	103
4.3	Crosstalk value in 5-cm GI and W-shaped PPOWs	103
4.4	Parameters for calculation by ray tracing method	107
4.5	Parameters for calculation	119
4.6	Numerical Results for SI waveguide without roughness	127
4.7	Numerical Results for SI waveguide with roughness	128
4.8	Numerical Results for GI waveguide without roughness	129
4.9	Numerical Results for GI waveguide with roughness	130
4.10	Measured parameters of the fabricated square shape GI-POW	135
4.11	Connection loss measurement	135
4.12	Total connection loss difference between GI and SI fiber based optical link	137
4.13	Calculation results of GI waveguide based optical link	145
4.14	Parameters for waveguide based optical with different core shapes	149
4.15	Parameters for waveguide based optical links	151
4.16	Parameters for waveguide based optical link	152

ABSTRACT

The increasing requirement of calculation power provided by high performance computers (HPCs) leads a trend in board level data communication from electrical to optical interconnections. Currently, much attention is focused on chip-to-chip data exchange realized with polymer parallel optical waveguides (PPOWs) integrated on printed circuit boards. The purpose of this research is to model the behavior of lightwave in PPOWs for the application of on-board optical interconnection. Particularly, the advantage of graded-index (GI) core PPOWs over the step-index (SI) core counterpart for high-speed and high-density wiring is quantitatively discussed by simulating the optical properties of PPOWs.

Chapter 1 is the introduction for short range optical interconnection and motivation of this research.

In Chapter 2, the author addresses the optical characteristics of waveguides with ray optics. Compared to various theoretical approaches based on wave optics to analyze optical waveguides, ray optics is less general and approximated. However, for this research, ray optics not only gives us more clear physical picture but is comprehensive, since PPOWs support large number of propagating modes (multimode waveguide). In this chapter, the ray trajectories in SI and GI media are described first. Next, the launching condition generated by Monte-Carlo method and imperfections in core area are discussed in order to make the model more practical.

In Chapter 3, the author starts from the scalar wave equation to describe the plane wave propagation inside optical waveguides. Then, the finite difference beam propagation method (FD-BPM) is applied to waveguide analysis, in order to simulate the optical loss caused by air gap at waveguides connections. In addition, the optical loss and inter-channel crosstalk caused by biased launching conditions and light scattering are simulated using the FD-BPM. All of the features can be realized by the equations mentioned in this chapter, so that the self-developed computer programs based on wave optics contribute to involve the desired considerations with higher degree of freedom.

In the first two sections of Chapter 4, two types of GI waveguides are experimentally fabricated using the preform method. Then, the fabricated waveguides are characterized, and the measured optical properties are compared with those simulated using the ray tracing method. Furthermore, the theoretical model is extended from each optical device to the total optical link. The behavior of lightwave inside a typical link model is simulated totally using the FD-BPM. All of the calculation results in this chapter show more or less coincidence with the observed

phenomena.

In Chapter 5, the author summarizes the prospects and concerns of proposed methods, and discuss about the future plans for successors. Through this research, the author develops numerical ways which are started from fundamental equations, and then the author shows the flexibility of the simulation models for the application of short range optical interconnection utilizing PPOWs. The development of these numerical ways can not only apply to the high speed optical interconnection, but for the next generation silicon photonics applications.

1

INTRODUCTION

1.1 SHORT RANGE OPTICAL INTERCONNECTION

1.2 ISSUES AND CHALLENGES

1.3 DISSERTATION OVERVIEW

In this dissertation, some numerical methods are presented in order to analyze the optical characteristics of parallel polymer optical waveguides (PPOWs) which are applied to board level interconnections. Although it is well recognized that optical interconnection has much higher potential than electrical interconnection such as low power dissipation, capability of more compact interface, etc., some better solutions are still aspired in the inter-component alignment issue and material of waveguides. In this dissertation, the best solution to address these issues are not necessarily proposed, instead, we try to understand the origins of the problems and think about how to improve the applications. We start from fundamental ray and wave optics to model the performance of optical links composed of PPOWs, and then the calculated results are verified experimentally. This helps us to improve the waveguide design and experimental setup for the next stage research topics.

In our laboratory, the PPOW have been developed by applying the techniques of designing and fabricating polymer optical fibers (POFs), where many harbingers have





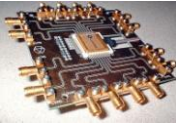
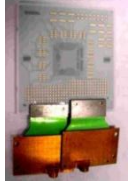

made it feasible in the past fifteen years. The advantages such as high bandwidth and low cost of POF have been extended to PPOW in these years, and many prominent experimental results have been published from our group. Hence, the main research topic of current our laboratory is shifting from meter-scale networks for appliances to the board level (less than 1-meter link length) computer communications. Although the propagation loss of the waveguides is less serious in such a short-reach link, there are still some key issues that limit the overall link performance. In the following sections, current trends and applications of short range optical interconnection are introduced. Then the issues are discussed in more detail and some specified solutions are described.

Table 1.1 OSI model for communication system

OSI Model			
	Data unit	Layer	Function
Host layers	Data	7. Application	Network process to application
		6. Presentation	Data representation, Encryption and decryption, Convert machine dependent data to machine independent data
		5. Session	Inter-host communication, Managing sessions between applications
	Segments	4. Transport	End-to-end connections, Reliability and flow control
Media layers	Packet/Datagram	3. Network	Path determination and logical addressing
	Frame	2. Data link	Physical addressing
	Bit	1. Physical	Media, Signal and binary transmission

1.1 SHORT RANGE OPTICAL INTERCONNECTION

Table 1.2 Server physical interconnection hierarchy

	Length	No. of lines per link	No. of lines per system	Standards	Use of optics
 WAN ¹¹	Multi-km	One	Tens	Internet Protocol, SONET, ATM	Since the 1980s
 Cables-long ¹²	100 - 300 m	One to tens	Tens to thousands	LAN/SAN (Ethernet, InfiniBand, Fiber Channel)	Since the 1990s
 Cables-short ¹³	1 - 10 m	One to tens	Tens to thousands	Design-specific, LAN/SAN (Ethernet, InfiniBand)	Present time, or very soon
 Card-to-card ¹⁴	0.3 - 1 m	One to hundreds	Tens to thousands	Design-specific and standards (PCI, backplane InfiniBand and Ethernet)	2005 - 2010 with effort
 Intra-card ¹⁵	0.1 - 0.3 m	One to hundreds	Thousands	Design-specific, generally	2010 - 2015
 Intra-module ⁴	5- 100 mm	One to hundreds	Approximately ten thousand	Design-specific	Probably after 2015
 Intra-chip ¹⁶	0 - 20 mm	One to hundreds	Hundreds of thousands	Design-specific	Later

It is persuasive to say that the information and communication technologies would remain one of the cutting-edge technologies in the near future. Particularly in recent five years, since the broadband internet access is realized with both wired and wireless networks such as fiber to the home (FTTH) and 3G network, the explosive growth of various kinds of internet services draws lots of attention world-wide. Behind our intensive daily use of information transfer, the well-developed communication hierarchy is no doubt to be the core of this technique. In our researches, we also belong to a part of this hierarchy, and more and more innovative ideas become feasible to make the quality of communication more smooth and cost effective.

Table 1.1 shows the Open System Interconnection (OSI) model which functionally divides the communication hierarchy into seven layers [1]. Each entity interacts directly only with the layer immediately beneath it, and provides facilities for use by the layer above it. As mentioned in the preface of this chapter, we have been engaged in research and development of information transmission media, which belongs to the most fundamental part: the physical layer of the communication system. We fabricated high-bandwidth (up to 25 Gbps) and low-cost (polymer as the raw material) optical waveguides [2, 3] as a data transfer medium enabling the optical interconnections inside HPCs (high performance computers) and supercomputers. Table 1.2 shows the server physical interconnection hierarchy from WAN (wide area network) to intra-chip scale [4]. Compared to the widely used optical fiber based communication developed in the past several decades, the target of this research is in much shorter range as several-centimeter, in general, to several meters in link length. Even in so-called “Computer communication” fields shown in Table 1.2, optical technology has already penetrated into the interconnections of backplanes and racks. For next generation, the

exaflop-scale computing systems, on-board and intra-chip optical interconnects are expected to provide even higher-density wiring, higher-speed transmission, and lower-power consumption.

The demand for short-distance optical interconnection is mainly to enable not only a bit rate higher than that of the conventional metal wire links which cannot keep up with the increasing clock speed of the processors, but also even more compact size of chip packaging. It is projected that while per-chip performance will continue to improve at a rate of approximately four times every three to four years [5], the number of signal pins per module will increase by only two times over the same period, and the maximum bit rate per signal pin will increase by only 35 %. Thus, the total off-chip I/O bandwidth (pin count times bit rate per pin) will increase by roughly 2.7 times; while the internal chip performance improves by four times that would dramatically affect balanced system design. Furthermore, the cost of packaging as a fraction of the overall packaged chip cost has been steadily increasing. Chip packages have increased in pin count at 10 % per year while decreasing per-pin cost only 5 % per year, yielding a per-chip increase in package cost of roughly 5 % per year, whereas silicon has provided a performance improvement of four times every three to four years, at a nearly constant cost [2]. Under these considerations, significant opportunities exist for the optical printed circuit boards (OPCBs), where it integrates the optical transceivers and multimode polymer optical waveguides are regarded as one of the most promising solutions.

There has been lots of articles talking about the optical performance for OPCBs with multimode waveguides embedded [6-10]. The design and quality of waveguides are surely the origin for these applications. In this dissertation, we fabricate some

featured multimode and multi-channel PPOWs, and we evaluate them both experimentally and theoretically, so that some innovative ideas make them more feasible to the practical use.

1.2 ISSUES AND CHALLENGES

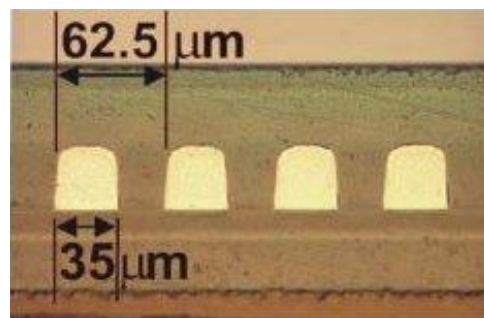


Fig. 1.1 The single layer PPOW fabricated by IBM Research - Zurich has 35- μm core size and 62.5- μm pitch [17].

Multimode and multi-channel PPOWs have been expected to be high-performance data communication devices for short range interconnections, ranging from on-board to board-to-board. Currently some key issues such as thermal stability and rough core/cladding boundary are hampering their practical usage.

For the polymer optical waveguides on PCBs, high thermal stability is required to endure the normal lamination ($\sim 180\text{ }^{\circ}\text{C}$) and solder reflow processes ($230\text{ }^{\circ}\text{C} \sim 260\text{ }^{\circ}\text{C}$) [17]. Hence, polymer materials that have high thermal stability have been chosen for comprising the polymer waveguides. However, there have been few polymer materials that satisfy the requirements of not only low optical loss but high thermal stability and low cost. Therefore, in most cases, polymer materials that show higher intrinsic scattering loss have been utilized, since thermal stability would be the first priority.

Furthermore, since photolithography or imprinting processes have been widely

utilized for fabricating the polymer waveguides directly on-board, the conventional polymer waveguides have had step-index (SI) rectangular cores, in which the lightwave coupled to cores propagates with total internal reflection. Thus, extra attention has been focused on the waveguide fabrication process to obtain a smooth surface at the core-cladding boundary in order to reduce the propagation loss [18]. However, the propagation loss would be 0.1 dB/cm or higher except for some state-of-the-art ones [6, 17], due to the excess scattering and absorption losses inherent to the polymer material and waveguide structure (SI core). Even in the case of polymer optical waveguides on-board, a data rate of 10 - 20 Gbps and less than 250- μm pitch are required in the past few years, and thus current trends of polymer waveguide design are in smaller core size ($\sim 35 \mu\text{m}$) and narrower inter-core pitch ($\sim 62.5 \mu\text{m}$) as shown in Fig. 1.1 [17]. Because of the high excess scattering loss, inter-channel crosstalk in those polymer optical waveguides is of great concern when much narrower pitch design is required for higher-density channel alignment [19, 20].

In order to address these problems, we have proposed to apply graded-index (GI) core polymer optical waveguides to such an on-board interconnection application [3, 21]. According to the previous studies, it was experimentally verified that the advantage of the GI-core polymer optical waveguide is the ability to reduce the propagation loss due to structural imperfections, transmitting a data rate of 12.5 Gbps and beyond through each channel, and decreasing the crosstalk value to less than -30 dB [3, 21]. However, since the previous GI-core waveguides we reported were composed of low-loss poly methyl methacrylate (PMMA), the thermal stability of the waveguides was not high enough. In particular, it was already confirmed that the GI profile formed by the concentration distribution of dopant was not stable at a temperature higher than

85 °C [22]. In order to increase the thermal stability of the GI-core polymer optical waveguides, it is required to substitute PMMA for other polymer materials with a high glass transition temperature, while it could have higher excess scattering loss. Therefore, in this dissertation, how the scattering loss affects the inter-channel crosstalk in GI-core polymer optical waveguides is investigated both theoretically and experimentally. Furthermore, the fabrication process of the GI-core polymer waveguides are actively improved, by which an index valley is involved between the core and cladding of GI-cores to obtain W-shaped index profile. The outstanding performance reducing inter-channel crosstalk is exhibited by the newly developed polymer waveguides with W-shaped cores.

Furthermore, the application of polymer waveguides in an optical link is highlighted, where it incorporates with vertical cavity surface emitting laser (VCSEL), a pair of optical waveguide for data transmitter (Tx) and receiver (Rx) which are connected together by a multimode fiber, and photo diode. In this application, another key issue is generated. Presently, the rectangular shape, multichannel and multimode step index (SI) polymer optical waveguides are extensively deployed in such optical links, and they are mainly applied to 10 Gbps links with several centimeter waveguide length. Under such a short length, the connection loss becomes the main role of link power budget. Furthermore, for the next generation HPCs with a bus speed up to 20 Gbps or even higher, the performance of the link is more sensitive to alignment and modal dispersion. Here, the GI waveguide based optical link could be one of the promising solutions to minimize the link power budget.

We have experimentally and theoretically demonstrated the superior optical characteristics of GI-POWs than the SI counterparts, such as better optical field

confinement and lower inter-channel crosstalk [23, 24]. In the later chapters of this dissertation, the connection loss evaluation of an optical link is discussed, where a pair of GI waveguides is applied as transmission (WG_{Tx}) and reception (WG_{Rx}) interface as mentioned before. In order to analyze optical performance and the cause of connection loss, a specified theoretical model for this optical link is created. A wide variety of algorithms have been developed for the simulation of passive photonic devices, where light is propagating in a medium whose refractive index has no big change. The beam propagation method (BPM) is one of these mainstream usages. In this study, in order to consider the features such as scattering effect and Fresnel reflection, the BPM algorithm with finite difference procedure (FD-BPM) is developed [25]. The theoretical modeling is started from the three-dimensional scalar wave equation under the consideration of slow varying envelop approximation (SVEA), the desired features mentioned above is modeled efficiently and straight forward.

1.3 DISSERTATION OVERVIEW

In chapter 2, the optical characteristics of waveguides are addressed utilizing ray optics. Compared to various theoretical approaches based on wave optics to analyze optical waveguides, ray optics is less general and approximated. However, for this research, ray optics not only gives us more clear physical picture but is comprehensive, since PPOWs support large number of propagating modes (multimode waveguide). In this chapter, the ray trajectories in SI and GI media are described first. Next, the launching condition generated by Monte-Carlo method and imperfections in core area are discussed in order to make the model more practical. In Chapter 3, the author starts from the scalar wave equation to describe the plane wave propagation inside optical

waveguides. Then, the finite difference beam propagation method (FD-BPM) is applied to waveguide analysis, in order to simulate the optical loss caused by air gap at waveguides connections. In addition, the optical loss and inter-channel crosstalk caused by biased launching conditions and light scattering are simulated using the FD-BPM. All of the features can be realized by the equations mentioned in Chapter 3, so that the self-developed computer programs based on wave optics contribute to involve the desired considerations with higher degree of freedom.

According to Chapters 2 and 3, we are well prepared to apply the required knowledge to simulate optical characteristics of PPOWs. In the first two sections of Chapter 4, two types of GI waveguides are experimentally fabricated using the preform method. Then, the fabricated waveguides are characterized, and the measured optical properties are compared with those simulated using the ray tracing method. Furthermore, the theoretical model is extended from each optical device to the total optical link. The behavior of lightwave inside a typical link model is simulated totally using the FD-BPM. All of the calculation results in this chapter show more or less coincidence with the observed phenomena.

Through this research, the authors develop numerical ways which are started from fundamental equations, and then the authors show the flexibility of our simulation models for the application of short range optical interconnection utilizing PPOWs. Finally the studies in this dissertation are summarized in Table 1.3.

In Chapter 5, the authors summarize the prospects and concerns of proposed methods, and discuss about the future plans for successors. The authors believe that the development of these numerical ways can not only apply to the high speed optical interconnection, but for the next generation silicon photonics applications. Table 1.3

summarized works in this dissertation.

Table 1.3 Summarized works in this dissertation

	Experiment and Measurement			Theoretical Modeling	
	Waveguide Fabrication	Crosstalk Evaluation	Loss Measurement	Ray Optics	Wave Optics
Copolymer Based PPOW	O	O	O	O	
W-shaped PPOW	O	O	O	O	
Optical Link				O	O

REFERENCES

1. OSI model
http://en.wikipedia.org/wiki/Osi_layer (2012.2.10)
2. A. F. Benner, et al., "Exploitation of optical interconnects in future server architectures," IBM J. Res. & Dev. 49(4/5), 755-775 (2005).
http://ieeexplore.ieee.org/xpl/freeabs_all.jsp?arnumber=5388810
3. Y. Takeyoshi and T. Ishigure, "High-density 2 × 4 channel polymer optical waveguide with graded-index circular cores," J. Lightw. Technol., 27(14), 2852-2861 (2009).
<http://ieeexplore.ieee.org/iel5/68/4351987/04367530.pdf?arnumber=4367530>
4. Evan G. Colgan, et al., "Direct integration of dense parallel optical interconnects on a first level package for high-end servers," Proc. 55th (ECTC), 228-233, (2005).
http://ieeexplore.ieee.org/xpls/abs_all.jsp?arnumber=1645749
5. International Technology Roadmap for Semiconductors (ITRS), Assembly and Packaging Chapter, Semiconductor Industry Association, 2003.
<http://www.itrs.net/links/2003itrs/execsum2003.pdf> (2012.2.10)
6. X. Wang, W. Jiang, L. Wang, H. Bi, and R. T. Chen, "Fully embedded board-level optical interconnects from waveguide fabrication to device integration," J. Lightw. Technol., 26(2), 243-250 (2008).
<http://ieeexplore.ieee.org/stamp/stamp.jsp?arnumber=04451236>
7. M. Karppinen, T. Alajoki, A. Tanskanen, K. Kataja, J.-T. Mäkinen, K. Kautio, P.

- Karioja, M. Immonen, and J. Kivilahti, "Parallel optical interconnect between ceramic BGA packages on FR4 board using embedded waveguides and passive optical alignments," Proc. 56th of ECTC, 219-225 (2006).
http://ieeexplore.ieee.org/xpl/freeabs_all.jsp?arnumber=1645749
8. Y. Taira, et al., "High channel-count optical interconnection for servers," Proc. 60th of ECTC, 282-286 (2010).
http://ieeexplore.ieee.org/xpl/freeabs_all.jsp?arnumber=5490959
 9. M. Tokunari, et al., "High-bandwidth density optical I/O for high-speed logic chip on waveguide-integrated organic carrier," Proc. 61st of ECTC, 819-822 (2011).
http://ieeexplore.ieee.org/xpl/freeabs_all.jsp?arnumber=5898605
 10. F. E. Doany, et al., "Terabit/sec-class board-level optical interconnects through polymer waveguides using 24-channel bidirectional transceiver modules," Proc. 61st (ECTC), 790-797, (2011).
http://ieeexplore.ieee.org/xpl/freeabs_all.jsp?arnumber=5898601
 11. WAN Acceleration from DataSpan
<http://www.dataspan.com/wan-acceleration> (2012.2.10)
 12. The case for data center power efficiency
<http://blog.cluttr.be/2011/01/26/the-case-for-data-center-power-efficiency/>
(2012.2.10)
 13. Data Center Cabling
<http://bored-bored.com/data-center-cabling> (2012.2.10)
 14. E2106: 2U INTEL rack mount server
<http://www.hpcsystems.com/products/servers/2U/E21066> (2012.2.10)
 15. CMOS Photonics: 10G modulator platform integrates high-speed optical fiber interfaces into high volume semiconductor chips (2005)
<http://www.yenra.com/photonics/> (2012.2.10)
 16. SPIE Professional: Foundry Service Aids Silicon Photonic Chips (2011)
<http://spie.org/x48934.xml> (2012.2.10)
 17. R. Dangel, C. Berger, R. Beyeler, L. Dellmann, M. Gmür, R. Hamelin, F. Horst, T. Lamprecht, T. Morf, S. Oggioni, M. Spreafico, and B. J. Offrein, "Polymer waveguide based board level optical interconnect technology for datacom applications," IEEE Trans. on Advanced Packaging, 31(4), 759-767 (2008).
http://ieeexplore.ieee.org/xpls/abs_all.jsp?arnumber=4674539
 18. W.M. Diffey, R.H. Trimm, M. G. Temmen, and P.R. Ashley, "Fabrication of low-loss optical-quality polymer waveguide facets in multilayer polymer devices using an inductively coupled plasma," J. Lightw. Technol., 23(4), 1787-1790

(2005).

http://ieeexplore.ieee.org/xpl/freeabs_all.jsp?arnumber=1424156

19. I. Papakonstantinou, D. R. Selviah, R. C. A. Pitwon, and D. Milward, "Low-cost, precision, self-alignment technique for coupling laser and photodiode arrays to polymer waveguide arrays on multilayer PCBs," *IEEE Trans. on Advanced Packaging*, 31(3), 502-511 (2008).
<http://ieeexplore.ieee.org/stamp/stamp.jsp?tp=&arnumber=4534823>
20. N. Bamiedakis, J. Beals, IV, R. V. Penty, I. H. White, J. V. DeGroot, Jr., and T. V. Clapp, "Cost-effective multimode polymer waveguides for high-speed on-board optical interconnects," *J. Quant. Electron.*, 45(4), 415-424 (2009).
<http://ieeexplore.ieee.org/stamp/stamp.jsp?tp=&arnumber=4803864>
21. T. Ishigure and Y. Takeyoshi, "Polymer waveguide with 4-channel graded-index circular cores for parallel optical interconnects," *Opt. Express*, 15(9), 5843-5850 (2007).
<http://www.opticsinfobase.org/abstract.cfm?uri=oe-15-9-5843>
22. M. Sato, T. Ishigure, and Y. Koike, "Thermally stable high-bandwidth graded-index polymer optical fiber," *J. Lightw. Technol.*, 18(7), 952-968 (2000).
<http://www.opticsinfobase.org/abstract.cfm?URI=jlt-18-7-952>
23. T. Ishigure and Y. Nitta, "Polymer optical waveguide with multiple graded-index cores for on-board interconnects fabricated using soft-lithography," *Opt. Express*, 18, 14191-14201 (2010).
<http://www.opticsinfobase.org/oe/abstract.cfm?uri=oe-18-13-14191>
24. H. H. Hsu and T. Ishigure, "High-density channel alignment of graded index core polymer optical waveguide and its crosstalk analysis with ray tracing method," *Opt. Express*, 18, 13368-13378 (2010).
<http://www.opticsinfobase.org/abstract.cfm?uri=oe-18-13-13368>
25. K. Okamoto, *Fundamentals of Optical Waveguides* (2nd edition, Elsevier, 2006).
<http://goo.gl/YnSy> (2012.2.10)

2

MODELING WITH RAY OPTICS

2.1 RAY TRAJECTORIES FOR GI CORE

2.2 RAY TRAJECTORIES FOR SI CORE

2.3 LAUNCHING CONDITION

2.4 SCATTERING EFFECT IN CORE AREA

2.5 ROUGH CORE/CLADDING BOUNDARY

Compared to various standard approaches based on wave optics to analyze optical waveguides, ray optics is less general and approximated. Due to the approximation that the physical dimension of the target is much larger than the wavelength ($\lambda \sim 0$), only multimode media can be applied. Particularly for our studies on weakly guiding ($\Delta < 1\%$) polymer optical waveguides, ray optics not only gives us more clear physical picture but is comprehensive, since PPOWs support large number of propagating modes. So far, ray tracing technique has been widely applied to analyze the behavior of light propagation in optical systems. In terms of our study, we combine the fundamental ray theory and some ideas about lightwave behavior within perturbed waveguide. The optical characteristics such as near field pattern (NFP), inter-channel crosstalk, and propagation loss can be theoretically estimated. In this chapter, the ray trajectories within SI and GI multimode waveguides are calculated first. Next, the launching

condition generated by the Monte-Carlo method and the consideration of imperfection within core area are investigated, which make the model more practical.

2.1 RAY TRAJECTORIES FOR GI CORE

GI polymer optical fibers (POFs) have been well developed in the past ten years. In order to obtain the best optical characteristics for Gbps level data communication applications, the refractive index profile is adjusted to be nearly a parabola. In recent years, our laboratory has extended the technique to form graded-index profiles to PPOWs, where we integrated several or even tens of GI cores in a bulk PMMA. The GI-PPOW makes it more practicable to realize high-speed and high-density board level data communications. In this section, we consider the ray behavior in single GI core first and then extend it to multiple GI cores. The GI and SI cores focused in this section have 50- μm core radius (ρ), and refractive indexes of cladding (n_{cl}) and core (n_{co}) to be 1.492 and 1.507, respectively.

2.1.1 Ray equations for a GI core

For analyzing the ray trajectories in graded index waveguides, the refractive index distribution is approximated by the power-law form shown by Eq. (2-1) in each circular-shaped core (channel) area of PPOWs. Here, the refractive index profile $n(r)$ as a function of the distance r from the core center is written with a parameter of index exponent g as [1]

$$n(r) = n_{co} \left[1 - 2\Delta \left(\frac{r}{\rho} \right)^g \right]^{1/2} \quad (2-1)$$

where Δ is the relative refractive index difference, n_{co} is the highest refractive index

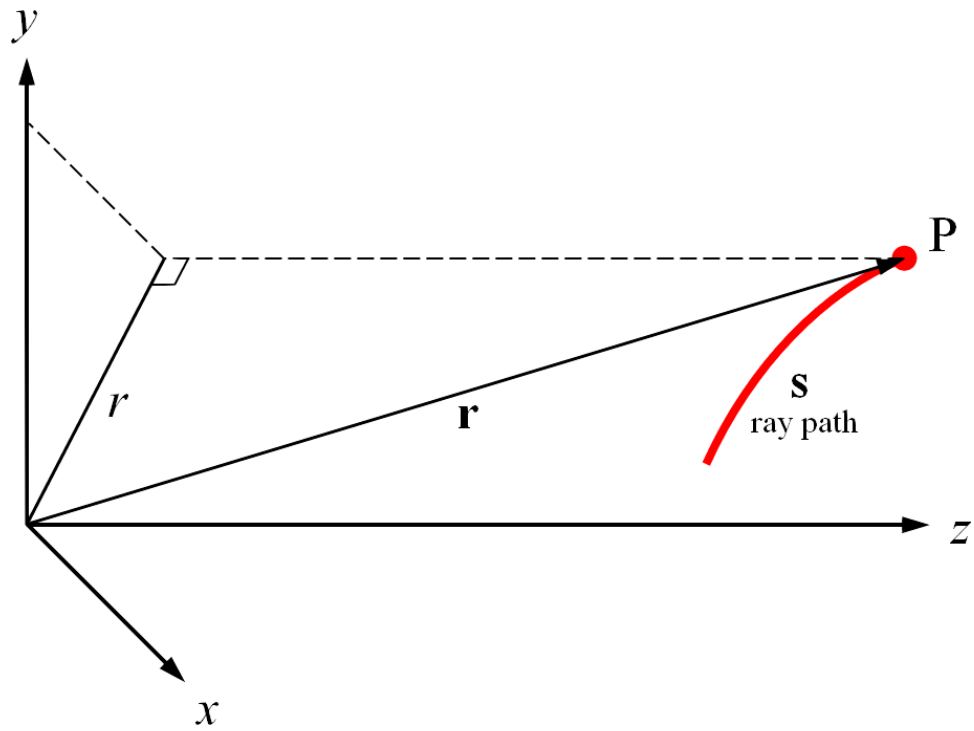


Fig. 2.1 Schematic representation of a ray path in GI medium.

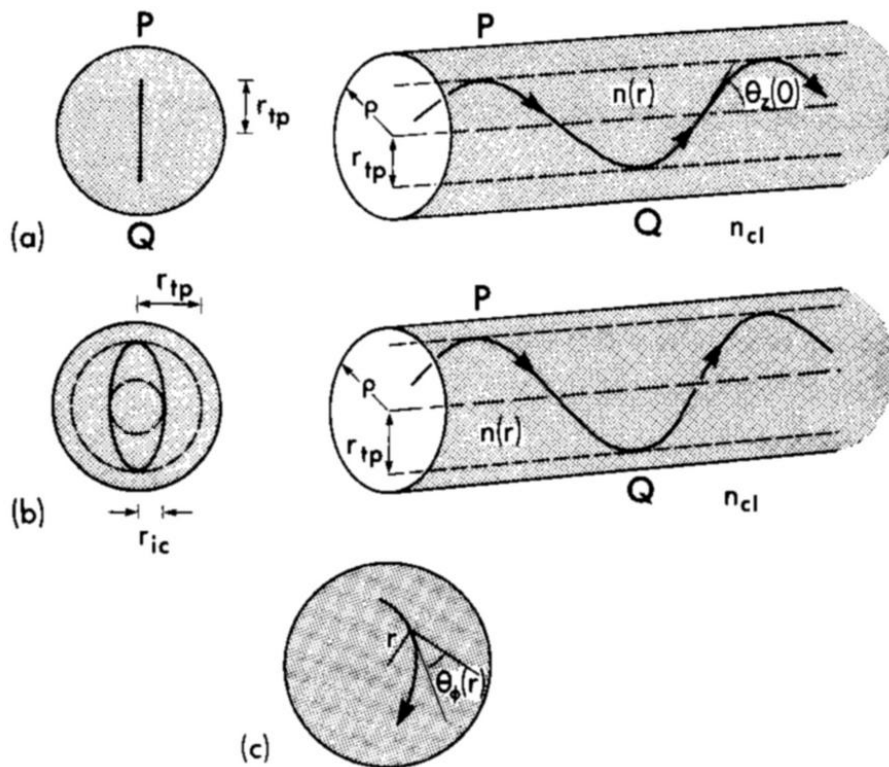


Fig. 2.2 Ray path in a parabolic profile fiber [3].

value in the core region (normally at the core center), and ρ is the core radius. In this section, we focus on a typical parabolic index profile ($g = 2$). The three dimensional route of rays in such a medium is obtained by solving the eikonal equation with the position vector (\mathbf{r}) expressed by spherical coordinate system. First, we consider a ray path in a three-dimensional space as shown in Fig. 2.1 [2]. For radially symmetric media, the general cylindrical form of the ray equations with respect to radial, azimuthal and longitudinal directions in (r, ϕ, z) is written as follows [3]:

$$\frac{d}{ds} \left\{ n(r) \frac{dr}{ds} \right\} - rn(r) \left(\frac{d\phi}{ds} \right)^2 = \frac{dn(r)}{dr} \quad (2-2a)$$

$$\frac{d}{ds} \left\{ n(r) \frac{d\phi}{ds} \right\} + \frac{2n(r)}{r} \frac{d\phi}{ds} \frac{dr}{ds} = 0 \quad (2-2b)$$

$$\frac{d}{ds} \left\{ n(r) \frac{dz}{ds} \right\} = 0 \quad (2-2c)$$

where s is the distance along the ray path. The zero at the right side of Eq. (2-2b) and Eq. (2-2c) leads the two invariants as follows:

$$\beta = n(r) \cos \theta_z(r) \quad (2-3a)$$

$$l = \frac{r}{\rho} n(r) \sin \theta_z(r) \cos \theta_\phi(r) \quad (2-3b)$$

where the definition of θ_z and θ_ϕ is shown in Fig. 2.2(a) and (c) [3]. The two invariants β and l which are constants independent of the position along ray path characterize the energy conservation of a ray, once the incident position is determined. Substitution of Eq. (2-3) to Eq. (2-2a) leads to the position of the ray along z direction:

$$z(r) = \bar{\beta} \int \frac{dr}{[n^2(r) - \beta^2 - l^2 \rho^2 / r^2]^{1/2}} \quad (2-4)$$

For an arbitrary GI profile, although the ray position along z direction can be easily obtained from Eq. (2.4), it is a quite tough work to find the position information in other two dimensions. In terms of this study, we consider the parabolic index profile as expressed by Eq. (2-1), the projection of a ray trajectory on the x - y plane could be an ellipse with the short axis r_{ic} (inner caustic) and the long axis r_{tp} (turning point) which are described as follows:

$$r_{ic} = \frac{\rho}{2n_{co}\Delta^{1/2}} [(n_{co}^2 - \beta^2) - \{(n_{co}^2 - \beta^2)^2 - 8\Delta l^2 n_{co}^2\}^{1/2}]^{1/2} \quad (2-5a)$$

$$r_{tp} = \frac{\rho}{2n_{co}\Delta^{1/2}} [(n_{co}^2 - \beta^2) + \{(n_{co}^2 - \beta^2)^2 - 8\Delta l^2 n_{co}^2\}^{1/2}]^{1/2} \quad (2-5b)$$

When r_{ic} is zero, so-called meridional ray, the projection of ray trajectory is a line as shown in Fig. 2.2(a). The general case that r_{ic} and r_{tp} are not zero, so-called skew ray, and the projection of ray trajectory is an ellipse as shown in Fig. 2.2(b).

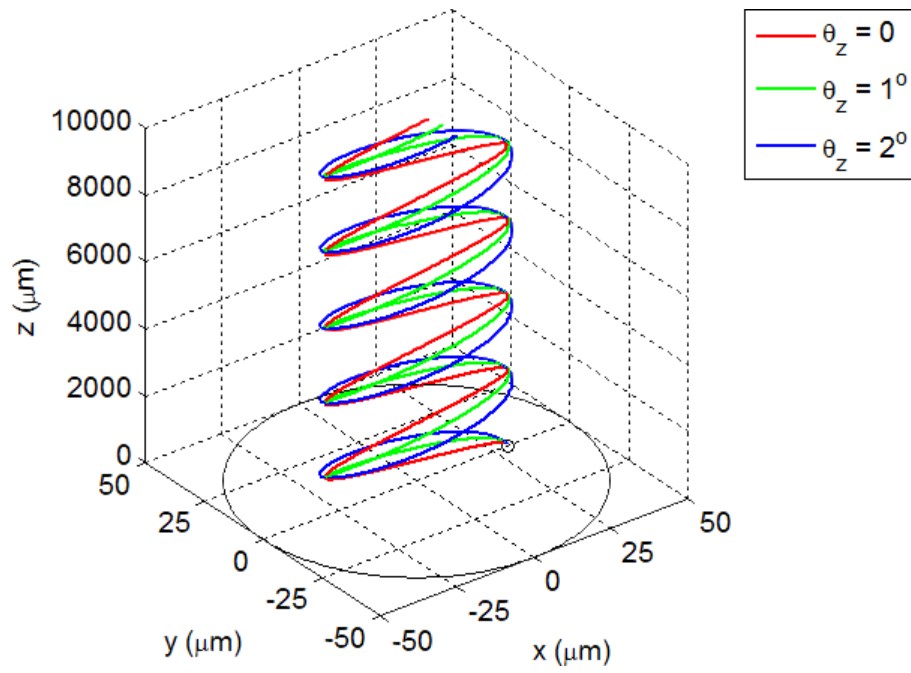
2.1.2 Classification of rays and ray trajectories

The characteristics of rays, such as trajectory and intensity, are determined by the incident position and angle to z -axis, i.e. the launching condition. Rays are classified into three: bound rays, tunneling rays, and refracting rays according to the level of intensity loss. The criterions of the classification of rays are as follows:

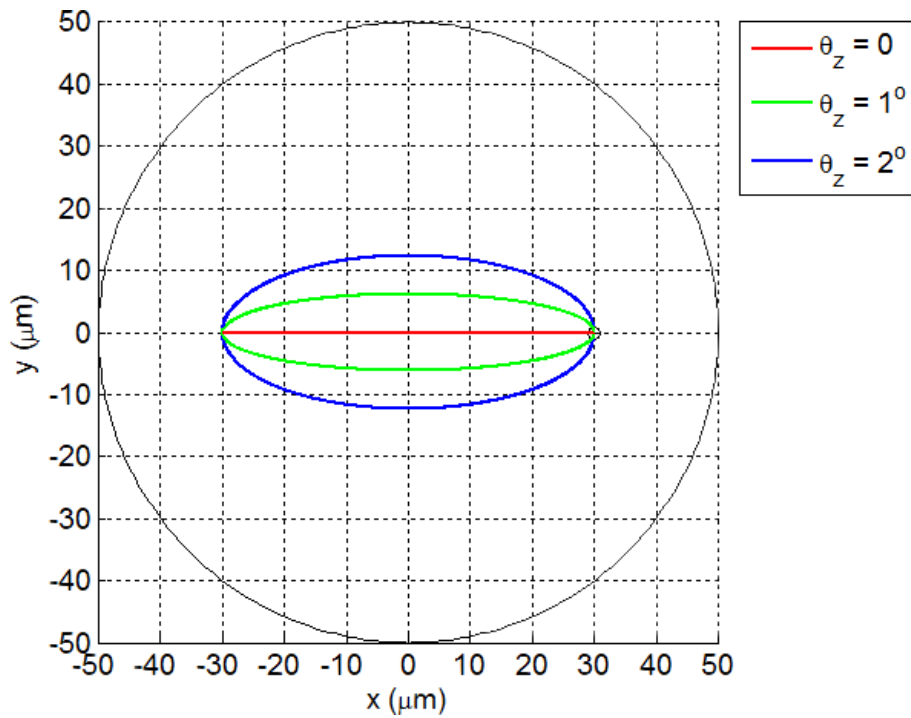
$$\begin{aligned} \text{Bound rays:} & \quad n_{cl} < \beta \leq n_{co} \\ \text{Refracting rays:} & \quad 0 \leq \sqrt{\beta^2 + l^2} < n_{cl} \\ \text{Tunneling rays:} & \quad \beta < n_{cl} \leq \sqrt{\beta^2 + l^2} \end{aligned} \quad (2-6)$$

- *Bound rays*

For bound rays, there is no intensity loss during propagation. According to Eq.



(a)



(b)

Fig. 2.3 Calculated ray path for parabolic index profile described by Eq. (2-4) with different initial conditions (a) three dimensional view and (b) two dimensional view. In this calculation, $n_{co} = 1.507$, $n_{cl} = 1.492$, and core size is $50 \mu\text{m}$. The starting point is $(30, 0, 0)$.

(2-3a), the more close to the boundary, the less tolerance of θ_z is allowed. That is to say, for rays parallel to the z axis never lose their intensity even the incident positions are very close to the core/cladding boundary. There is no question about calculation of ray path for the bound rays in a GI core with the parabolic index profile. Figure 2.3 shows the calculated ray trajectories and their projections with different θ_z .

- *Tunneling rays:*

It is proved that the intensity gradually lose and then radiate to the cladding when the trajectory closer and closer to the boundary with nonzero θ_z . Such rays are classified to tunneling rays. It is not enough to address the behavior of tunneling rays with conventional ray theories, so that the approximation based on so-called local plane wave is considered near the core/cladding boundary [2]. Except for some strongly wavelength dependent effects, the refractive index is regarded as nearly constant and changes slowly over a nearly distance of wavelength. Under this assumption, the electromagnetic fields can be expressed as individual plane waves. Based on the local plane wave approximation, the intensity of the ray exponentially decreases with the following transmission coefficient:

$$T_{tun} = \exp \left[-\frac{4\pi}{\lambda} \int_{r_p}^{r_{rad}} \{ \beta^2 + (l\rho/r)^2 - n^2(r) \}^{1/2} dr \right] \quad (2-7)$$

where the radiation caustic (r_{rad}) is defined as:

$$r_{rad} = \frac{\rho l}{(n_{cl}^2 - \beta^2)^{1/2}} \quad (2-8)$$

Figure 2.4 shows the concept of radiation loss for a tunneling ray. A part of power leaks when the ray reaches the turning point caustic (r_{tp}), and the level of power leakage is determined by Eq. (2-7). Note that the tunneled ray shown in Fig. 2.4 goes straight to

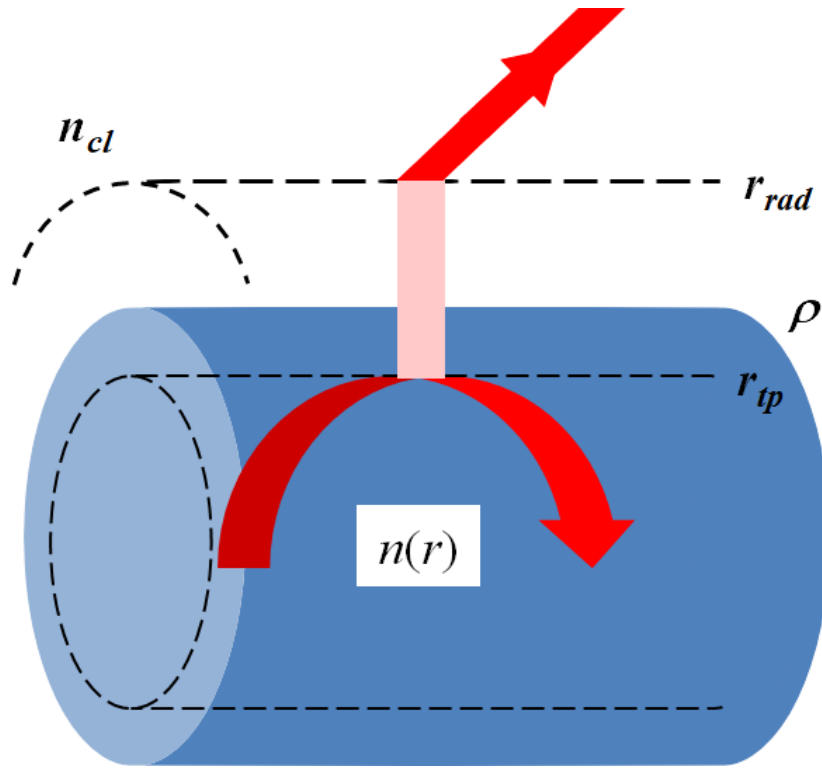


Fig. 2.4 The configuration of tunneling ray in a GI circular core.

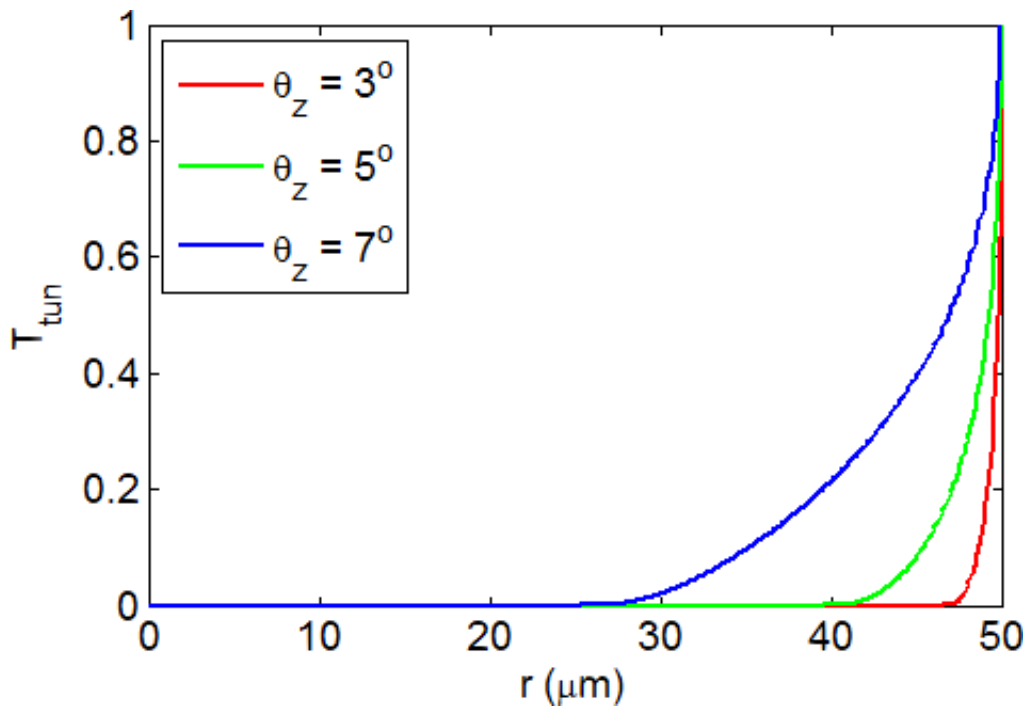


Fig. 2.5 The exponential decay of transmission coefficient (T_{tun}) of tunneling ray. In this calculation, $n_{co} = 1.507$, $n_{cl} = 1.492$, and core size is $50 \mu\text{m}$.

the cladding. The angle between the ray and z -axis determines whether it penetrates the cladding/air boundary or reflects continuously in the waveguides. Figure 2.5 shows the transmission coefficients calculated according to Eq. (2-7), where various incident angles to z -axis (θ_z) indicate different launching conditions. The larger the θ_z , the less tolerance for offset launch. Although actually there exists discontinuity of refractive index profile at the core/cladding boundary ($r = \rho$ and $r = \rho_+$), which makes T_{tm} never really equals to one, we still calculate the corresponding T_{tm} value under small enough dr (ex: $0.1 \mu\text{m}$) in Eq. (2-7).

- *Refracting rays:*

The name of refracting ray signifies the reflection and refraction happens simultaneously at the core/cladding boundary. When we focus on a circular core with parabolic index profile as given by Eq. (2-1), the $n(r)$ decreases monotonically from the center (z -) axis to the core/cladding boundary ($r = \rho$) and be constant n_{cl} in the cladding ($r > \rho$). The refracting ray actually includes reflecting and refracting parts, which correspond to inside and outside to the core. The trajectory inside the core is a combination of a part of ellipse, and some more mathematical treatments are required. First, the reflection part of trajectory is introduced. According to Eq. (2.3) to (2.5), the trajectory starts from the launching point and then stops at $r = \rho$. So far the formula of plane where original (\mathbf{O}) to the end point (\mathbf{P}) lie on can be calculated as follows:

$$ax + by + cz + d = 0 \quad (2-9)$$

Here, we choose five points $((x_i, y_i, z_i), i = 1 \text{ to } 5)$ on the previously calculated trajectory and find the corresponding symmetric points (x_i', y_i', z_i') with respect to line \mathbf{OP} :

$$(x'_i, y'_i, z'_i) = \left(x_i - \frac{2ak}{a^2 + b^2 + c^2}, y_i - \frac{2bk}{a^2 + b^2 + c^2}, z_i - \frac{2ck}{a^2 + b^2 + c^2} \right) \quad (2-10a)$$

where

$$k = ax_i + by_i + cz_i + d \quad (2-10b)$$

Next, we apply the general form of an ellipse:

$$Ax^2 + Bxy + Cy^2 + Dx + Ey = 1 \quad (2-11)$$

Substitution of the five symmetric points to Eq. (2-11) allows to obtain coefficients A and E and the reflected ray trajectory can also be obtained.

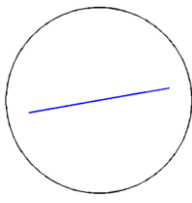
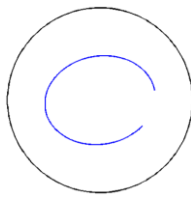
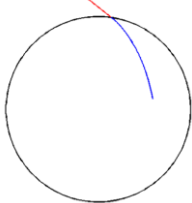
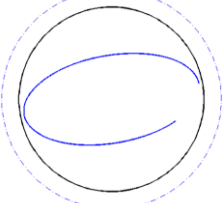
The calculation of refraction ray is relatively simpler. Since the refractive index is almost identical in a very tiny area of the interface, we can treat that the direction of refraction is determined by the gradient at the end of the first trajectory. Finally, the refraction part propagates as a straight line toward to cladding. By repeating the above procedures, the trajectory of refracting ray can be calculated. For the refracting rays, only the transmission coefficient (T_{ref}) located at the core/cladding boundary is required. Under the weakly guided approximation, the T_{ref} is expressed as follows:

$$T_{ref} = 1 - \frac{\lambda}{16\pi n_{cl}^3 \sin^6 \theta_t} \cdot \left(\left. \frac{dn^2(r)}{dr} \right|_{r=\rho^-} \right)^2 \quad (2-12)$$

where θ_t is the transmission angle between refracting ray and z -axis. Equation (2-12) is valid for all angles except that it is very close to zero. From the above descriptions, it is known that the calculation of ray trajectories of refracting rays is quite complicated. Fortunately, as we are considering the applications for POWs whose core/cladding interface is not clear, the refracting rays absolutely penetrate the interface and go

forward the cladding, hence, the T_{ref} is actually 1 for the actual situation. Those rays whose ray invariants fall into the criterion of refracting rays are no more calculated in single core condition, which is demonstrated in Fig. 2.6. In multi-channel waveguides, the refracting rays are continued to trace since they could be re-coupling to another core, which is one of the causes of inter-channel crosstalk. The classification of rays is summarized in Table 2.1 and examples of corresponding ray trajectories projected on the x - y plane are illustrated at the bottom of Table 2.1.

Table 2.1 Classification of rays and corresponding calculated ray paths

Ray Classification	Bound Ray		Leaky Ray	
	Meridional Ray	Skew Ray	Refracting Ray	Tunneling Ray
Ray Invariant	$n_{cl} < \beta \leq n_{co}$		$0 < \beta^2 + l^2 \leq n_{cl}^2$	$\beta < n_{cl} \leq \sqrt{l^2 + \beta^2}$
r_{tp}	$0 \leq r_{tp} < \rho$		ρ	$0 \leq r_{tp} < \rho$
r_{rad}	∞		ρ	$\rho \leq r_{rad} < \infty$
Examples				

2.1.3 Ray equations for a rectangular GI core

A rectangular-shape core is more general for optical waveguides, where the Cartesian coordinate system is applied. Compared to axially symmetric case expressed by Eq. (2-1), the refractive index profile should be modified as a two-dimensional index

map as follows:

$$n(x, y) = n_{co} \{1 - 2\Delta[f(x) + g(y)]\}^{1/2} \quad (2-13)$$

where $f(x) = |x/a_x|^p$ and $g(y) = |y/a_y|^q$ are two homogeneous functions with degree of p and q along x and y direction, respectively. Similarly, the ray equations along x , y , and z direction can be written as follows [3]:

$$\frac{d}{ds} \left[n(x, y) \frac{dx}{ds} \right] = \frac{\partial n(x, y)}{\partial x} \quad (2-14a)$$

$$\frac{d}{ds} \left[n(x, y) \frac{dy}{ds} \right] = \frac{\partial n(x, y)}{\partial y} \quad (2-14b)$$

$$\frac{d}{ds} \left[n(x, y) \frac{dz}{ds} \right] = 0 \quad (2-14c)$$

Note that only the right side of Eq. (2-14c) is zero, so that only translation ray invariant β can be expressed as [3, 4]:

$$\beta = n(x, y) \cos \theta_z(x, y) \quad (2-15a)$$

or in more specific form:

$$\beta = n_{co} \{1 - 2\Delta[f(x_{tp}) + g(y_{tp})]\}^{1/2} \quad (2-15b)$$

where x_{tp} and y_{tp} are the turning points in x and y direction, respectively. In this case, the z position of the ray is derived as follows:

$$z = \frac{1}{\Omega} \int \frac{dx}{[f(x_{tp}) - f(x)]^{1/2}} \quad (2-16a)$$

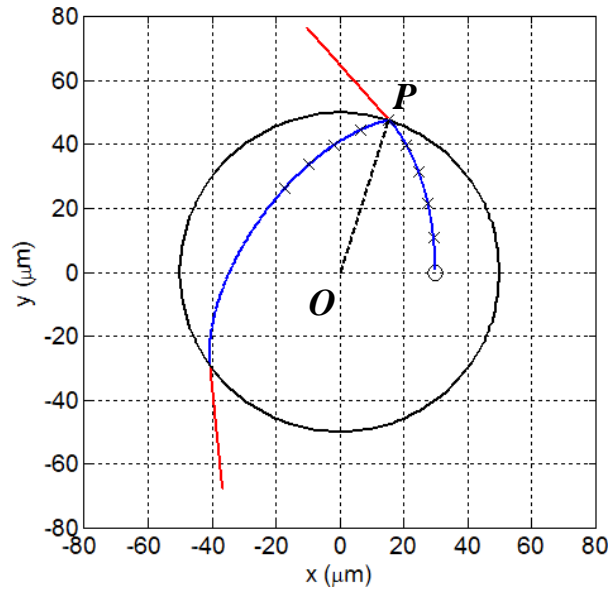


Fig. 2.6 An example of refracting ray with a starting point $(30, 0, 0)$ and $\theta_z = 7^\circ$. The cross points are mutually symmetric points according the line OP .

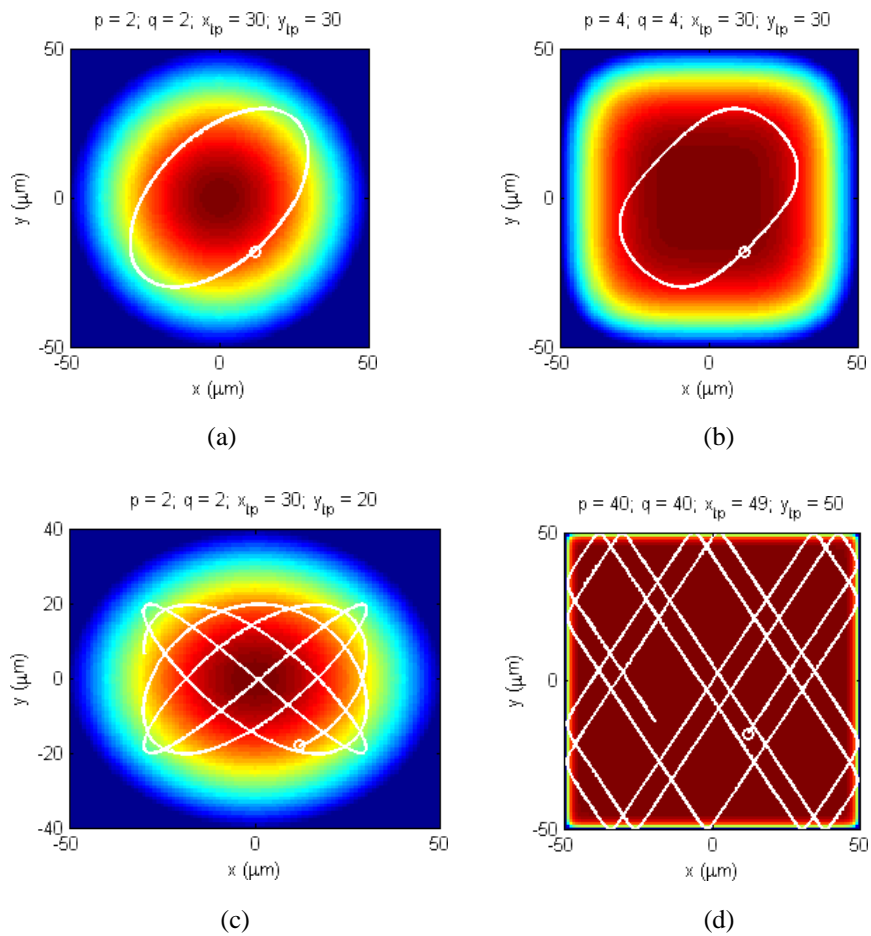


Fig. 2.7 Examples of ray path for rectangular shape GI media. The launching point in all the cases is the same, and other parameters are shown above of each figure.

$$z = \frac{1}{\Omega} \int \frac{dy}{[g(y_p) - g(y)]^{1/2}} \quad (2-16b)$$

where $\Omega = n_{co} \sqrt{2\Delta} / \beta$. Although it looks redundant for two expressions in Eq. (2-16), it is actually easier to obtain all the information about the ray trajectory. Figure 2.7 shows some examples of calculated ray trajectories with the same launching point, and an example code is shown in Appendix A.

2.2 RAY TRAJECTORIES FOR SI MEDIA

Step index media are generally regarded as a special case of GI media, that means g in Eq. (2-1) and p, q in Eq. (2-13) are infinity theoretically. The corresponding ray trajectories are composed of straight lines both in core and in cladding. Similar to GI cores, the ray invariants for SI core are defined as [3]

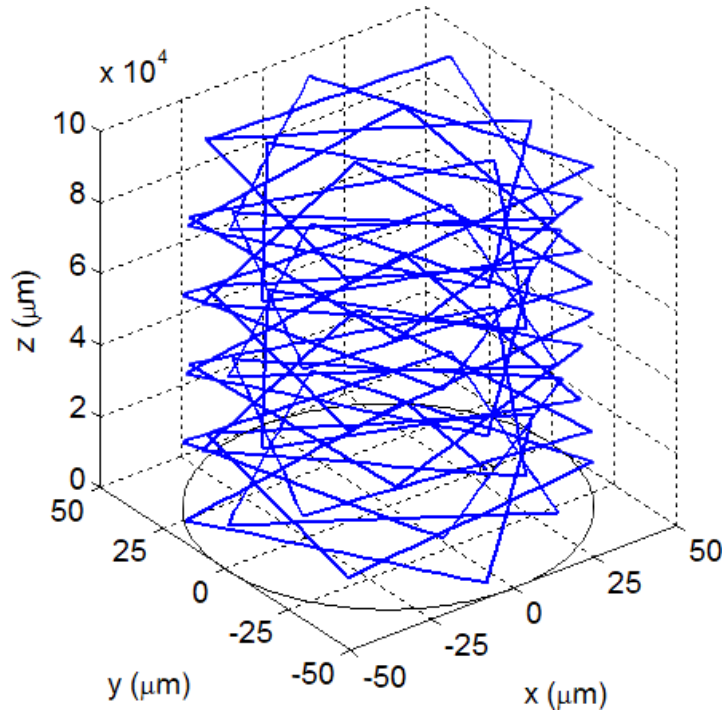
$$\beta = n_{co} \cos \theta_z \quad (2-17a)$$

$$l = n_{co} \sin \theta_z \cos \theta_\phi \quad (2-17b)$$

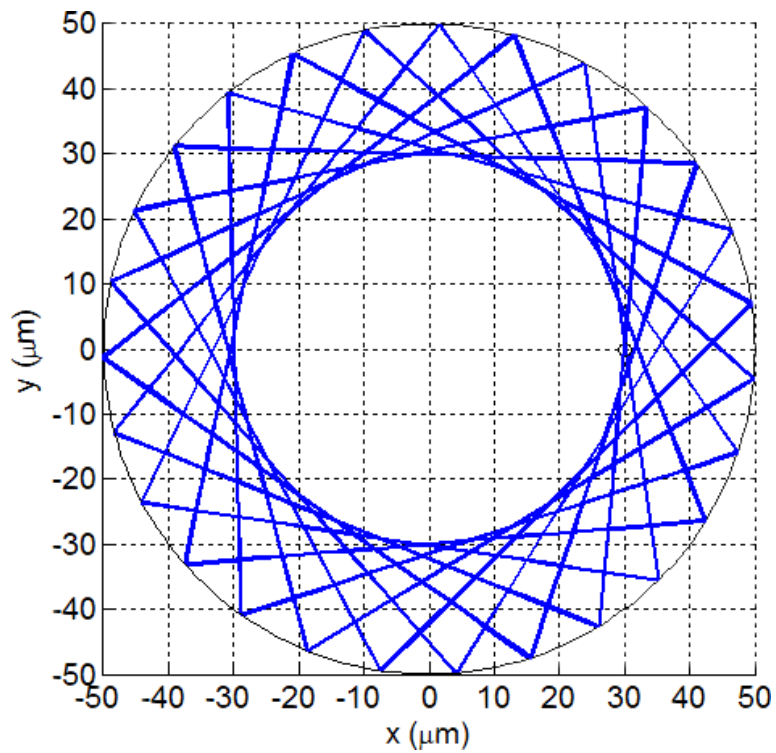
The classification of rays is:

$$\begin{aligned} \text{Bound rays: } & n_{cl} < \beta \leq n_{co} \\ \text{Refracting rays: } & 0 \leq \sqrt{\beta^2 + l^2} < n_{cl} \\ \text{Tunneling rays: } & n_{cl} < \sqrt{\beta^2 + l^2} \leq n_{co} \quad \text{and} \quad 0 < \beta \leq n_{cl} \end{aligned} \quad (2-18)$$

In order to reduce the calculation time, the integration mentioned in the previous section is not carried out while the direction vector with a practical usage is traced. Figure 2.8 is an example of ray path in an SI circular core, where the inner caustic can be easily



(a)



(b)

Fig. 2.8 Ray trajectories in an SI circular core (a) 3D view and (b) top view. The launching point is $(30, 0, 0)$, $n_{co} = 1.507$, $n_{cl} = 1.492$, and $\theta_z = 3^\circ$.

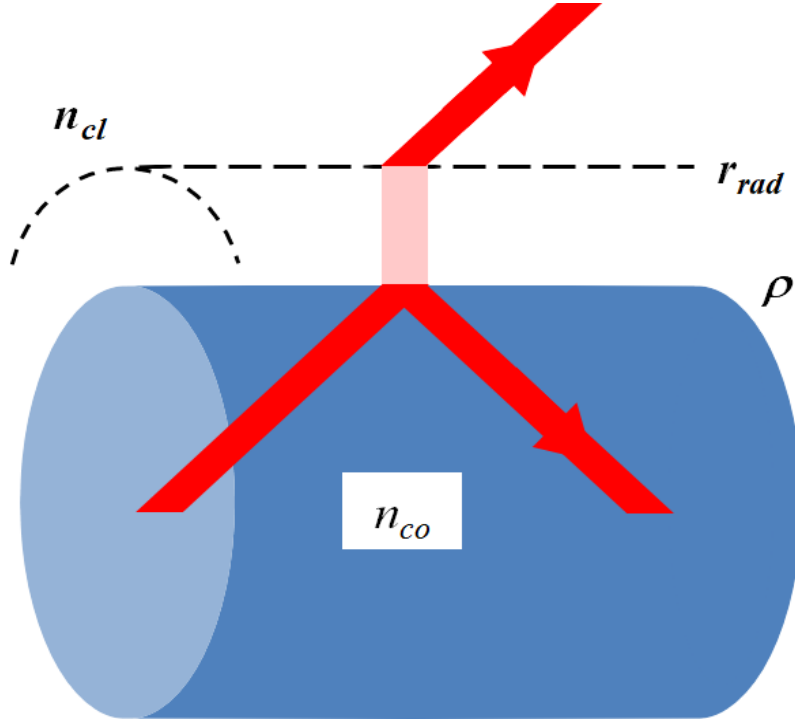


Fig. 2.9 The configuration of tunneling ray in an SI circular core.

recognized in Fig. 2.8(b). In SI cores, the transmission coefficient of tunneling rays is

$$T_{tun} = |T_f| \exp \left[-\frac{4\pi}{\lambda} \int_a^{r_{rad}} \{ \beta^2 + (l\rho/r)^2 - n^2(r) \}^{1/2} dr \right] \quad (2-19a)$$

where r_{rad} is given in Eq. (2-8) and T_f is the analytic continuation of classical Fresnel transmission coefficient defined for the incident angles less than the critical angle θ_c

Thus, it can be expressed as follows:

$$T_f = \frac{4}{n_{co}^2 - n_{cl}^2} (n_{co}^2 - \beta^2 - l^2)^{1/2} (\beta^2 + l^2 - n_{cl}^2)^{1/2} \quad (2-19b)$$

For refracting rays, the transmission coefficient (T_{ref}) is written as

$$T_{ref} = \frac{4 \sin \theta_z \sin \theta_\phi (\sin^2 \theta_z \sin^2 \theta_\phi - \theta_c^2)^{1/2}}{[\sin \theta_z \sin \theta_\phi + (\sin^2 \theta_z \sin^2 \theta_\phi - \theta_c^2)^{1/2}]^2} \quad (2-20)$$

Equation (2-20) also can be applied to rectangular-shape SI core when $\theta_\phi = \pi/2$. In SI cores, the T_{ref} is not surely 1 anymore, which means, the refracting and reflecting rays are actually generated each time when the rays hit the boundary. This implies the calculation sometimes takes much longer time than GI-core case when multiple cores are considered.

2.3 LAUNCHING CONDITION

In order to cover all the cases: SI, GI, circular and rectangular core shape, the characteristics of a single ray is described by the following format:

$$[x_0, x_1, y_0, y_1, z_0, z_1, I_0, x_{tp}, y_{tp}] \quad (2-21)$$

where the definition of each element is listed as follows:

x_0 : x -coordinate of the starting point

x_1 : x -coordinate of the end point

y_0 : y -coordinate of the starting point

y_1 : y -coordinate of the end point

z_0 : z -coordinate of the starting point

z_1 : z -coordinate of the end point

I_0 : intensity of the ray

x_{tp} : turning point in x direction (always positive)

y_{tp} : turning point in y direction (always positive)

Upon the above definition, a single ray is described as a 1x9 array, hence, a launching filed composed of 1000 rays forms a 1000x9 matrix. How to find proper parameters (elements of array) is based on the Gaussian intensity profile and Monte-Carlo method.

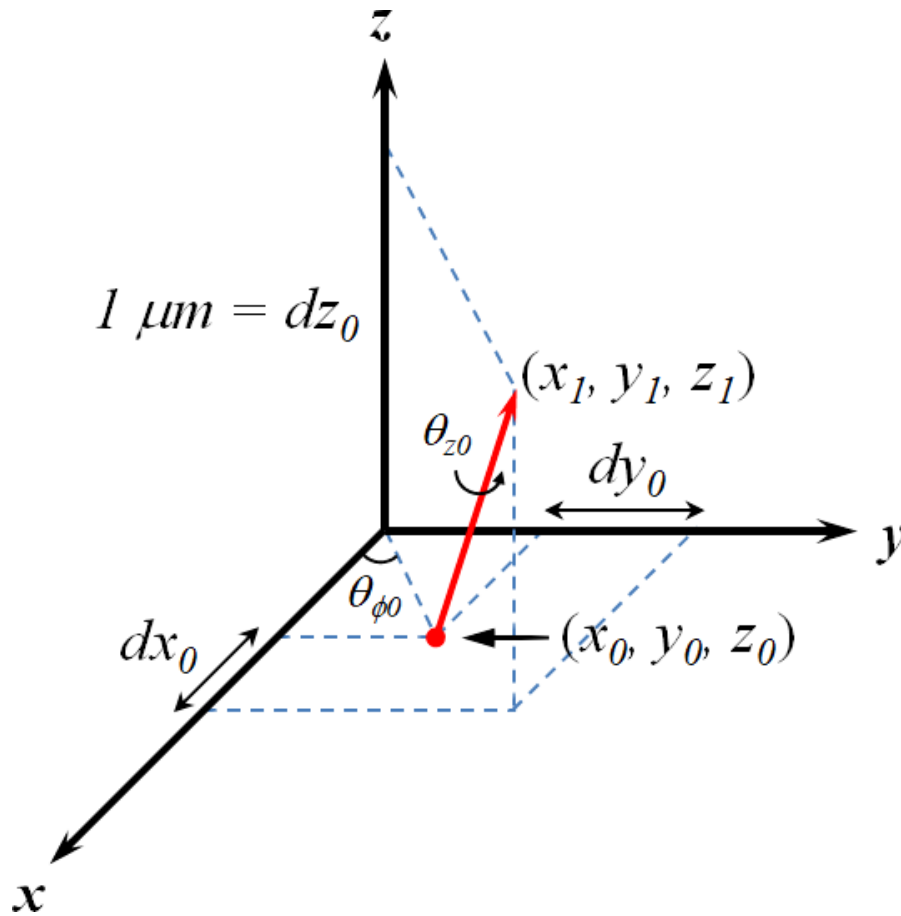
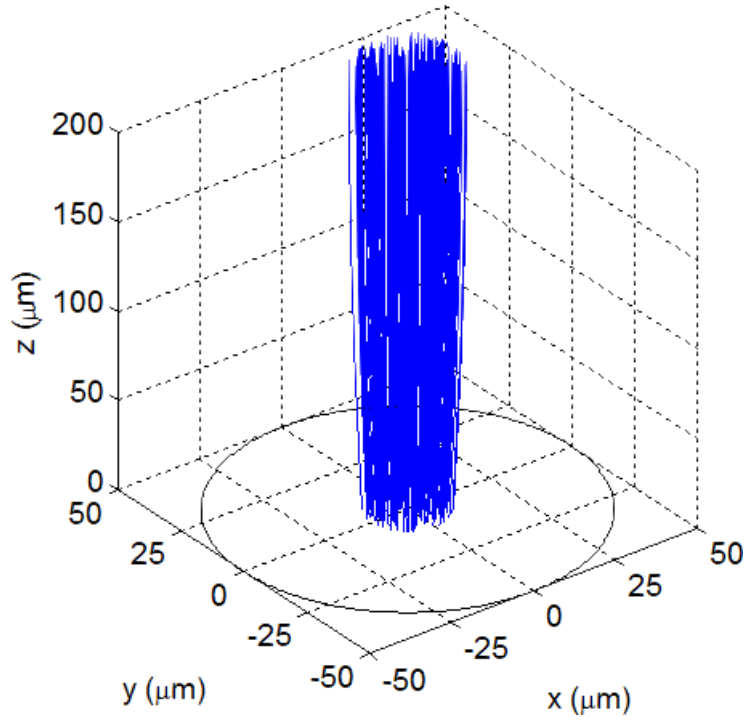


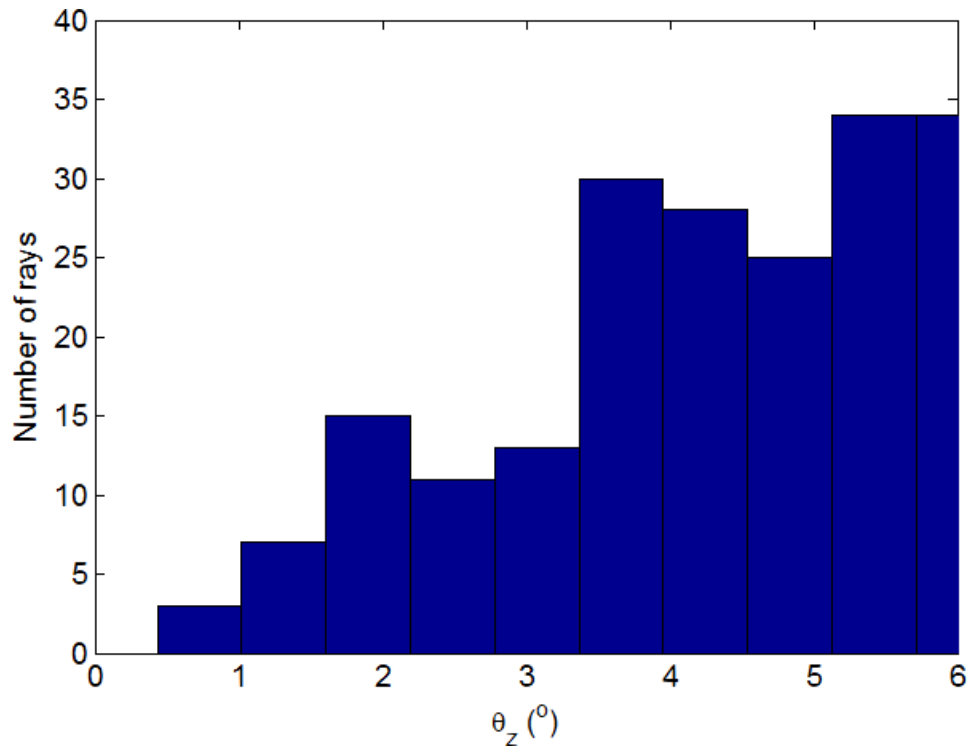
Fig. 2.10 A single ray is launched at the exit of light source.

Here, the general case that a waveguide is launched by a VCSEL is considered, which is regarded as a Gaussian beam. In terms of ray optics, the launching field is characterized by a Gaussian intensity profile rather than overlap of modes with different orders. Once the launching position is determined, the intensity I_0 of the ray is also attached by mapping the position of a Gaussian profile.

Monte-Carlo method is a stochastic technique which is based on the use of random numbers and probability statistics to investigate problems. Here, we apply the concept of this method rather than the rigorous mathematical treatment. The scheme of a ray incident from the plane $z = 0$ with a direction vector (dx_0, dy_0, dz_0) is considered as shown in Fig. 2.10. For convenience, dz_0 is set to be $1 \mu\text{m}$. In order to fit the NA of the



(a)



(b)

Fig. 2.11 Multiple rays injected into the core. (a) 200 bound rays generated by the Monte-Carlo method. (b) Angle (θ_z) distribution of the 200 rays in (a).

waveguide when launching (i.e. all the incident rays are bound rays), the θ_{z0} and $\theta_{\phi0}$ are required to fall into a limited range individually. Furthermore, for graded index cores, the ray invariant is determined by x_{ip} and y_{ip} described by Eq. (2-15), and some more constrains in the ray injection is required. Once these parameters are determined, the similar process runs automatically and a matrix for multiple rays is formed. Figure 2.11(a) shows a bundle of bound rays launched within a circle with 10 μm in radius surrounding the origin, where the parameters are the same as those used in Sec. 2.1. In this example, the maximum angle between one ray and z -axis (θ_z) is set to 6° , and the angle distribution of these rays is shown in Fig. 2.11(b). According to the Monte-Carlo method, in a unit area the density of ray number must be almost uniform in whole launched area. This result in the number of ray shows the trend: larger number of rays with increasing the θ_z value, as shown in Fig. 2.11(b).

2.4 SCATTERING EFFECT IN CORE AREA

According to the formulations mentioned in previous sections, we can model the behavior of rays and calculate reliable optical characteristics for ideal waveguides. But it is not practical enough for PPOWs which show relatively high scattering loss compared to silica based waveguides. Figure 2.12(a) experimentally demonstrates an example of a GI-POF launched by a SMF. The incident light (ray) is either split by scattering, or its direction is changed by the non-uniform refractive index distribution. The splitting process could be repeated and the number of total rays increases. After reaching the output end, the overall scattering effect leads to wide-output field (from whole core) despite a small beam spot at the launching end, which is so-called mode conversion. The phenomenon illustrated in Fig. 2.12(a) is of concern because it can

dominate the inter-channel crosstalk particularly in waveguides with high propagation loss.

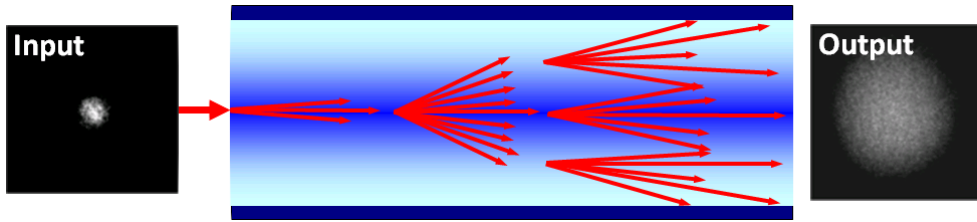
The mode conversion due to light scattering happens ubiquitously under practical conditions. The related theories are well developed for specified targets, such as particle shape, size parameter, and polarization. The more accurate way to solve the field of electromagnetic wave scattered by a spherical particle is introduced in chapter 3. From ray optics point of view, some assumptions are made for evaluating the influence of light scattering in the core regions by the simulation. First, no back scattering is considered and there is no real entity for a scatterer. Next, the ray splitting due to scattering happens randomly within the core area, that implies the propagation length is randomly determined and generally is in a range of several hundred micrometers in our simulation algorithm. When a ray propagates this one unit of length, three parameters are incorporated to include the influence of light scattering:

p : probability of scattering

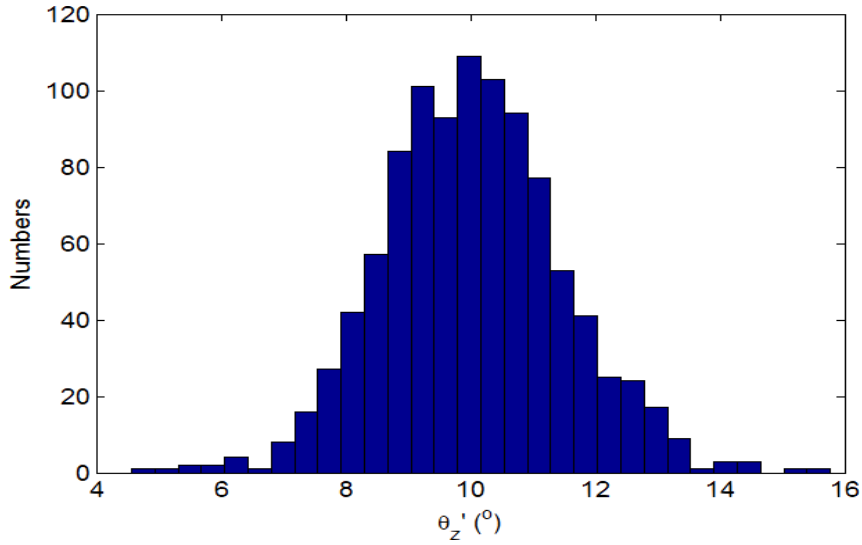
N_s : maximum number of scattered ray

θ_m : maximum angle difference to the original ray direction

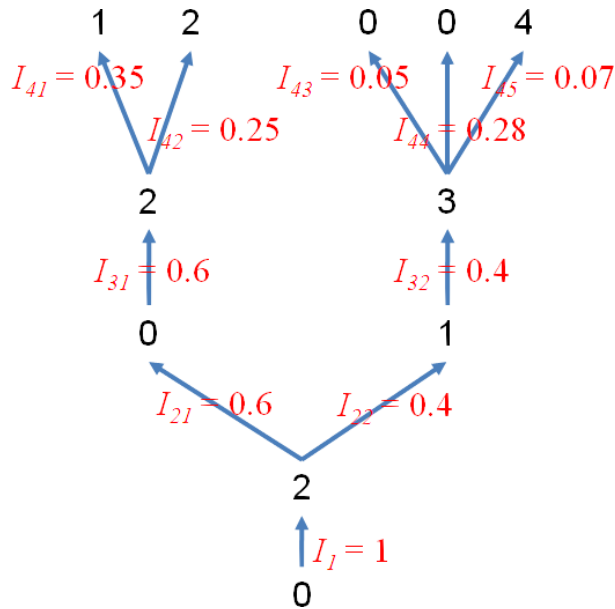
The probability of scattering ranges from 0 to 100 %, which corresponds to no scattering and absolute scattering, respectively. When the random number is smaller than p value, the ray splits to n ($1 \leq n \leq N_s$) rays at this node, and the maximum value of N_s which is set to be 5 in this model, determines how many rays are generated at this node, i.e. the number of scattered ray could be 0 to N_s . The maximum angle difference to the original ray direction (θ_m) is determined by the numerical aperture of the channel. Once a ray is scattered, it splits to several rays with individually specified directions with the angle θ_m to the original ray direction. Here, we suppose that the angle θ_m



(a)



(b)



(c)

Fig. 2.12 (a) The small light spot is enlarged by the scattering effect. (b) Simulated angle distribution according to Eq. (2-22) with $\theta_z = 10^\circ$ and $\sigma = 3$ (1000 examples). (c) An example for the calculation.

satisfies a Gaussian distribution. Each of the scattered rays carries different intensity that depends on the angle θ_m . Hence, the split ray with smaller angle difference can possess higher intensity. The angle difference of split ray ($\Delta\theta_k = \theta'_z - \theta_z$, k is an integer from 1 to n) and k^{th} intensity (I_k) for the split ray is written as follows:

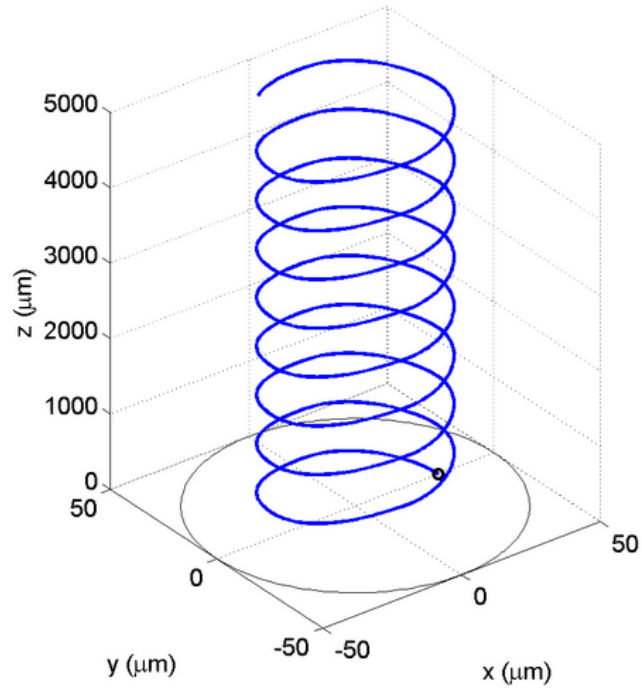
$$\theta'_z = \theta_z \pm \sigma \sqrt{-\log(R)} \quad (2-22)$$

and

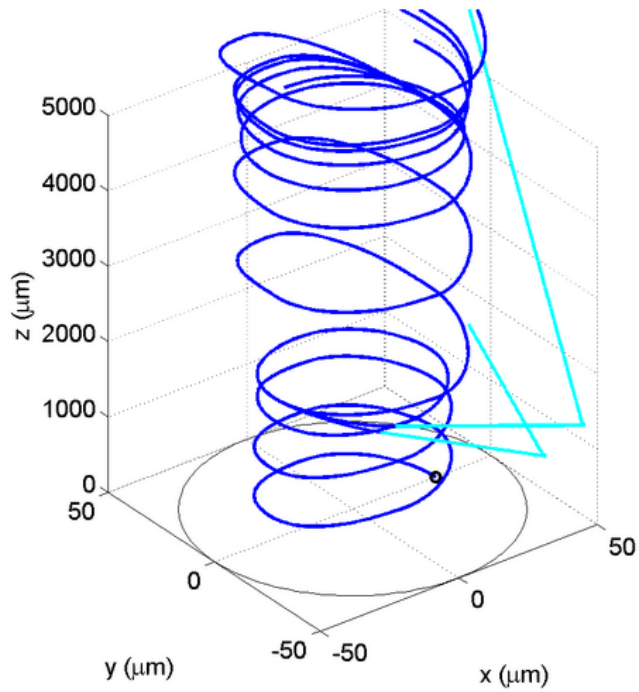
$$I_k = \frac{|\Delta\theta_k|^{-1}}{\sum_{k=1}^n |\Delta\theta_k|^{-1}} I_0 (1 - T_k) \quad (2-23)$$

where, σ is standard deviation, R is random number (from 0 to 1), I_0 is the intensity of the original ray, and T_k is the transmission coefficient of k^{th} tunneling rays calculated from Eq. (2-7) or Eq. (2-19a). Then, each ray proceeds to the next node. Once the characteristics of a ray are changed by one scattering event the classification of the ray could be also changed by chance. Figure 2.12(b) shows the simulation result of angle distribution for 1000 scattered rays according to Eq. (2-22), where original ray has 10° in θ_z .

Figure 2.12(c) shows an example how a single ray (initial intensity is 1) split into many other rays by scattering effect. In the beginning, the 0 for N_s is determined randomly from 0 to 5, where it means no scattering happens and the ray keeps all the original properties. Next, N_s is determined to be 2, which indicates one ray split into two. At this moment, the corresponding angles for the two rays are also randomly determined according to θ_m , and then the intensity of each rays is also calculated by Eq. (2-22) and Eq. (2-23). In this case, the angle of I_{21} is closer to the angle of the previous

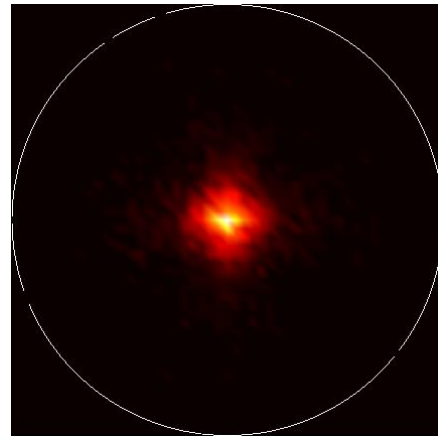
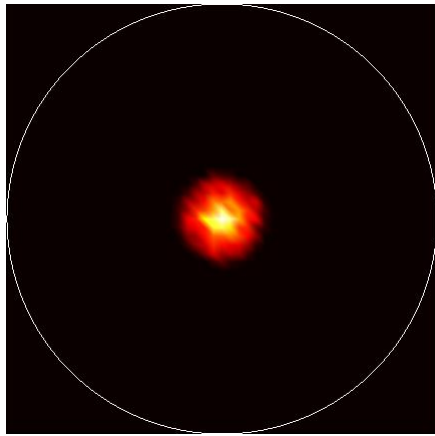


(a)

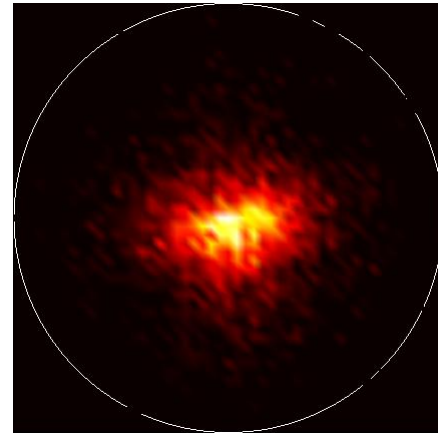
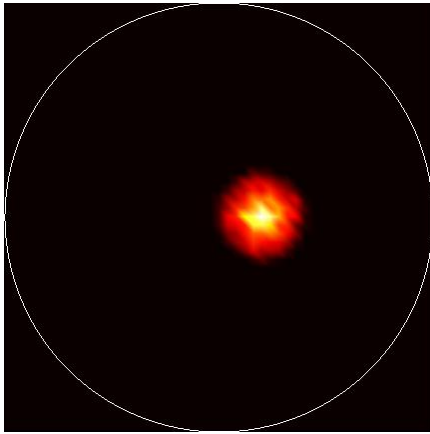


(b)

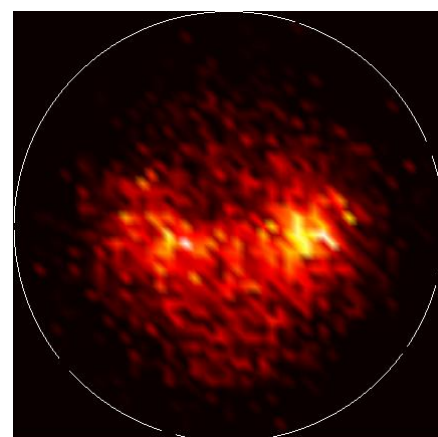
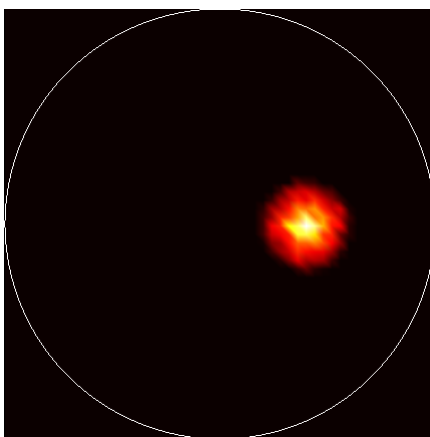
Fig. 2.13 The same launching position (a) without and (b) with scattering effect considered. In this calculation, the launching point is $(30, 0, 0)$, $n_{co} = 1.507$, $n_{cl} = 1.492$, and $\theta_z = 3^\circ$.



(a)



(b)



(c)

Fig. 2.14 The biased launch with a Gaussian distributed field: (a) no offset, (b) 10 μm offset, and (c) 20 μm offset. The $n_{co} = 1.507$, $n_{cl} = 1.492$, and core size is 50 μm .

ray compared to that of I_{22} because I_{21} has higher intensity. The next steps follow a similar way until the output end ($z = L$). Figure 2.13 shows the comparison between a single ray with and without scattering effect considered, where the launching position is $(30, 0, 0)$ in both cases. In Fig. 2.13(a) a perfect condition is considered, and the ray path for a parabolic profile core is undoubtedly a helical trajectory. Under the same launching condition when scattering effect is considered, the ray split into several rays and sometimes it could be scattered outside to the core, as shown in Fig. 2. 13(b). Surely this implies the ray properties could be deteriorated when a scattering event occurs.

Finally, it is possible to simulate NFPs under the considerations mentioned above. Here is an example that we consider a GI circular core with parabolic refractive index profile launched by a Gaussian beam. Both biased launching and scattering effect are involved as Fig. 2.14 shows.

2.5 ROUGH CORE/CLADDING BOUNDARY

According to the previous sections, the behavior of rays in SI and GI cores is quite different. Since the refractive index profile is a constant inside the core, the rays propagate in an SI core by total internal reflection: ray hits the core/cladding boundary and continues to go forward. In the case of a silica fiber, the interface is rather clear, whereas the situation in PPOW is not the same anymore. According to various kinds of fabrication processes of PPOWs, the deformation of waveguide structure along the propagation direction is always somehow exists.

The mode conversion cause by the deformation of cores is modeled by coupled mode theory [5], that local normal modes are used for field expansion as function of z .

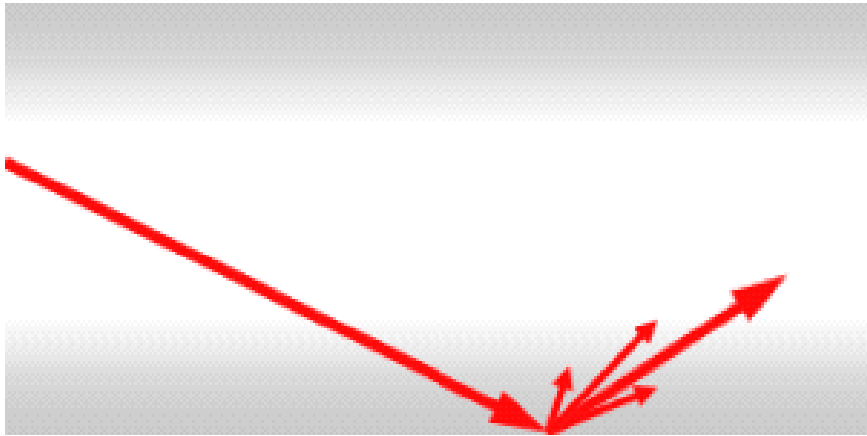


Fig. 2.15 The concept of a ray scattered by rough core/cladding boundary.

Although these modes themselves are not the original solutions of Maxwell's equations, they can be superimposed to yield one of solutions of Maxwell's equation. In multimode PPOWs with a pitch as wide as 250 μm , mode coupling effect shows a relatively weak impact on the inter-channel crosstalk. Similar to the consideration of scattering effect which commonly occurred in polymer core materials, we believe the mode conversion results from the imperfect core/cladding boundary would be another key issue. Particularly as an essential difference between SI and GI cores, we propose to involve the roughness at the core-cladding boundary, which may change the behavior of rays.

The concept of rays scattered by rough core-cladding boundary is shown in Fig. 2.15. We treat the direction of reflected ray is slightly changed from its reflection angle obtained from Snell's law, and it happens in each reflection in the core. According to Eq. (2-15a), the change of θ_z implies the ray invariant also changes, hence, a bound ray could become a leaky ray and vice versa. Although some limitations of ray optics make such a consideration be somewhat unpractical, we focus on how behavior of rays is changed rather than the scattered field profile. In this section, we combine the theoretical analysis based on wave optics with ray tracing method. The random rough

surface obtained by a certain algorithm is introduced first. Next, the obtained rough surface is fitted to the Kirchhoff approximation, which is regarded as the most understandable and widely used theory for electromagnetic wave scattering from rough surface.

2.5.1 Random rough surface

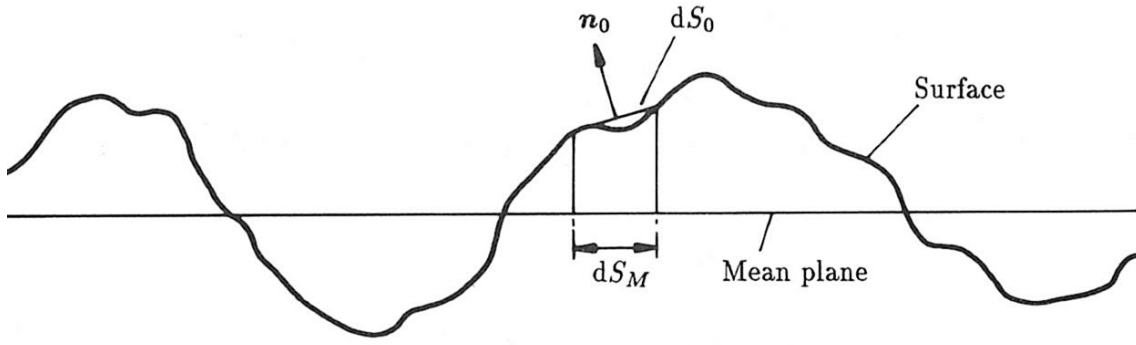


Fig. 2.16 Random rough surface and its mean plane [6].

Although the measurement of surface roughness at core-cladding boundary is very difficult, it is intuitively found that the structure at the boundary is a random rough surface. The term ‘random’ emphasizes that no two rough surfaces are identical. A random rough surface is generally described in terms of its deviation from the smooth ‘mean plane’ as shown in Fig. 2.16. There are various statistical ways to describe the nature of random rough surface: in short it is characterized by RMS height and correlation length. Here we propose to apply the Gaussian correlation function C to two-dimensional surfaces as follows [6]:

$$C(x, y) = \exp \left[- \left(\frac{x^2}{\lambda_x^2} + \frac{y^2}{\lambda_y^2} \right) \right] \quad (2-24)$$

where λ_x and λ_y are correlation length: the distance over which the correlation function

falls by $1/e$.

2.5.2 Moving average method

A variety of numerical methods have been used to realize the rough surface function $h(x, y)$. Here a simple but robust algorithm called moving average method is introduced. A random variable h_n is written in the general form [6]:

$$h_n = \sum_{j=0}^N w_j u_{n-j} \quad (2-25)$$

where the u_n is uncorrelated random process of certain variance, N is the order of moving average process (generally $N = 1$), and weights w_j are defined as follows:

$$w_{x,j} = \frac{w_0}{\sqrt{\lambda_x}} \exp\left(-\frac{2(j\Delta x)^2}{\lambda_x^2}\right) \quad (2-26a)$$

$$w_{y,j} = \frac{w_0}{\sqrt{\lambda_y}} \exp\left(-\frac{2(j\Delta y)^2}{\lambda_y^2}\right) \quad (2-26b)$$

Figure 2.17 shows calculated curves with corresponding variance (σ^2) and correlation length (λ).

2.5.3 Kirchhoff approximation

Kirchhoff theory is the most widely used theory in the study of wave scattering because it shows relatively simple analytical expressions for scattered field. The geometry of incident and scattered field is depicted in Fig. 2.18, where a plane, monochromatic, scalar wave is incident onto a rough surface. Under the assumption of the reflection coefficient (R_0) is independent of position along the surface, the general

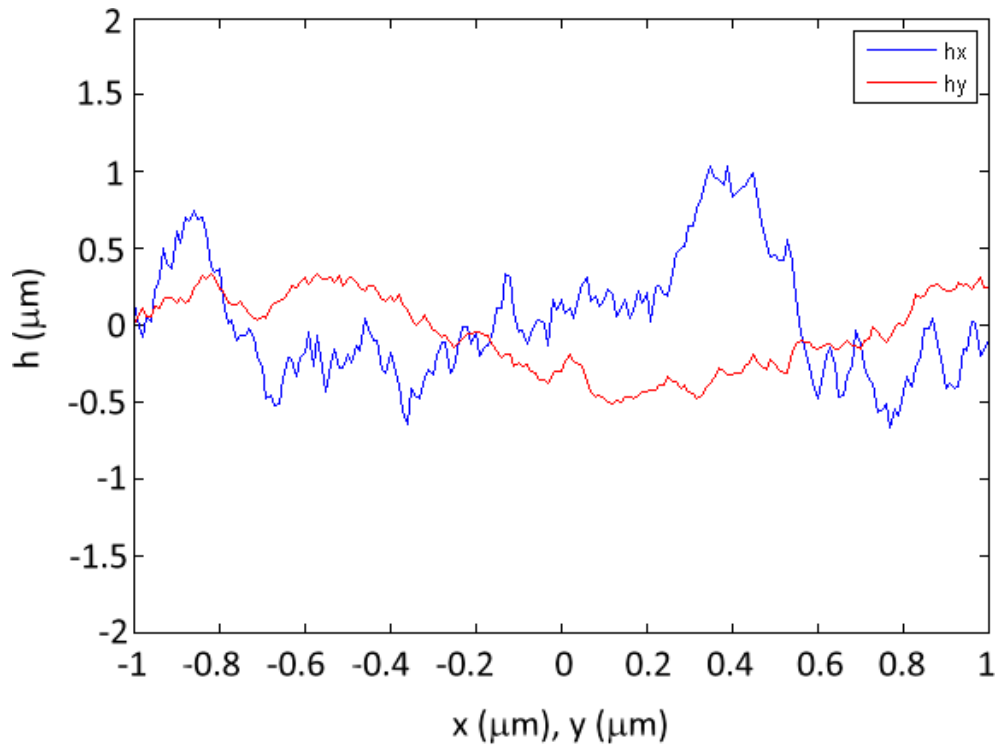


Fig. 2.17 Random rough surface generated by moving average method. In this calculation, $\sigma_x = 0.4 \mu\text{m}$, $\lambda_x = 0.3 \mu\text{m}$, $\sigma_y = 0.25 \mu\text{m}$, $\lambda_y = 0.6 \mu\text{m}$.

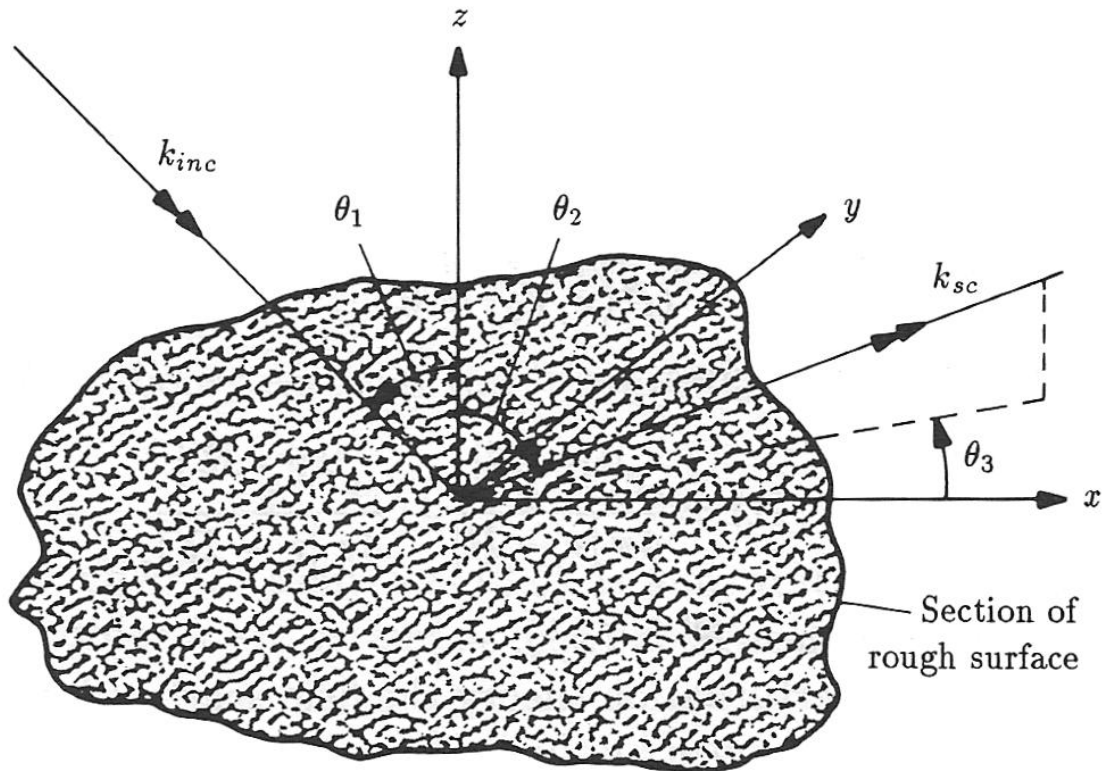


Fig. 2.18 Scattering geometry for plane wave incident [6].

form is derived as follows [6]:

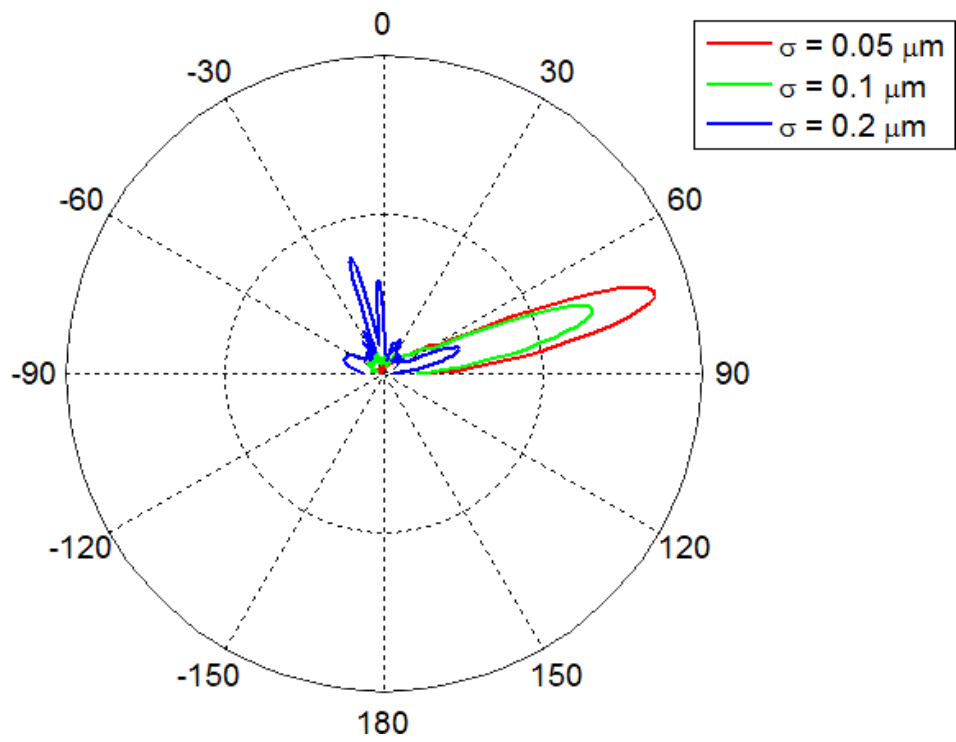
$$\psi^{sc}(\mathbf{r}) = \frac{ike^{ikr}}{4\pi r} \int \left(a \frac{\partial h}{\partial x} + b \frac{\partial h}{\partial y} - c \right) \exp \{ ik[Ax + By + Ch(x, y)] \} dx dy \quad (2-27a)$$

with

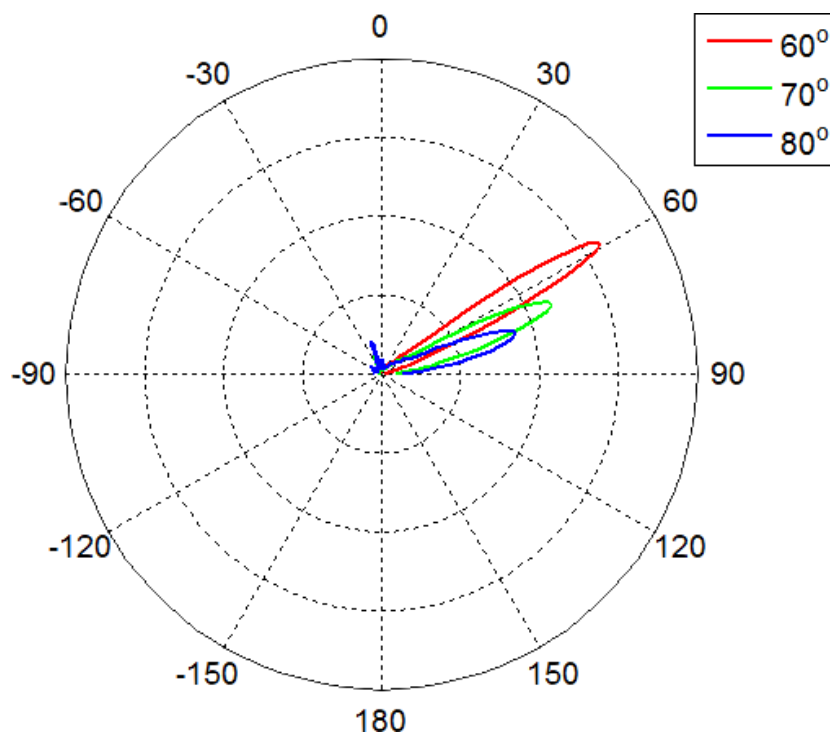
$$\begin{aligned} a &= R_0 (\sin \theta_1 - \sin \theta_2 \cos \theta_3) \\ b &= R_0 \sin \theta_2 \sin \theta_3 \\ c &= R_0 (\cos \theta_1 + \cos \theta_2) \\ A &= \sin \theta_1 - \sin \theta_2 \cos \theta_3 \\ B &= -\sin \theta_2 \sin \theta_3 \\ C &= -(\cos \theta_1 + \cos \theta_2) \end{aligned} \quad (2-27b)$$

where h is the height of random rough surface generated by certain methods, for example, the moving average method introduced in the previous section, and θ_1 , θ_2 , and θ_3 are defined in Fig. 2.18.

Figure 2.19 shows two-dimensional calculation results, where the incident beam comes from the left. In Fig. 2.19(a), the incident beam is 70° and fixed. When the ray injects the surface with different roughness, different scattered fields are obtained, and side-lobe patterns increase when σ is close to the wavelength ($0.85 \mu\text{m}$). For a relatively flat surface ($\sigma = 0.1 \mu\text{m}$), the scattered field is concentrated on the specular direction [7]. In Fig. 2.19(b), σ is chosen to be $0.1 \mu\text{m}$. It is rather clear to see the larger the incident angle, the larger the side lobe area. Although it is observed in the far field, we care about how much direction will be changed rather than the profile of scattered field. We propose the angle change under our applications is limited to $10^\circ (\pm 5^\circ)$.



(a)



(b)

Fig. 2.19 The calculated scattered pattern based on Eq. 2-27. In both cases, $x = -5 \sim 5 \mu\text{m}$. (a) $\theta_i = 70^\circ$ is fixed. (b) $\sigma = 0.1 \mu\text{m}$ is fixed.

REFERENCES

1. T. Ishigure, E. Nihei, S. Yamazaki, K. Kobayashi, and Y. Koike, "Formation of the refractive index profile in the graded index polymer optical fiber for gigabit data transmission," *J. Lightw. Technol.*, 15(11), 2095-2100 (1997).
<http://www.opticsinfobase.org/abstract.cfm?URI=jlt-23-6-2062>
2. A. Ankiewicz, C. Pask, "Geometric optics approach to light acceptance and propagation in graded index fibers," *Opt. Quant. Elect.* 9, 87-109 (1977).
<http://www.springerlink.com/content/k603102073069750/>
3. A. W. Snyder and, J. D. Love, *Optical Waveguide Theory* (Chapman & Hall, 1983).
<http://goo.gl/VK07D> (2012.2.10)
4. K. F. Barrell and C. Pask, "Geometric optics analysis of non-circular, graded-index fibers," *Opt. Quant. Elect.*, 11(3), 237-251 (1979).
<http://www.springerlink.com.kras3.lib.keio.ac.jp:2048/content/h0062m1w484q8885/>
5. D. Marcuse, *Theory of Dielectric Optical Waveguides* (2nd Edition Academic Press Inc., 1971).
6. J. A. Ogilvy, *Theory of Wave Scattering From Random Rough Surface*, (Adam Hilger, 1991).
7. Y. Cocheril, R. Vauzelle, and L. Aveneau, "3D channel simulations including scattering from non-Gaussian rough surfaces," in proceedings of 64th Vehicular Technology Conference, (2006).
<http://ieeexplore.ieee.org/stamp/stamp.jsp?tp=&arnumber=4109297>

3

MODELING WITH WAVE OPTICS

3.1 MODAL SOLUTION BY SERIES EXPANSION METHOD

3.2 BEAM PROPAGATION METHOD

3.3 RADIATION FIELD FROM WAVEGUIDE

3.4 MIE SCATTERING

3.5 COMPARISON OF SCATTERED FAR FIELD PATTERN

In chapter 2, we characterize the optical properties of multi-channel polymer optical waveguides based on ray optics, where some key features are modeled reasonably. Although it is already well proved that the propagating mode concept is equivalent to the trajectories computed by ray theory, it still lacks generality particularly for some parameters with physical dimension close to the wavelength. In this chapter, several required formulas and solutions based on wave equation are introduced. Under the consideration of multimode and weakly guiding polymer waveguides, the polarization of incident light plays a minor role in influencing on the optical characteristics. The scalar wave equation performs a promising starting point to describe the plane wave propagation inside optical components. In the next chapter, the related formulations are introduced in order to analyze the optical characteristics of total optical links, which is

composed of VCSELs, multi-channel multimode waveguides, multimode fibers, and photo detectors. Moreover, in order to realize the practical experiment setup for characterizing the waveguides, three parameters, air gap, biased launching condition, and scattering effect, should be taken into consideration. For characterizing the total loss of the link, we separate the propagation loss and material loss from connection losses. All of the features can be realized by the equations mentioned in the following sections, so-that the computer program based on wave optics developed through this research helps us to involve the desired considerations with higher degree of freedom.

3.1 MODAL SOLUTION BY SERIES EXPANSION METHOD

In some cases, it is required to find modal fields before the light propagates into waveguides, particularly when light coupling to multiple different modes are of our interest. For example, we consider a case that a lower order mode is excited under a restricted mode launching (RML) condition. The coupled power to lower order modes could be transferred to higher order modes by imperfections in the core area. With those calculated modal fields, we can find coupling coefficients between different modes and estimate the perturbed near field pattern (NFP).

The modal solutions for SI core are analytically obtained much easier than those in GI core: only some special cases are resolvable for GI core. As the calculation power of personal computer nowadays increases, finding numerical modal solutions in GI cores based on wave equation is no more a tough work. For a dielectric structure with arbitrary shape, the finite element method (FEM) could be one of the most promising ways to find both bound and radiation modes. Such a method is also widely used in lots of commercially available mode solvers which perform versatilely with high efficiency.

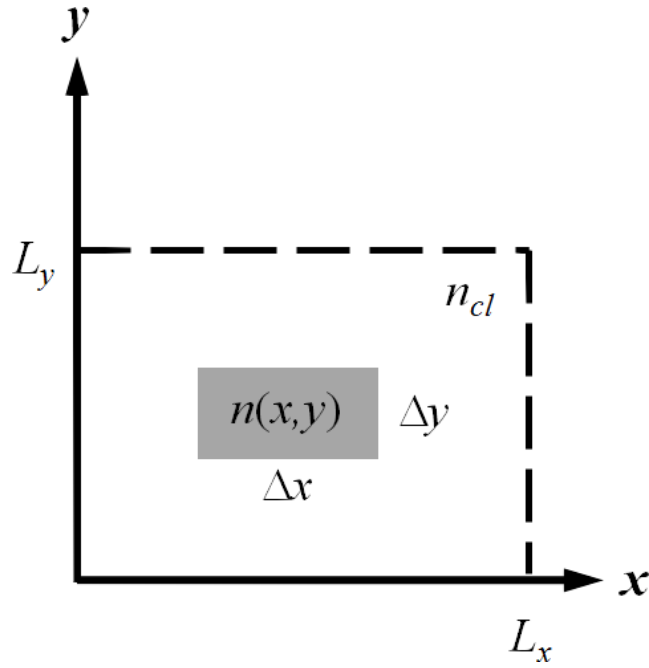


Fig. 3.1 The layout of a rectangular dielectric waveguide core embedded in a homogeneous media.

In this section, the so-called series expansion method is introduced, which is a relatively old method but applicable to all guided mode problems that can be approximated as solutions of scalar wave equation. The main idea of this method is that an arbitrary function which satisfies certain restraints can be decomposed by a complete set of orthogonal basis. Although it is necessary to restrict solutions of the wave equation to a finite domain, it is still suitable for our application about multi-channel square shape GI-PPOWs.

When a 2-D refractive index profile $n(x, y)$ is introduced as shown in Fig. 3.1, the scalar wave equation one of whose solution is supposed to be ψ is written as follows:

$$\frac{\partial^2 \psi}{\partial x^2} + \frac{\partial^2 \psi}{\partial y^2} + \frac{\partial^2 \psi}{\partial z^2} + n^2(x, y)k_0^2 \psi = 0 \quad (3-1)$$

where, k_0 is the wave number in free-space. Here, the $n(x, y)$ is regarded as a rectangular dielectric waveguide core embedded in a homogeneous media, which corresponds to the

cladding in this dissertation. The L_x and L_y shown in the figure indicate the auxiliary base domain. Here, L_x and L_y are divided into N_x and N_y equal parts, and the complete orthogonal set is written as follows [1]:

$$\phi_{\mu\nu}(x, y) = \frac{2}{\sqrt{L_x L_y}} \sin\left(\frac{\pi}{L_x} \mu x\right) \sin\left(\frac{\pi}{L_y} \nu y\right) \quad (3-2)$$

where u and v are integers from 1 to N_x and 1 to N_y , respectively. The set of bases are required to satisfy the orthogonality condition as follows:

$$\int_0^{L_x} \int_0^{L_y} \phi_{\mu\nu}(x, y) \phi_{\mu'\nu'}(x, y) dx dy = \delta_{\mu\mu'} \delta_{\nu\nu'} \quad (3-2)$$

where δ is the Kronecker delta. An arbitrary solution (ψ) of scalar wave equation Eq. (3-1) can be written as the series expansion as follows:

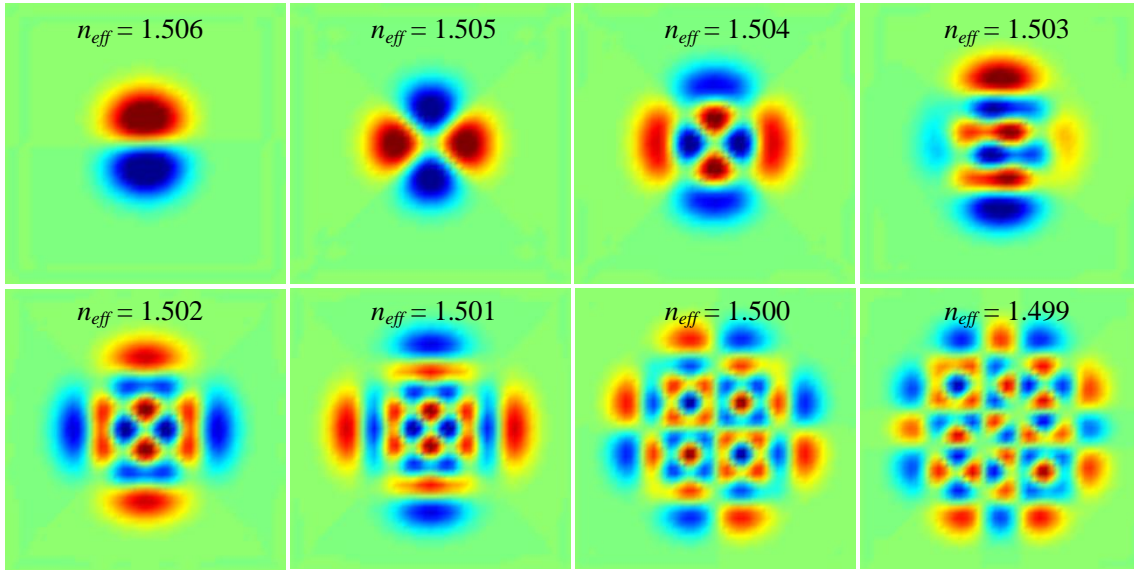
$$\psi = \exp(-j\beta z) \sum_{\mu=1}^{N_x} \sum_{\nu=1}^{N_y} c_{\mu\nu} \phi_{\mu\nu}(x, y) \quad (3-3)$$

where $c_{\mu\nu}$ is the expansion coefficient. Substitute Eq. (3.3) to Eq. (3.1) and use the orthonormality relation shown in Eq. (3.2), a system of eigenvalue equation is obtained:

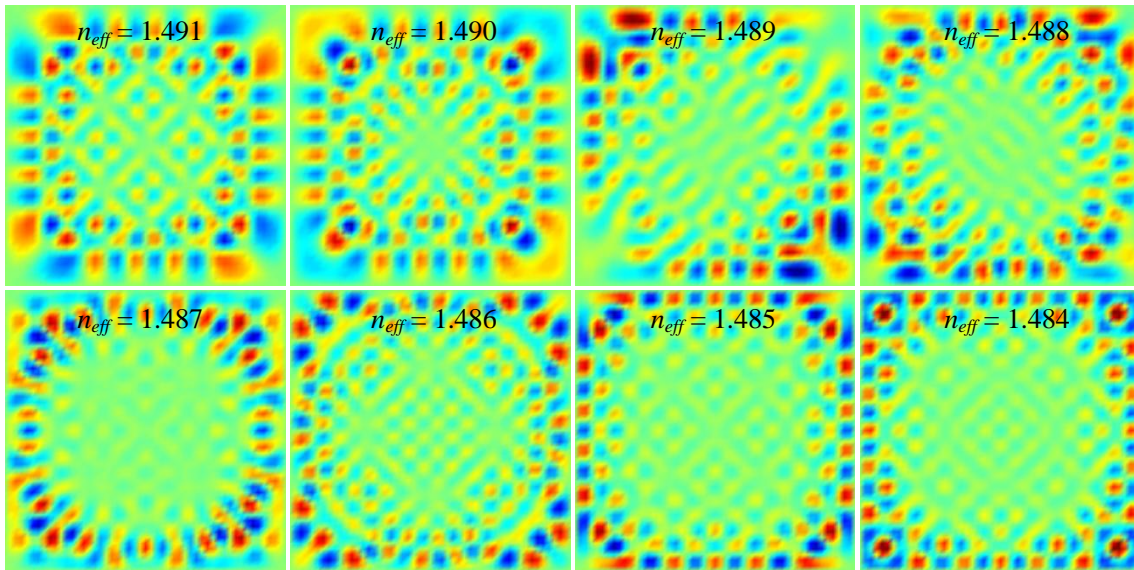
$$\sum_{\mu=1}^{N_x} \sum_{\nu=1}^{N_y} A_{\mu'\nu', \mu\nu} c_{\mu\nu} = (n_{eff}^2 - n_{cl}^2) c_{\mu'\nu'} \quad (3-4a)$$

where $A_{\mu'\nu', \mu\nu}$ are defined as

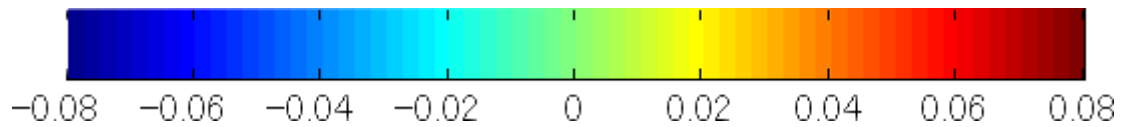
$$A_{\mu'\nu', \mu\nu} = \int_0^{L_x} \int_0^{L_y} [n^2(x, y) - n_{cl}^2] \phi_{\mu\nu}(x, y) \phi_{\mu'\nu'}(x, y) dx dy - \frac{\pi^2}{k_0^2} \left(\frac{\mu^2}{L_x^2} + \frac{\nu^2}{L_y^2} \right) \delta_{\mu\mu'} \delta_{\nu\nu'} \quad (3-4b)$$



(a)



(b)



(c)

Fig. 3.2 Examples of modes calculated from series expansion method with corresponding effective indices. Each of figures represents the amplitude of a modal field within core area. (a) Bound modes with $n_{eff} > 1.492$. (b) Leaky modes with $n_{eff} < 1.492$. (c) The color map applied to the above figures.

In addition, the effective index of modes are $n_{eff} = \beta/k_0$. Find the eigenvalue and eigenvector in Eq. (3-4) and then substitute them into Eq. (3.3), then, the modal solutions ψ can be calculated numerically. Intuitively, it is required that N_x and N_y are large enough for obtaining sufficiently precise modal fields and effective indices. Figure 3.2 shows some calculated modal fields for a rectangular shape GI core with index profile shown in Eq. (2-13). The parameters applied here are listed in Table. 3.1. Similar to the criteria for the ray classification mentioned in Sec. 2.1.2, the criteria for modes are listed below:

$$\begin{aligned} \text{Bound modes : } n_{cl} < n_{eff} \leq n_{co} \\ \text{Leaky modes : } n_{eff} \leq n_{cl} \end{aligned} \quad (3-5)$$

According to Fig. 3.2, it is rather clear that the bound mode fields are distinguishable from those of leaky modes. Although the accuracy of the calculation is more significant particularly in higher order modes, it is still applicable to the lower order modes for realizing the waveguide applications focused in this dissertation.

Table. 3.1 Parameters applied in Fig. 3.2

Parameters	Value
Number of division in both x and y direction (N_x, N_y)	20
Waveguide width (L_x) and height (L_y)	50 μm
Index exponent in both x and y direction (p, q)	2.4
Refractive index of core (n_{co})	1.507
Refractive index of cladding (n_{cl})	1.492

3.2 BEAM PROPAGATION METHOD

The beam propagation method (BPM) is one of the most powerful calculation

methods for analyzing linear and nonlinear light propagation in slowly varying, non-uniform guiding, and weakly guiding waveguides. There are various implementations of BPM differ by the method used for calculations of the derivatives with respect to the coordinates in the propagation directions, including fast Fourier transform (FFT), finite difference method (FDM), and finite element method (FEM). BPM is also applicable to relatively high-index contrast structures based on semi-vectorial and vectorial formulations. Furthermore, the advanced features like wide-angle formulation and bi-directional propagation also have already been proposed and implemented in commercially available software [2]. For the purpose of involving some perturbations in waveguide structure like scattering in the core area, the newly developed computer program is capable of combining them with other features for analyzing the coupling loss in optical links.

The optical characteristics along the GI-POW are calculated by BPM versus the length of the waveguide. A parallel-aligned, multimode, GI-POW is illustrated by formulating the problem under the restrictions of a scalar field (i.e. neglecting polarization effects) and paraxiality (i.e. propagation direction is restricted to a narrow range of angles) [3]. Compared to Eq. (3-1), a more general case with $n = n(x, y, z)$ is considered here, and the three-dimensional scalar wave equation is expressed by the following equation:

$$\frac{\partial^2 \psi}{\partial x^2} + \frac{\partial^2 \psi}{\partial y^2} + \frac{\partial^2 \psi}{\partial z^2} + n^2(x, y, z)k_0^2 \psi = 0 \quad (3-6)$$

where the definition of ψ and k_0 are the same as in previous cases. Under the slowly varying envelope approximation (SVEA), the field $\psi(x, y, z)$ can be separated into the production of the axially slowly varying envelope term (ϕ) and the rapidly varying

phase term as follows:

$$\psi(x, y, z) = \phi(x, y, z) \exp(-jkn_{cl}z) \quad (3-7)$$

Substitute Eq. (3-7) to Eq. (3-6) and neglect the second order partial differential of $\phi(x, y, z)$ with respect to z (according to the paraxial approximation), Eq. (3-6) is converted to the general beam propagation form as follows:

$$\frac{\partial \phi}{\partial z} = -j \frac{1}{2kn_{cl}} \nabla^2 \phi - j \frac{k}{2n_{cl}} [n^2(x, y, z) - n_{cl}^2] \phi \quad (3-8)$$

Although the applications in the next chapter are about the weakly guiding PPOWs launched by a normal incident field under an RML, which corresponds to the requirement of Pedé approximation, the $(n^2 - n_{cl}^2)$ term is still maintained instead of using $2n_{cl}(n - n_{cl})$ despite less simplifications.

3.2.1 Implementation by finite difference method

The standard form of implementation of the FD-BPM is based on Crank-Nicholson method, which solves both the accuracy and the stability problems. Here we divide the calculation area along x , y , and z direction to N , L , and M divisions, respectively. Electric field at the grid point at $x = i\Delta x$ ($i = 0$ to N), $y = \ell\Delta y$ ($\ell = 0$ to L), and $z = m\Delta z$ ($m = 0$ to M) is expressed by

$$\phi(i\Delta x, \ell\Delta y, m\Delta z) = \phi_{i,\ell}^m \quad (3-9)$$

After converting the above differential equation in eq. (3-8) to finite difference form, the propagation mode field ϕ is discretized by $i+1$, $\ell+1$, and $m+1$ steps along x , y , and z direction, respectively.

$$\begin{aligned}
\frac{\partial \phi}{\partial z} &\rightarrow \frac{\phi_{i,\ell}^{m+1} - \phi_{i,\ell}^m}{\Delta z} \\
\frac{\partial^2 \phi}{\partial x^2} &\rightarrow \frac{\phi_{i-1,\ell}^m - 2\phi_{i,\ell}^m + \phi_{i+1,\ell}^m + \phi_{i-1,\ell}^{m+1} - 2\phi_{i,\ell}^{m+1} + \phi_{i+1,\ell}^{m+1}}{2(\Delta x)^2} \\
\frac{\partial^2 \phi}{\partial y^2} &\rightarrow \frac{\phi_{i,\ell-1}^m - 2\phi_{i,\ell}^m + \phi_{i,\ell+1}^m + \phi_{i,\ell-1}^{m+1} - 2\phi_{i,\ell}^{m+1} + \phi_{i,\ell+1}^{m+1}}{2(\Delta y)^2} \\
\phi &\rightarrow \frac{1}{2}(\phi_i^{m+1} + \phi_i^m) \\
n^2(x, y, z) &\rightarrow n^2(i, \ell, m + 1/2)
\end{aligned} \tag{3-10}$$

The propagation fields along z direction at m , $m+1/2$, and $m+1$ step have the following relation:

$$-\phi_{i-1,\ell}^{m+1/2} + s_{i,\ell}^m \phi_{i,\ell}^{m+1/2} - \phi_{i+1,\ell}^{m+1/2} = \left(\frac{\Delta x}{\Delta y} \right)^2 (\phi_{i,\ell-1}^m + Q_{i,\ell}^m \phi_{i,\ell}^m + \phi_{i,\ell+1}^m) \tag{3-11a}$$

$$-\phi_{i-1,\ell}^{m+1} + S_{i,\ell}^m \phi_{i,\ell}^{m+1} - \phi_{i+1,\ell}^{m+1} = \left(\frac{\Delta y}{\Delta x} \right)^2 (\phi_{i-1,\ell}^{m+1/2} + q_{i,\ell}^m \phi_{i,\ell}^{m+1/2} + \phi_{i+1,\ell}^{m+1/2}) \tag{3-11b}$$

with

$$s_{i,\ell}^m = 2 - \frac{k^2(\Delta x)^2}{2} [n^2(i, \ell, m + 1/2) - n_{cl}^2] + j \frac{4kn_0(\Delta x)^2}{\Delta z} \tag{3-12a}$$

$$S_{i,\ell}^m = 2 - \frac{k^2(\Delta y)^2}{2} [n^2(i, \ell, m + 1/2) - n_{cl}^2] + j \frac{4kn_0(\Delta y)^2}{\Delta z} \tag{3-12b}$$

$$q_{i,\ell}^m = -2 - \frac{k^2(\Delta x)^2}{2} [n^2(i, \ell, m + 1/2) - n_{cl}^2] + j \frac{4kn_0(\Delta x)^2}{\Delta z} \tag{3-12c}$$

$$Q_{i,\ell}^m = -2 - \frac{k^2(\Delta y)^2}{2} [n^2(i, \ell, m + 1/2) - n_{cl}^2] + j \frac{4kn_0(\Delta y)^2}{\Delta z} \tag{3-12d}$$

where Δx , Δy , and Δz are the minimum steps along x , y , and z directions, respectively. Equations (3-9) to (3-12) lead to a recurrence process to calculate the propagation field once the launching field ($\phi^{m=0}$) is designated. Note that there are only $(N - 1)$ equations

($i = 1$ to $N-1$) in Eq. (3.11a) for ($N + 1$) unknown variables. Similarly, this happens again in that only ($L - 1$) equations ($\ell = 1$ to $L-1$) for ($L + 1$) unknown variables in Eq. (3.11b). It is required to involve other boundary conditions except Dirichlet and Neumann condition that we should treat the radiation fields penetrate away from the calculation window.

3.2.2 Transparent boundary condition

In order to include the radiation field outside the core area, the transparent boundary condition (TBC) is taken into account. The TBC is to simulate a nonexistent boundary that the radiation fields are allowed to freely escape from the problem without appreciable reflection, whereas radiation flux back into the problem region is prevented [4]. Furthermore, it is easy to be incorporated into a standard Crank-Nicholson differencing scheme in both two and three dimensions, and is applicable to longitudinally varying structures of our potential applications.

For simplification, the two dimension (x - z) condition is introduced in this section, so that Eq. (3-11) can be reduced to [3]

$$-\phi_{i-1}^{m+1} + s_i^m \phi_i^{m+1} - \phi_{i+1}^{m+1} = \phi_{i-1}^m + q_i^m \phi_i^m + \phi_{i+1}^m \quad (3-13)$$

with

$$s_i^m = 2 - k^2 (\Delta x)^2 [(n_i^{m+1/2})^2 - n_{cl}^2] + j \frac{4kn_{cl}(\Delta x)^2}{\Delta z} \quad (3-14a)$$

$$q_i^m = -2 + k^2 (\Delta x)^2 [(n_i^{m+1/2})^2 - n_{cl}^2] + j \frac{4kn_{cl}(\Delta x)^2}{\Delta z} \quad (3-14b)$$

Note that i is from 1 to $N - 1$. In TBC method, the field at the boundary is assumed to be a plane wave, and the phase difference between small steps in both ends (left and right)

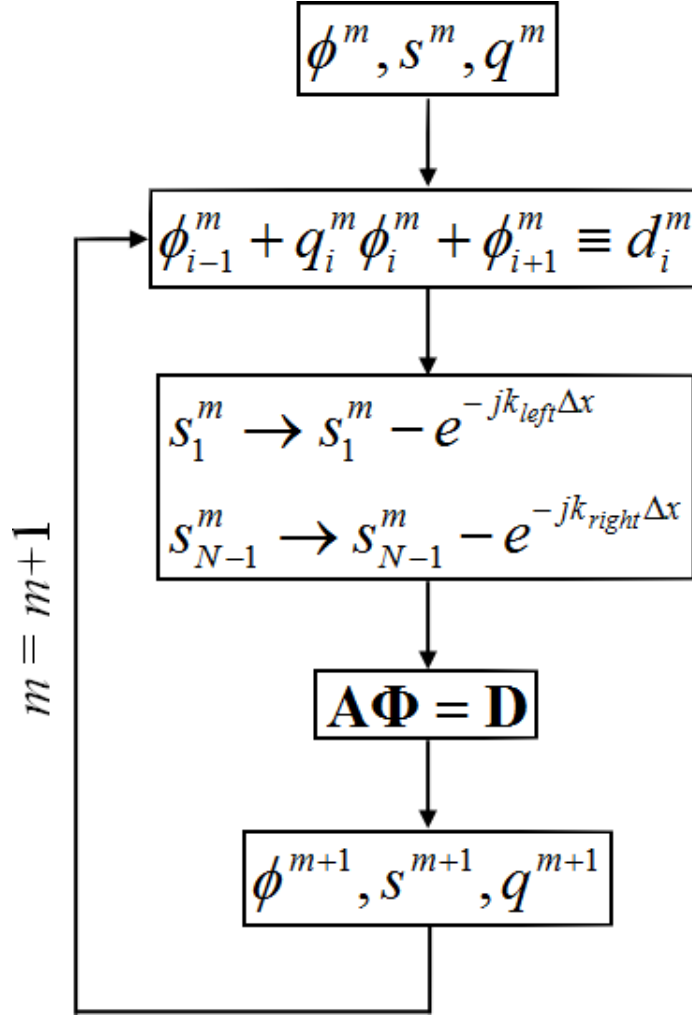


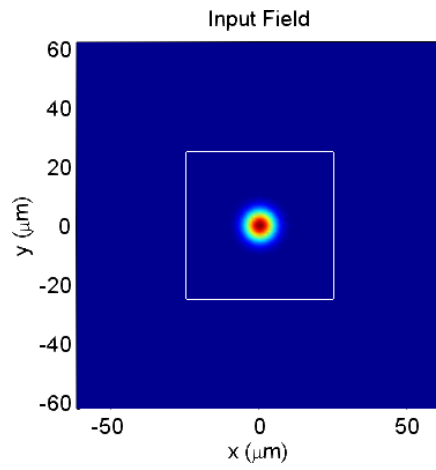
Fig. 3.3 Flow chart of FD-BPM in two dimension condition.

can be expressed as follows [4,5]:

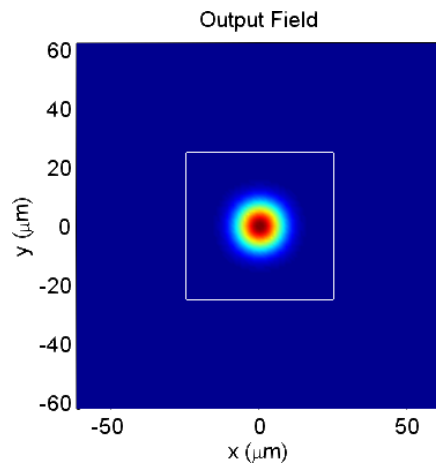
$$\frac{\phi_0^{m+1}}{\phi_1^{m+1}} = \frac{\phi_1^m}{\phi_2^m} = \exp(-jk_{left}\Delta x) \quad (3-15a)$$

$$\frac{\phi_{N+1}^{m+1}}{\phi_N^{m+1}} = \frac{\phi_N^m}{\phi_{N-1}^m} = \exp(-jk_{right}\Delta x) \quad (3-15b)$$

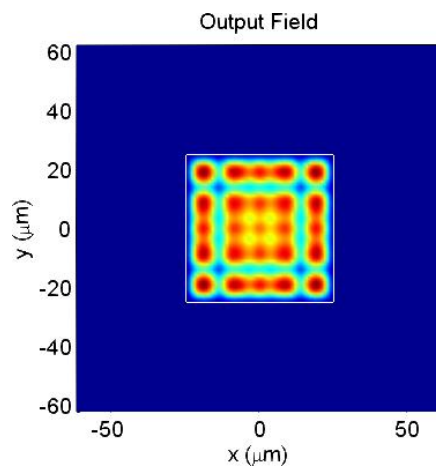
where k_{left} and k_{right} are wave numbers. The two ends of Eq. (3-14a) are modified as follows:



(a)



(b)



(c)

Fig. 3.4 Output profile calculated by three dimensional FD-BPM (a) launching field in a (b) GI waveguide (c) SI waveguide.

$$s_1^m \rightarrow s_1^m - \exp(-jk_{left}\Delta x) \quad (3-16a)$$

$$s_{N-1}^m \rightarrow s_{N-1}^m - \exp(-jk_{right}\Delta x) \quad (3-16b)$$

In the first round of iteration ($m = 0$), the right side of Eq. (3-13) can be directly calculated first and $\phi_0^{m=0}$ and $\phi_N^{m=0}$ can be determined by Eq. (3-15) and Eq. (3-16). The similar process goes forward to the next round ($m = 1$) until the loop stops. The calculation procedure for 2D case can be summarized to the flow chart, as Fig. 3.3 shows. Figure 3.4 shows the calculation results for a three dimension condition, where the parameters are listed in Table 3.1.

3.3 RADIATION FIELD FROM WAVEGUIDE

The Fresnel reflection occurs when light meets different refractive index medium and then results in partial reflection and transmission near to the interface. According to the experimental conditions, the lightwave with normal incident should be mainly considered, and then butt-couple between two media with refractive indexes of n_1 and n_2 are employed for modeling. The transmission coefficient T is given by

$$T = \frac{4n_1n_2}{(n_1 + n_2)^2} \quad (3-17)$$

In the loss evaluation experiment of an optical link performed in Sec. 4.4, no matching oil is used and an air gap could be involved between two components: waveguide and fiber. In the case of the normal incident lightwave from an air gap to a GI waveguide mentioned above, only 96 % of light penetrate the interface and couple into the waveguide, that is to say, 0.18-dB loss is inevitable.

Furthermore, we consider a uniform medium (n_{med}) is inserted between the two components as schematically described in Fig. 3.5. When applying the Fresnel–Kirchhoff diffraction formula, the far field $f(x, y, z)$ is related to the near field $g(x_0, y_0, 0)$ as [3]

$$f(x, y, z) = \frac{jk_0 n_{med}}{2\pi} \int_{-\infty}^{\infty} \int_{-\infty}^{\infty} g(x_0, y_0, 0) \frac{\exp(-jk_0 n_{med} r)}{r} dx_0 dy_0 \quad (3-18)$$

where r is the distance between arbitrary two points located on the near field and far field planes, respectively. Equation (3-18) also is applied to an oblique surface, for example a tilt mirror.

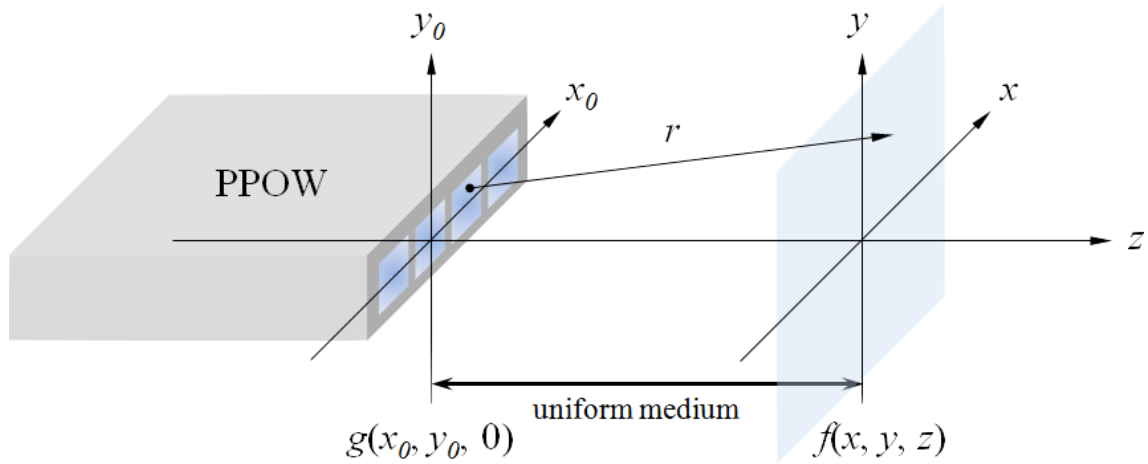


Fig. 3.5 Coordinate system for waveguide output and far field plane.

3.4 MIE SCATTERING

It is inevitable to investigate how scattering effect influences the modes propagation in polymer waveguides. In this study, the Mie scattering theory is referred. Mie scattering, also known as the Lorenz–Mie–Debye solution, is widely applied to particle absorption and scattering inspection. Compared to some ambiguous definition

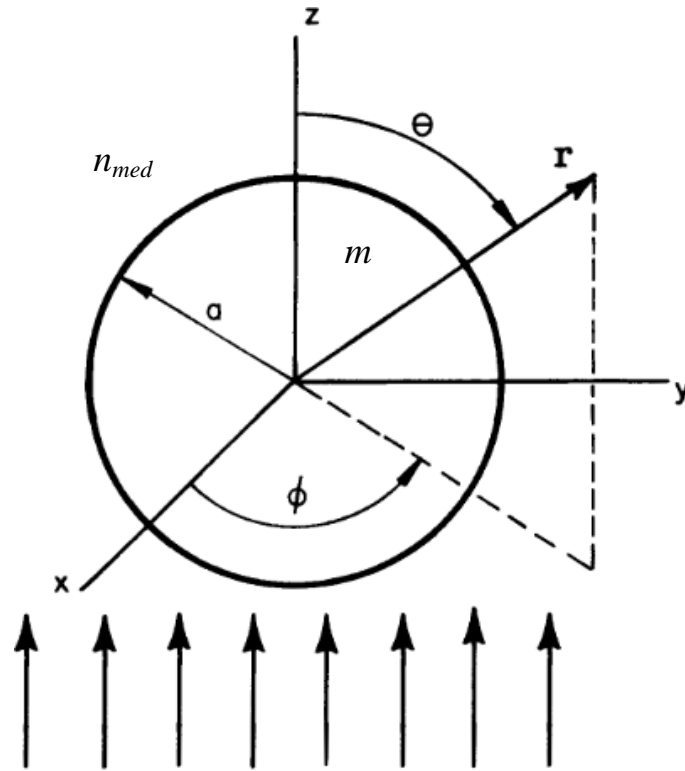


Fig. 3.6 Coordinate geometry for and Mie scattering.

mentioned in Sec. 2.4, the Mie scattering offers a set of exact solution for describing the behavior of electromagnetic field scattered by a perfect sphere with arbitrary radius and refractive index. Accordingly, Mie scattering theory has no limitations about size and converges to the limit of ray optics for large particles [6]. Although the formal solution to this problem has been available for many years, only since the advent of powerful enough computers, the embedded Bessel functions and solutions of associated Legendre functions are not a problem anymore. In this section, we introduce some useful formulations that are auxiliary tools for characterizing the scattering effect by FD-BPM introduced in Sec. 3.2.

In the case of our application, the absorption of the particle is neglected. Figure 3.6 shows the spherical coordinate of scattering geometry used for Mie scattering

corresponding to a single incident light on a single spherical particle with refractive index m . First, a dimensionless size parameter α is given by the expression [7]:

$$\alpha = \frac{2\pi a n_{med}}{\lambda} \quad (3-19)$$

where a is the radius of the particle, λ is wavelength of the incident beam, and n_{med} is the refractive index of the surrounding media. Although generally it is convenient to express the scattered intensity profile for each scattering angle (I_ϕ and I_θ), for perfectly spherical particles, polarized incident radiation produces similarly polarized scattered radiation; hence the scattering problem may be redefined in terms of the polarization. In the Mie scattering regime, the intensity profile related to polarizations is expressed in terms of differential scattering cross sections (σ), as follows:

$$I_{VW} = I_0 \frac{\sigma_{VW}}{r^2} \quad (3-20a)$$

$$I_{HH} = I_0 \frac{\sigma_{HH}}{r^2} \quad (3-20b)$$

with

$$\sigma_{VW} = \frac{\lambda^2}{4\pi^2 n_{med}^2} S_1 \quad (3-21a)$$

$$\sigma_{HH} = \frac{\lambda^2}{4\pi^2 n_{med}^2} S_2 \quad (3-21b)$$

$$\sigma_{un} = \frac{1}{2} (\sigma_{VW} + \sigma_{HH}) \quad (3-21c)$$

where I_0 is the intensity of the incident beam. The subscripts in Eq. (3-20) and Eq. (3-21) refer to the state of polarization of the incident and scattered light, respectively. The

subscripts VV refer to both vertically polarized incident light and vertically polarized scattered light with respect to the scattering plane ($\phi = 90^\circ$). Similarly, the subscripts HH refer to both horizontally polarized incident light and horizontally polarized scattered light with respect to the scattering plane ($\phi = 0^\circ$). For non-polarized incident light, the differential scattering cross sections is given by Eq. (3-21c) [7, 8]. The field functions S_1 and S_2 in Eq. (3.21) are calculated from the infinite series as follows:

$$S_1 = \frac{2n+1}{n(n+1)} [a_n \pi_n(\cos \theta) + b_n \tau_n(\cos \theta)] \quad (3-22a)$$

$$S_2 = \frac{2n+1}{n(n+1)} [a_n \tau_n(\cos \theta) + b_n \pi_n(\cos \theta)] \quad (3-22b)$$

where n is degree of Legendre functions. The angle-depend functions are:

$$\pi_n(\cos \theta) = \frac{P_n^{(1)}(\cos \theta)}{\sin \theta} \quad (3-23a)$$

$$\tau_n(\cos \theta) = \frac{d}{d\theta} P_n^{(1)}(\cos \theta) \quad (3-23b)$$

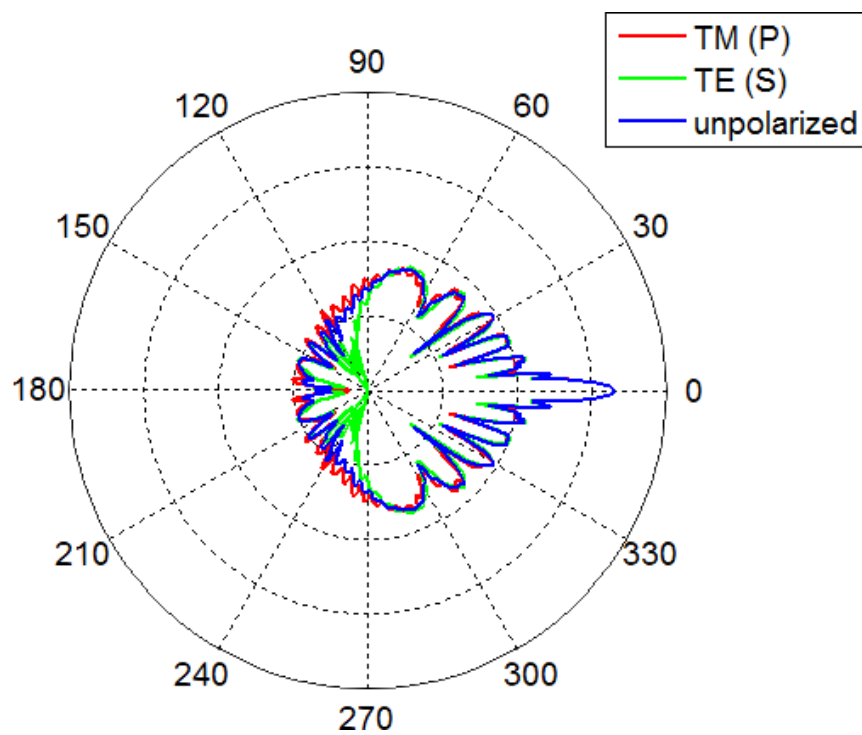
where $P_n^{(1)}$ is the solution of first order associated Legendre functions with degree of n .

Furthermore, the Mie coefficients are given by:

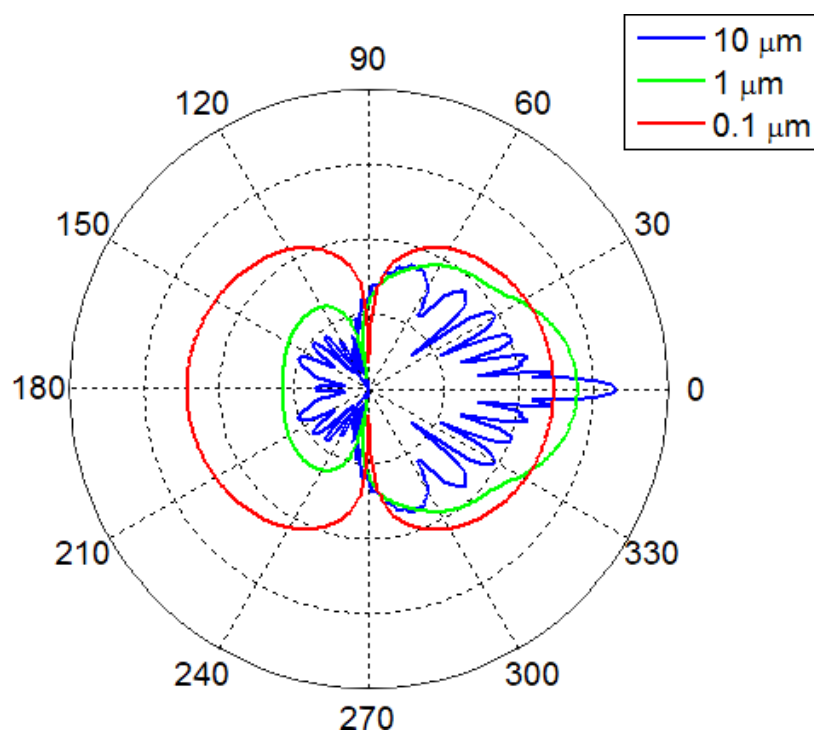
$$a_n = \frac{\Psi_n(\alpha)\Psi_n'(m\alpha) - m\Psi_n(m\alpha)\Psi_n'(\alpha)}{\xi(\alpha)\Psi_n'(m\alpha) - m\Psi_n(m\alpha)\xi_n'(\alpha)} \quad (3-24a)$$

$$b_n = \frac{m\Psi_n(\alpha)\Psi_n'(m\alpha) - \Psi_n(m\alpha)\Psi_n'(\alpha)}{m\xi(\alpha)\Psi_n'(m\alpha) - \Psi_n(m\alpha)\xi_n'(\alpha)} \quad (3-24b)$$

The Ricatti-Bessel functions Ψ and ξ in Eq. (3-24) are defined in terms of the half-integer-order Bessel function of the first kind ($J_{n+1/2}(z)$) and half-integer-order Hankel function of the second kind ($H_{n+1/2}(z)$) as follows:



(a)



(b)

Fig. 3.7 Scattered pattern with corresponding (a) polarization state (particle diameter is $10\ \mu\text{m}$) and (b) particle diameters (incident light is **S** polarized). Both cases are calculated under $m = 1$, $n_{med} = 1.5$, $\lambda = 0.85\ \mu\text{m}$ and in logarithm scale.

$$\Psi_n(z) = \sqrt{\frac{\pi z}{2}} J_{n+1/2}(z) \quad (3-25a)$$

$$\xi_n(z) = \sqrt{\frac{\pi z}{2}} H_{n+1/2}(z) \quad (3-25b)$$

So far, the formulations for Mie scattering with arbitrary spherical particle size and polarization state are introduced. The precision of Mie coefficients highly depend on the orders infinite series mentioned above. Figure 3.7 shows the calculated scattered field based on these formulations.

3.5 COMPARISON OF SCATTERED FAR FIELD PATTERN

In order to model how scattering effect influences on the mode conversion, the preferred refractive index profile is involved during iteration shown in Fig. 3.3. The interest in this study is in how the beam profiles calculated by FD-BPM realize the real conditions. In Sec. 3.4, the far field scattered pattern based on Mie scattering was obtained by Eq. (3-20) to Eq. (3-25), which is confirmed by lots of prior arts. In this section, we show the scattered pattern based on FD-BPM, and then confirm it by a spherical particle illuminated by a Gaussian beam.

3.5.1 Partial wave decomposition for Gaussian beam

So far, it is possible to calculate the far field scattered pattern for a spherical particle with an arbitrary radius which is illuminated by not only polarized but non-polarized light. For our application, PPOWs are launched by VCSELs with 0.85- μm wavelength, which are considered to be one of the best light-source candidates in the field of optical interconnections. In this study, we approximate that VCSELs emit a Gaussian beam

with multimode Hermite-Gaussian modes, which satisfies paraxial Helmholtz equation. The scattering problem of Gaussian beams by spherical shaped particles is of importance in various fields of optics. The particular fact that the scattering by individual particles having a high degree of symmetry by a transversely focused beam is called generalized Lorenz-Mie theory (GLMT), which expands the application of Mie scattering to an spherical particle illuminated by incident beam with arbitrary intensity profile [9]. The basic idea of GLMT is that a transversely localized beam that is a solution of Maxwell's equations can be decomposed to an infinite series of spherical Bessel functions and spherical harmonics, each of them is multiplied by a beam shape coefficient (g_n and h_n), which is called partial wave decomposition method. The partial waves decomposition method consists of the expansion of a Gaussian beam in terms of spherical vector wave functions. This method is based on Davis' description of Gaussian beams [10], accounting to axial and transverse field components. Moreover, the coordinate geometry is identical to Mie Scattering as shown in Fig. 3.6.

For the purpose of finding the radial profile by a Gaussian beam; it is required to involve some more physical treatment for converting a Gaussian beam composed by polar components. An on-axis focused electromagnetic beam (E_b) in a medium with a refractive index of n_{med} is given by [11,12]

$$\begin{aligned}
E_b(r, \theta, \phi) = & -E_0 \sum_{n=1}^{\infty} i^{n+1} (2n+1) g_n \frac{J_n(n_{med} k_0 r)}{n_{med} k_0 r} \pi_n \sin \theta \cos \phi \mathbf{u}_r \\
& + E_0 \sum_{n=1}^{\infty} i^n \frac{2n+1}{n(n+1)} [h_n J_n(n_{med} k_0 r) \pi_n - i g_n L_n(n_{med} k_0 r) \tau_n] \cos \phi \mathbf{u}_\theta \\
& - E_0 \sum_{n=1}^{\infty} i^n \frac{2n+1}{n(n+1)} [h_n J_n(n_{med} k_0 r) \tau_n - i g_n L_n(n_{med} k_0 r) \pi_n] \sin \phi \mathbf{u}_\phi
\end{aligned} \quad (3-26)$$

For far field ($r \rightarrow \infty$), E_b can be reduced as follows:

$$E_b(r, \theta, \phi) = -iE_0 \frac{\exp(in_{med}k_0r)}{n_{med}k_0r} [-S_{2b}(\theta) \cos \phi \mathbf{u}_\theta + S_{1b}(\theta) \sin \phi \mathbf{u}_\phi] + O(1/r^2) \quad (3-27)$$

Here, the S_{1b} and S_{2b} are far zone beam amplitudes for incident beam:

$$S_{1b}(\theta) = -(1/2) \sum_{n=1}^{\infty} \frac{2n+1}{n(n+1)} [g_n \pi_n + h_n \tau_n] \quad (3-28a)$$

$$S_{2b}(\theta) = -(1/2) \sum_{n=1}^{\infty} \frac{2n+1}{n(n+1)} [g_n \tau_n + h_n \pi_n] \quad (3-28b)$$

where g_n and h_n are beam coefficients (weights) and π_n and τ_n are defined by Eq. (3-23). For an axial symmetric Gaussian beam, g_n and h_n are equal and are given by [12]

$$g_n = h_n = D \exp(-in_{med}k_0z_0) \exp[-Ds^2(n+1/2)^2] \quad (3-29a)$$

with

$$D = (1 - 2isz_0/w)^{-1} \quad (3-29b)$$

$$s = (n_{med}k_0w)^{-1} \quad (3-29c)$$

where w is the width of the Gaussian beam and will be mentioned again later. Next, we consider the scattered field E_s when a spherical particle is illuminated by a vector decomposed Gaussian beam. The parameters of the particle are identical to Sec. 3.4.

The scattered field (E_s)

$$E_s(r, \theta, \phi) = -iE_0 \frac{\exp(in_{med}k_0r)}{n_{med}k_0r} [-S_{2s}(\theta) \cos \phi \mathbf{u}_\theta + S_{1s}(\theta) \sin \phi \mathbf{u}_\phi] + O(1/r^2) \quad (3-30)$$

Similarly, the S_{1s} and S_{2s} are far zone beam amplitudes for scattered field:

$$S_{1s}(\theta) = \sum_{n=1}^{\infty} \frac{2n+1}{n(n+1)} [a_n g_n \pi_n + b_n h_n \tau_n] \quad (3-31a)$$

$$S_{2s}(\theta) = \sum_{n=1}^{\infty} \frac{2n+1}{n(n+1)} [a_n g_n \tau_n + b_n h_n \pi_n] \quad (3-31b)$$

Compared to Eq. (3-28) the non-scattered condition; it is rather clear to see the beam amplitudes for scattered field is weighted by Mie coefficients mentioned in Eq. (3-24). Finally, the total amplitude can be expressed by the overlap of both as follows:

$$S_1(\theta) = S_{1b}(\theta) + S_{1s}(\theta) \quad (3-32a)$$

$$S_2(\theta) = S_{2b}(\theta) + S_{2s}(\theta) \quad (3-32b)$$

3.5.2 The coincidence between BPM and Mie scattering

In Sec. 3.2, the output field for an incident beam can be obtained step by step from Eq. (3-11) and (3-12). In order to involve some imperfections in core area, it is intuitively to modify the refractive index profile $n(x, y, z)$ for next $m+1/2$ step. For example, a certain area of $n(x, y, z)$ is designated to be 1, which means that an air bubble is located there. Whether this idea is valid or not is of our interest. In this section, we compare the results between FD-BPM and GLMT under the same conditions. The parameters applied in this section are listed in Table. 3.2.

First, similar consideration for a paraxial expression Gaussian beam propagates in a medium with a refractive index n_{med} , the beam width (w) as a function of z -position is given by

$$w(z) = w_0 \sqrt{1 + 4 \left(\frac{z - z_0}{n_{med} k_0 w_0^2} \right)^2} \quad (3-33)$$

where w_0 is the waist size, k_0 is the wave number in free space, and z_0 is the position of

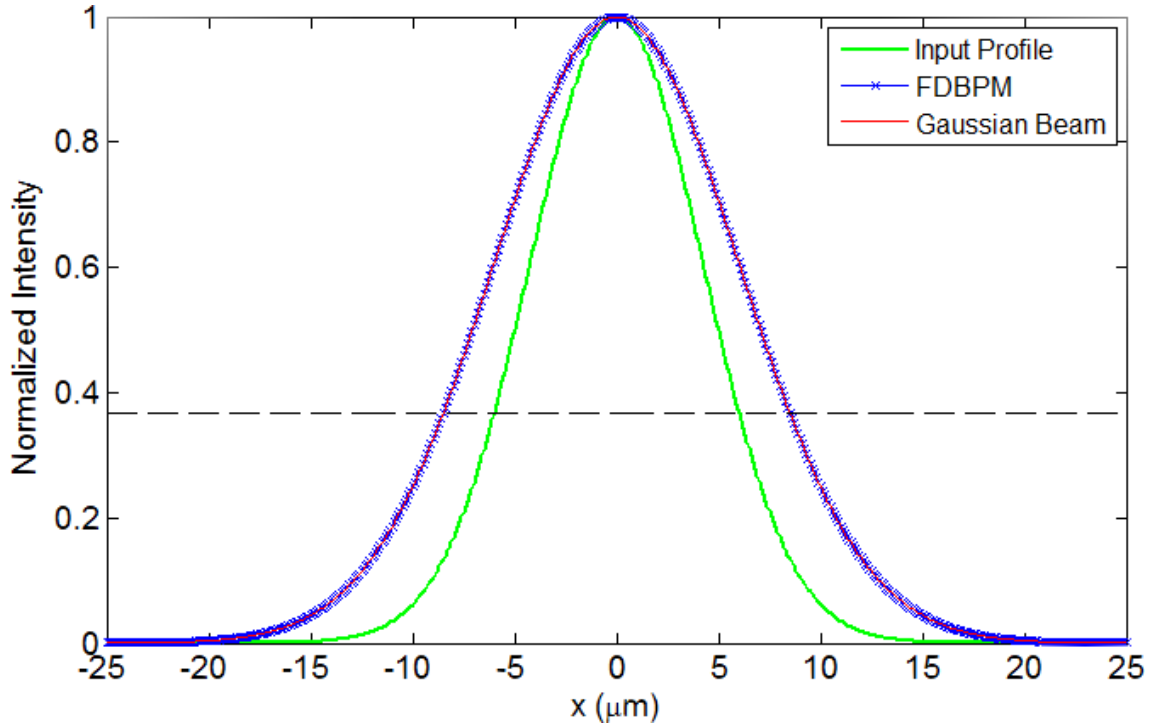


Fig. 3.8 Comparison of output pattern between a typical Gaussian profile broadened in a uniform media and calculated by FD-BPM.

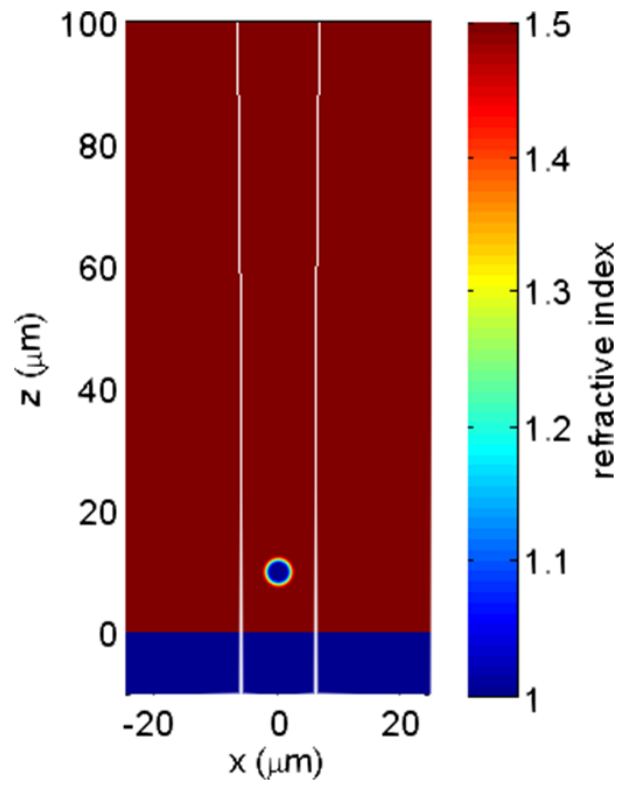
w_0 . In this example, we propose the w_0 is located on the origin, i.e. the entrance of the waveguide. We consider an SI waveguide whose core has a refractive index of 1.5 is launched via an SMF which guides the light from a VCSEL source. The wavelength is $0.85 \mu\text{m}$ and w_0 is designated to $6 \mu\text{m}$. Figure 3.8 shows the comparison of the intensity profile of the input Gaussian beam, the diffracted beams at $z = 20 \mu\text{m}$ (after propagating through a uniform medium) according to Eq. (3-33) and the beam profile calculated by FD-BPM. The two results (red line and blue cross line) look almost identical. This result indicates the validity of the programs created for this calculation and helps us to go forward.

As mentioned in Sec. 3.5.1, formulations for GLMT have no specific limitations for the particle size. Hence, a $4 \mu\text{m}$ circular particle ($n_{par} = 1$) is assumed to be centered at $z = 10 \mu\text{m}$ as shown in Fig. 3.9(a), and then the corresponding far field intensity profile is

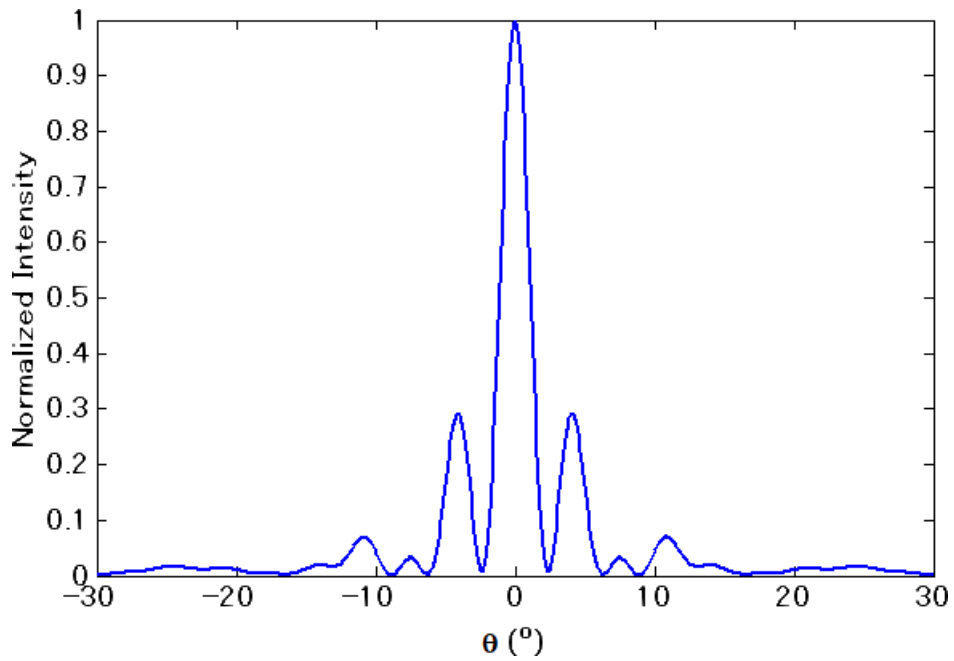
calculated using Eq. (3-29) to Eq. (3-32). The result is shown in Fig. 3.9(b). A sinc-function like pattern is clearly observed, which is a typical far field diffraction pattern for a beam scattered by an aperture. Next, we monitor how intensity profile changes along z-direction by applying FD-BPM. Figure 3.10 shows the calculated normalized intensity profile with respect to different z position. When it is near to the particle ($z = 20 \mu\text{m}$), the center of medium shows lower intensity than the lateral side. This is resulting from the interference and diffraction of scattered beam. When the beam propagates farther ($z = 60$ and $200 \mu\text{m}$ as shown in Fig. 3.10(b) and (c)), gradually the sinc-function like profile forms. Until $z = 1000 \mu\text{m}$, the side lobes become even lower and more close to the profile shown in Fig. 3.9(b). Although the corresponding local minimum is not fit very well between Fig. 3.9(b) and Fig. 3.10(d), it is not necessary for us to find the real far field profile because only near field is meaningful inside waveguides.

Table. 3.2 Parameters applied in Sec. 3.5.2

Parameters	Value
Wavelength (λ)	$0.85 \mu\text{m}$
Gaussian beam waist (w_0)	$6 \mu\text{m}$
Position of w_0 (z_0)	0
Refractive index of media (n_{med})	1.5
Refractive index of the particle (n_{par})	1
Coordinate of the particle center on x - z plane	(0, 10)

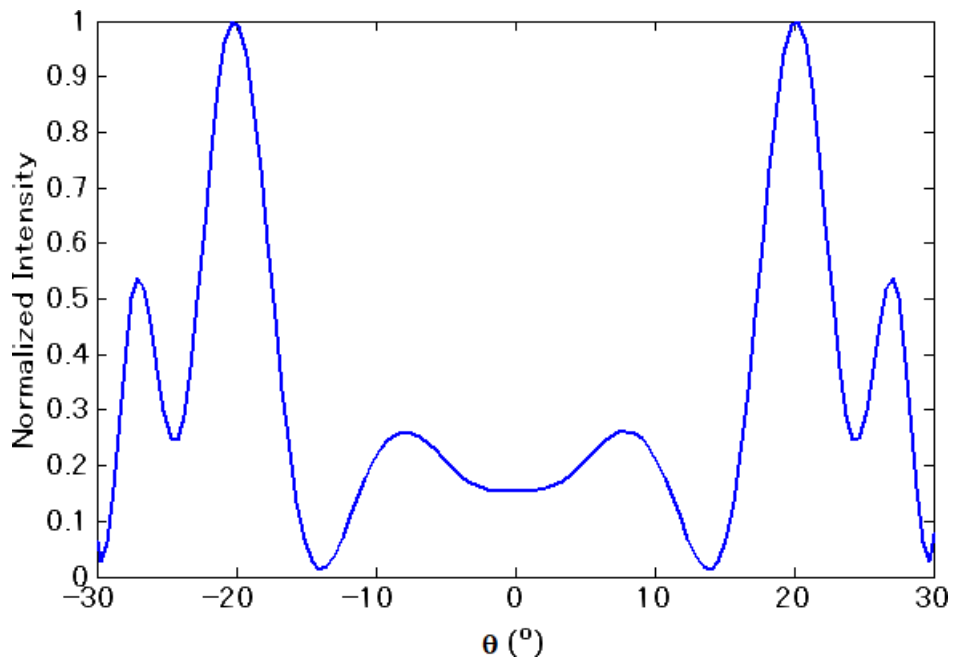


(a)

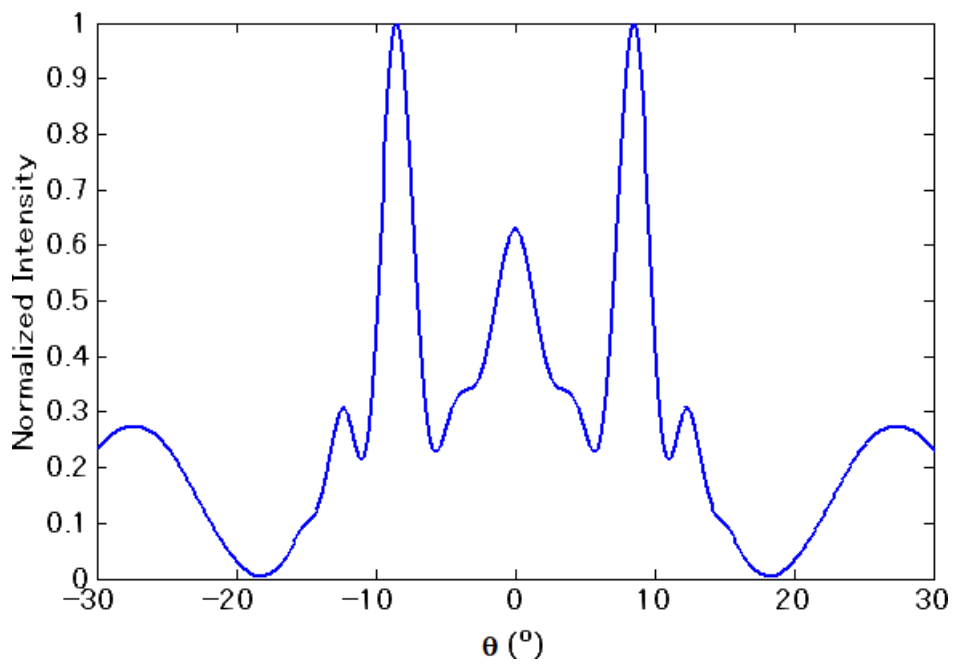


(b)

Fig. 3.9 (a) The particle with index of 1 is centered at $z = 10 \mu\text{m}$, where the two white curves beside the particle represent estimated width of the Gaussian beam. (b) The far field profile based on formulations introduced in Sec. 3.5.1.

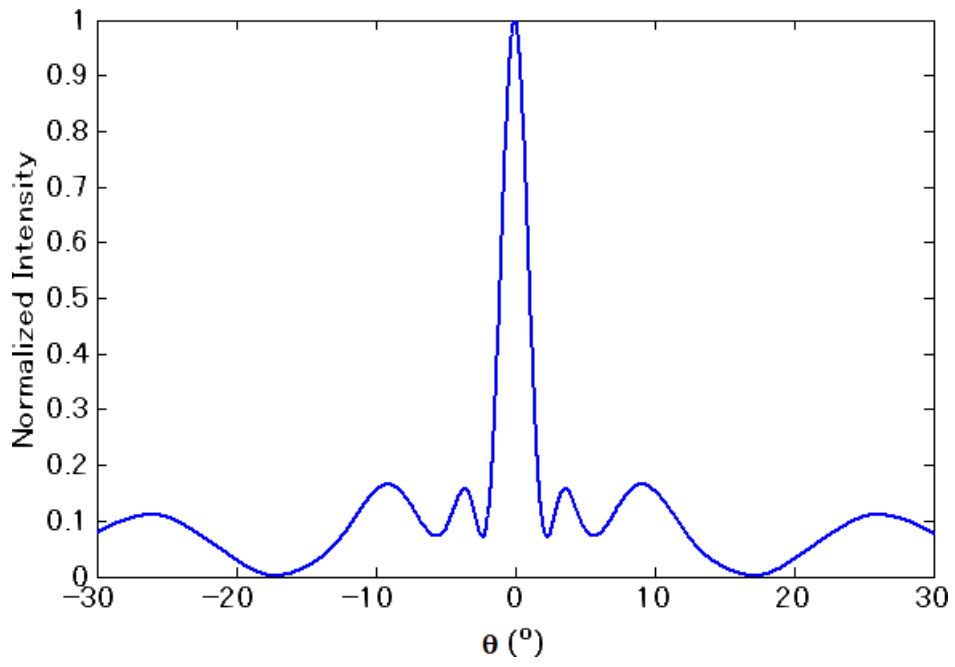


(a)

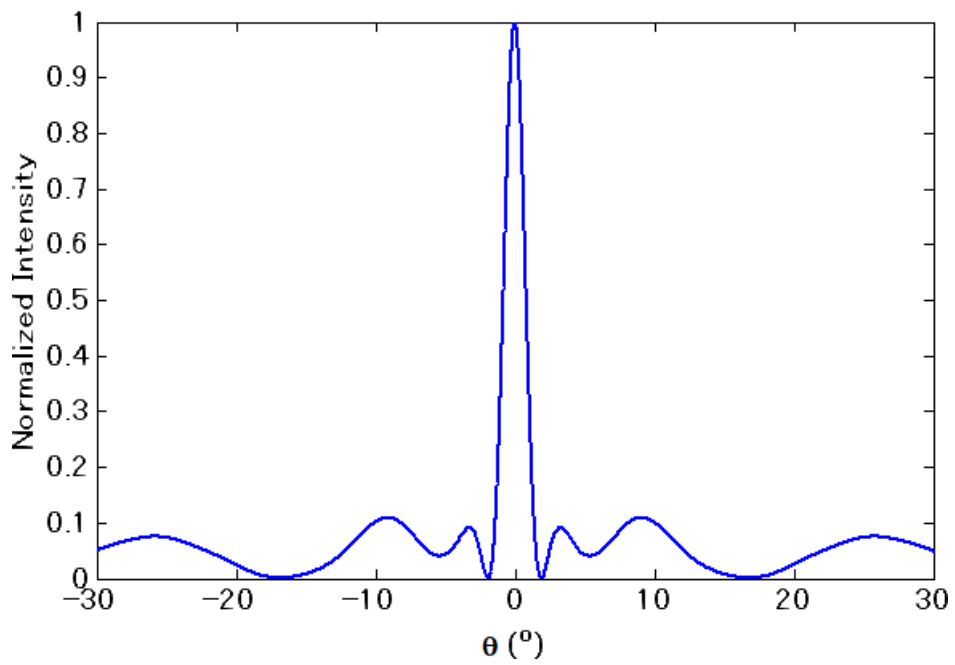


(b)

Fig. 3.10 Intensity profile by FD-BPM at (a) 20 μm (b) 60 μm.

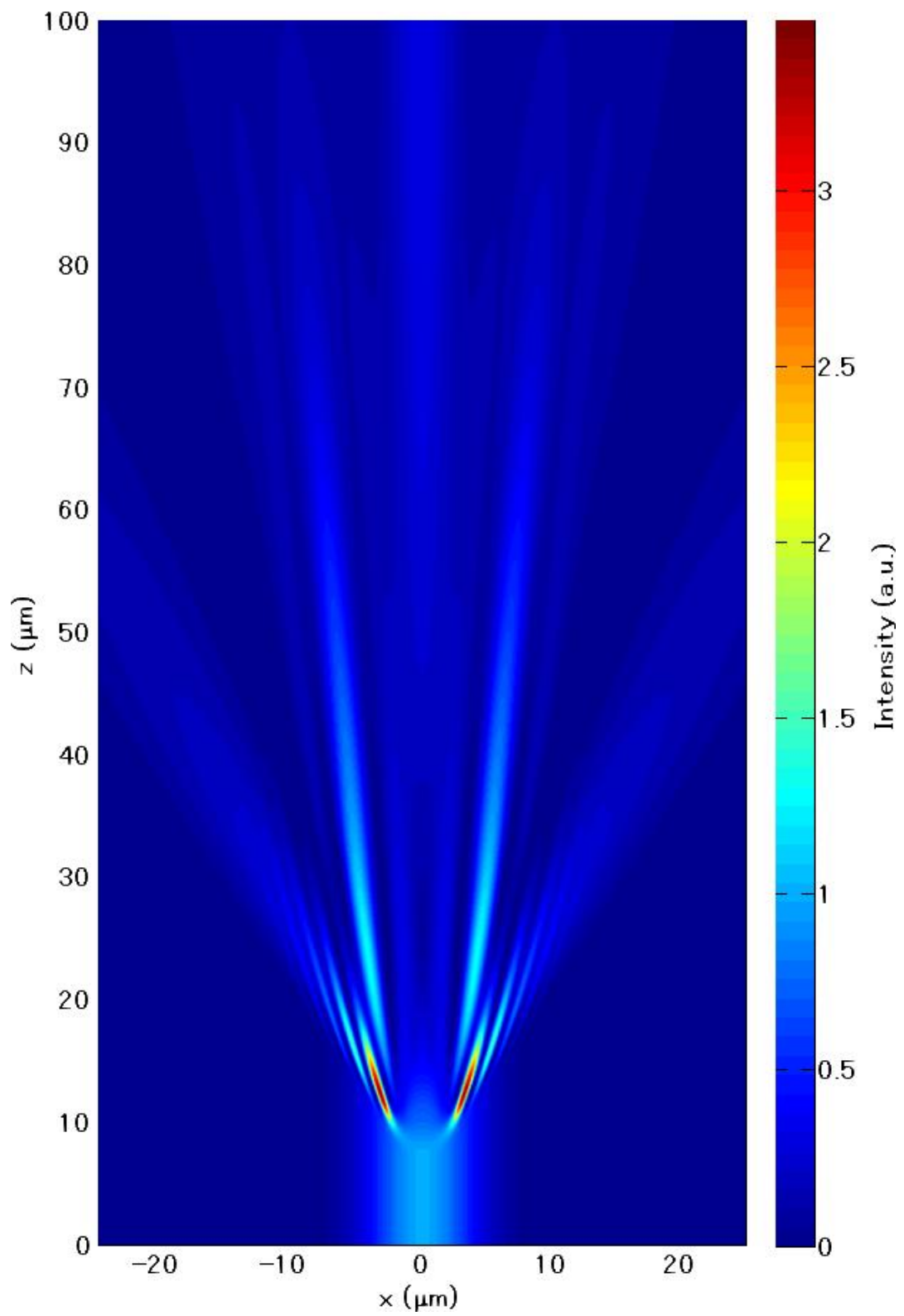


(c)



(d)

Fig. 3.10 Intensity profile by FD-BPM at (c) 200 μm (d) 1000 μm .



(e)

Fig. 3.10 (e) The intensity profile of a Gaussian beam scattered by a circular particle.

REFERENCE

1. D. Marcuse, *Theory of Dielectric Optical Waveguides* (2nd Edition Academic Press Inc., 1971).
2. Optical Waveguides: Numerical Modeling
<http://optical-waveguides-modeling.net/wave-propagators.jsp> (2012.2.10)
3. K. Okamoto, *Fundamentals of Optical Waveguides* (2nd edition, Elsevier, 2006).
<http://goo.gl/Ds9Fx> (2012.2.10)
4. G. R. Hadley, "Transparent boundary condition for beam propagation method," *J. of Quant. Elect.*, 28(1), 363-370 (1992).
http://ieeexplore.ieee.org/xpls/abs_all.jsp?arnumber=119536&tag=1
5. Tetsuro Yabu, *Introduction of Optical Waveguide Analysis* (Morikita Publishing Co., Ltd., 2007).
6. Craig F. Bohren and Donald R. Huffman, *Absorption and Scattering of Light by Small Particles* (Wiley, 1983).
<http://goo.gl/4L0P7> (2012.2.10)
7. D. W. Hahn, "Light Scattering Theory," (2009)
<http://plaza.ufl.edu/dwhahn/Rayleigh%20and%20Mie%20Light%20Scattering.pdf>
(2012.2.10)
8. B. M. Herman, "Note Concerning The Mie Scattering Of Unpolarized Incident Radiation," *J. Met.* 18(4), 558-560 (1961).
<http://journals.ametsoc.org/doi/abs/10.1175/1520-0469%281961%29018%3C0558%3E%3A%3A%3E2.0.CO%3B2>
9. G. Gouesbet and G. Gréhan, *Generalized Lorenz-Mie Theories* (Springer, 2011).
<http://goo.gl/ch9X1> (2012.2.10)
10. L. W. Davis, "Theory of electromagnetic beams," *Phys. Rev. A*, 19(3), 1177-1179 (1979).
http://pra.aps.org/abstract/PRA/v19/i3/p1177_1
11. J. A. Lock, "Calculation of the radiation trapping force for laser tweezers by use of generalized Lorenz-Mie theory. 1. Localized model description of an on-axis tightly focused laser beam with spherical aberration," *Appl. Opt.* 43(12), 2532-2544 (2004).
<http://www.opticsinfobase.org/abstract.cfm?URI=ao-43-12-2532>
12. James A. Lock, Susan Y. Wrbanek, and Kenneth E. Weiland, "Scattering of a tightly focused beam by an optically trapped particle," *Appl. Opt.*, 45(15), 3634-3645 (2006).
<http://www.opticsinfobase.org/ao/abstract.cfm?URI=ao-45-15-3634>

4

APPLICATIONS

4.1 CROSSTALK ANALYSIS FOR CO-POLYMER WAVEGUIDES

4.2 CROSSTALK ANALYSIS FOR W-SHAPED WAVEGUIDES

4.3 OPTICAL LINK ANALYSIS WITH RAY OPTICS

4.4 OPTICAL LINK ANALYSIS WITH WAVE OPTICS

4.5 THE OPTIMIZATION OF WAVEGUIDE DESIGN

In chapter 2 and 3, several fundamental theories and physical phenomena are introduced. In this chapter, the knowledge in the previous chapters is utilized for real applications. In section 4.1 and 4.2, we pay attention to discreet single devices, and then, co-polymer based GI-PPOWs and so-called W-shaped PPOWs are fabricated. Although the co-polymer based waveguides show slightly higher scattering loss than the DPS-doped counterparts, it exhibits better thermal stability for on-board wiring. Furthermore, although it was already reported that W-shaped POF showed lower modal dispersion, the outstanding performance in decreasing the inter-channel crosstalk is also found in W-shaped PPOWs. In our previous studies, we did lots of works for experimentally confirm the relation between index profile difference and crosstalk in PPOWs. In the first two sections we combine the simulation and experiment results to explain the mechanism of the inter-channel crosstalk. For expanding the application of

these knowledge, we applied both ray and wave optics for optical link in section 4.3 and 4.4. From different point view, we know some limitation about the connection between several components for short range optical interconnections.

4.1 CROSSTALK ANALYSIS FOR CO-POLYMER WAVEGUIDES

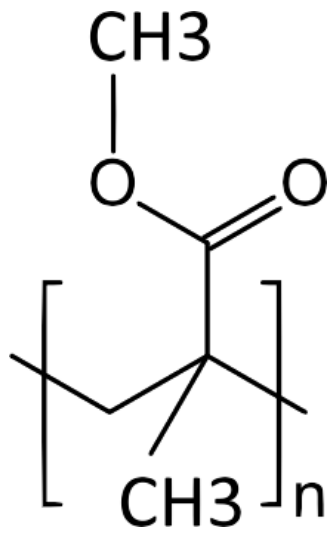
We fabricate GI PPOWs comprised of PMMA-poly benzyl methacrylate (PBzMA) copolymer for the purpose of achieving high thermal stability in the GI profiles. The waveguides obtained show slightly higher propagation loss (0.033 dB/cm at 850 nm) than doped PMMA based GI-core polymer waveguides we have reported (0.027 dB/cm), due to the excess scattering loss inherent to the mixture of copolymer and homo-polymer in the core area. In this study, we focus on the influence of the excess scattering loss on mode conversion and inter-channel crosstalk. We simulate the behavior of light propagating inside the core with and without the light scattering. Using the simulation, the excess loss experimentally observed in the copolymer-core waveguide is successfully reproduced, and then, we find that the excess scattering loss of 0.008 dB/cm could increase the inter-channel crosstalk from -30 dB to -23 dB, which agrees with the experimentally observed value. Although the simulation of the inter-channel crosstalk was performed only on our GI-core polymer optical waveguides, it is capable of modeling the conventional SI rectangular-core waveguides. Some amount of excess scattering is generally observed in the conventional SI-core waveguides, and thus, the application of this simulation to SI-core waveguides allows a feasible design for high-density alignment of the waveguides.

4.1.1 Waveguide fabrication and characterization

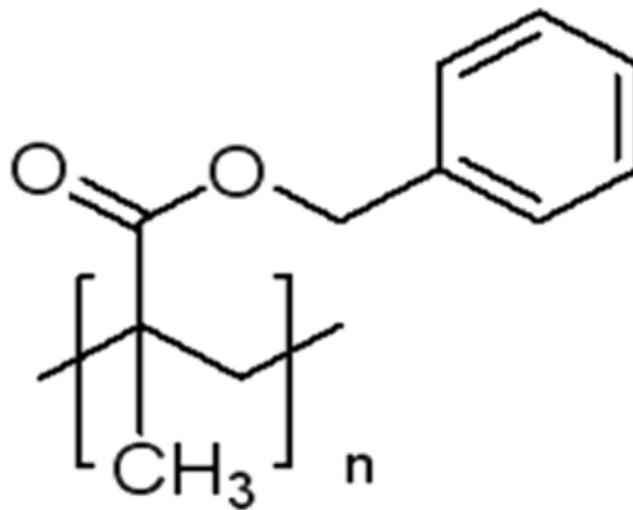
We fabricate copolymer based multi-channel polymer optical waveguides by means of the preform method we have reported in [1]. In this study, we use a monomer mixture composed of 20-wt.% BzMA in MMA instead of diphenyl sulfide (DPS) doped PMMA for the core material. Our target is to form a graded refractive index distribution approximated by the power-law form shown by Eq. (2-1) in each circular-shaped core (channel) area. The related molecular structures in this study are shown in Fig. 4.1.

When we apply the GI-core polymer optical waveguides to board-level optical interconnections, the thermal stability of the dopant added polymer has been of a great concern. Actually, it was already reported that the refractive index profile formed in a GI POF comprised of dopant added PMMA degraded after aging at 85 °C due to the diffusion of dopant in the PMMA matrix [2]. On the other hand, the refractive index profile formed with copolymer is stable enough because the copolymer molecules do not diffuse easily. On the other hand, it was also reported that [3] a copolymer of MMA and BzMA in the GI POF showed higher scattering loss due to large heterogeneous structure attributed to its long chain molecules with different refractive index, compared to DPS doped PMMA. In particular, when the GI preforms were fabricated by means of the interfacial-gel polymerization technique, excess scattering loss is clearly observed.

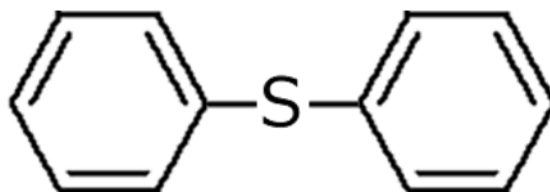
Therefore, we focus on the “excess scattering loss,” of the MMA-BzMA copolymer based GI-core polymer optical waveguides in this study. The processes of the preform fabrication and refractive index profile control are described in [1,4], and basically, we use the same processes in this study. First, a mold composed of two glass plates and a Teflon flange was filled with MMA monomer, in which several round brass rods were aligned in parallel. The mold was placed in an autoclave under 60 °C and 0.3-MPa N₂



(a)



(b)

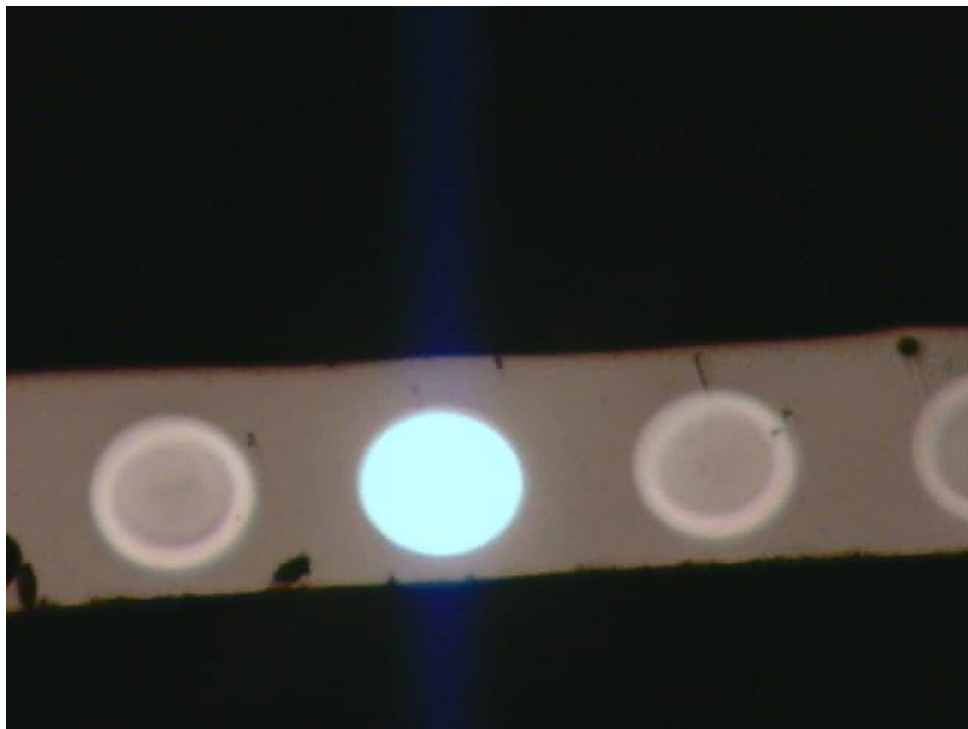


(c)

Fig. 4.1 The molecule of (a) poly methyl methacrylate (PMMA) (b) poly benzyl methacrylate (PBzMA) (c) diphenyl sulphide (DPS).



(a)



(b)

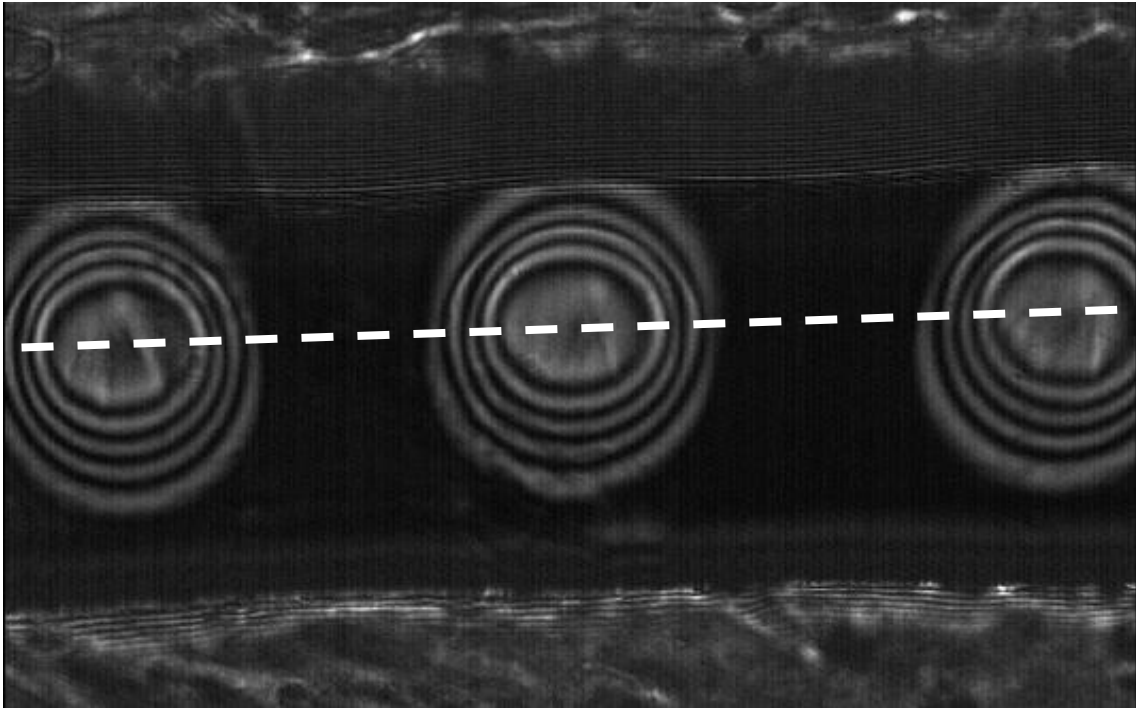
Fig. 4.2 The GI PPOW with 20-wt.% BzMA for core material. (a) Cross section image, and (b) the waveguide is launched by a white light source.

gas atmosphere for four hours in order to polymerize the monomer. After the polymerization reaction completed, the rods were removed to form holes for the cores, and then a plate-like PMMA based cladding was fabricated.

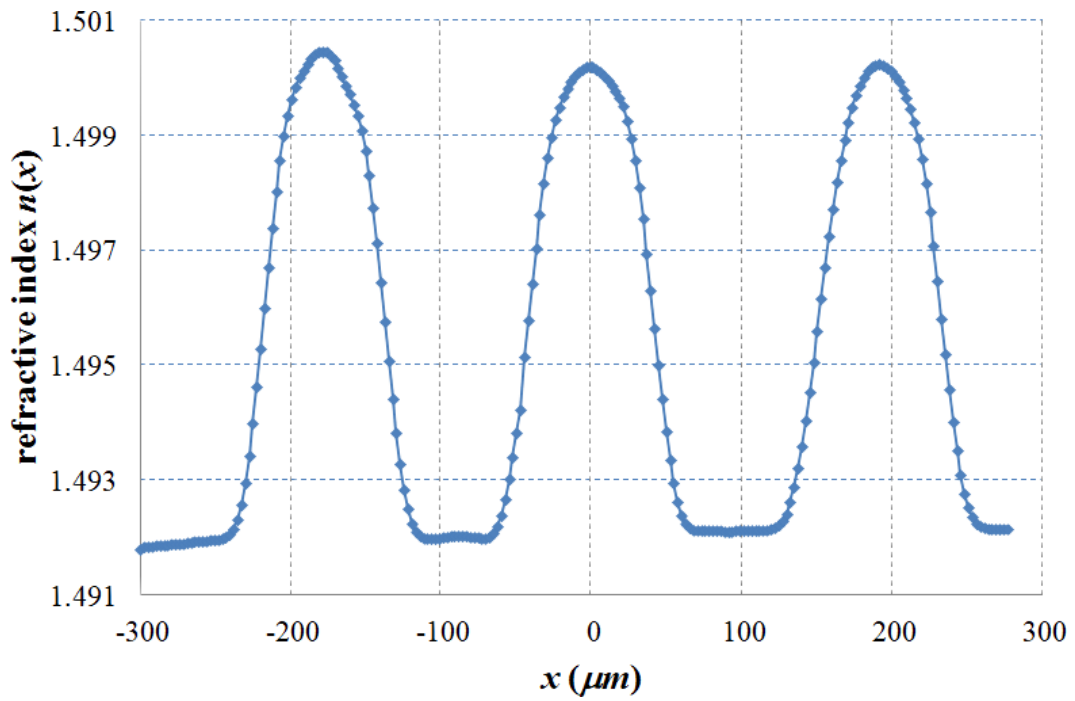
For the core area, a mixture of 20-wt.% BzMA in MMA monomer was used. Secondly, the core area was polymerized in an autoclave at 120 °C for 48 hours to obtain a preform. During the core polymerization reaction, a concentration distribution of BzMA-MMA copolymer is formed in each core area, which makes a near-parabolic refractive index distribution. This process is so-called the interfacial-gel co-polymerization technique [5].

Finally, the preform was heat-drawn to a multi-channel polymer optical waveguide with several hundreds of meters long. Figure 4.2(a) shows the cross section image grabbed by a microscope, which clearly shows four circular cores are integrated inside the waveguide. The diameter of each core is controlled around 100 μm during the heat-drawing process. In Fig. 4.2(b), the second core from the left of the waveguide is launched by a white light source and not only from the launched core but also bright rims in other cores is observed. Note that the rims of the adjacent cores are brighter than their inner area. This means even if the light is well confined near the launched core center, a little power leaks out and then re-couples to the adjacent channels (mode conversion). This phenomenon is a result of the crosstalk in our waveguide and will be discussed later.

The measurement of refractive index profile is based on the dual-beam transmission interference microscopy. Two beams from the same light source (a halogen-tungsten lamp) transmit through a sample slice and the reference medium (a glass plate in this experiment) individually, and finally they interfere with each other. Here, the sample



(a)



(b)

Fig. 4.3 (a) The white light interference fringes and (b) the measured refractive index profile along the white dash line in Fig. 4.3(a)

slice is polished until its thickness is small enough (c.a. 250 μm), and then, the thickness of the reference (glass plate) is adjusted to have almost the same optical path through the waveguide sample. The sample slice is immersed in matching oil for reducing measurement errors particularly surface roughness of the slice. Figure 4.3(a) shows the interference fringes of the sample slice in Fig. 4.2(a). With assists from the photomicrograph shown in Fig. 4.3(a), the refractive index difference (Δn) can be calculated by the following equation [6]:

$$\Delta n = \frac{d(x, y) \lambda}{D t} \quad (4-1)$$

where $d(x, y)$ is the phase difference inside the core area, D is the phase difference of cladding area (the bulk PMMA in this experiment), λ is the illuminating wavelength, and t is the thickness of the sample slice. In Fig. 4.3(a), the round shape interference fringes confirm the radial symmetric distribution of GI refractive index profile with numerical results shown in Fig. 4.3(b). The core radius of each core is approximately 50 μm and pitch (from the center to center) is approximately 200 μm . The refractive indices of the core (n_{co}) and cladding (n_{cl}) are 1.5005 and 1.492. The fitted g values correspond to Eq. (2-1) are 2.461, 2.476, and 2.460 for the left, middle, and right channel, respectively.

4.1.2 Loss and crosstalk measurement

Here, we discuss about the excess scattering loss caused from the copolymer core as follows: during the core polymerization process, the homo-polymer of PMMA comprising the cladding is dissolved into the monomer mixture in the core, while the newly polymerized copolymer of MMA and BzMA also exists in the core region. Thus, the GI-cores formed by the interfacial-gel co-polymerization process are composed of a

PMMA homo-polymer and a copolymer of MMA and BzMA. This mixture of two kinds of polymers with different refractive indices leads to large heterogeneous structures that enhance the scattering loss [7].

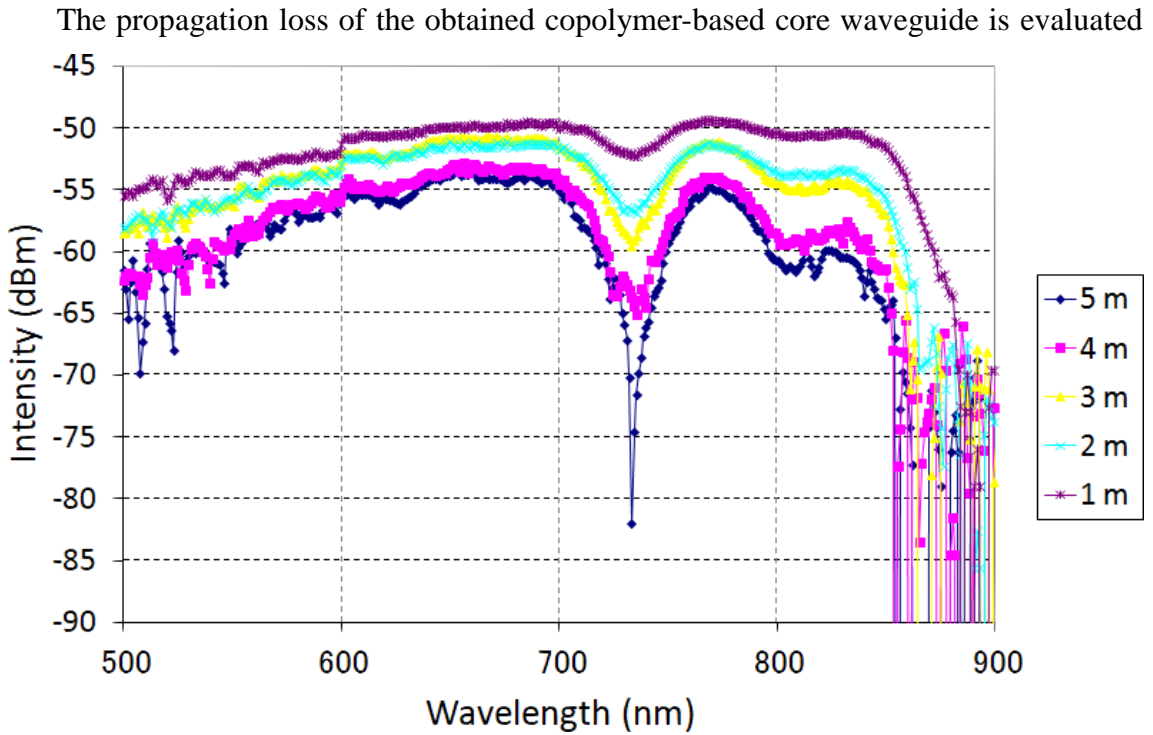


Fig. 4.4 The measured spectrum with corresponding waveguide length for loss measurement.

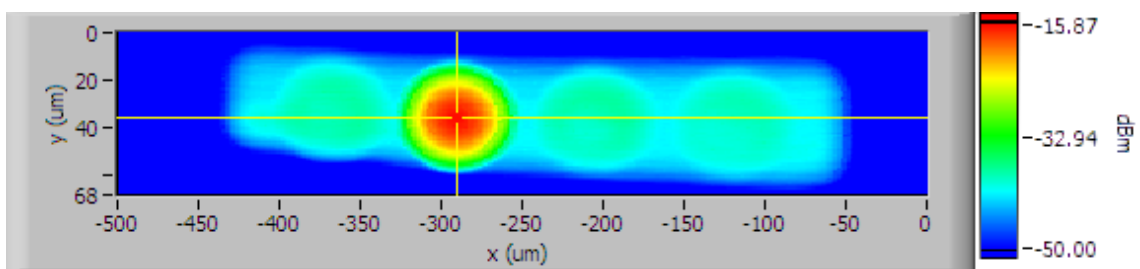


Fig. 4.5 The measured intensity map for crosstalk measurement

by utilizing the cut-back method [1]. In this measurement, incoherent light from a Halogen-Tungsten lump is coupled to a core of the waveguide (shown in Fig. 4.2(b)) via a 50- μm core multimode fiber (MMF) probe (1-m length), and the output light from the

core is coupled to another 50- μm core MMF probe to guide to the optical spectrum analyzer (ANDO AQ-6315B). Figure 4.4 shows the spectrum with corresponding waveguide length. From the slope of the output power variation at a wavelength of 850 nm, the propagation loss is obtained as 0.033 dB/cm, which is higher than that (0.028 dB/cm) of a DPS doped core waveguide [1, 8]. As expected, an excess scattering loss of 0.005 dB/cm from the copolymer based core increases the total propagation loss. Although the excess loss of 0.005 dB/cm seems very low, the loss measurement using the cut-back method was carried out for the waveguides with several-meters long, which is long enough for evaluating the loss with good accuracy.

In a previous report where a P(MMA-BzMA) core GI polymer optical fiber (POF) is fabricated using the interfacial-gel co-polymerization technique, the loss of the copolymer based POF was as high as 0.002 to 0.0025 dB/cm at 650-nm wavelength, while a dopant-based GI POF showed 0.0015 dB/cm at the same wavelength. Therefore, an excess scattering loss of approximately 0.001 dB/cm was caused in the copolymer-based core GI POF. For optical links that need to connect a distance of hundreds of meters, the “excess scattering loss” of even 0.001 dB/cm is seriously high. Meanwhile, an excess loss of 0.005 dB/cm observed in our waveguide looks very low for a link with a few tens of centimeters [7]. We will discuss the influence of the excess scattering loss on the performance of the waveguides.

For the crosstalk measurement, the middle of the three cores was launched via an SMF probe, and we use a 50- μm core MMF to scan the entire output end of the waveguide, where the intensity is measured by a power meter and the results are shown in Fig. 4.5. The definition of crosstalk (XT) is as follows:

$$XT(\text{dB}) = 10 \log \frac{I_1}{I_0} \quad (4-1)$$

where I_0 is the intensity of launched core and I_1 is the intensity of one of adjacent cores. The copolymer based waveguide fabricated in this study is 1-m long, which exhibits higher crosstalk (-23.47 dB for the left channel and -23.71 dB for the right) than the DPS doped waveguide which showed a crosstalk of -30 dB and less [1]. Due to the higher excess scattering loss from the copolymer based waveguide, higher power light is leaked from the core and would increase the crosstalk value. Table 4.1 shows comparison between DPS doped and copolymer based waveguides.

Table 4.1 Measurement results of the waveguides

Waveguide type	DPS dopant	Copolymer based
Loss (dB/cm)	0.028	0.033
Crosstalk at 1 m (dB)	< 30	~ -23.6

4.1.3 Calculated NFP from waveguides with high scattering loss

In this section, we apply the equations previously introduced in chapter 2 to do the theoretical analysis. As mentioned in the previous section, the copolymer based optical waveguides exhibited higher scattering loss than dopant based ones. It is believed that loss caused by light scattering is one of the factors enhancing mode conversion. Therefore, there is a concern that the higher scattering loss broadens the optical field in the whole core and even into the cladding region. Subsequently, when the light signal is no longer confined in the core due to the mode conversion caused by multiple scatterings, it leaks out and could re-couple to the adjacent channels. It is not easy to find an appropriate way based on wave-optics theory to simulate the light scattering phenomena by randomly distributed polymer chain structures.. Thus, in this study,

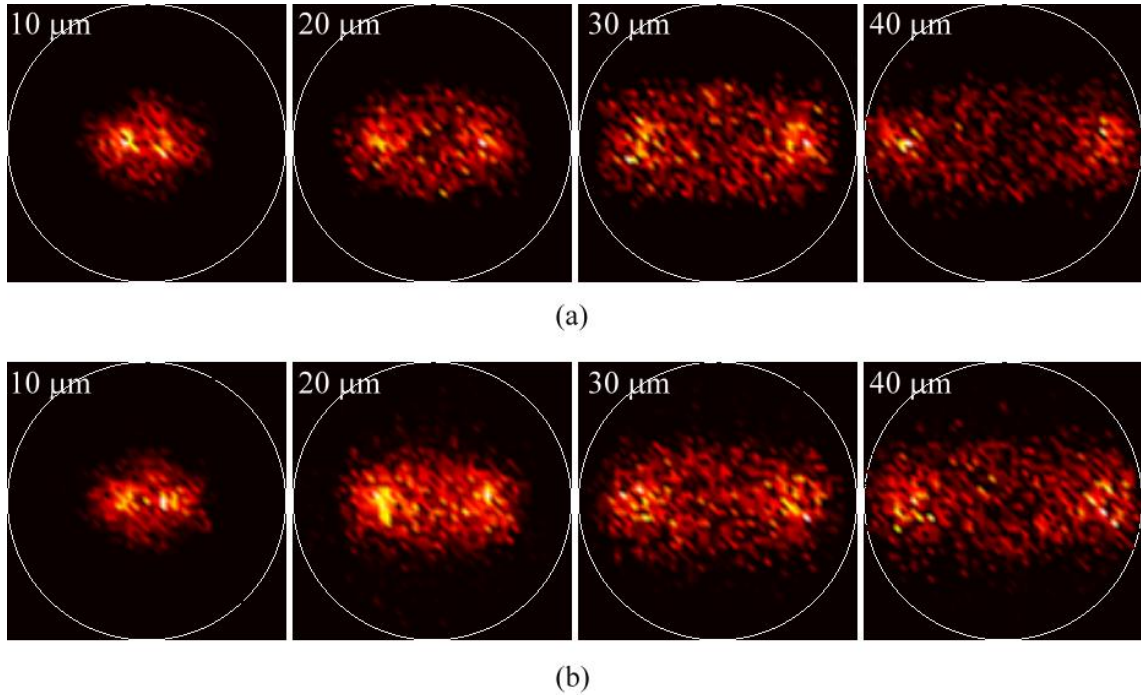


Fig.4.6 The calculated NFP under offset launching conditions (a) without and (b) with scattering effect. The offset distance from left to right is 10, 20, 30 and 40 μm . In this simulation $p = 10\%$, $N_s = 5$ and $\theta_m = 20$ is applied. The white circle surround the calculated NFP is the assumed core-cladding boundary.

instead, the ray tracing method is applied for the simulation. Although the zero-wavelength ($\lambda = 0$) condition is assumed, we can still apply the local plane wave theory near the core-cladding boundary, where the refractive index is nearly constant within the range of wavelength-scale distance [9]. It is well known that ray trace simulation is applicable when the waveguides support large number of propagating modes, while wave optics theory should be applied with decreasing the propagating mode number. Thus, the 50- μm core which is a typical core size of multimode fiber was very important for analyzing the waveguides with ray trace simulation. However, in this case, the signal wavelength would be 1.3 μm . On the other hand, in this study, since a shorter wavelength (850 nm) is utilized, the number of propagation modes would be large enough even for 35- μm core waveguide to apply this ray-trace model. Here, it is very important that we suppose only mode conversion is the dominant factor for the

inter-channel crosstalk here.

Based on the ray theory introduced in chapter 2, the intensity profile at the output end can be calculated. We simulate the NFPs under the offset launching condition from 10 to 40 μm . For more realistic case, we consider multiple rays launched with the Monte-Carlo method. The rays are injected into a restricted area in the core as a bundle of divergent rays, while the input intensity profile of this area is assumed to have a Gaussian distribution. Figure 4.6 shows how light scattering influences the calculated NFPs after a 3-cm propagation distance by varying the offset distance from 10 to 40 μm . When all the rays propagate with no scattering, as shown in Fig. 4.6(a), an ellipsoidal ring-like pattern is observed and higher output power is accumulated as two peaks near the launching and its conjugating positions. It is found that the output power is still mostly confined in the core. On the other hand, the influence of light scattering is taken into account, as shown in Fig. 4.6(b). When the offset is 10 μm , the NFP still looks similar to that with no scattering in Fig. 4.6(a). However, the number of the output rays near the rim area increases, with increasing the offset distance, and under 40- μm offset launch, the output rays are observed from whole core area even for such a short distance as 3 cm. Thus, we confirm high scattering loss of the waveguide broadens the output NFP to the area near the core-cladding boundary, and the rays could be easily leaked out from the core: this is one of the causes of inter-channel crosstalk.

4.1.4 Calculated crosstalk for high scattered waveguides

For the GI multi-channel waveguide simulation, the three cores (left, middle, and right) cases are considered. The middle core is launched as is the case of Fig. 4.2(b). For more a realistic condition, the unclear core-cladding boundary shown in Fig. 4.3(a) is

also taken into account. We assume the refracted rays project into the other channels with a skin depth of 5 μm . If the ray path grazes under the simulated core-cladding boundary with a distance smaller than the skin depth, it would directly penetrate that area and keep its intensity unchanged. Besides, three channels with the same characteristics are considered. Those re-coupled rays follow the same algorithm mentioned above and they also propagate with scattering.

Figure 4.7 shows the calculated NFPs without and with light scattering for the multi-channel waveguide, where the colored-bar beside each graph shows the intensity normalized by the intensity of all the injected rays. The parameters describing the light scattering are the same as those of previous single channel condition. In the calculated NFP without scattering case shown in Fig. 4.7(a), we hardly observe any output rays from the adjacent channels. On the other hand, in the case with scattering-included condition, some amount of output power from the adjacent channels is clearly observed, and they form a circular pattern near the core-cladding boundary. This is due to the leaked rays that are trapped by the GI profile in the adjacent core. Moreover, this simulation also confirms the superior performance of GI profile compared to the conventional waveguide with step index cores.

4.1.5 Calculated loss for high scattered waveguides

The relationship between the scattering loss and inter-channel crosstalk is analyzed using the similar algorithm to the multi-channel case mentioned above. In the MMA-BzMA copolymer based GI-core waveguides, excess scattering loss is experimentally observed; it is well known that the propagation loss at 850-nm wavelength includes the inherent absorption loss of approximately 0.025 dB/cm due to

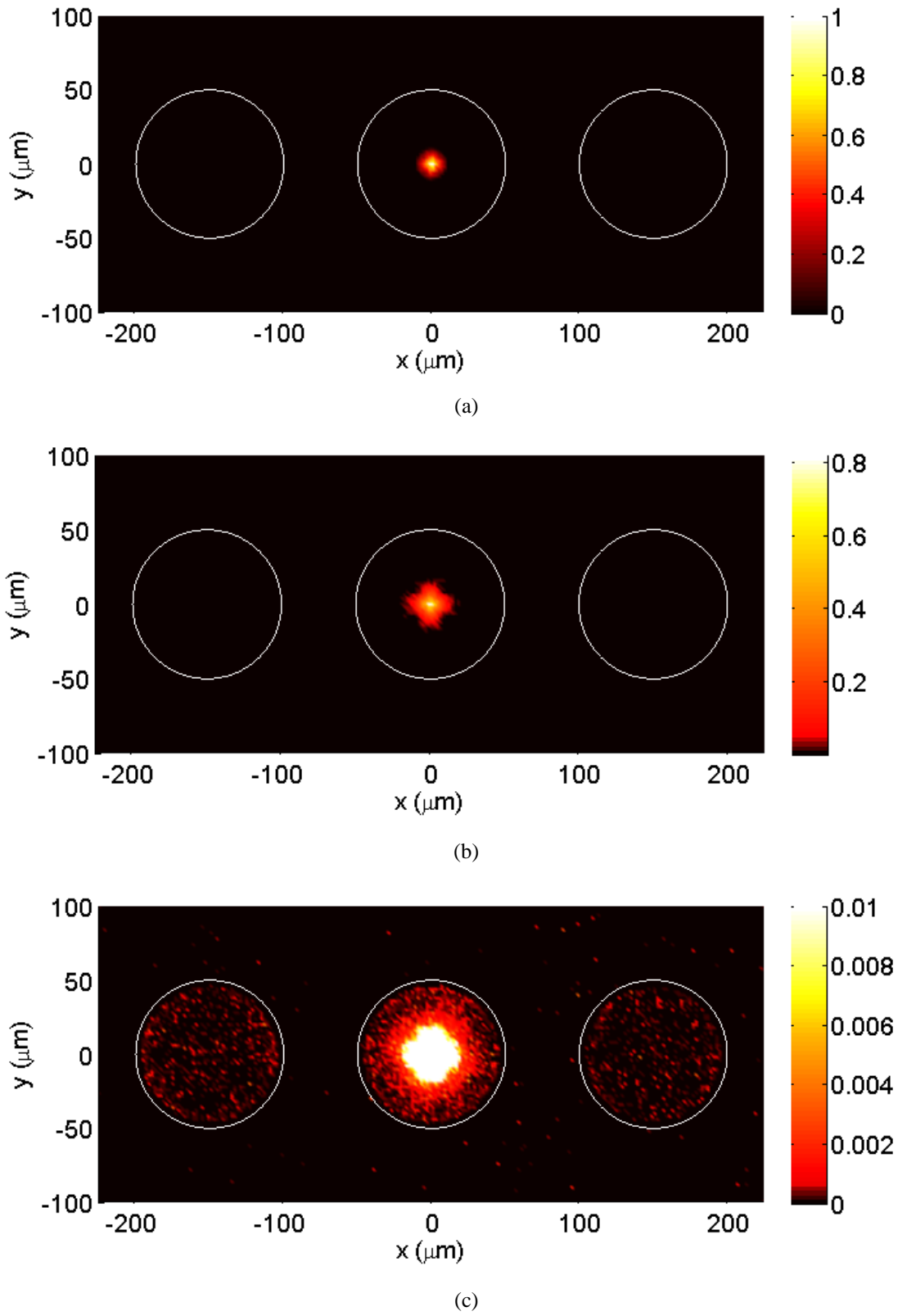


Fig. 4.7 The calculated NFP for (a) launching condition (b) without and (c) with scattering effect included for a GI multi-channel waveguide. In this simulation, the parameters are identical as single channel case.

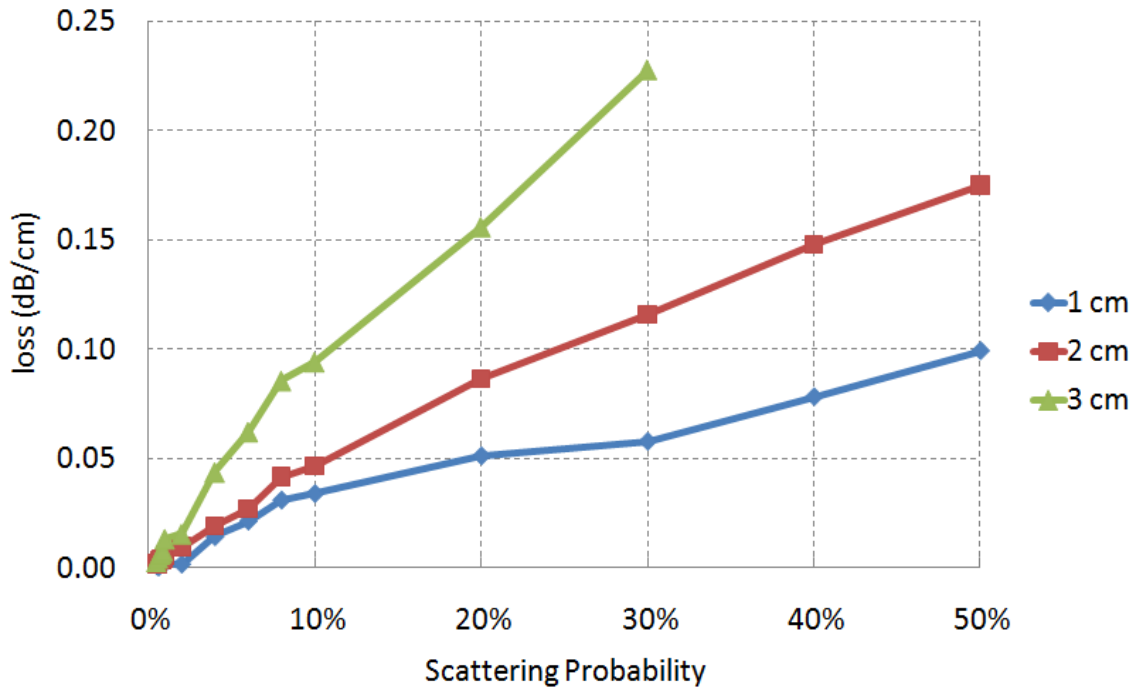
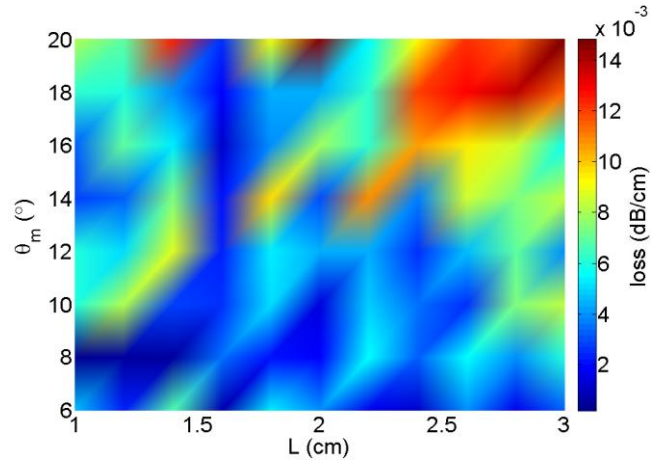


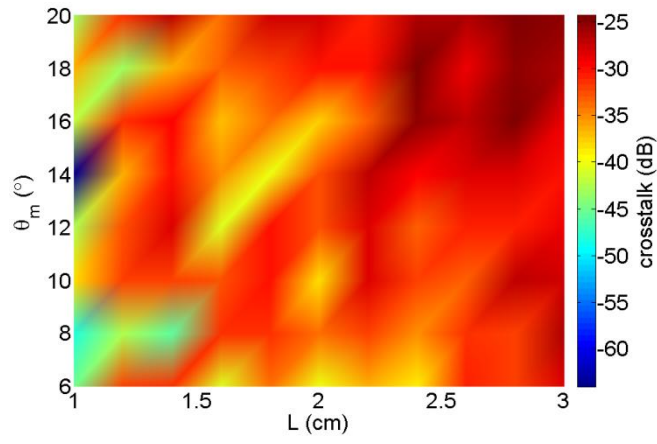
Fig. 4.8 The scattering probability p dominates the scattering loss and shows the unexpected propagation length dependence.

the carbon-hydrogen stretching vibration [7]. Therefore, the experimentally measured propagation loss of 0.033 dB/cm (as shown in Table 4.1) includes the scattering loss of 0.008 dB/cm. Meanwhile, in the simulation, the center of the middle core in a three-channel waveguide is launched. Here, the scattering probability is varied from 0.5 % to 50 % and then calculate the propagation loss in dB/cm in order to find the reasonable initial values of the parameters realizing the excess scattering loss of 0.008 dB/cm.

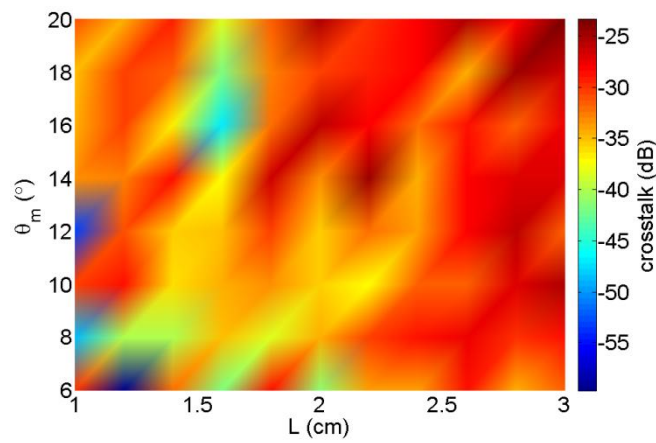
The calculated propagation loss is shown in Fig.4.8. Here, it is found that the scattering probability p dominates the loss value. Even a scattering probability of 10 % is still too high for obtaining the scattering loss of 0.008 dB/cm. When p increases, propagation length dependence of the scattering loss also increases, as shown in Fig. 4.8. Although this length dependence can be observed in multimode core under a restricted



(a)



(b)



(c)

Fig. 4.9 (a) The loss value (in dB/cm) for the center channel. (b) The crosstalk value (in dB) for the right channel and (c) left channel.

launch condition, other two parameters, N_s and θ_m , are slightly adjusted in order to obtain reliable results. Then we theoretically verify that an excess scattering increases the inter-channel crosstalk as follows.

After some calculations, we can conclude the maximum number of scattered rays plays a minor role in this simulation. Here, $N_s = 5$ is fixed and the scattering probability is determined to be 1 %. The relationship among the propagation distance L , the maximum scattered angle θ_m , and propagation loss is investigated. Figure 4.9 (a) shows when θ_m is smaller than 14 degrees, the propagation loss is as low as 0.01 dB/cm, and is almost independent on the waveguide length. Thus, we succeeded in modeling the copolymer based GI core waveguide shown in Fig. 4.2(b). Using these parameters, inter-channel crosstalk is calculated, and the results are shown in Fig. 4.9(b) and Fig. 4.9(c). As expected, the crosstalk values are a little lower than -30 dB in the area where θ_m is smaller than 14 degrees. Meanwhile, with increasing the value of θ_m , the crosstalk increases to -25 dB. Thus, it is obvious that the excess scattering loss of the waveguide significantly increases the crosstalk, and a good coincidence with the experimental result shown in Table 4.1 is observed.

4.1.6 Conclusion

A polymer optical waveguide with GI-circular cores is fabricated using P(MMA-BzMA) copolymer for the core. Although the copolymer core possesses higher thermal stability in the refractive index profile than doped PMMA core waveguides, an excess scattering loss as high as 0.008 dB/cm is observed. Hence, we evaluated the influence of the excess scattering loss on the mode conversion and inter-channel crosstalk in the multi-channel GI-core polymer optical waveguide. The ray tracing

method is utilized for the simulation. In the single channel condition, the calculated output NFP showed the optical confinement effect of the GI profile when no scattering was taken into account, while a significant NFP degradation was observed due to the mode conversion caused by the light scattering. For the multi-channel condition, the loss and crosstalk value can be clearly quantified by the similar way. The results encourage us toward further optimization processes and add more practical considerations.

Although the simulation of the inter-channel crosstalk was performed only on our GI-core polymer optical waveguides, it is capable of modeling the conventional SI rectangular-core waveguides. As aforementioned, some amount of excess scattering is generally observed in the conventional SI-core waveguides, and thus, the application of this simulation to SI-core waveguides helps finding a feasible design for high-density alignment of the waveguides.

4.2 CROSSTALK ANALYSIS FOR W-SHAPED WAVEGUIDES

For applications in high-density and high-speed optical interconnections, we propose to utilize PPOWs with so-called W-shaped refractive index profile in the core area. A W-shaped index profile is composed of a parabolic index distribution surrounded by a narrow index valley, followed by a cladding with a uniform refractive index. It is expected that W-shaped index profiles contribute to decrease the inter-channel crosstalk due to mode conversion in the waveguides. In this study, how much the index difference of the index valley improves the crosstalk value is investigated. First, polymer waveguides with various index profiles are fabricated by changing the composition of the copolymer for cladding. Then, the results are shown

where a 1-m long W-shaped profile PPOW has not only low propagation loss (0.027 dB/cm), but an inter-channel crosstalk (~ -40 dB) lower than those of GI core PPOW we previously fabricated. Next, the propagation loss and inter-channel crosstalk in polymer waveguides with different index profiles are theoretically analyzed by means of a ray tracing model introduced in Chapter 2, in which the light scattering effect is included. The calculation results indicate that the index valley surrounding each core works properly for preventing the power coupling from the cladding modes to the propagation modes, and consequently, very low inter-channel crosstalk is realized with W-shaped index profiles.

4.2.1 Waveguide fabrication and characterization

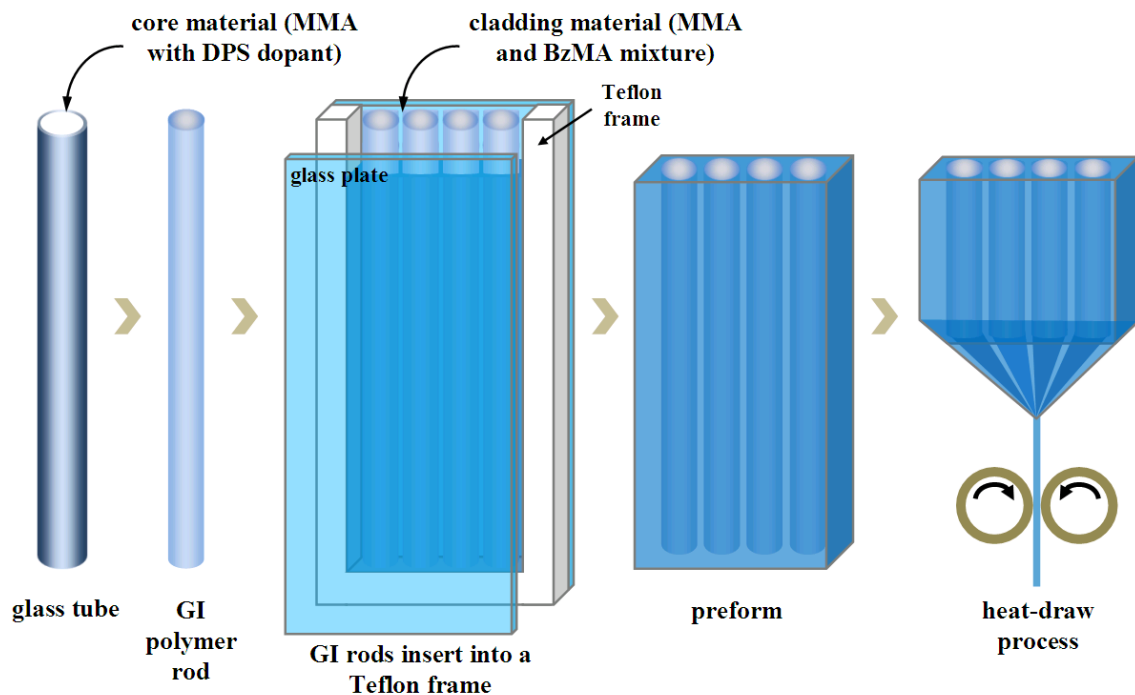


Fig. 4.10 Fabrication process of W-shaped refractive index profile PPOW.

The fabrication process of W-shaped PPOWs employed in this study is shown in Fig. Fig. 4.10. It is based on the preform method in which the refractive index of cladding is

controlled by adjusting the feed concentration of BzMA monomer to MMA monomer in the cladding. [10]. Here, a graded refractive index distribution modeled by the power-law form shown by Eq. (4-2) should be formed in each circular core (channel) area. Outside each core area, a refractive index valley is added, and the refractive index profile $n(r)$ as a function of the distance r from the core center is written with a parameter of index exponent g as,

$$\begin{cases} n(r) = n_1[1 - 2\Delta(r/a)^g]^{1/2}, & 0 \leq r \leq a \\ n(r) = n_2, & a < r \leq (a + w) \\ n(r) = n_3, & (a + w) < r \end{cases} \quad (4-2)$$

where, Δ is the relative refractive index difference, a is the core radius, and w is the width of the valley. In addition, n_1 is the highest refractive index value in the core region (normally at the core center), n_2 is the lowest refractive index of the valley, and n_3 is the refractive index of the cladding which is slightly larger than n_2 . If n_2 and n_3 are equal, a GI refractive index profile is described by the same equation.

The first step is to fabricate several GI rods for the cores of the W-shaped waveguides, as shown in Fig. 4.10. Several 50-cm long glass tubes with 10-mm inner diameter are filled with a specified amount of MMA monomer with a polymerization initiator and chain transfer agent. The tube is rotated on its axis at 2000 to 3000 rpm in an oven at 70 °C. After several hours of polymerization reaction, a hollow PMMA tube is formed. Then, the glass tubes are removed and the PMMA tubes are filled with the core material, and then heated up in an oil bath at 120 °C in order to polymerize the core material. Here, the core material is composed of MMA monomer doped with an 11 wt. % of DPS. After the polymerization completes, a rod with a near-parabolic refractive index profile is obtained. Similar to the method applied to the previous

section, the interfacial-gel polymerization technique is already well established as a preparation method of GI polymer optical fiber [11].

Next, those GI rods are arranged in a line and inserted in a mold composed of a Teflon frame and two glass plates, as shown in Fig. 4.10. Then, the space between the inner mold and GI rods are filled with a plenty of MMA and BzMA monomer mixture, followed by polymerization of the monomer to form a preform plate. In the obtained preform plate, the GI core in all the rods are surrounded by a thin PMMA-homopolymer layer, while the outermost layer is composed of a PMMA-BzMA copolymer. Since the refractive index of BzMA is higher than that of PMMA, the PMMA homopolymer layer works as a refractive index valley in a W-shaped index profile. After heat-drawing the preform, a multi-channel W-shaped PPOW is obtained.

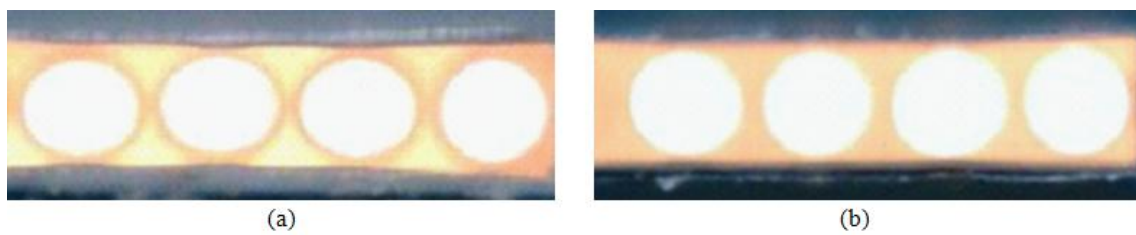


Fig. 4.11 (a) W-shaped and (b) previously obtained GI-PPOW illuminated by a Halogen-Tungsten lump.

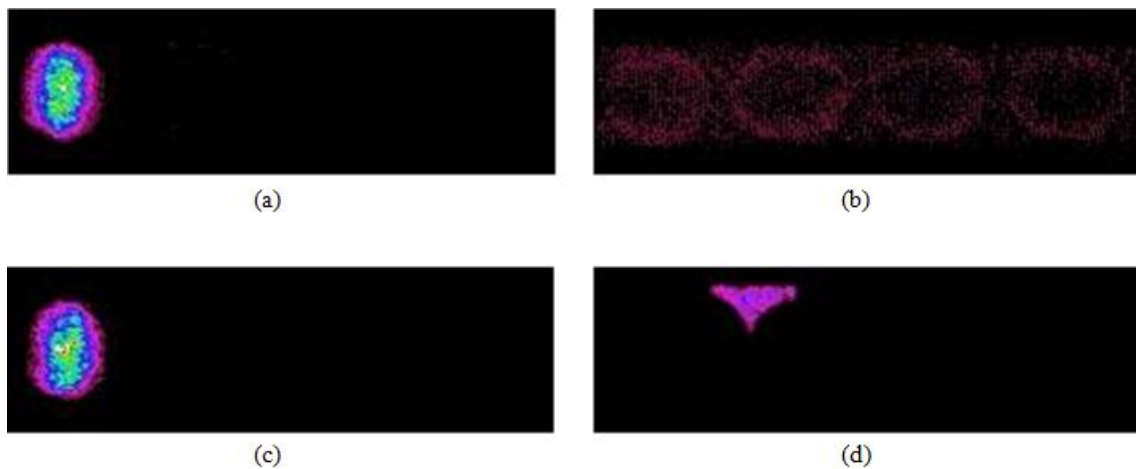


Fig. 4.12 Near-field patterns of GI PPOW (a) when the core center and (b) cladding are launched and W-shaped PPOW (c) when the core center and (d) cladding are launched.

4.2.2 Near field pattern and propagation loss

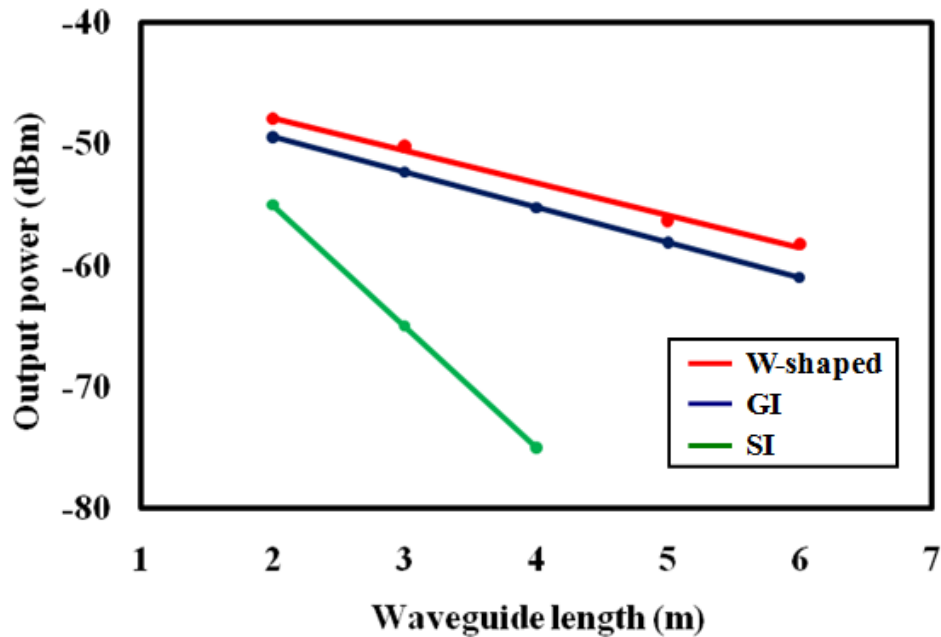


Fig. 4.13 Propagation loss of SI, GI, and W-shaped PPOW.

Figure 4.11 shows cross-sections of W-shaped and GI waveguides illuminated by a Halogen-Tungsten lamp at the input ends. Note that in the case of W-shaped waveguide, as Fig. 4.11(a) shows, even if the waveguide is launched under the overfilled mode launching (OML) condition, a dark ring is observed around each core, which corresponds to the refractive index valley. This implies most of the light may either couple to one of the cores or be restrained inside the cladding, and hardly remain at the index valley. This phenomenon will be simulated and discussed in later pages of this section.

As mentioned in the previous section, because of the same composition of the core materials in both waveguides, the optical performance of the GI and W-shaped PPOWs such as NA, propagation loss, etc., is expected to be similar. Here, the effect of the index valley in the W-shaped waveguide is evaluated by observing the output NFP

under a restricted mode launch (RML) condition that uses a SMF probe. Figure 4.12(a) and (c) show the results of GI and W-shaped PPOW, respectively, when the SMF probe is butt-coupled to the center of the far-left edge core, while Fig. 4.12(b) and (d) are launched at the over-cladding area between the far-left edge and second core. As expected, similar NFPs are shown in Fig. 4.12(a) and (c), by which similar optical field confinement to near the core center is confirmed. However, when the cladding modes are selectively launched, as in Fig. 4.12(b) and (d), the W-shaped refractive index profile is apparently advantageous for preventing the cladding light from re-coupling to the adjacent cores. We show this light localization in the cladding improves the inter-channel crosstalk due to mode conversion from the cladding modes to propagating modes in cores [12].

On the other hand, the propagation loss of the obtained W-shaped waveguide is evaluated by utilizing the cut-back method. In this measurement, incoherent light from a Halogen-Tungsten lamp is coupled to a core of the waveguide via a 50- μm core multimode fiber (MMF) probe (1-m long), and the output light from the core is coupled to another 50- μm core MMF probe to guide to an optical spectrum analyzer (ANDO AQ-6315B). From the slope of the output power variation at a wavelength of 850 nm as shown in Fig. 4 (red points), the propagation loss is obtained as 0.027 dB/cm, which is very close to that (0.028 dB/cm) of the previously obtained GI-PPOW (blue points). In Fig. 4.13 we also indicate an averaged loss (0.01 dB/cm) of a typical step index (SI) type waveguide for a comparison. It is confirmed that the newly developed W-shaped PPOW maintains the features of GI core waveguides: both good optical field confinement and low propagation loss.

4.2.3 Refractive index profile and inter-channel crosstalk

Referring to the NFP shown in Fig. 4.12(d), the W-shaped refractive index profile reduces the re-coupling of cladding modes to propagating modes in the adjacent cores. This implies the inter-channel crosstalk can also be reduced. How the light can be restrained in the cladding depends on the depth of the refractive index valley, namely, the index profile. Therefore, the refractive index profiles in the two waveguides are measured. The interference fringe images measured for slab samples of the two waveguides are shown in Fig. 4.14 (top), and their refractive index profiles are calculated from the fringe patterns as shown in Fig. 4.14 (bottom). These results indicate that the similar quadratic index distribution is formed inside the both cores, while an explicit difference is observed in the vicinity of core-cladding boundary, where an index valley exists in the W-shaped PPOW as shown in Fig. 4.14(a). In order to clarify how much the depth of the index valley really contributes to the inter-channel crosstalk reduction, we adjust the concentration of BzMA in MMA monomer from 3.66 to 25 wt. % for the cladding, by which the refractive index of outermost cladding is varied as summarized in Table 4.2. Here, as the refractive index of the bottom of index valley is almost uniform (1.492), the depth of the index valley is varied. Note that when the concentration of BzMA is higher than 15 wt. %, the refractive index of cladding is even higher than that of the core center.

The inter-channel crosstalk is evaluated using the experimental setup shown in Fig. 4.15. The waveguides in this measurement are 1-m in length. One of the cores is launched via an SMF probe or an MMF probe with a 50- μm core diameter, which corresponds to RML and near OML conditions, respectively. The output power from the specified points on the cross-section of the output end was measured using another

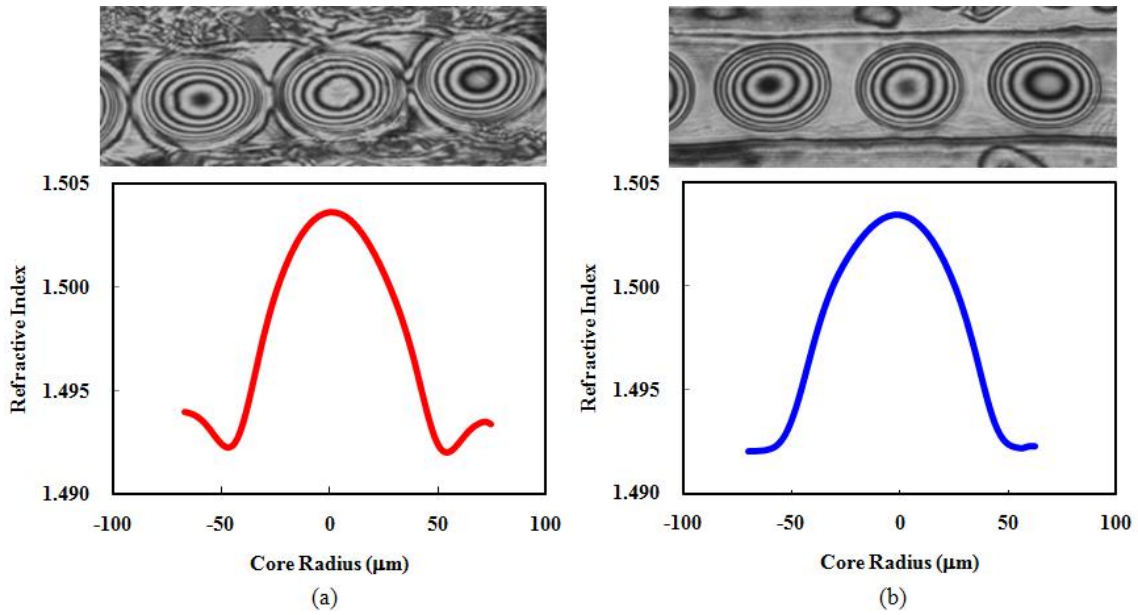


Fig. 4.14 The interference fringe patterns (top) and its corresponding refractive index profile (bottom) of (a) GI (b) W-shaped profile with 3.66 wt. % BzMA PPOW.

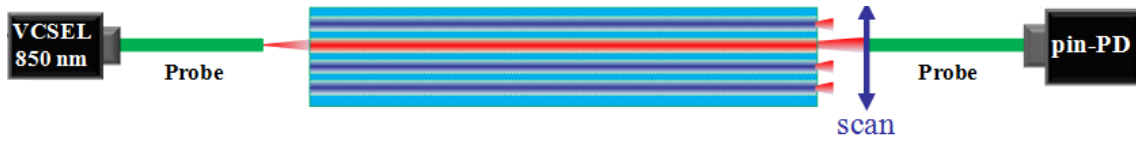


Fig. 4.15 Experimental setup for inter-channel crosstalk measurement.

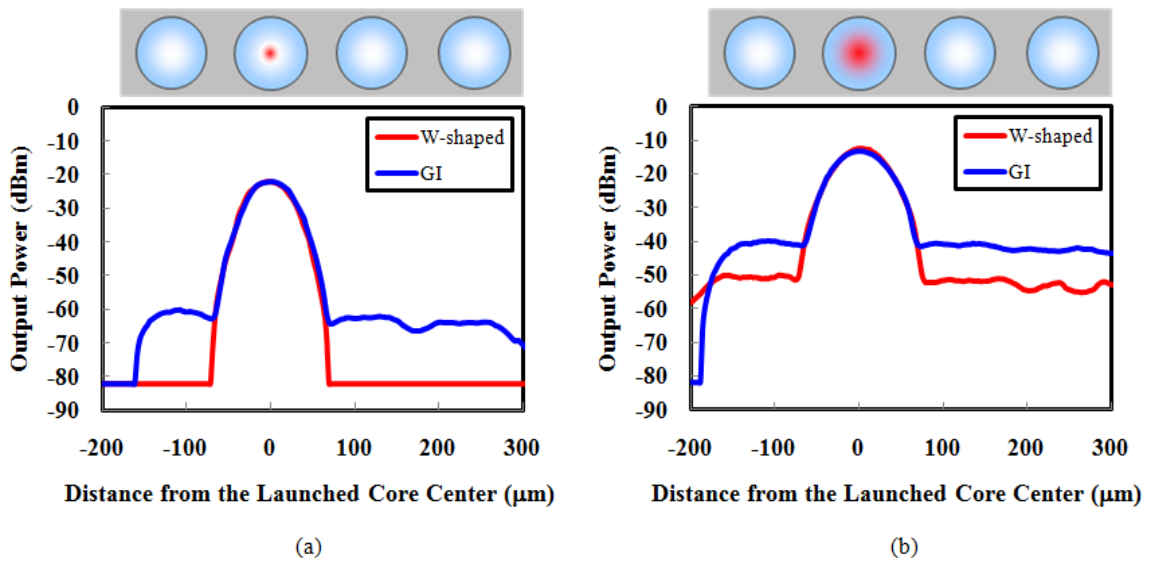


Fig. 4.16 Output intensity when one of the cores (second from the left) in waveguides is launched via (a) SMF probe (RML condition) and (b) MMF probe (near OML condition). The concentration of BzMA for W-shaped profile PPOW here is 10 wt. %.

MMF probe for detection.

Figure 4.16 shows the comparison of GI core and W-shaped profile with 10 wt. % of BzMA in the outermost cladding. In the case of W-shaped PPOW under the RML condition as shown in Fig. 4.16(a), the other three cores show almost no detectable output intensity. Meanwhile, in Fig. 4.16(b), under the near OML condition, an output power of -55 dBm is observed both from the cladding and other cores in the W-shaped PPOW. However, the output intensity from the right edge core is even weaker than that of the cladding. Under both launching conditions, the output power from the GI waveguide (blue curve) is higher than that from the W-shaped waveguide (red curve). It is confirmed that the W-shaped profile effectively reduces the crosstalk. Table 4.3 shows the numerical results of different waveguides under both RML and near OML conditions. The crosstalk values in Table 4.2 are measured at the center of the right-neighbor core. Note that under the near OML condition, when the concentration of BzMA is 10 wt.%, the crosstalk value as low as -40.3 dB is observed, while the crosstalk value increases with increasing the concentration of BzMA in the cladding from 10 wt. % to 20 wt. %. As it was already confirmed in Fig. 4.12, the lower crosstalk in W-shaped PPOW than in GI one is attributed to low mode conversion from cladding modes to propagating modes. However, when the BzMA concentration is higher than 20 wt. %, the refractive index of the outermost layer is higher than that of the core center, and thus, the light rather could be tightly confined in the outermost layer, although the copolymer cladding could have high excess scattering loss. Therefore, the crosstalk decreases again to the minimum at 25 wt. % of BzMA concentration. In the case when BzMA concentration is 10 wt.%, n_3 is 1.499 which is almost half value between the core center (1.504) and the bottom of valley (1.492), which could be

optimum.

Table 4.2 Crosstalk value and refractive index with corresponding concentration

Waveguide type	Index of the cladding	Crosstalk value (RML condition)	Crosstalk value (near OML condition)
GI	1.492	-40.1 dB	-27.5 dB
W-shaped (3.66 wt. %)	1.495	< -59.6 dB	-32.0 dB
W-shaped (10 wt. %)	1.499	< -59.8 dB	-40.3 dB
W-shaped (15 wt. %)	1.502	< -59.6 dB	-36.1 dB
W-shaped (20 wt. %)	1.506	< -44.3 dB	-33.5 dB
W-shaped (25 wt. %)	1.509	< -59.2 dB	-41.5 dB

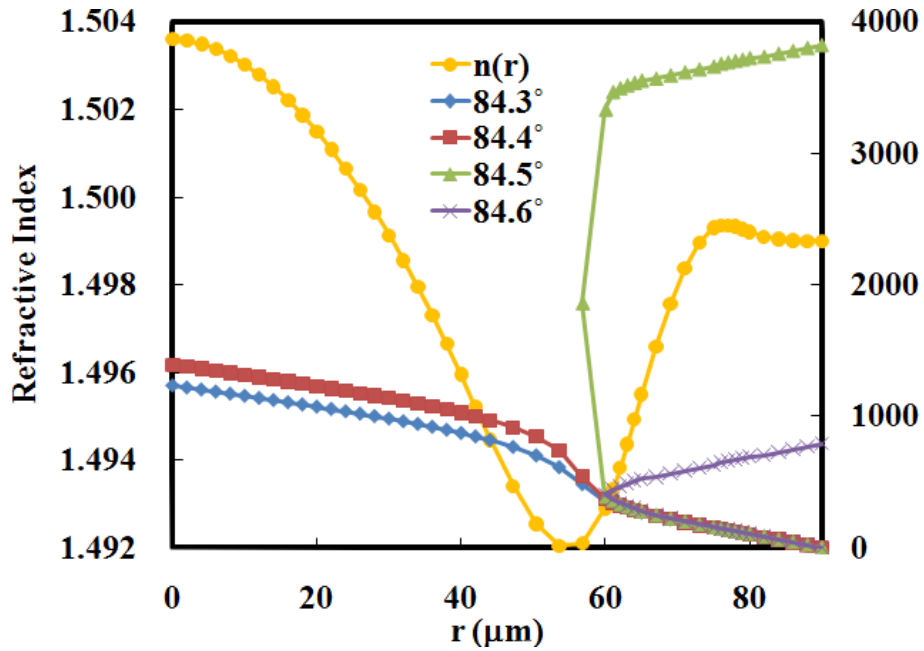
4.2.4 Inter-channel crosstalk in short length waveguides

For board level optical interconnections, the physical dimension of the optical waveguides generally could be centimeter scale in length. In this part, we apply 5-cm long waveguides with both index profiles (GI and W-shaped) to the same experimental setup as shown in Fig. 4.15. Table 4.3 shows the results of these short waveguides. Compared to the results in Table 4.3, the crosstalk reduction by a W-shaped profile is not apparent in the shorter waveguide. Actually, only about a 6-dB difference in crosstalk value is observed between the W-shaped and GI PPOWs in Table 4.3 (MMF launch), while there is a 12.8-dB difference between the corresponding waveguides in Table 4.3.

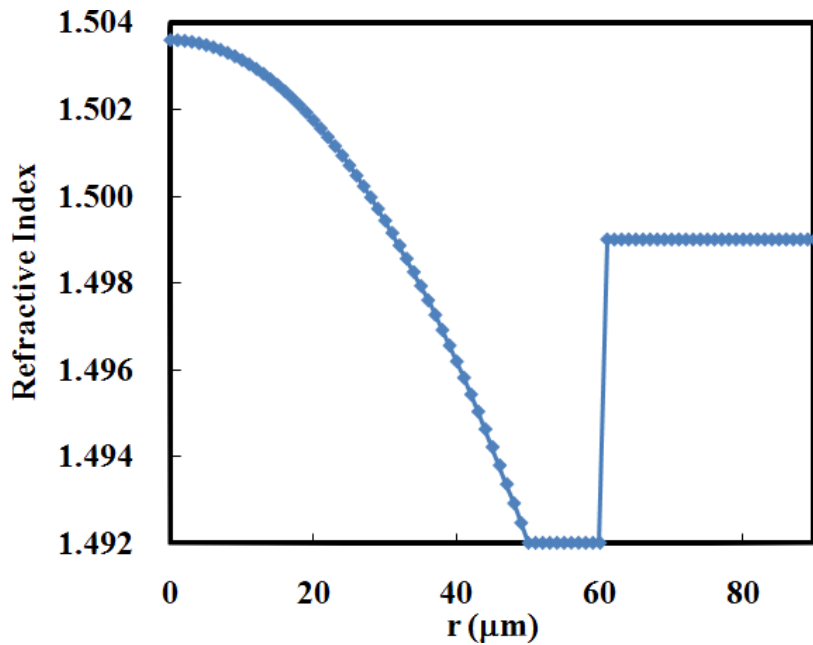
Table 4.3. Crosstalk value in 5-cm GI and W-shaped PPOWs

Waveguide type	Crosstalk value (launched by SMF)	Crosstalk value (launched by MMF)
GI	< -61.1 dB	-33.7 dB
W-shaped (10 wt. %)	< -61.3 dB	-39.6 dB

4.2.5 Theoretical analysis of inter-channel crosstalk



(a)



(b)

Fig. 4.17 (a) The measured refractive index profile of W-shaped profile PPOW with 10 wt. % BzMA in cladding. In the right side are the calculated ray trajectories with different incident angles. (b) The theoretical modeling of refractive index profile according to Eq. (1).

A ray tracing simulation program was already created to analyze the propagation loss and inter-channel crosstalk in PPOWs taking the light scattering effect into consideration [12]. From the ray optics point of view, when a ray in the cladding propagates toward the boundary of valley and cladding, either it reflects back or penetrates into the index valley, depending on the incident angle. Here, our concern is how the rays behave in the vicinity of steep and gradually varying index valleys. In Fig. 4.17(a), one of the measured refractive index profiles $n(r)$ corresponding to a BzMA concentration of 10 wt. % is drawn with the yellow (round dotted) curve. Actually, a gradually-varying index valley (not a steep one) is observed. The calculated ray-trajectories with incident angles from 84.7° to 84.9° are shown in the right side of Fig. 4.17(a). Here, the incident rays are injected from the outside of the index valley (at $r = 90 \mu\text{m}$). It is clearly illustrated that the rays with an incident angle lower than 84.5° penetrate into the core, while the rays with an incident angle higher than 84.5° follows the trajectory similar to the “reflected” rays. The angle of 84.5° is very close to the theoretically calculated critical angle ($\sin^{-1}(1.492/1.499) = 84.461^\circ$). Hence, in the developed ray tracing simulation, it is confirmed that the trajectory of light in such a narrow area like 10- μm thick index valley is calculated properly. This gives us a reasonable approximation for applying Eq. (4-2) to theoretical model. The modeled refractive index profile is shown in Fig. 4.17(b), where a steep index valley is applied.

The parameters for the calculation are listed in Table. 4.4. The core radius is $50 \mu\text{m}$, where the refractive index of the core center is 1.5036, refractive index of the bottom of valley is 1.492, and the core pitch is $125 \mu\text{m}$, all of which are identical to those of the fabricated waveguide. The index exponent g is set to 2.0 as the parabolic index profile within the core area. Furthermore, in order to include the light scattering effect in the

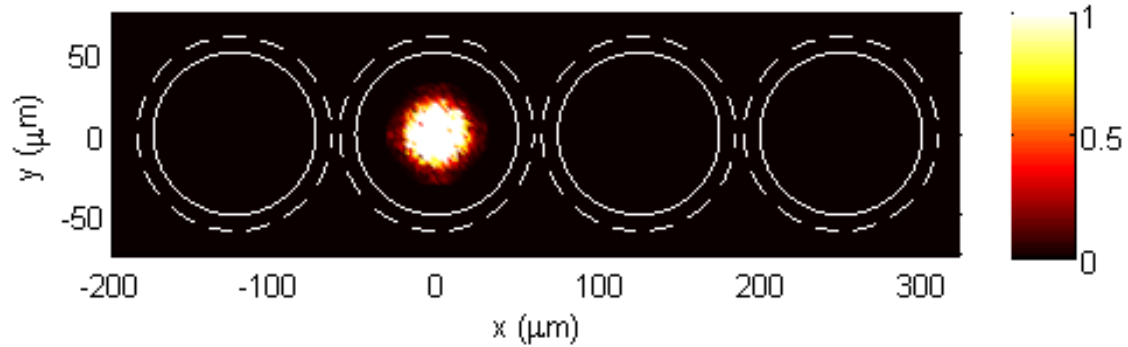


Fig. 4.18 The launching condition for the simulation. We apply the same condition as the experimental setup in which the second core from the left side is launched by an MMF (50 μm in diameter).

ray tracing, three parameters are incorporated: probability of scattering (p), maximum number of split rays after one scattering (N_s) and maximum angle difference of scattered ray to the original ray direction (θ_m) which are already introduced in section 2.4. The parameter p is set to a predetermined value from 0 to 1 for the calculation. During the ray tracing, we randomly add the “light scattering” event to split the original ray to n ($1 \leq n \leq N_s$) rays using random numbers also ranging from 0 to 1. The ray splits when the random number is smaller than the predetermined p value at each decision point along with the ray trajectory. Therefore, when the p value is set to 1, the scattering occurs at all the decision points, while no scattering occurs when p is 0. Here, the N_s and θ_m are set to be 2 and 10, respectively. This is only preliminarily determined for minimizing the calculation time. We can vary these parameters, but these original settings are good enough, because we would like to obtain the relationship between the scattering loss and inter-channel crosstalk. So, the validity of these settings will be discussed elsewhere in detail. Furthermore, in order to obtain the relationship between the refractive index valley depth and inter-channel crosstalk, four n_3 values (1.492, 1.495, 1.499, and 1.502) are applied. Furthermore, we assume a low-loss and very-lossy

core materials, which correspond to the parameter p of 0.02 and 1, respectively. For more promising calculation results and shortening the calculation time, we focus on the performance of short waveguide length (~ 5 cm). After tracing all of the rays (bound, tunneling, reflected, and refracted rays), the intensity and location information of each ray are stored. Then, the propagation loss and crosstalk values are quantitatively calculated at the output end of the waveguide.

According to the experimental results, we can visually observe some light leakage outside the launched core at the output end in the case under the MMF launch. This implies the inter-channel crosstalk is unavoidable under this launching condition. Here, we pay attention to the difference between GI and W-shaped PPOWs. It is assumed that there are four cores in the calculation model and that the second core from the left is launched with a spot size of $50 \mu\text{m}$ at the core center. Under this launching condition, approximately 5000 rays form a 2D Gaussian profile as shown in Fig. 4.18. The intensity of the left core, right core, and cladding are expressed as I_{left} , I_{right} , and I_{clad} , respectively, which are initially set to zero at the launching plain ($z = 0$). In Fig. 4.18, the inner white circles indicate the core/valley boundary; the white dotted circles indicate the outer edge of the valley. The medium outside the waveguide is air ($n_{air} = 1$).

Table 4.4. Parameters for calculation by ray tracing method

Parameters	Value
Core radius (a)	$50 \mu\text{m}$
Index valley width (w)	$10 \mu\text{m}$
Refractive index of core center (n_1)	1.5036
Refractive index of valley (n_2)	1.492
Index exponent (g)	2
Core pitch	$125 \mu\text{m}$

4.2.6 Calculation results

First, a very lossy condition ($p = 1$) is considered and the calculated NFPs are shown in Fig. 4.19. In these calculated NFP data, we remove the white-color boundary shown in Fig. 4.18, while we adjust the color map to clearly visualize the weak output intensity. In Fig. 4.19, we observe the length dependence of NFP which shows the light gradually diffuses toward the cladding area. In the case of W-shaped PPOW (Fig. 4.19(b), (c), and (d)), the index valley around each core is confirmed as a dark ring, which is also observed in the NFP experimentally obtained in Fig. 4.11(a). Furthermore, compared to the GI PPOW shown in Fig. 4.19(a), with increasing the depth of index valley, the core areas except for the launched one are visualized more clearly as dark circles. The dark cores indicate low output power (low crosstalk).

Figure 4.20 shows the numerical results of absolute output intensity and crosstalk values. In Fig. 4.20(a), the output intensity from the launched cores (I_{mid}), shows the trend that decreases linearly with respect to the waveguide length in all PPOWs including the GI case ($n_2 = 1.492$), which indicates that the propagation loss due to scattering is almost identical in all the waveguides. From the slope of Fig. 4.20(a), the propagation loss (due to scattering) of these waveguides is calculated to be 0.58 - 0.60 dB/cm, which is quite high. On the contrary, the output intensity from the whole cladding, I_{clad} , obviously depends on n_3 value, and in the case of the highest $n_3 = 1.502$, I_{clad} is the highest for any waveguide lengths. Hence, it can be concluded that the larger the difference of n_2 and n_3 , the higher intensity remains in the cladding. Moreover, when there is no index valley ($n_3 = 1.492$), once the light is scattered from the launched core, it may easily re-couple to the other cores and increase the crosstalk value. Actually, as shown in Fig. 4.20(c) and (d), the crosstalk value (XT) decreases with increasing the

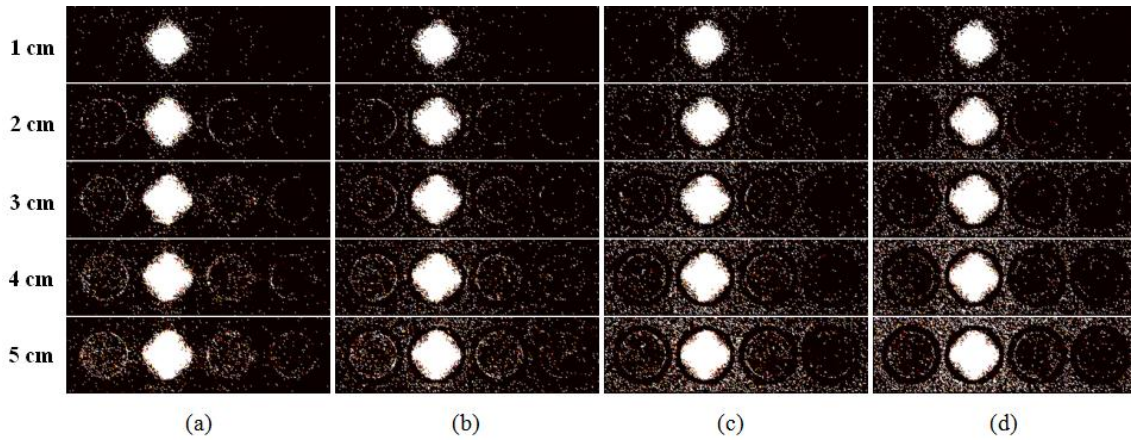


Fig. 4.19 Calculated NFP and propagation loss with corresponding output end (1 cm to 5 cm) for various refractive index of cladding under very lossy condition: (a) 1.492 (GI), 0.56 dB/cm (b) 1.495 (3.66 wt. %), 0.58 dB/cm (c) 1.499 (10 wt. %), 0.60 dB/cm (d) 1.502 (15 wt. %), 0.60 dB/cm.

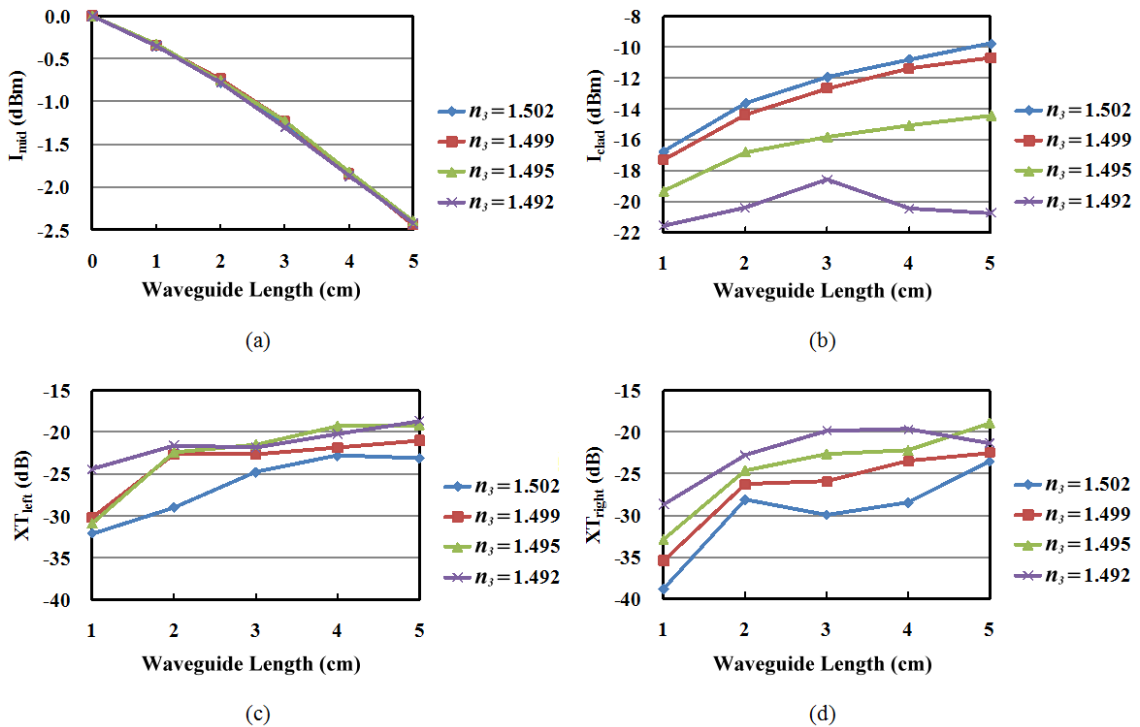


Fig. 4.20 Calculated results by ray trace simulation: (a) Output intensity from the launched core. (b) Output intensity from the whole cladding. (c) Crosstalk value (XT) to the left-edge core. (d) Crosstalk value to the third core from the left edge.

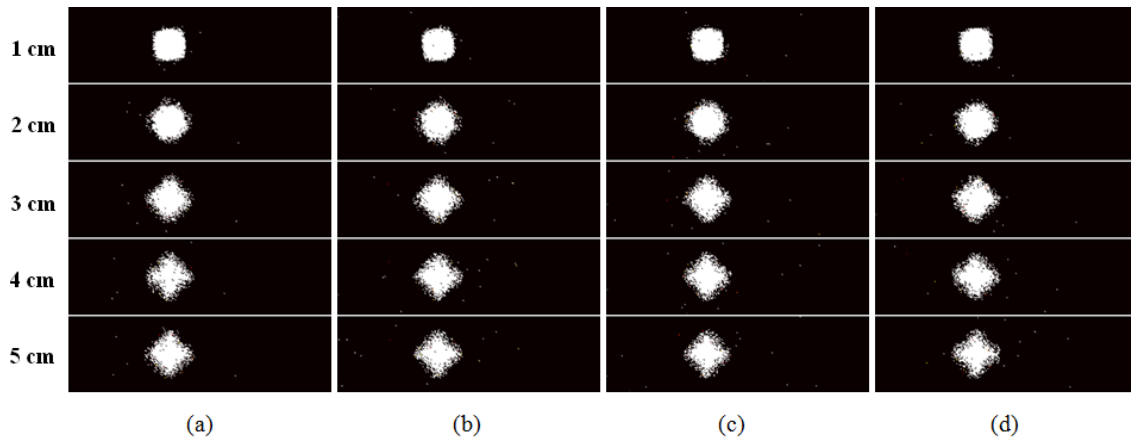


Fig. 4.21 Calculated NFP and propagation loss of W-shaped PPOWs with various refractive index of cladding compared to that of GI PPOW: (a) 1.492 (GI), 0.26 dB/cm (b) 1.495 (3.66 wt. %), 0.26 dB/cm (c) 1.499 (10 wt. %), 0.27 dB/cm (d) 1.502 (15 wt. %), 0.26 dB/cm.

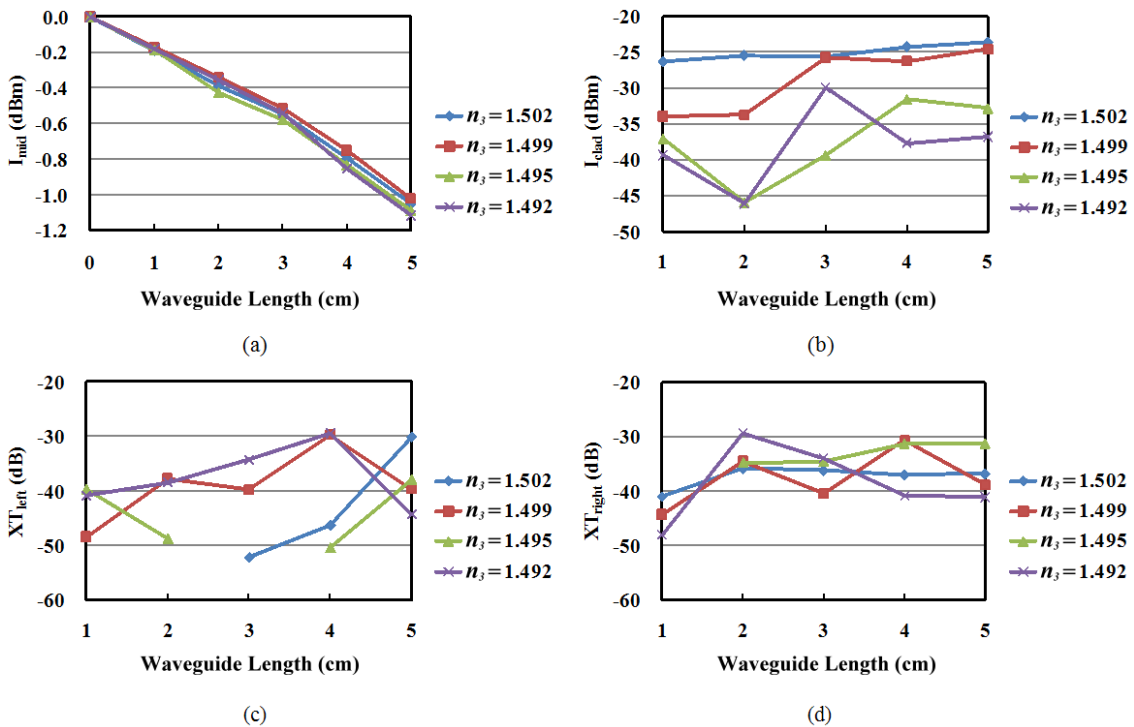


Fig. 4.22 Calculated results by ray trace simulation (a) Output intensity from the launched core. (b) Output intensity from the whole cladding. (c) Crosstalk value (XT) to the left-edge core. (d) Crosstalk value to the third core from the left edge.

depth of index valley (higher n_3 value), and approximately 5 dB difference in crosstalk is observed between the GI and W-shaped PPOWs with the deepest valley after a 5-cm propagation.

However, in order to simulate real applications for board-level optical interconnections, i lower-loss conditions than that in the previous section should be considered, because the propagation loss of 0.6 dB/cm calculated in Fig. 4.19 is too high compared to those of actually obtained waveguides. Therefore, in the calculation of this section, the scattering probability p is set to 0.02. In this case, the propagation loss is calculated to be 0.26 - 0.27 dB/cm. The calculated NFPs and numerical results are shown in Fig. 4.21 and Fig. 4.22, respectively. In Fig. 4.21, all the cases show very similar results: the adjacent cores have very weak output intensities, namely, very low crosstalk. Figure 4.22(a) shows similar trend to Fig 4.20(a): the propagation losses are still identical in all the waveguides. The highest output intensity from the cladding is observed when the index valley depth is the highest ($n_3= 1.502$), as shown in Fig. 4.22 (b). However, it is noteworthy that the absolute value of I_{clad} is much smaller than that in Fig. 4.20(b). The crosstalk values are shown in Fig. 4.22(c) and (d), where some empty values (plots) indicate no rays could be counted. Some unexpected fluctuations in the XT value are observed because the optical power coupled to the other cores is too low. Hence, the W-shaped index profile is effective for reducing the inter-channel crosstalk mainly due to mode conversion, particularly when polymer waveguides are composed of polymer materials that exhibit essentially high scattering loss. Therefore, with increasing the waveguide length, the W-shaped index profile works more effectively, as experimentally shown in Tables 4.2 and 4.3, since the longer length propagation corresponds to high probability of scattering (highly accumulated scattering loss).

4.2.7 Conclusion

W-shaped PPOWs with desired refractive index profiles were successfully fabricated. This is a reliable solution that can simultaneously realize low propagation loss (0.027 dB/cm) and low inter-channel crosstalk (-40.3 dB). In the case of higher concentration of BzMA in the cladding material, it realizes an unexpectedly higher crosstalk value which could result from the higher refractive index of cladding (outermost layer) than that of the cores.

It is theoretically confirmed that the larger the depth of index valley, the lower inter-channel crosstalk. Furthermore, for centimeter scale optical interconnections, we apply the ray tracing method to confirm the advantages of W-shaped profile PPOW visually and numerically. We conclude that W-shaped refractive index profiles perform as low propagation loss as GI waveguides with the additional characteristic of inter-channel crosstalk suppression for the application of high dense aligned optical interconnections.

4.3 OPTICAL LINK ANALYSIS WITH RAY OPTICS

So far, the ray tracing method has been applied to address optical properties of single waveguide; we show this method can be extended to a system level. The study in this section describes an advanced multimode waveguide based optical link model that is used to aid the development of low-power, high-density, high-speed multi-channel optical link. The model consists of VCSEL, multi-channel rectangular shape SI and GI type optical waveguides, multimode fiber, and photo detector, and takes into account the couplings of these link components, as shown in Fig. 4.23. For low power optical link, the link power budget has to be minimized. In this study, the benefits of GI waveguides,

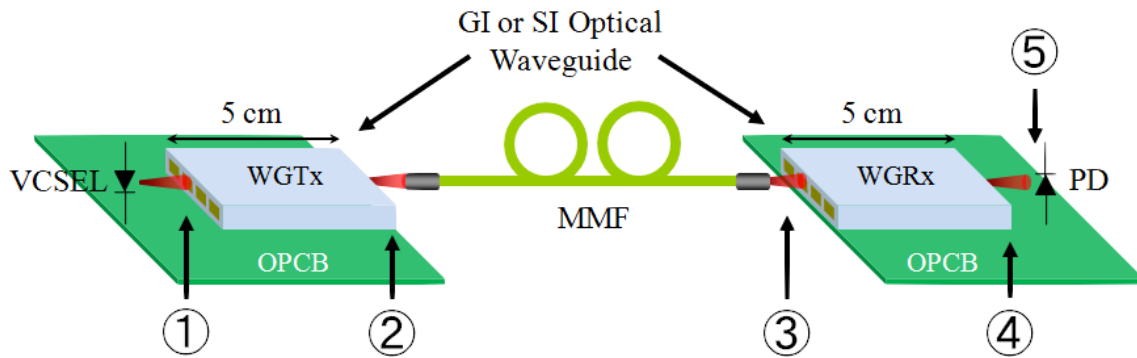


Fig. 4.23 Modeling layout of this calculation.

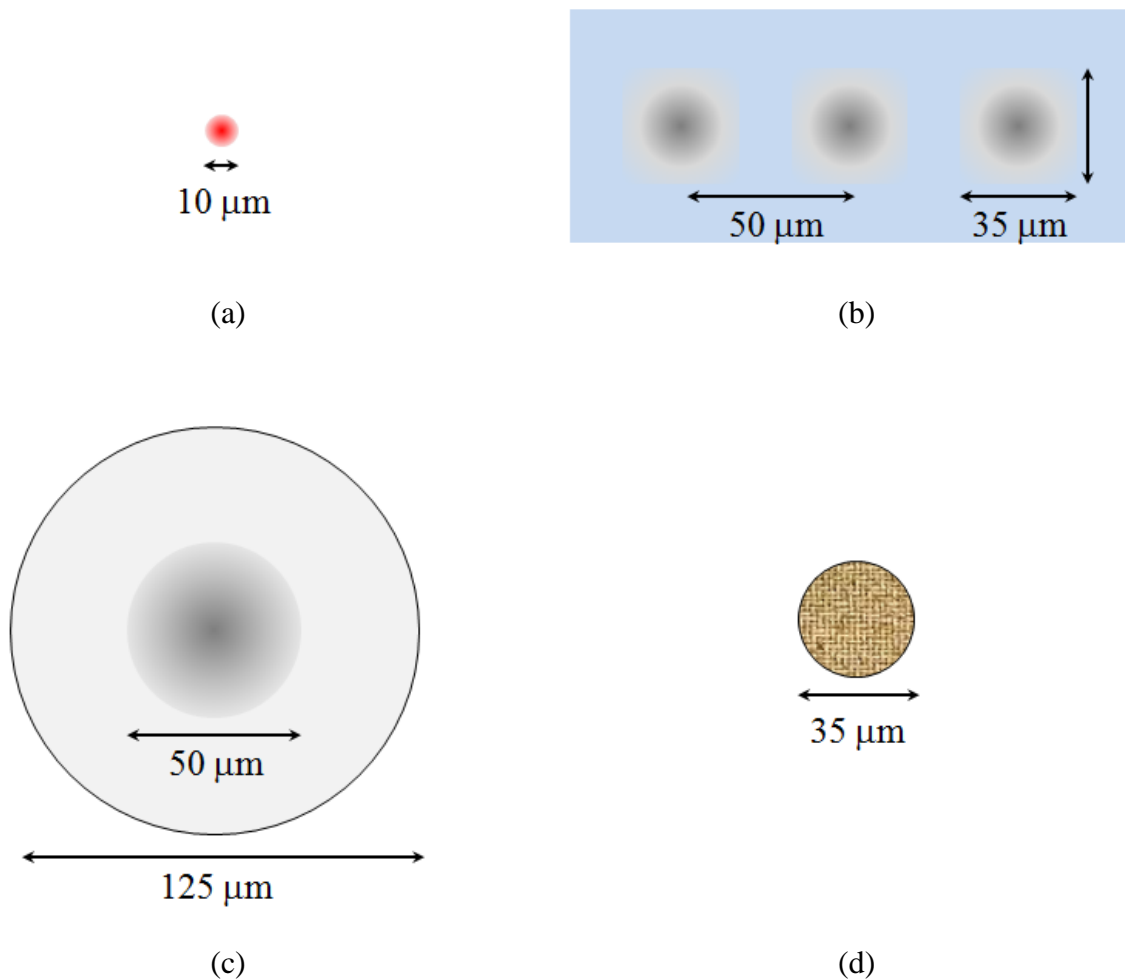


Fig. 4.24 (a) VCSEL output pattern after SMF. (b) Multi-core GI or SI PPOW ($n_{co} = 1.581$, $n_{cl} = 1.541$, $NA = 0.35$). (c) MMF ($n_{co} = 1.4525$, $n_{cl} = 1.43866$, $NA = 0.2$). (d) Photo diode.

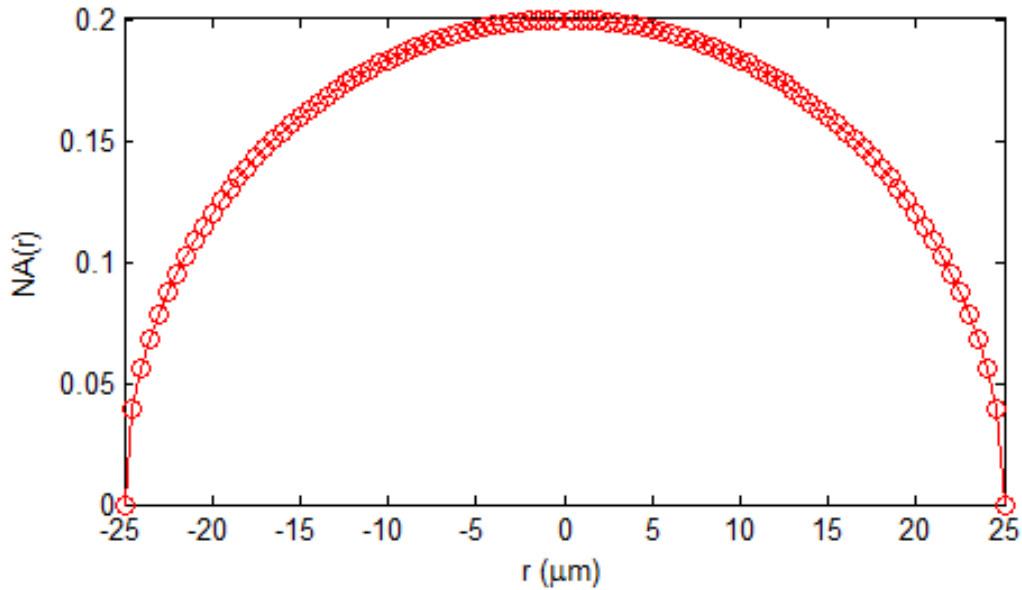


Fig. 4.25 NA(r) of MMF for this calculation.

particularly for the coupling losses, were investigated and compared to SI waveguides. We start from the formulations introduced in Chapter 2, in which the rays emitted from the VSCSEL with Gaussian intensity distribution. Both between the laser source and the waveguide (the Tx side), and between the waveguide and the photo diode (the Rx side), a 50 μm gap is assumed, which is filled with a uniform medium with similar refractive index to the core center for the purpose of reducing the connection loss. Furthermore, the two waveguides are connected by a GI-MMF, which guides the light from the Tx side to the Rx side. The characteristics such as NFPs and connection loss are highlighted. The calculated results show the GI waveguides confine the optical intensity near the core center stronger than the SI waveguide, which results in lower coupling loss (0.46 dB vs. 1.35 dB) between the 35 μm core size waveguides and the 35- μm diameter photo diode (PD). This calculation helps us to characterize the high performance optical link with a more reliable model.

4.3.1 Modeling layout

The proposed model is composed of two OPCBs with embedded multi-channel POWs as depicted in Fig. 4.23. From the Tx side, a VCSEL source emits lightwave to the entrance of WGTx, where a 50 μm gap is placed here. After the light propagates to a commercially available GI-MMF with an NA of 0.2, it couples into the WGRx. Finally, the output light emitted from WGRx is received by the PD, where another 50 μm gap exists. For addressing the optical characteristics, we define the interfaces 1 to 5, where the descriptions are listed as follows:

- 1: Entrance of the WGTx side (with 50 μm gap)
- 2: Exit of the WGTx side (no gap)
- 3: Exit of the MMF (no gap)
- 4: Exit of the WGRx side (with 50 μm gap)
- 5: Input of the PD

Figure 4.24 shows the physical dimension of each component in the optical link. In Fig. 4.24(c), the MMF with parabolic profile, whose n_{co} value is obtained from the website [13] for fused silica with 1.4525 at 850 nm, and n_{cl} is directly calculated from the following formula:

$$n_{cl} = \sqrt{n_{co}^2 - \text{NA}^2} \quad (4-3)$$

This implies the NA of the MMF in this calculation is actually smaller than 0.2, and Fig. 4.25 shows the calculated $\text{NA}(r)$ (local NA). Other related parameters are listed in Table 4.5. Furthermore, the NA of the SI waveguide is 0.35 ($\sim 20^\circ$) which is much larger than the NA of MMF.

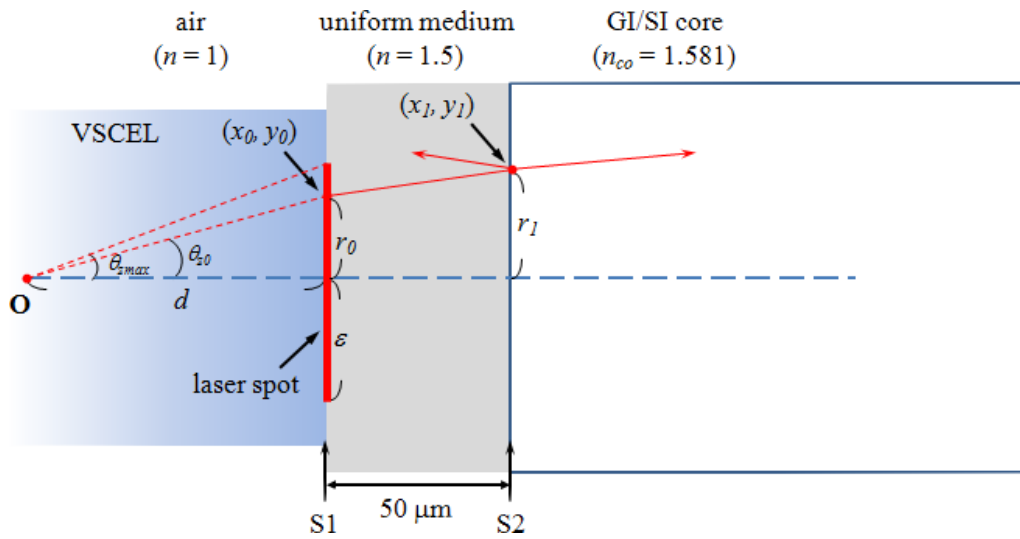


Fig. 4.26 Centered launching condition in this calculation. A ray originates from a virtual point inside VCSEL. The ray is reflected by uniform medium ($n = 1.5$).

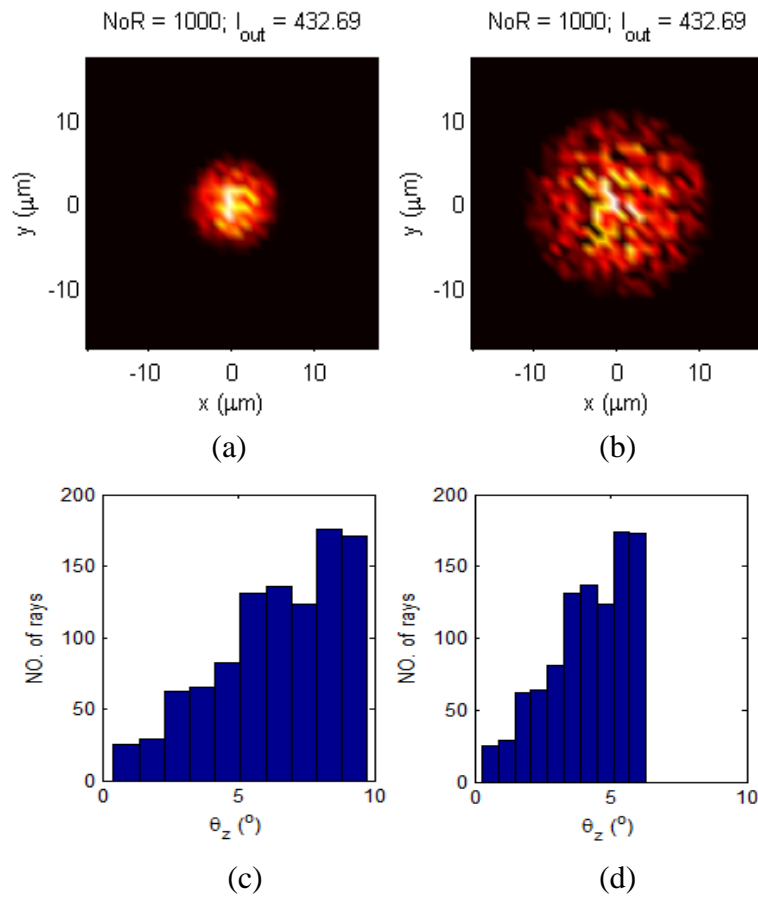
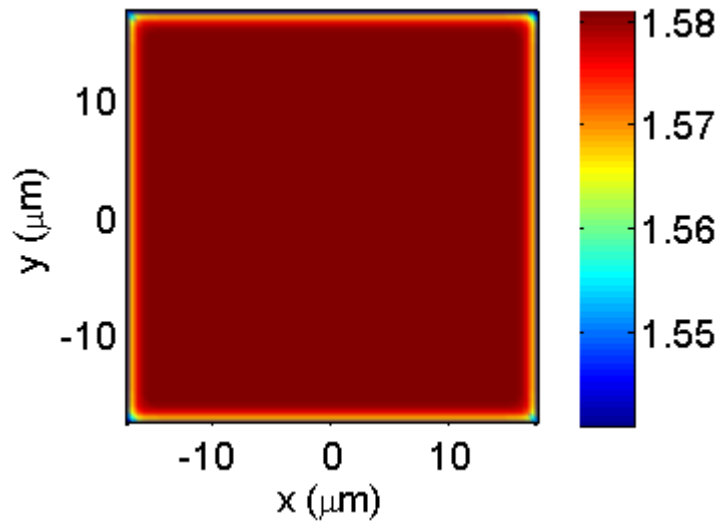
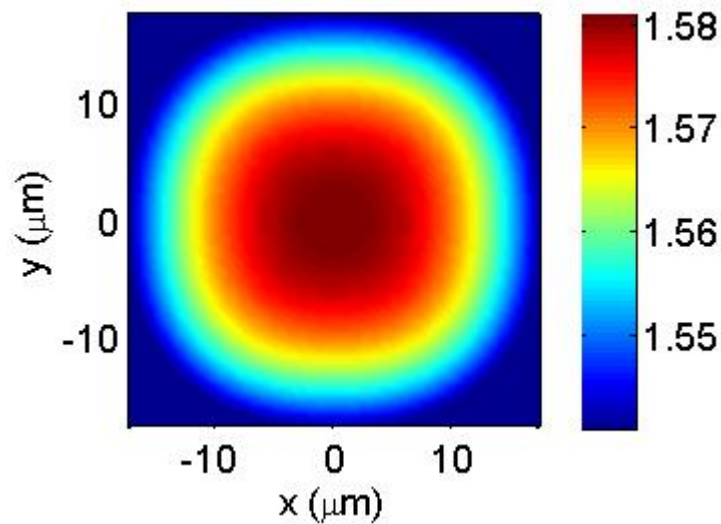


Fig. 4.27 Number of rays is 1000 and total intensity is 432.69. (a) NFP of VCSEL exit (S1) (b) NFP of the waveguide entrance (S2) (c) angle distribution of rays in (a). (d) Angle distribution of rays in (b).



(a)



(b)

Fig. 4.28 Refractive index profile for (a) SI (b) GI waveguides.

4.3.2 Theoretical calculation

- *Launching condition*

First, the launching condition is considered. Figure 4.26 shows the centered launching condition, where the maximum divergence angle from the VCSEL is 10° ($\theta_{zmax} = \pm 10^\circ$) with a total intensity of 432.69. In the case of a 50- μm gap considered, the space is

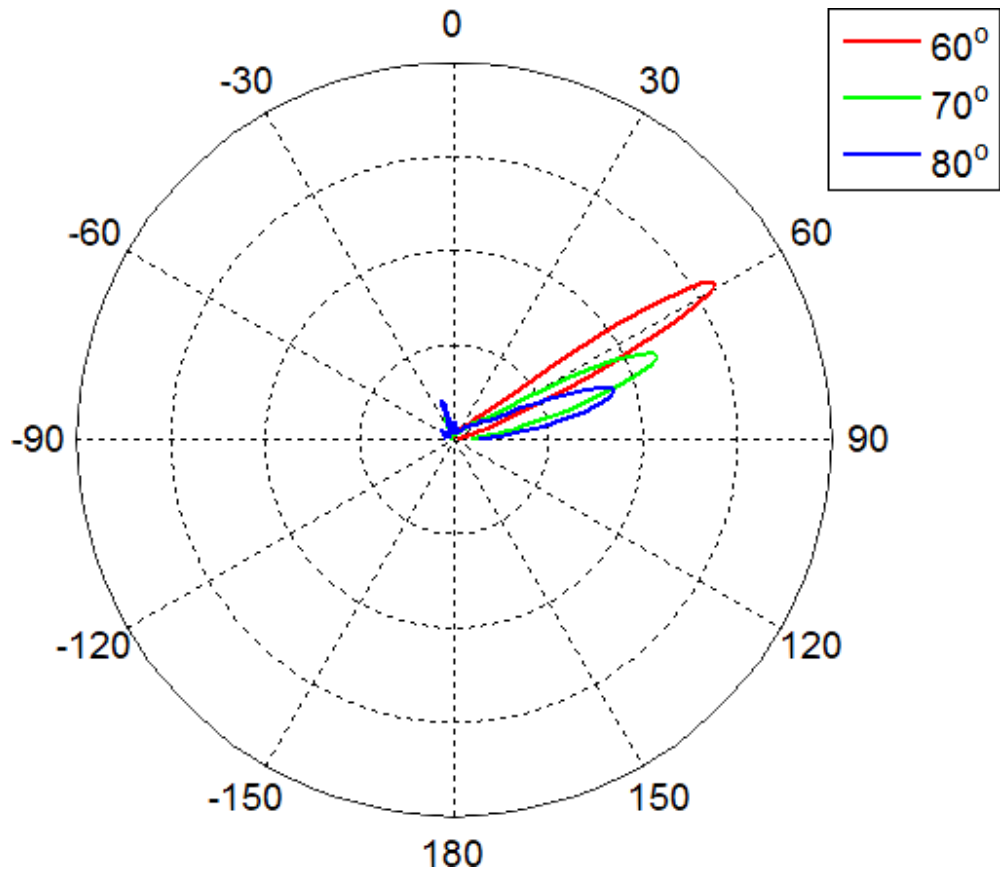


Fig. 4.29 Calculated scattered field with roughness around $0.1 \mu\text{m}$.

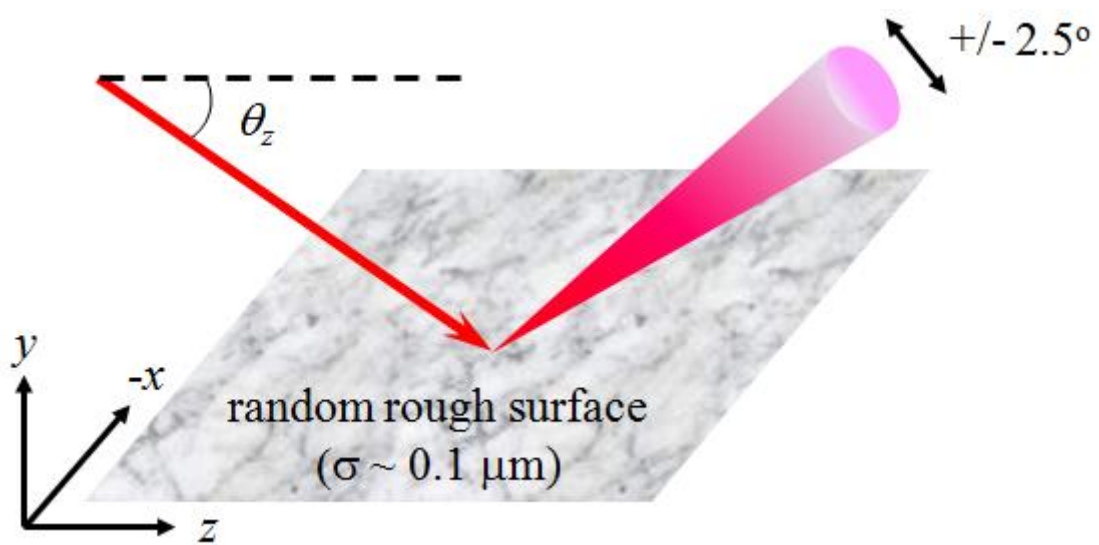


Fig. 4.30 The relation between incident and scattered rays.

treated as a uniform medium ($n = 1.5$) which involves between the VCSEL and waveguide. The NFP at end 1 and angle distribution of incident rays are shown in Fig. 4.27. Next, the waveguide based optical link is composed of SI or GI waveguides with the same parameters. The refractive index profile is based on Eq. (2-13). Here, the index exponents (p and q) are 2.4 for GI and 40 for SI, where the NA of SI waveguide is around 0.35. Figure 4.28(a) and (b) show the cross section of index profile of SI and GI, respectively. The calculation processes of ray tracing are discussed in chapter 2.

Table 4.5 Parameters for calculation

Parameters	Value
Waveguide length	5 cm
Core diameter ($2a$)	35 μm
Core pitch	50 μm
Index exponent for SI waveguide	40
Index exponent for GI waveguide	2.4
Index of the core (n_{co})	1.581
Index of the cladding (n_{cl})	1.541
MMF	50/125/0.2
Diameter of PD	35 μm

- *Rough core/cladding boundary*

Furthermore, in order to simulate how rough core/cladding boundary influence on the optical properties, the consideration of light scattering effect introduced in Sec. 2.5 is involved in the computer programs. Here, we involve rough core/cladding boundaries with a surface roughness level of 0.1 μm . Figure 4.29 shows the scattered pattern with respect to different roughness level and incident angle. Here, the light incident from the left half plane. From the above diagram, it is found that the angle distribution in specular direction is less than 5° ($\pm 2.5^\circ$). The scattered angles change in

3D space, as Fig. 4.30 shows.

4.3.3 Calculation results

The equations introduced in chapter 2 are applied again, and all the rays launched in Fig. 4.27 are traced. There are four cases considered in this calculation:

Case 1: SI waveguides without rough core/cladding boundary

Case 2: SI waveguides with rough core/cladding boundary

Case 3: GI waveguides without rough core/cladding boundary

Case 4: GI waveguides with rough core/cladding boundary

Figure 4.31 shows the calculated NFPs for all the cases. In the above area, the NFPs for WGTx with respect to 1- to 5-cm waveguide length are shown. Below the NFPs of WGTx, the NFPs from the exit of the GI-MMF (interface 3) of four cases are shown in the middle. Similarly, the NFPs from WGRx with corresponding position are shown below. In this calculation, all the components are perfectly aligned. Moreover, in order to clearly recognize how rough core/cladding boundary influences on the optical properties between SI and GI waveguides based optical link, no scattering effect is included in all the cases.

In terms of the computer program developed in this research, all information of rays such as direction vector, intensity, and classification of the ray are recorded. It is rather substantial to monitor the behavior of rays by the ray invariant β . According to Sec. 2.3, the ray invariant can be written as

$$\beta = n_{co}(x, y) \cos \theta_z(x, y) \quad (4-4)$$

where $n_{co}(x, y) = n_{co}$ for SI waveguides. We show figures of ray invariant for bound rays

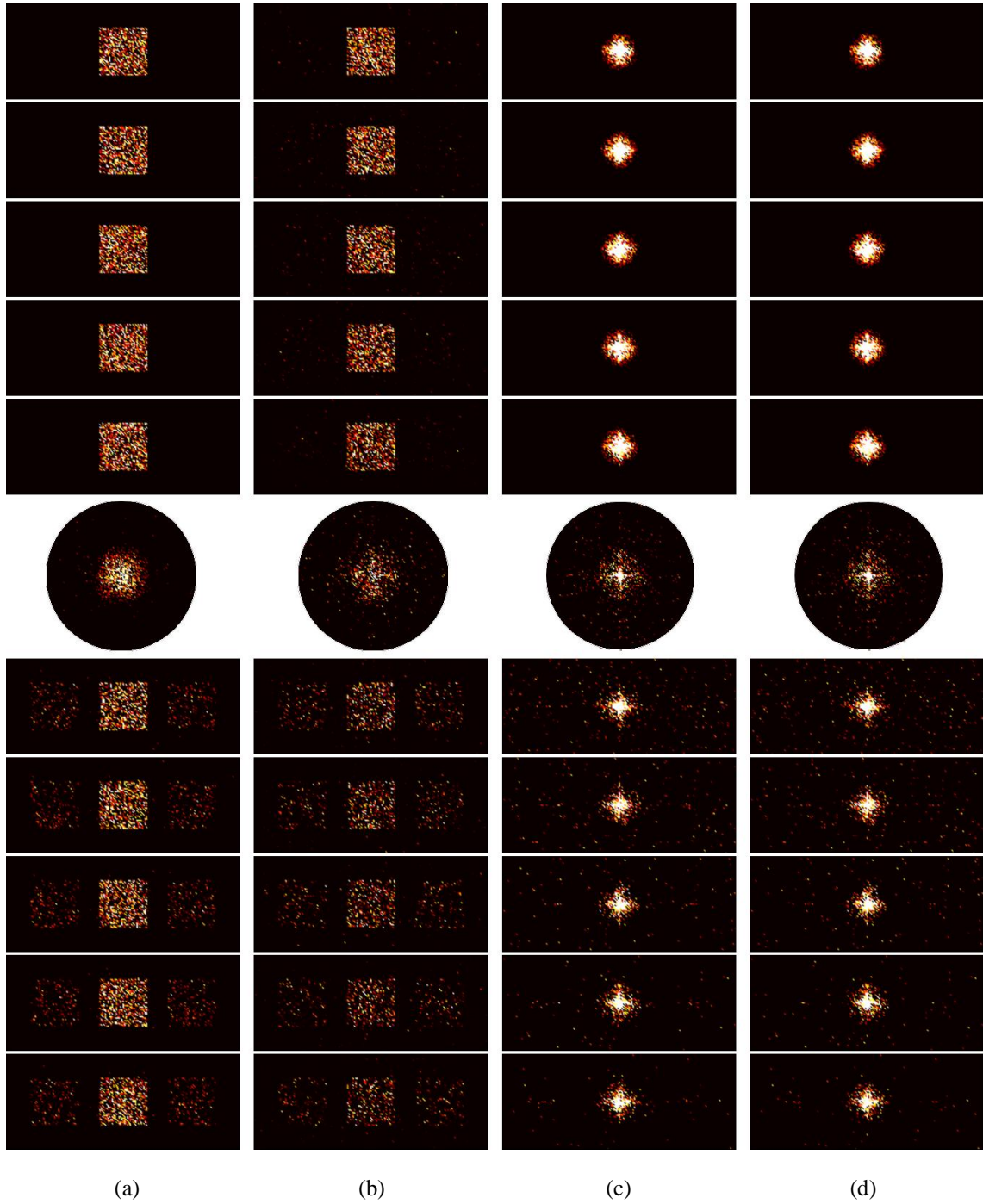


Fig 4.31 NFP for end 2, 3 and 4. (a) SIWG (b) SIWGr (c) GIWG (d) GIWGr. From top to down of terminal II and IV corresponds to 1 to 5 cm. All of the calculated NFPs are shown with the same thermal color table (maximum value = 1).

($\beta > n_{cl}$) versus intensity in Fig. 4.32 to Fig. 34. Here, only the rays inside the launched

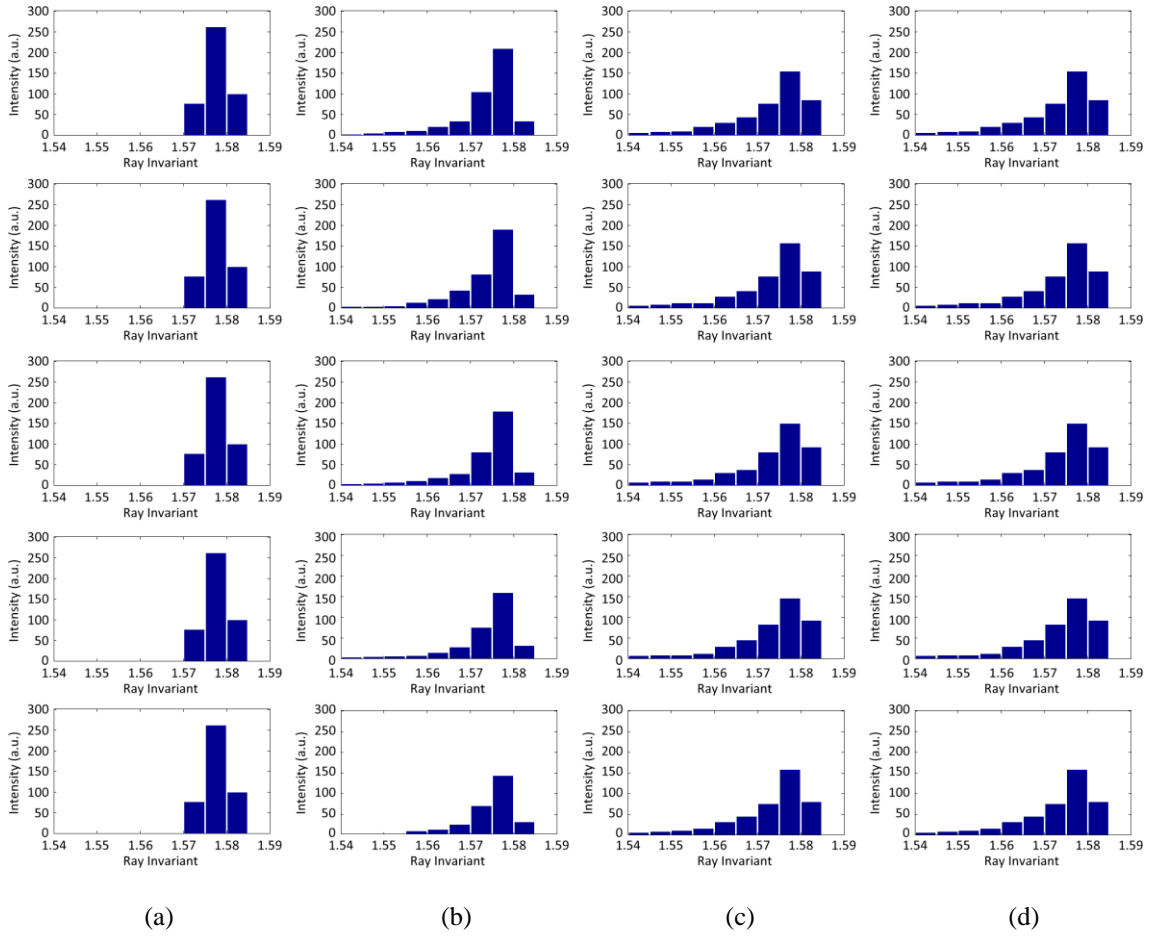


Fig 4.32 Intensity distribution of rays for (a) TxSIWG (b) TxSIWGr (c) TxGIWG (d) TxGIWGr. From top to down corresponds to 1 to 5 cm. Here, $n_{co} = 1.581$ and $n_{cl} = 1.541$.

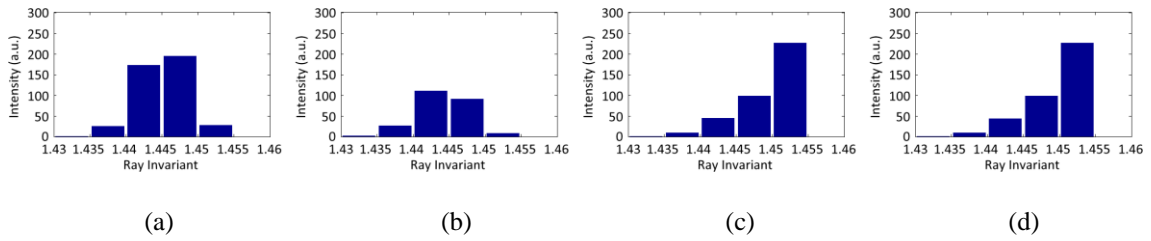


Fig 4.33 Intensity distribution of rays right after MMF for (a) TxSIWG (b) TxSIWGr (c) TxGIWG (d) TxGIWGr. Here, $n_{co} = 1.4525$ and $n_{cl} = 1.4387$.

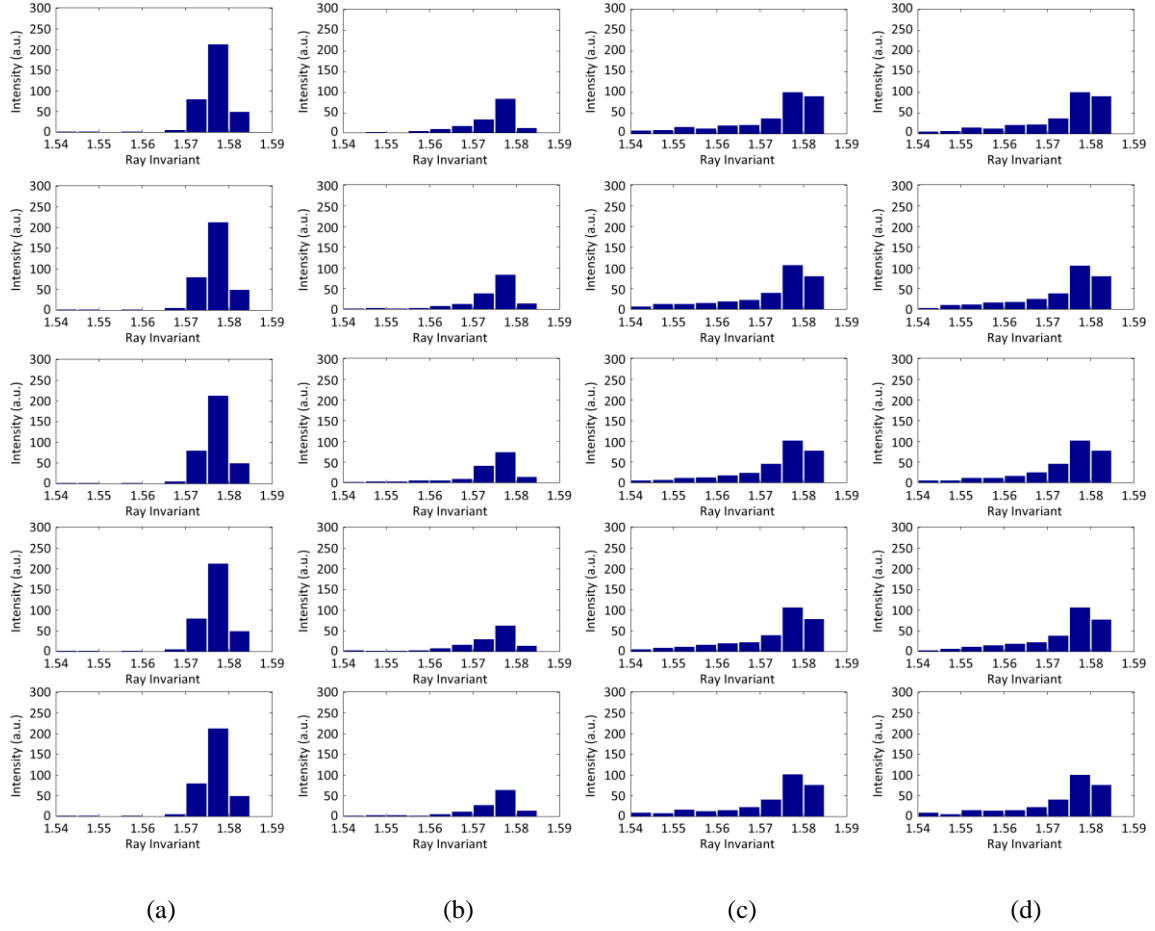


Fig. 4.34 Intensity distribution of rays for (a) RxSIWG (b) RxSIWGr (c) RxGIWG (d) RxGIWGr. From top to down corresponds to 1 to 5 cm. Here, $n_{co} = 1.581$ and $n_{cl} = 1.541$.

core are counted. For specifying the intensity change along the propagation direction, it is necessary to list the numerical results including the intensity for all the cores and cladding. Table 4.6 to Table 4.9 list the numerical results for each cases. Moreover, the figures for intensity change along z direction are also shown in Fig. 4.35 to Fig. 4.38.

4.3.4 Discussion

- *Case 1: SI waveguides without rough core/cladding boundary*

A perfect condition of an SIWG-MMF-SIWG link is considered. Because the maximum incident angle is around 7° , which is much smaller than the NA (20°), all rays

are well bounded as expected. There is no intensity drop and inter-channel crosstalk within the WGTx. Not only the NFPs look almost identical, but the numerical results confirm this fact. When the output light is coupled into the MMF, even if the core size of WGTx is smaller than MMF, the capability of collecting light by MMF, namely local NA radially decreases as shown in Fig. 4.25. Although most of rays are still projected on the core of MMF, some light leakage to the cladding of MMF is caused due to the local NA, which can be observed in the corresponding NFP.

When the light is coupled to the WGRx, the larger core of MMF is a disadvantage for the coupling. In the lower part of Fig. 4.31(a), we can clearly observe the leaky rays exist from the entrance, and no more chance to escape from the adjacent cores, which is confirmed by the straight line as I_Rx shown in Fig. 4.35. In this case, no propagation loss but only connection loss exists.

- *Case 2: SI waveguides with rough core/cladding boundary*

Compared to the case 1, the rough core/cladding boundary is involved according to the parameters mentioned in previous section. As discussed before, the rough surface makes the angle of rays change, which corresponds to the change of ray invariant. According to the NFPs shown in Fig. 4.31(b), some rays leak from the launched core at the input of WGTx. In this calculation, the rough core/cladding boundary exists in all the cores in waveguides (not in the MMF). This leads to the fact that the leaky rays are not surely well confined in the adjacent cores. According to the ray invariants shown in Fig. 4.32(b), the re-coupled rays are still much weaker compared to the leaky rays, hence, the intensity of bound rays gradually decreases. This rather deteriorates the coupling efficiency to MMF and then to the WGRx. From the numerical results listed in Table 4.7, it is confirmed that the intensity drop between I_Tx and I_Rx is larger than

the case 1. Furthermore, in both waveguides the intensity drops significantly with similar trend, from which 0.173 dB/cm and 0.218 dB/cm propagation loss are observed in WGTx and WGRx, respectively.

- *Case 3: GI waveguides without rough core/cladding boundary*

For the real condition, the SI and GI PPOWs with almost identical parameters are hardly can be obtained. However, it would be expected and interesting to investigate what kind of role the rough core/cladding boundary plays in GI PPOW. Here, a perfect condition of a GIWG-MMF-GIWG link is considered.

The NFPs shown in Fig. 4.31(c) shows expected results. The incident rays are well confined near the core center in WGTx. However, when the light is coupled to the MMF, even if the core center shows the higher optical intensity, the number of leaky rays looks much more than the same condition in case 1. This presumably the higher coupling loss happens when the light propagating from MMF to WGRx. We believe that the design of GI profile is the key point. According to numerical results shown in Table 4.8 and Fig. 4.37, although the intensity can be confined as the same level to case 1, the coupling loss is larger and weaker intensity remains in the launched core (343.21 vs. 315.87) and slight loss (0.03 dB/cm) occurred in WGRx. However, it is noteworthy that the power received by photo diode (50 μm away from the output end of WGRx) is the highest in all the cases (298.30).

- *Case 4: GI waveguides with rough core/cladding boundary*

Now we consider the rough core/cladding boundary for GI waveguides. Regardless of the tiny difference of intensity at interface 3 (379.77 vs. 380.42), it performs almost identical until the exit of MMF between case 3 and 4. After the light propagates from

MMF to WGRx, although the connection loss still exists, the degree of intensity drop is significantly smaller than that in case 2 (0.041 dB/cm vs. 0.218 dB/cm). Similar to case 3, the power received by PD is still much higher even compared to optical link composed of perfect SI media. This illustrates a big advantage for decreasing the connection loss with GI waveguides for practical use.

4.3.5 Conclusion

According to formulations introduced in Chapter 2, we address optical characteristics of optical links using a ray tracing method. We highlight four typical cases including SI and GI waveguides based optical link, where the waveguides features on correlated parameters based on physical appearance. Actually the parameters of waveguides are referred to the experimentally measured values on the real samples; the high NA and small core size are specified features. Although GI media performs much less sensitive to rough core/cladding boundary, as expected, the drawback of lower capability to collect the light near to the boundary is critical, particularly the scattering effect is inevitable in the real samples. Finally, the optimization of choosing parameters for an optical link requires more consideration.

Table 4.6 Numerical Results for SI waveguide without roughness

	z	I_l	I_m	I_r	I_{cl}	I_{pd}	I_{total}
①	50 μm	-	432.69	-	-	-	432.69
②	1 cm	0.00	432.69	0.00	0.00	-	432.69
	2 cm	0.00	432.69	0.00	0.00	-	432.69
	3 cm	0.00	432.69	0.00	0.00	-	432.69
	4 cm	0.00	432.69	0.00	0.00	-	432.69
	5 cm	0.00	432.69	0.00	0.00	-	432.69
③	-	-	424.50	-	8.20	-	432.69
④	1 cm	38.79	343.07	39.67	3.44	-	424.96
	2 cm	38.77	343.21	39.81	2.88	-	424.66
	3 cm	38.77	343.21	40.27	2.41	-	424.66
	4 cm	38.77	343.21	40.27	2.41	-	424.66
	5 cm	38.77	343.21	40.27	2.41	-	424.66
⑤	50 μm	-	-	-	-	252.30	-

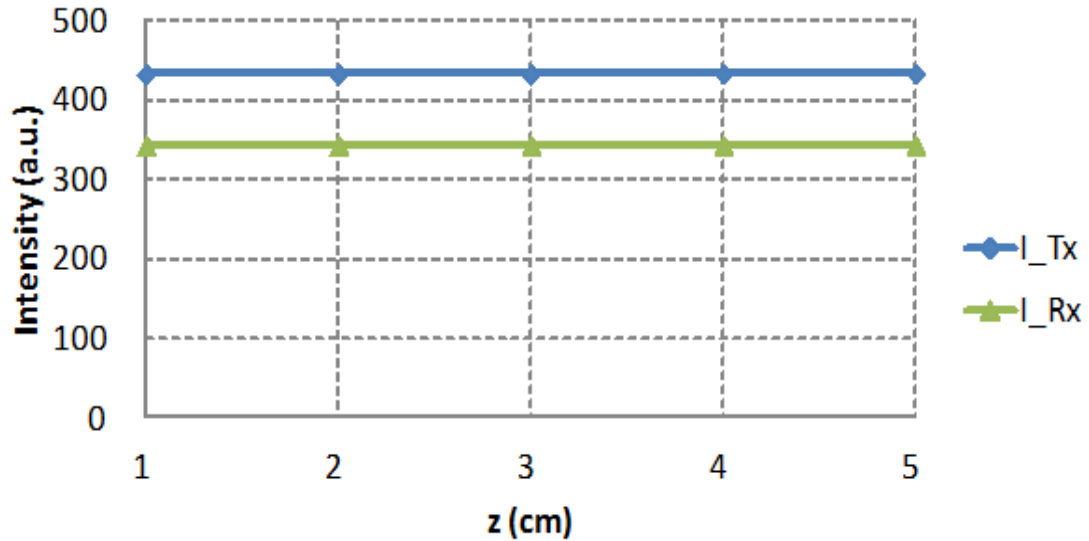


Fig. 4.35 Numerical results of optical link with SIWG-MMF-SIWG configuration without rough core/cladding boundary. There is almost no loss in both Tx and Rx parts.

Table 4.7 Numerical Results for SI waveguide with roughness

	z	I_l	I_m	I_r	I_{cl}	I_{pd}	I_{total}
①	50 μm	-	432.69	-	-	-	432.69
②	1 cm	4.28	404.81	4.23	14.59	-	427.92
	2 cm	3.24	378.98	2.98	11.75	-	396.95
	3 cm	2.19	365.54	2.10	6.78	-	376.62
	4 cm	3.06	351.47	2.67	7.12	-	364.32
	5 cm	1.79	345.05	2.01	4.01	-	352.87
③	-	-	339.32	-	12.01	-	351.33
④	1 cm	7.71	302.18	11.46	16.38	-	337.72
	2 cm	6.96	277.41	9.24	13.72	-	307.34
	3 cm	4.91	263.51	6.76	7.02	-	282.20
	4 cm	4.86	251.50	6.49	6.39	-	269.25
	5 cm	4.66	247.11	5.93	2.51	-	260.20
⑤	50 μm	-	-	-	-	190.8	-

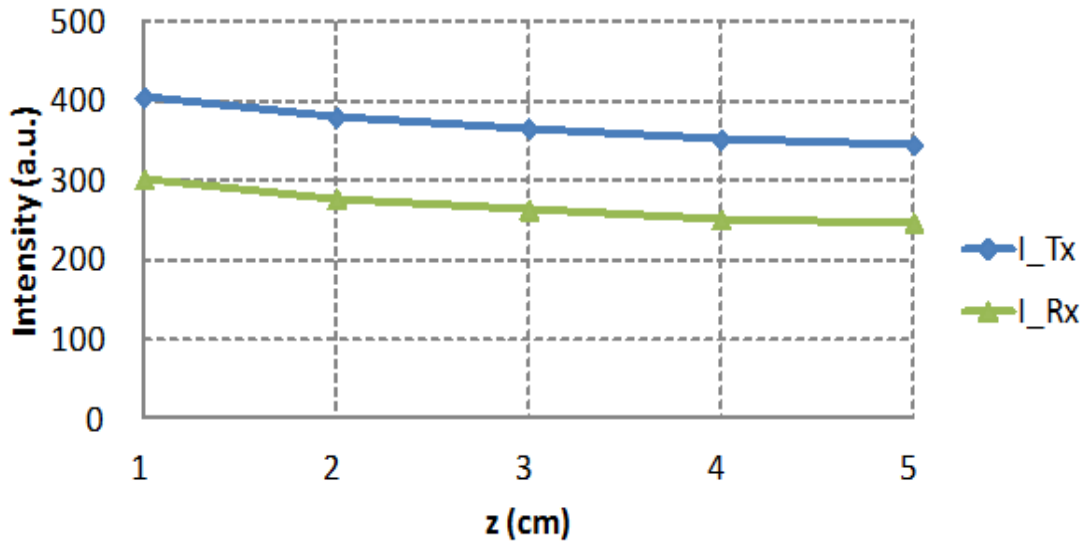


Fig. 4.36 Numerical results of optical link with SIWG-MMF-SIWG configuration with rough core/cladding boundary. The loss is 0.173 dB/cm and 0.218 dB/cm for TxSIWGr and RxSIWGr, respectively.

Table 4.8 Numerical Results for GI waveguide without roughness

	z	I_l	I_m	I_r	I_{cl}	I_{pd}	I_{total}
①	50 μm	-	432.69	-	-	-	432.69
②	1 cm	0.00	432.69	0.00	0.00	-	432.69
	2 cm	0.00	432.69	0.00	0.00	-	432.69
	3 cm	0.00	432.69	0.00	0.00	-	432.69
	4 cm	0.00	432.69	0.00	0.00	-	432.69
	5 cm	0.00	432.69	0.00	0.00	-	432.69
③	-	-	379.77	-	52.49	-	432.25
④	1 cm	6.12	324.79	11.32	52.78	-	395.01
	2 cm	7.44	317.39	6.37	39.07	-	370.27
	3 cm	5.96	317.08	5.01	26.40	-	354.45
	4 cm	3.74	315.81	3.61	18.44	-	341.60
	5 cm	3.97	315.87	3.31	11.78	-	334.93
⑤	50 μm	-	-	-	-	298.30	-

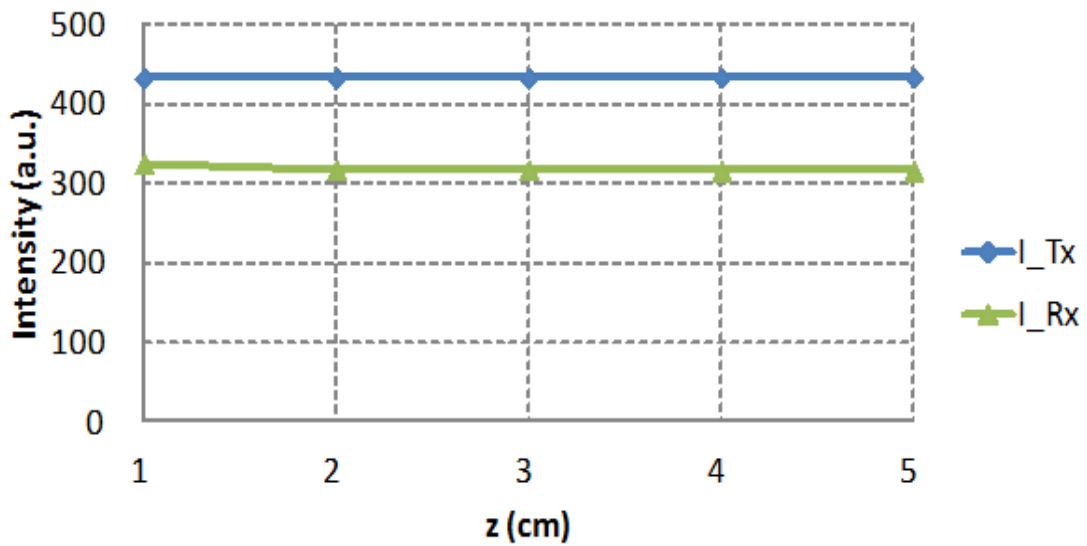


Fig. 4.37 Numerical results of optical link with GIWG-MMF-GIWG configuration without rough core/cladding boundary. There is almost no loss in WGTx and 0.03 dB/cm loss in WGRx parts.

Table 4.9 Numerical Results for GI waveguide with roughness

	z	I_l	I_m	I_r	I_{cl}	I_{pd}	I_{total}
①	50 μm	-	432.69	-	-	-	432.69
②	1 cm	0.00	432.69	0.00	0.00	-	432.69
	2 cm	0.00	432.69	0.00	0.00	-	432.69
	3 cm	0.00	432.69	0.00	0.00	-	432.69
	4 cm	0.00	432.69	0.00	0.00	-	432.69
	5 cm	0.00	432.69	0.00	0.00	-	432.69
③	-	-	380.42	-	51.41	-	431.82
④	1 cm	6.41	319.11	11.03	55.31	-	391.86
	2 cm	6.34	311.03	7.38	40.17	-	364.92
	3 cm	5.42	309.11	5.64	24.82	-	345.00
	4 cm	2.73	306.57	2.88	19.26	-	331.44
	5 cm	3.60	307.37	2.34	11.17	-	324.47
⑤	50 μm	-	-	-	-	291.72	-

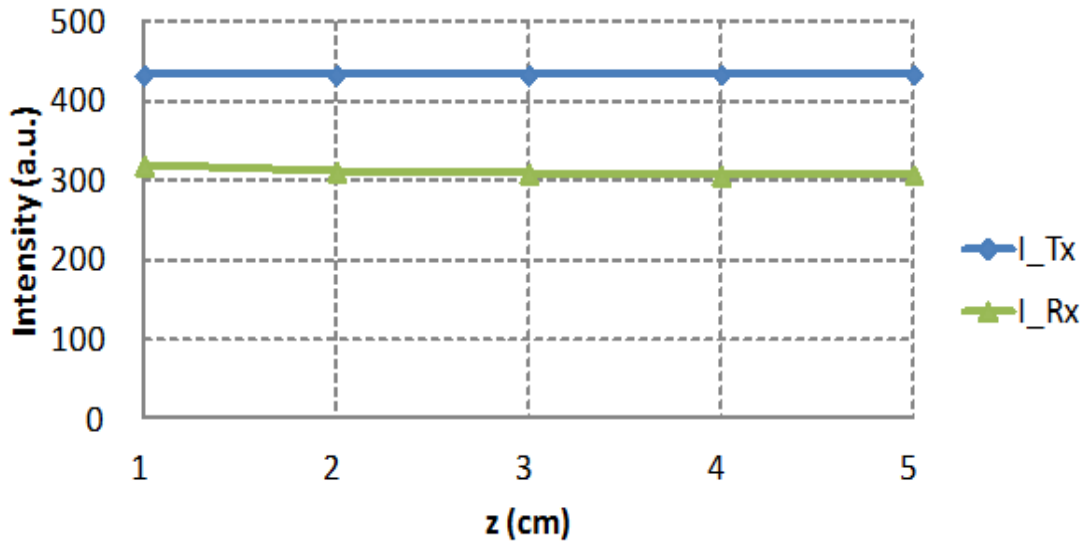


Fig. 4.38 Numerical results of optical link with GIWG-MMF-GIWG configuration with rough core/cladding boundary. There is almost no loss in WGTx and 0.041 dB/cm loss in WGRx parts.

4.4 OPTICAL LINK ANALYSIS WITH WAVE OPTICS

As introduced in Chapter 1, the performance of optical links dominates the overall performance for a HPC system, and the ray tracing method was applied to the performance comparison between SI and GI waveguide based links. In this section, the GI-PPOW based optical link is focused and both some key parameters which influence on mostly the connection loss are experimentally and theoretically investigated.. The link in the experiment is launched via an SMF and the connection loss is measured at certain ends. The results show the connection loss between GI-MMF and WGRx is around 0.4 dB higher than WGTx to GI-MMF. For the theoretically modeling, we start from the fundamental scalar wave equation, and utilize the finite difference beam propagation method (FD-BPM) to simulate the behavior of lightwave in the waveguide. Furthermore, the Fresnel reflection between two media with different refractive index, and light scattering effect in polymer optical waveguides are also taken into account. The simulated results show good coincidence to actually measured values, thus we can conclude that the scattering effect could be one of the key issues for GI-PPOW under this application.

4.4.1 Connection loss evaluation of GI-PPOW based optical link

Figure 4.39 shows a GI-POW with square shaped cores fabricated using the perform method [1, 8]. The core material is composed of PMMA doped with an 11 wt. % of DPS, which shows a propagation loss of approximately 0.03 dB/cm at 850-nm wavelength. The fabricated GI-PPOW is a long and thin slab so that we cut a 5-cm long piece for the experiment, as shown in Fig. 4.39(a). Figure 4.39(c) and (d) show the waveguide has four cores (channels) which are parallel aligned, and the index profile

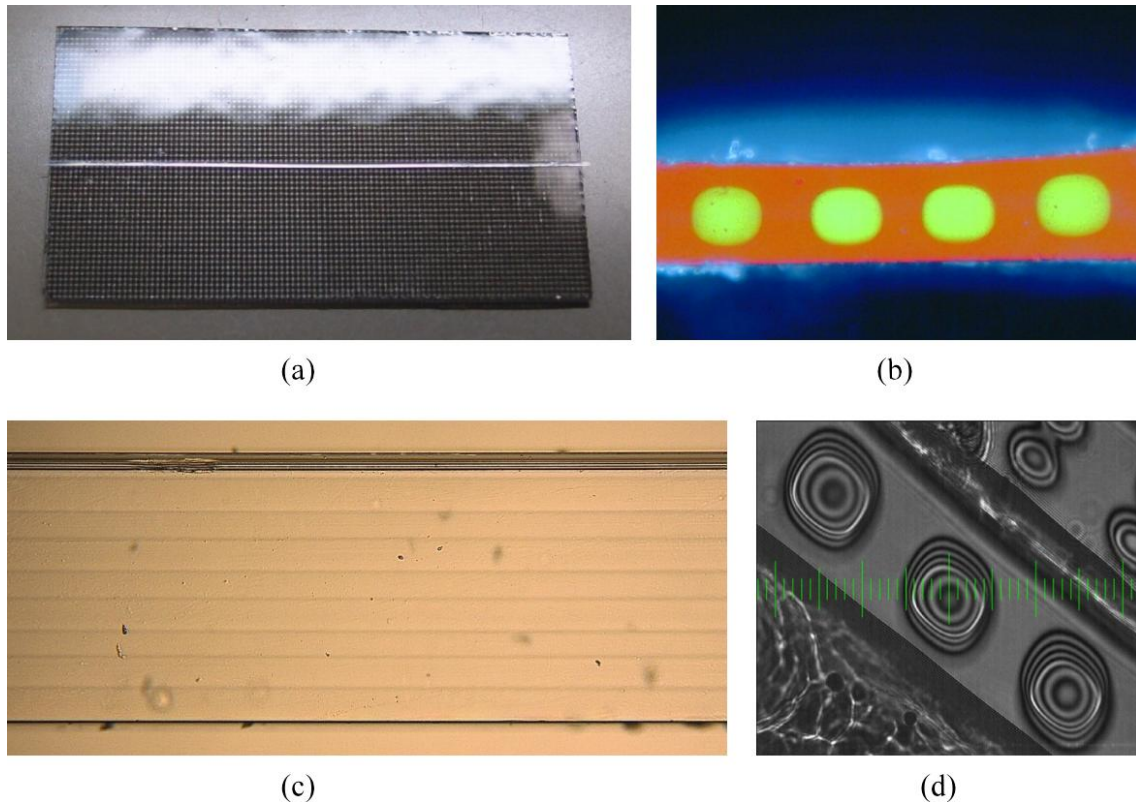


Fig. 4.39 The PMMA based GI-PPOW with square shape cores fabricated using the preform method. (a) The waveguide is attached on a glass plate. (b) cross section and (c) top view image of the waveguide. (d) interference fringes show the graded index profile in the core area.

within each core area is near parabolic. The proposed two-dimensional index profile is expressed by Eq. (2.13). The measured properties of the waveguide are listed in Table 4.10.

The connection loss of a board level optical interconnection circuit is evaluated using the experimental setup shown in Fig. 4.40 and Fig. 4.41. In this measurement, the light from a VCSEL module with 850 nm wavelength (Newfocus 1780) is coupled to an SMF and then coupled into the waveguide. In order to obtain the lowest connection loss, the WGTx is launched under restricted mode launch (RML), hence an SMF is used for guiding the lightwave to the WGTx. In the right side of Fig. 4.40 and Fig. 4.41, the lightwave from the output end of WGRx is collected by an SI-MMF (50 μm core), and

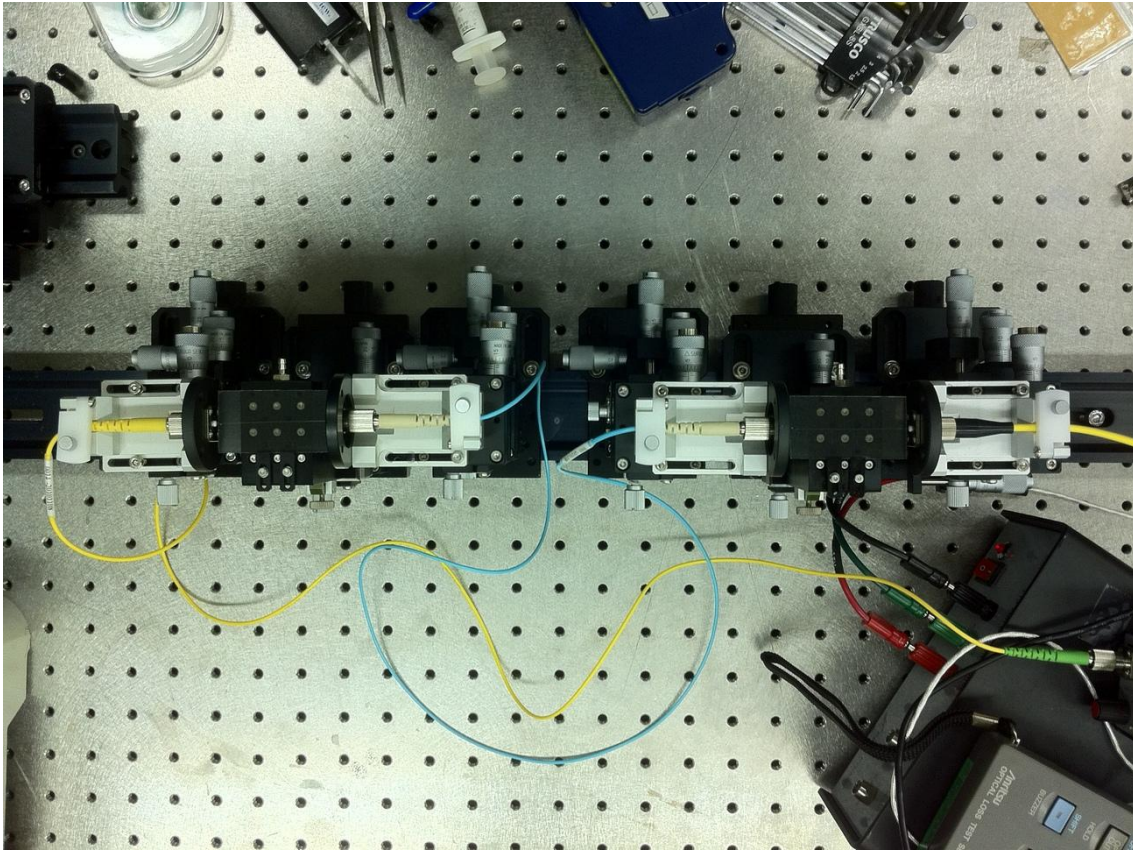


Fig. 4.40 Experimental setup of the optical link.

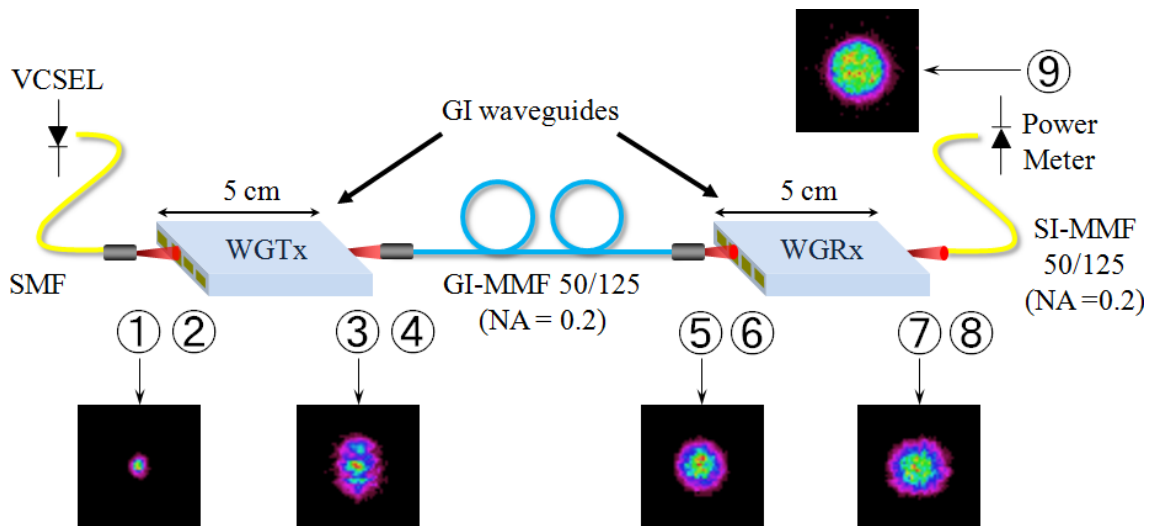


Fig. 4.41 For convenience, we designate nine ends (1 to 9) to show the optical properties when the light propagates from VCSEL to the power meter. The corresponding measured NFP are also shown for the ends 1, 3, 5, 7, and 9.

then connected to an optical power meter. Similar to the experimental setup in Section 1, the WGTx and WGRx are connected by a GI-MMF. All the fibers used here are commercially available (standardized fibers).

For convenience, the experimental setup is simplified as Fig. 4.40. The ends 1 to 9 are described individually as follows:

- 1: output end of SMF.
- 2: either the far field of 1 or the input of WGTx.
- 3: output end of WGTx.
- 4: either the far field of 3 or the input of GI-MMF.
- 5: output end of GI-MMF.
- 6: either the far field of 5 or the input of WGRx.
- 7: output end of WGRx.
- 8: either the far field of 7 or the input of SI-MMF.
- 9: final output end.

The measured NFPs for the corresponding ends are also shown in Fig. 4.41, where the GI waveguide used for the WGTx performs less mode confinement (in end 3) than that expected. This makes more numbers of modes are launched in the GI-MMF, as shown by the NFP in end 5. Nonetheless, due to the similar core size between GI-MMF and WGRx, the output light from end 7 fills almost the entire core area. Finally, we measure the power of ends 1, 5, and 9 and then calculate the loss with the following equation:

$$Loss(dB) = -10 \log \frac{P_1}{P_0} \quad (2)$$

where P_0 is the power of an input end and P_1 is the power of the corresponding output end. Furthermore, in order to confirm the reproducibility of the alignment, we exchange the position and the input/output end of two waveguides. Table 4.11 shows the five times connection loss measurement of end 5 to 1 and end 9 to 5, where the results show

good reproducibility: the connection loss of later part is, on average, 0.4 dB higher than the prior part.

Table 4.10 Measured parameters of the fabricated square shape GI-POW

Parameters	Value
Index of core (n_{co})	1.507
Index of cladding (n_{cl})	1.492
Core size (a_x)	50 μm
Core size (a_y)	50 μm
Index exponent (p)	2.2
Index exponent (q)	2.2

Table 4.11 Connection loss measurement

Loss (dB)	exp 1	exp 2	exp 3	exp 4	exp 5	Average
⑤ → ①	0.80	0.94	0.76	0.83	0.79	0.82
⑨ → ⑤	1.30	1.18	1.30	1.19	1.22	1.24
Total	2.10	2.12	2.06	2.02	2.01	2.06

4.4.2 Connection loss evaluation of fiber based optical link

In the above section, we demonstrated a typical GI waveguide based link budget. The interest of this study is in how much the total loss decreased compared to that of the conventional SI waveguide based links. Practically it is not easy to find a similar SI polymer optical waveguides counterparts. Therefore, we replace the waveguides for TX and RX by 1-m long commercial available silica base SI and GI MMFs which are regarded as almost perfect (lossless) media. The total link loss in this study between GI and SI media is characterized by the experimental setup shown in Fig. 4.42, where two GI or SI MMFs are connected with each other by another GI-MMF. The purpose of the experiment is to address the tolerance of misalignment (0, 5 μm , and 10 μm) between GI

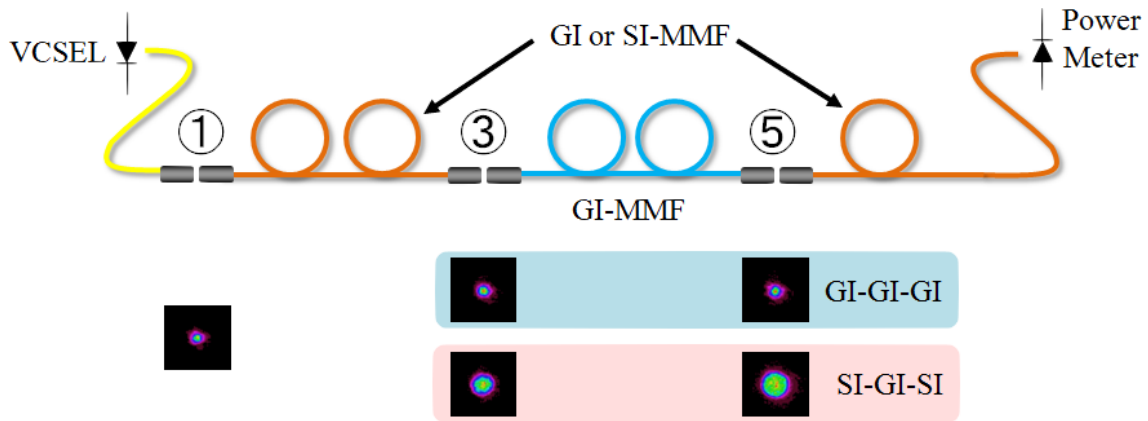


Fig. 4.42 Evaluation of alignment tolerance between GI-GI-GI and SI-GI-SI connection. The corresponding NFPs without offset for end 1, 3, and 5 are also listed.

and SI cores. Similar to the experimental setup in Fig. 4.40, a VCSEL module at 850-nm wavelength is used and then the lightwave from the VCSEL is coupled into multimode fiber which is exchangeable as GI or SI-MMF via an SMF probe. After the light propagates to the GI-MMF, as shown in Fig. 4.42, the output is coupled into another identical counterpart. Here, some radial offset in ends 1, 3, and 5 is deliberately added, and then the total loss difference between GI and SI fiber based optical link is evaluated. The measured results are listed in Table 4.12.

When there is no offset involved, the GI-GI-GI connection shows only 0.1 dB lower loss than SI-GI-SI connection (0.371 dB vs. 0.477 dB). In this case, the corresponding NFPs are shown in Fig. 4.42. The NFPs which show smaller light spots confirm that the modes are well confined from end 1 to end 5 in GI-GI-GI connection. However, in the case when the offset is involved separately in ends 1, 3, or 5, even if the offset is as large as 10 μm , the GI-GI-GI connection shows less sensitivity compared with SI-GI-SI connection: less than 0.4 dB of total loss in GI-GI-GI link is much more remarkable than 1.246 dB loss in the SI-GI-SI link. Furthermore, when 10 μm offset is added in all the ends simultaneously, the GI-GI-GI connection maintains less than 1

dB total loss, while SI-GI-SI connection shows more than twice loss (0.889 dB vs. 1.940 dB). According to the experimental results, it can be concluded that SI core shows higher connection loss under all the conditions. Moreover, compared to the 2 dB link budget listed in Table. 12, the loss of 0.371 dB could be the minimum loss of the GI-GI-GI connection for the focused optical link. In the following sections, GI waveguides are chosen for data transmission (WG_{Tx}) and reception (WG_{Rx}) media, and then where the losses come from is discussed both experimentally and theoretically.

Table 4.12 Total connection loss difference between GI and SI fiber based optical link

Loss (dB)	Offset ①		Offset ③		Offset ⑤		Offset ①③⑤	
	SI	GI	SI	GI	SI	GI	SI	GI
0	0.477	0.371	0.477	0.371	0.477	0.371	0.477	0.371
5 μm	0.490	0.378	0.684	0.371	0.536	0.373	0.864	0.391
10 μm	0.522	0.375	1.246	0.393	0.805	0.392	1.940	0.889

4.4.3 Theoretical modeling

The modeling layout of the optical link is illustrated in Fig. 4.41. The VCSEL source is assumed to be multimode and to emit Hermite-Gaussian beam. Under the consideration of multimode and multichannel GI-PPOW, the polarization of incident light plays a minor role on the optical characteristics. The scalar wave equation performs a promising starting point to describe the plane wave propagation in each of components. Moreover, according to the actual experimental setup, three parameters, air gap, biased launching condition, and scattering effect, are of our concern. For characterizing the total loss of the link, the propagation loss and material loss are separated in order to distinguish the cause from connection and component itself. All of the features can be realized by the equations mentioned in the following sections, so that

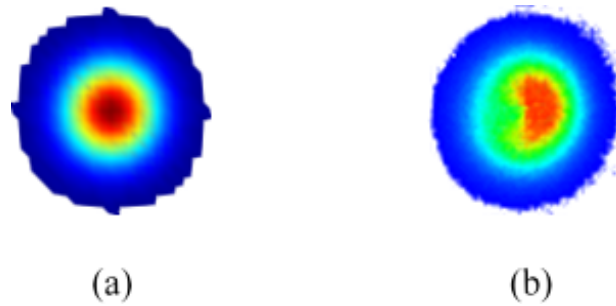


Fig. 4.43 (a) The modal field applied in the simulation and (b) measured output modal field from SMF.

the computer program based on wave optics created in this study helps us to involve desired parameters and conditions with higher degree of freedom.

The output modal field of SMF shown in Fig. 4.43(a) is a Gaussian distribution that results from the lowest order mode of a Hermite-Gaussian beam filtered by the SMF. Since the NA of the incident beam is much smaller than the NA of the GI-PPOW, all the light can be coupled into the waveguide even if a 50- μm air-gap exists. However, due to not only the mode field mismatch between 850 nm VCSEL and SMF for 1550nm but the inevitable fiber bending during the experiment, the real output field at the end of SMF is not necessarily illustrated like Fig. 4.43 (a). Figure 4.43(b) shows a typical measured NFP from the output end of SMF. The featured biased modal field results in an unexpected misalignment, even if all the components are perfectly aligned. In the following calculation process, the biased launching condition shown in Fig. 4.43(b) is also taken into account in some cases. Note that the pseudo color with corresponding value is different from Fig. 4.43(a) and (b).

Moreover, the parameters of GI-PPOWs applied in the simulation are referred to the measured results shown in Fig. 4.39. There are four parallel aligned square cores with 90 μm pitch in the waveguide and the refractive indexes of core center and cladding are 1.507 and 1.492, respectively, as listed in Table 4.12. Furthermore, all the

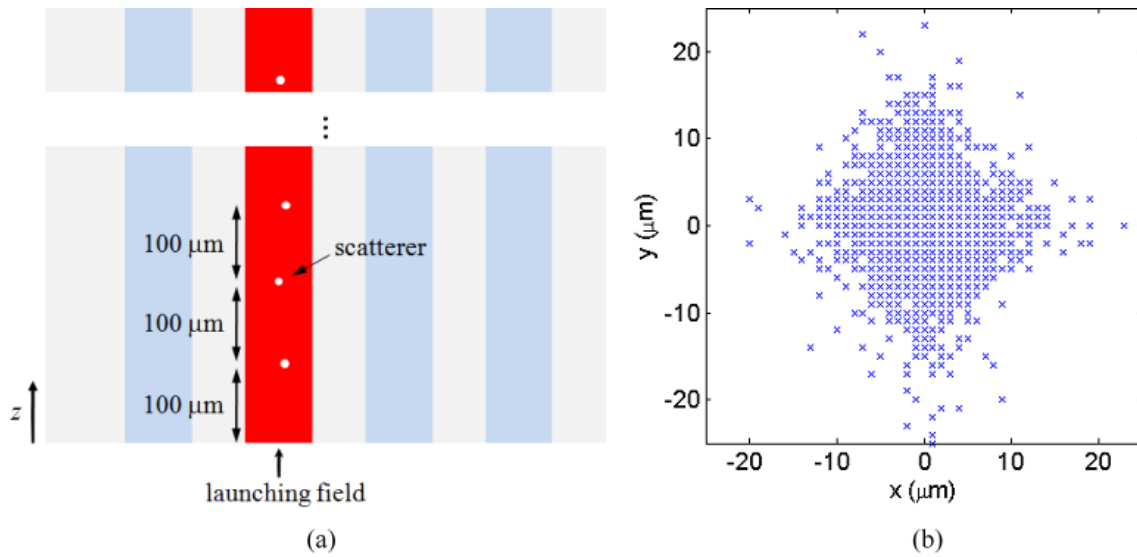


Fig. 4.44 (a) The scatterers are randomly distributed in the launched core with 100 μm space along propagation (z) direction. (b) Projection on the x - y plane of 1000 scatterers within the core area where scatterers are randomly placed as Gaussian distribution.

fibers in the model are treated as perfect media.

4.4.4 The scattering effect

Compared to silica based media, polymer features on its complicated structure which results in excess light scattering. In the previous sections, it is not only theoretically confirmed that the scattering effect plays an important role in the inter-channel crosstalk, but also experimentally concluded that the scattering loss itself is pretty low particularly for centimeter long PPOWs [12]. The light scattering effect modeled by ray tracing method is that rays are split when hitting scatterers. Due to the approximation of zero wavelength in ray optics, the size of scatterers are determined by the number of split rays and corresponding angle distribution rather than the size parameter. Here, wave propagation inside a perturbed GI medium is considered. Thus, it could be assumed that the wavefront could be distorted by the abrupt change of refractive index profile.

The purpose of modeling for scattering effect is qualitative rather than quantitative. In order to see how the mode fields are distorted by scatterers in polymer materials, the spherical air bubbles ($n = 1$) with a 1- μm in diameter is regarded as the scatterers. The equivalence of scattered profile calculated by FD-BPM is confirmed by GLMT under on-axis Gaussian beam illumination [14] as introduced in Sec. 3.5. The minor modification of our FD-BPM computer program for far field angular distribution scattered by a sphere will be discussed elsewhere. We consider the 1 μm diameter is too large compared with the real scatterers, they are placed 100 μm separately along the propagation (z) direction as shown in Fig. 4.44(a). Moreover, in terms the fabricated GI-PPOW, the core material is composed of higher concentration of DPS dopant near the core center: the scatterers could be located closer to the core center with randomly Gaussian distribution. Figure 4.44(b) shows the projection of 1000 scatterers on the cross section of the core area.

4.4.5 Calculation Results

Four cases are discussed as shown below:

Case 1: SI waveguides without rough core/cladding boundary

Case 2: SI waveguides with rough core/cladding boundary

Case 3: GI waveguides without rough core/cladding boundary

Case 4: GI waveguides with rough core/cladding boundary

Case 1: the perfect conditions

First, the perfect connection of the optical link is focused. Thus, it is assumed that no air-gap exists and all the components are ideal (structure and alignment). In this case, nothing but the light propagates in each component is calculated. The calculated NFPs

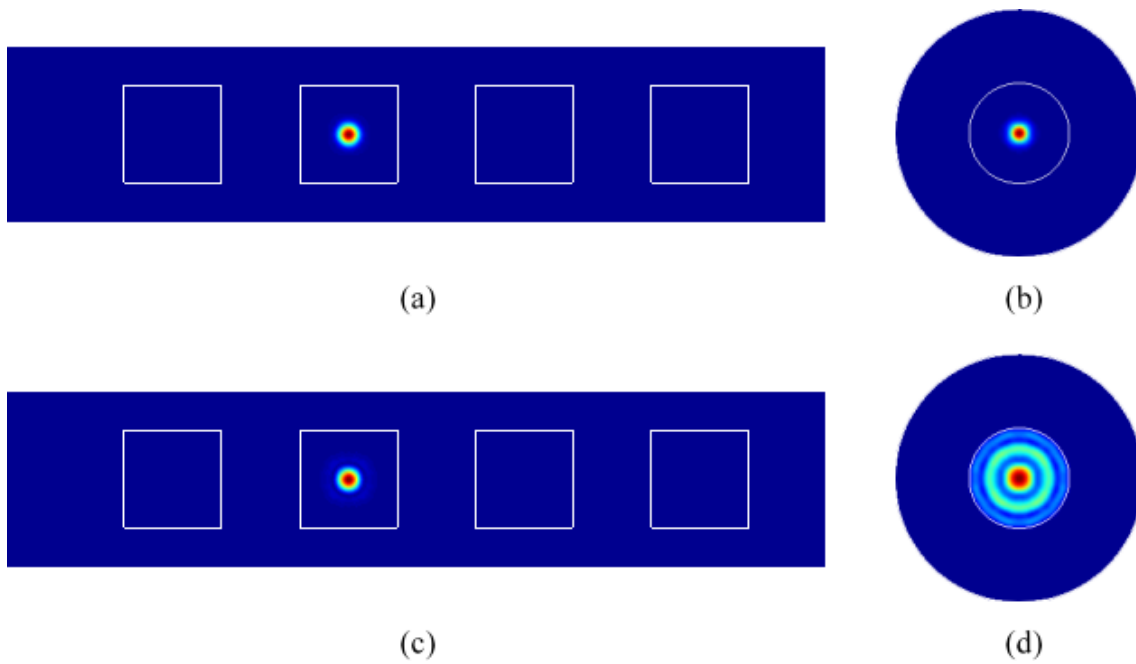


Fig. 4.45 The calculated NFPs of the perfect condition: (a) NFP of end 3, (b) NFP of end 5, (c) NFP of end 7, and (d) NFP of end 9.

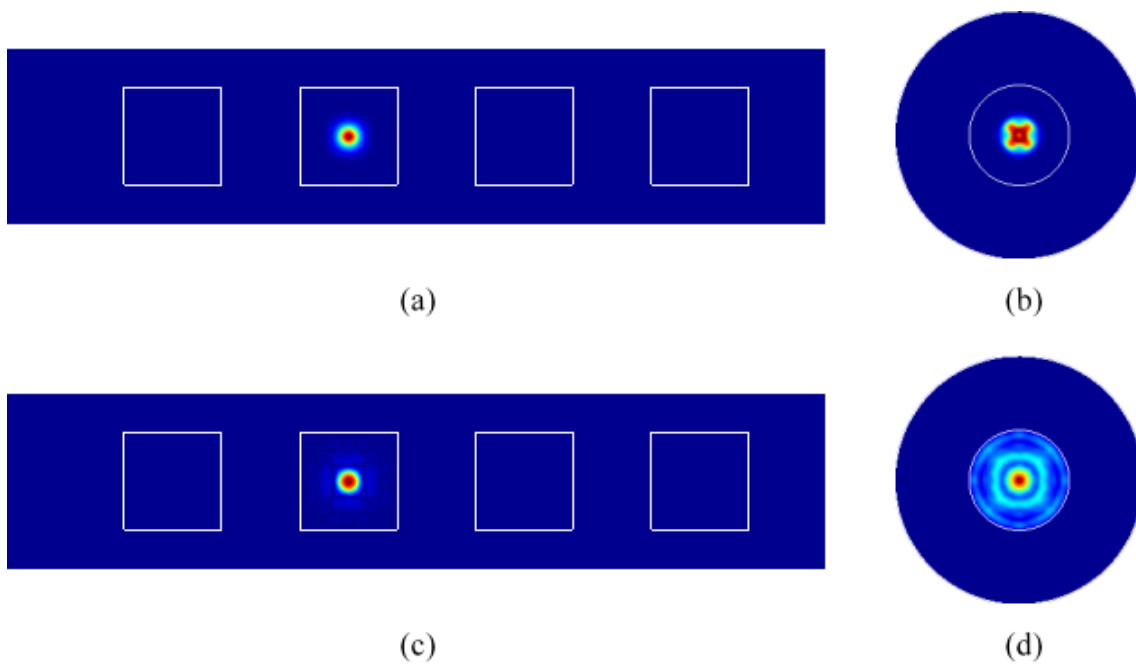


Fig. 4.46 The calculated NFPs of the second consideration: (a) NFP of end 3, (b) NFP of end 5, (c) NFP of end 7, and (d) NFP of end 9.

of corresponding ends are listed in Fig. 4.45. In Fig. 4.45 (a), the NFP of the output end of WGTx shows the optical confinement by GI profile. Similarly, while the light continues to propagate via GI-MMF and WGRx, the optical field is always restricted near the core center as Fig. 4.45 (b) and (c) show. Finally, more modes are excited in the SI-MMF by the output field shown in Fig. 4.45 (c). Fig. 4.45 (d) shows the NFP of end 9. The numerical results calculated by FD-BPM are listed in Table 4.13. As expected, no propagation loss and only 0.15 dB material loss for each waveguides are counted. Under this consideration the total loss is 0.3 dB which is still far away from the experiment results and some modifications to this model are required.

Case 2: the perfect components with an air gap intermediated

Similar to the previous consideration, all the components perform perfectly but a 50- μm air gap is involved in each connection ends. Here, the Fresnel reflection expressed by Eq. (3-17) is taken into consideration, and the far field is calculated by Eq. (3-18). Compared to Fig. 4.45(a), Fig. 4.46(a) shows a slightly larger light spot because of the launching field is broaden after propagating through the air gap. Similarly, Fig. 4.46(a) to (c) clearly show the influence of the air gap that more modes are launched in all the components. The calculated numerical results in Table 4.13 show larger connection loss (0.48 dB loss from end 5 to 1 and another 0.48 dB loss from end 9 to 5), which are mainly due to the Fresnel reflection. Although the results are closer to the experimental results compared to the previous condition (Case 1), the loss in Rx part is almost identical to the Tx part, which is not reasonable enough.

Case 3: the biased launching condition with air gaps intermediated

Based on the real measurement, the launching condition in the optical link is not a

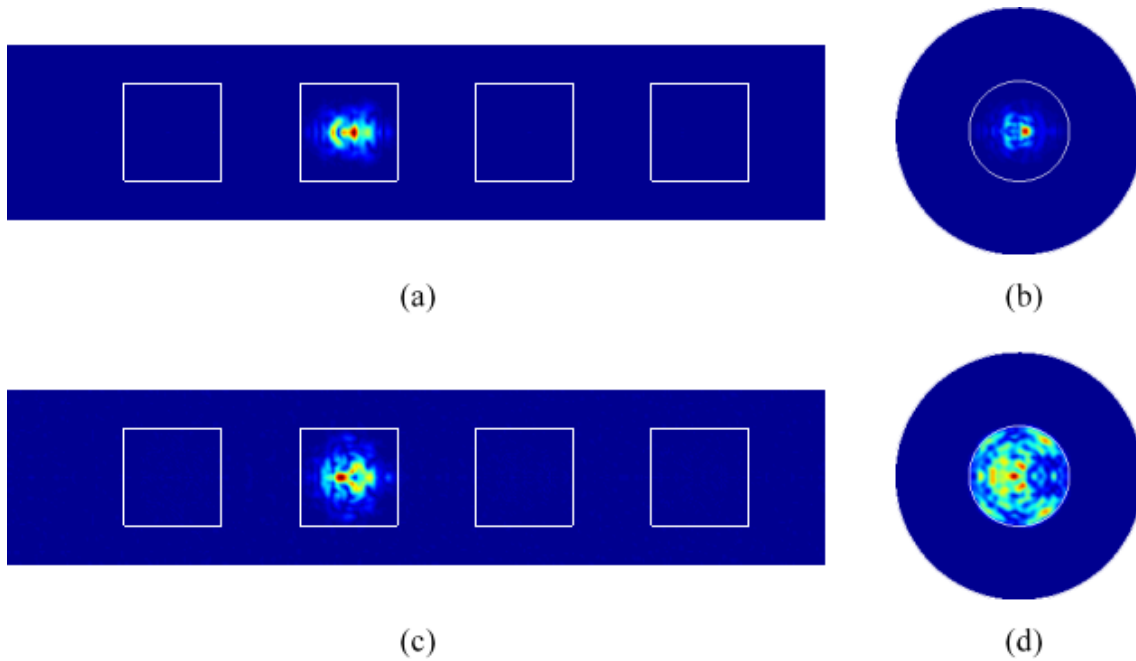


Fig. 4.47 The calculated NFPs of the third consideration: (a) NFP of end 3, (b) NFP of end 5, (c) NFP of end 7, and (d) NFP of end 9.

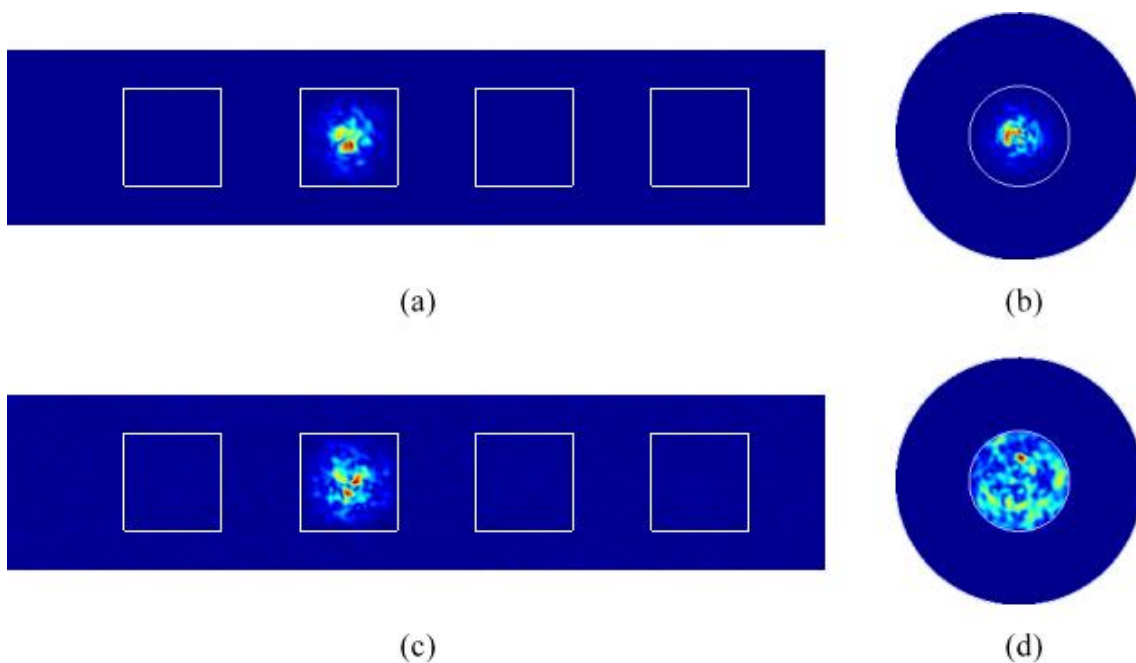


Fig. 4.48 The calculated NFPs of the fourth consideration: (a) NFP of end 3, (b) NFP of end 5, (c) NFP of end 7, and (d) NFP of end 9.

Gaussian like field as shown in Fig. 4.43(a). In this case, not only air gaps but another biased launching field shown in Fig. 4.43(b) is applied. In the NFP of end 3 as Fig. 4.47(a) shows, even higher order modes are launched, they are still confined by the GI profile and the highest intensity is located near the core center. This indicates that the slight misalignment can be compensated by GI profile. However, after propagating through the air gaps and other GI media, some radiation modes are generated, as Fig. 4.47(c) and (d) show. The calculated loss including the material loss is listed in Table 4.13. Due to the higher order and radiation modes launched by biased launching condition, the loss for end 9 to 5 is higher than that of end 5 to 1. This feature is also confirmed by the experimental results so that we can conclude the biased launching condition is one of the causes. However, compared to the 0.4 dB differences in experimental results, the difference calculated here is only 0.13 dB, which implies some other reasons dominate this phenomenon..

Case 4: the biased launching condition with scattering effect

In this consideration, not only the scattering effect into the GI waveguides (WGTx and WGRx) is involved but also both of air gaps and biased launching condition are taken into account in the optical link model. The consideration of the scattering effect is mentioned in the above section. Although this model is still far away from the real condition in the waveguides, how the scattering effect influence on the connection loss is of great interest. As predicted in Sec. 4.4, the mode confinement in GI cores is distorted by scattering effect and thus, the maximum intensity in each output ends displaced away from the core center and some of them even have more than one peak, as shown in Fig. 4.48(a) to (c). Similar to the previous condition, Fig. 4.48(c) shows that

some radiation modes are also generated, thereby bigger core area is filled and makes the connection loss even higher. The numerical results listed in Table 4.13 confirm the scattering effect is another important role to deteriorate the coupling near to the WGRx (end 5). The connection loss from end 9 to 5 is 0.3 dB higher than that of end 5 to 1, and the 0.63 dB and 0.93 dB losses is closer to the experiment results. Although it is not possible to make the calculated values to be almost identical to the measured results, we can conclude that the scattering effect is inevitable in polymer optical waveguides even if it is perfectly aligned and launched by a perfect Gaussian like field.

Table 4.13 Calculation results of GI waveguide based optical link

Features	exp	case 1	case 2	case 3	case 4
air gap	O ¹	X ²	O	O	O
biased launch	O	X	X	O	O
scattering effect	O	X	X	X	O
⑤ → ①	0.82	0.15	0.48	0.55	0.63
⑨ → ⑤	1.24	0.15	0.48	0.68	0.93
total loss	2.06	0.30	0.96	1.23	1.56

1: included

2: not included

4.4.6 Conclusion

The GI media is confirmed to have better optical characteristics about the mode propagation. In the beginning of this paper, we experimentally illustrate the benefit of GI-GI-GI connection for the purpose of optical link. The measured NFPs clearly show the confined modal field from SMF to final output. This encourages us to apply GI waveguides to another experiment setup for a more practical optical link. From the experiment result, the averaged 0.4 dB higher loss between GI-MMF to WGRx and

SMF to WGTx could result from the unexpected biased launching condition and the scattering effect originated from polymer core material.

Based on the experiment setup and measured features, we established a flexible and reliable theoretical model to analysis connection loss for the optical link. The modulized algorithms help us to clarify the causes of connection loss step by step. It is theoretically confirmed that the scattering effect plays the most important role to the connection loss even such low loss waveguides (~ 0.03 dB/cm) are equipped. According to some prior articles as mentioned in Sec. 4.4, although the scattering loss in a short length waveguide is neglectible, it plays an important role for mode conversion (lower order modes convert to higher order modes and vice versa). We can conclude that the mode conversion excites higher order modes and then results in higher connection loss when coupling the light from GI-MMF to WGRx side. Furthermore, even it is still far away to manufacture polymer material with almost no scattering loss, we can conclude that the GI-POW perform the characteristic of connection loss suppression for the application of high dense aligned optical interconnections.

4.5 THE OPTIMIZATION OF WAVEGUIDE DESIGN

In terms of the GI waveguide based optical link model shown in Fig. 4.41, the total link budget is contributed by various factors, such as launching condition, gap between two components, imperfection of core material, core size of waveguides, and refractive index profile of cores. Some of these are demonstrated in the previous section, where significant losses resulted from the Fresnel reflection are proved even under the conditions of perfect alignment and ideally low-loss core materials. Under the consideration of practical usage, SI waveguides are still the main stream. However, the

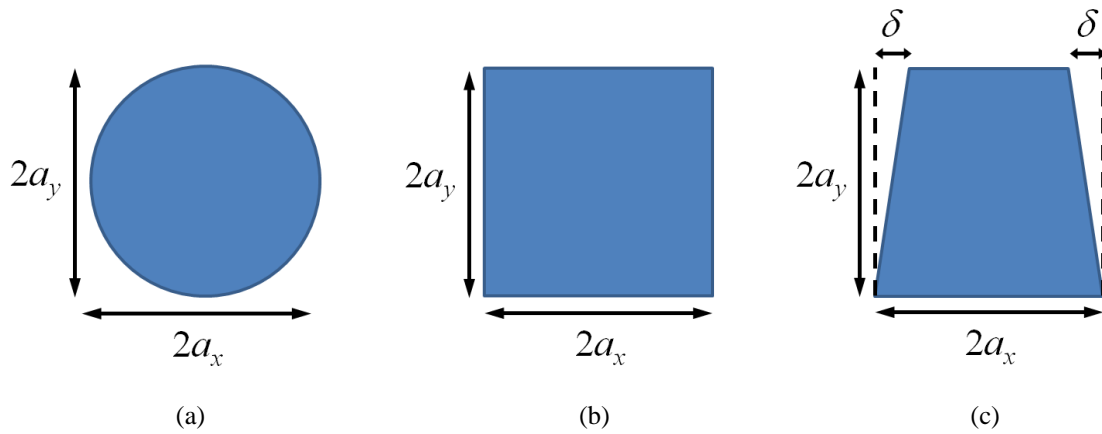


Fig. 4.49 Three kinds cores considered in Sec. 4.5.1 and their physical dimensions. (a) Circular core, (b) Square core. (c) Trapezoidal core.

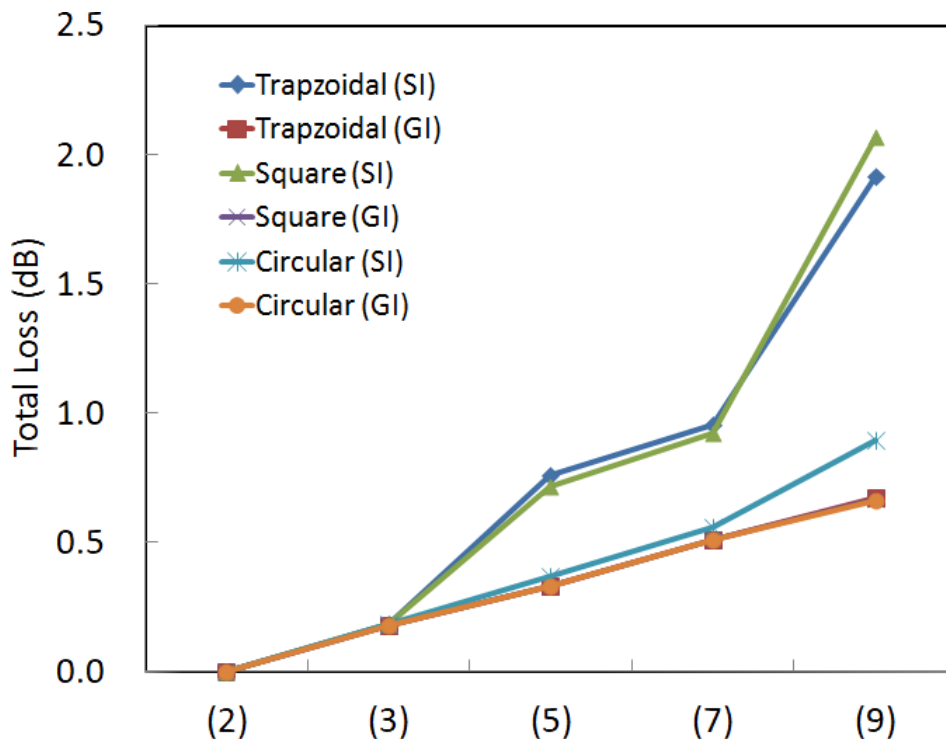


Fig. 4.50 The total losses with corresponding core shapes and refractive index profiles. The meaning of ends (2), (3), (5), (7), and (9) in abscissa refer to Fig. 4.41.

design of multimode waveguide based optical links becomes more complicated, because the modal fields distribution influences on the coupling losses significantly, so that the studies for optimized waveguide structural parameters are highly required. In this

section, the prior three conditions are considered for the purpose of optimizing the link budget: core shape, core size, and NA of SI cores. Furthermore, in order to clarify the trend of total link loss under the above considerations, the imperfections in core are removed in the most of calculations here. Finally, another condition is considered. The scattering effect is involved in SI cores, where the same mechanism of this is mentioned in Sec. 4.4.

4.5.1 Connection losses with various core shapes

In this section, three kinds of cores are modeled: circular, square and trapezoidal core. The circular and square cores are typical models for waveguide design because of their axially symmetric structure. However, for PPOWs on OPCB, trapezoidal cores are obtained in some cases, as shown in Fig. 1.1 because of the limit of fabrication process. Figure 4.49(a) and (b) are commonly used circular and square cores, and Fig. 4.49(c) illustrates the trapezoid modeled in this calculation, where width difference δ is designated to 5 μm . Other parameters are listed in Table. 4.14.

In this calculation, the launching field is identical to that in the previous section as shown in Fig. 4.43(a). A 50- μm air gap adopted in Sec. 4.4.5 exists between all the components. Figure 4.50 shows the calculated loss at each end: end (2) – (7), and the total loss counted at end (9), which refers to Fig. 4.41. It is noteworthy that results for three types of core shape with GI profile are almost identical, where the total losses are only around 0.67 dB. In these cases, the almost linear increment of total losses indicates that there is almost no loss due to mode field mismatch is observed in GI cores, while only losses originated from the Fresnel reflection contribute to the total loss. On the other hand, in the case of SI cores, the trapezoidal and square cores show similar trends

with 2 dB in total loss, whereas only 0.89 dB for that of circular SI core based link. According to the calculated results, the benefit in reducing the connection loss by GI profile is clearly demonstrated, where the outer shapes play a minor role. Furthermore, the same outer core shape also reduces the connection loss significantly, even if the index profiles of them are different. Based on this model for optical links, the waveguides with circular cores are proved to be the best choice.

Table 4.14 Parameters for waveguide based optical with different core shapes

	Circular		Square		Trapzoidal	
	SI	GI	SI	GI	SI	GI
Refractive index of core (n_{co})	1.507	1.507	1.507	1.507	1.507	1.507
Refractive index of cladding (n_{cl})	1.492	1.492	1.492	1.492	1.492	1.492
Core width and height (a_x, a_y)	25 μm	25 μm	25 μm	25 μm	25 μm	25 μm
Index exponents (p, q)	100	2	100	2.4	100	2.4
Waveguide length (L)	5 cm	5 cm	5 cm	5 cm	5 cm	5 cm
Width difference (δ)	0 μm	0 μm	0 μm	0 μm	5 μm	5 μm

4.5.2 Connection losses with various NAs of SI cores

The optical link model composed of waveguides with 50 μm square SI core showed the highest connection loss (2.07 dB) in Sec. 4.5.1. Based on practical conditions that SI waveguides are still the main stream usage, how to enhance their coupling efficiency is of interest. First, the all the parameters are fixed except for the NA of waveguides. The parameters are listed in Table 4.15.

Figure 4.51(a) shows the results of total losses for different NAs. At end (3), the output of WGTX, all the cases show very similar value (~ 0.19 dB) because all the light can be coupled into the WGTX, and only loss due to Fresnel reflection exists. However, after

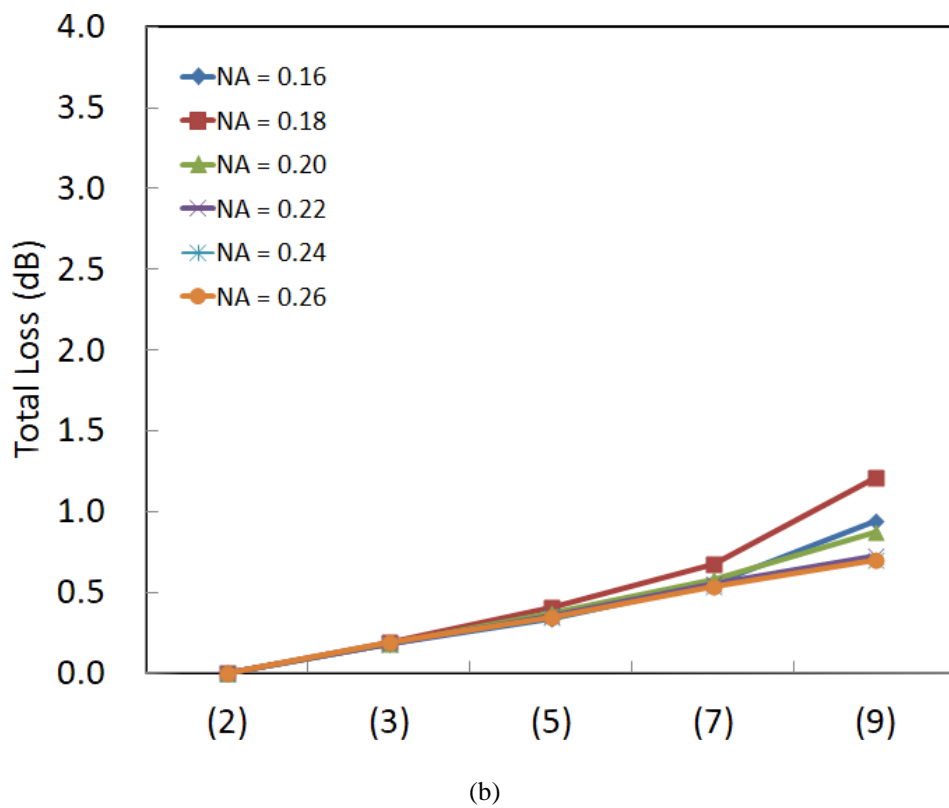
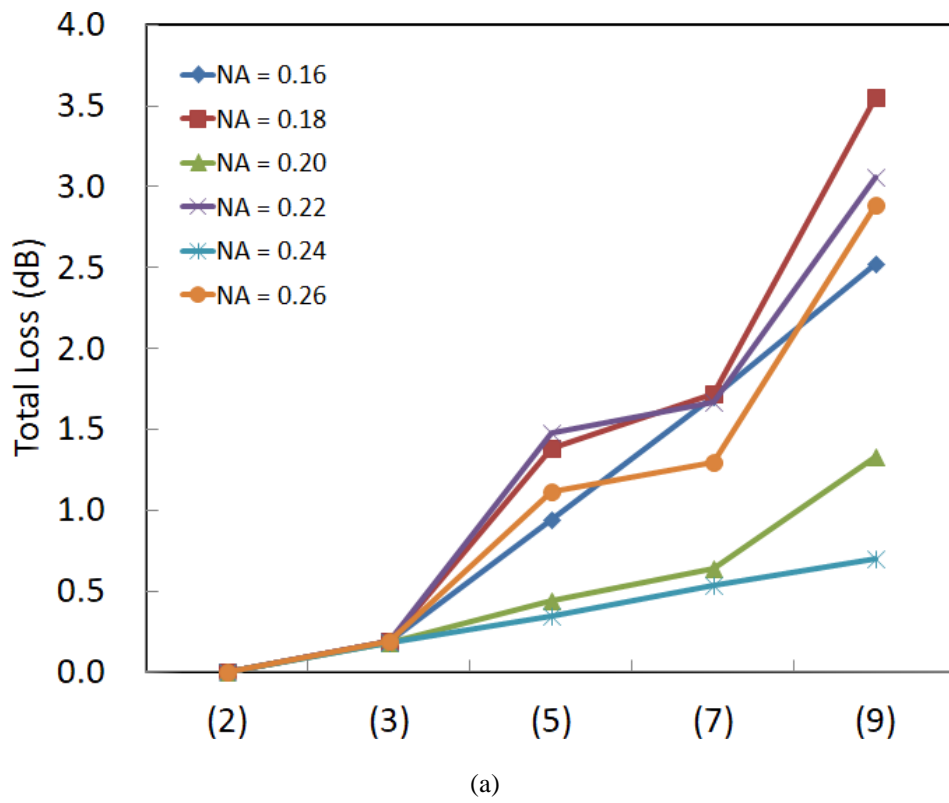


Fig. 4.51 The total loss for corresponding ends of (a) 50 μm and (b) 40 μm in diameter SI core waveguide based optical link. The meaning of ends (2), (3), (5), (7), and (9) in abscissa refer to Fig. 4.41.

the light propagates through the GI-MMF and then finally received by PD, there is no strong relation between the total loss and NA of SI waveguides. This is because the cross section area of 50 μm square core is slightly larger than that of GI-MMF. In some cases the significant losses occur particularly when stronger modal fields distribute close to core/cladding boundary. Furthermore, in the case of $\text{NA} = 0.24$, the value of total loss (0.696 dB) is very close to GI waveguide based optical link shown in Fig. 4.50, which implies other possibilities also play important roles.

Next, the smaller core size (40 μm) is considered. In this case, all the parameters are identical to Table. 4.16, while the core width and height (a_x, a_y) of SI waveguides are changed to 20 μm . The calculated results are shown in Fig. 4.51(b), where all the cases show much lower loss than that of 50 - μm core. Note that those cases with NA higher than that of GI-MMF ($\text{NA} = 0.2$) exhibit similar loss to GI waveguides based links (~ 0.7 dB).

Table 4.15 Parameters for waveguide based optical links

Numerical aperture	0.16	0.18	0.20	0.22	0.24	0.26
Refractive index of core (n_{co})	1.5006	1.5028	1.5053	1.5081	1.5112	1.5145
Refractive index of cladding (n_{cl})	1.492	1.492	1.492	1.492	1.492	1.492
Core width and height (a_x, a_y)	25 μm	25 μm	25 μm	25 μm	25 μm	25 μm
Index exponents (p, q)	100	100	100	100	100	100
Waveguide length (L)	5 cm	5 cm	5 cm	5 cm	5 cm	5 cm

4.5.3 Connection losses with various core sizes

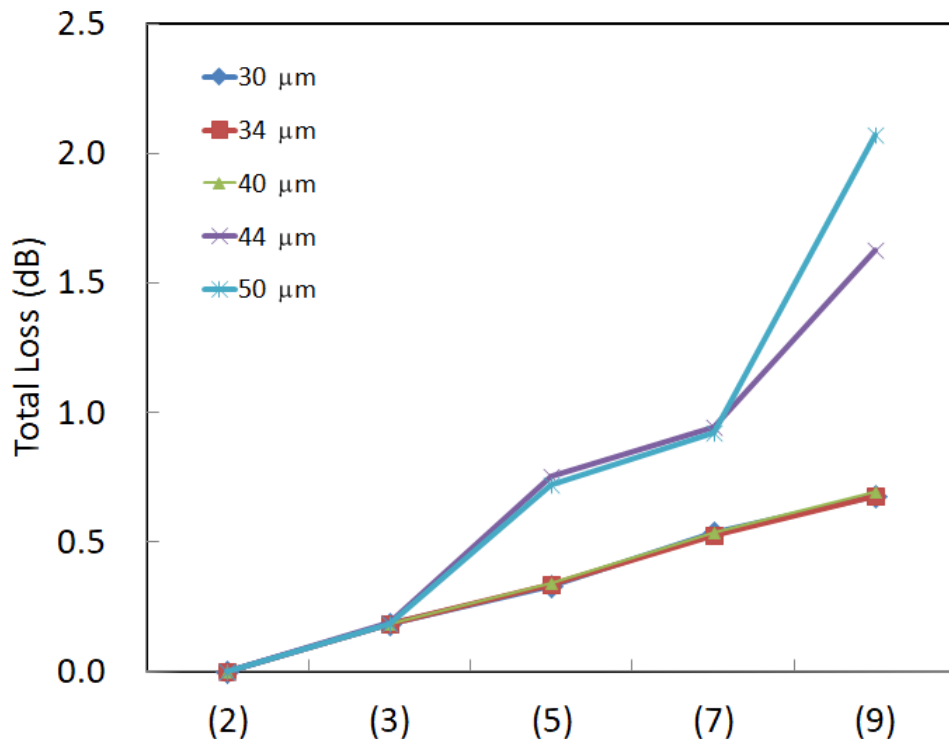
So far, it is confirmed that even if the modal field distribution influences on the coupling efficiency a lot in SI core waveguide links, this can be improved by shrinking the core size. Under this assumption, the low total loss is obtained even with high NA of

SI cores. However, in terms of real applications, there could be only limited choices of material candidates for varying values of NA, that is to say, changing the core size could be one of the good solutions. In this section, both square shape SI and GI waveguides with different core sizes are considered. As discussed in Sec. 4.5.1, the ideal case: no propagation loss within all the components and only losses due to Fresnel reflection are counted, which shows the lowest total loss (0.67 dB). As adopted in Sec. 4.5.1, the refractive indexes of core and cladding are 1.507 and 1.492, respectively. The rest parameters are listed in Table. 4.16.

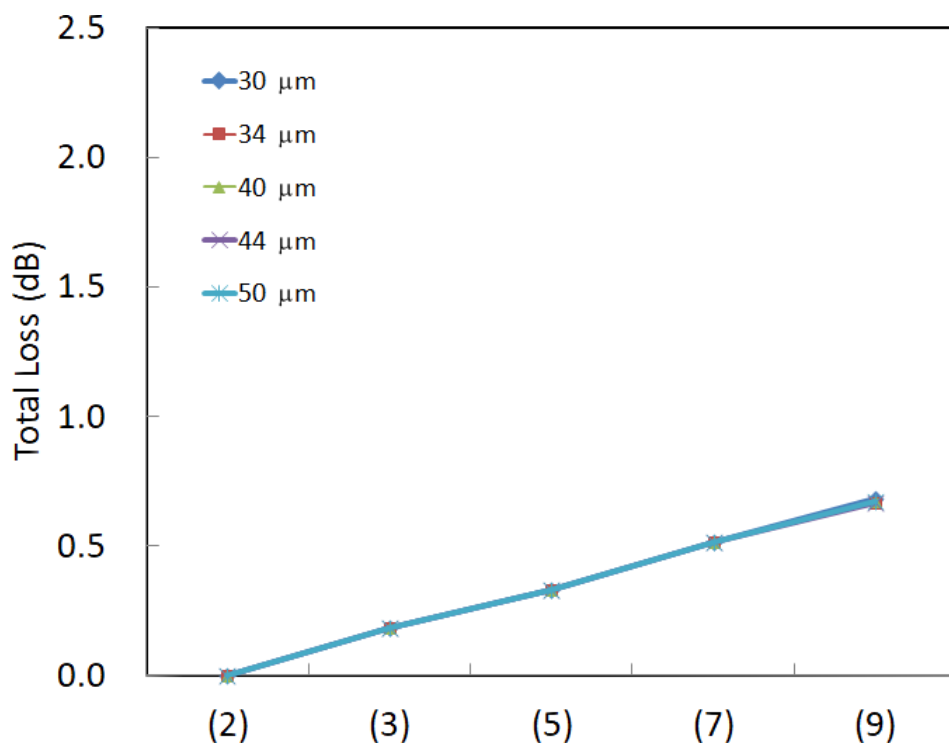
Figure 4.52 shows the calculation results of total losses from both SI and GI waveguides based optical link. In Fig. 4.52(a), the results of SI cores with 30 μm , 34 μm , and 40 μm in size show very similar trends. The three cases shows around 0.68 dB of total loss, which is very close to the lowest value mentioned in the previous paragraph. Furthermore, the GI waveguide losses are insensitive to the core size as shown in Fig. 4.52(b). Except slight differences are due to the difference of transmission coefficients expressed by Eq. 3-17, but the value of total losses are still lower than 0.7 dB.

Table 4.16 Parameters for waveguide based optical link

	SI	GI
Refractive index of core (n_{co})	1.507	1.507
Refractive index of cladding (n_{cl})	1.492	1.492
Core width and height (a_x, a_y)	30, 34, 40, 44, 50 μm	30, 34, 40, 44, 50 μm
Index exponents (p, q)	100	2.4
Waveguide length (L)	5 cm	5 cm



(a)



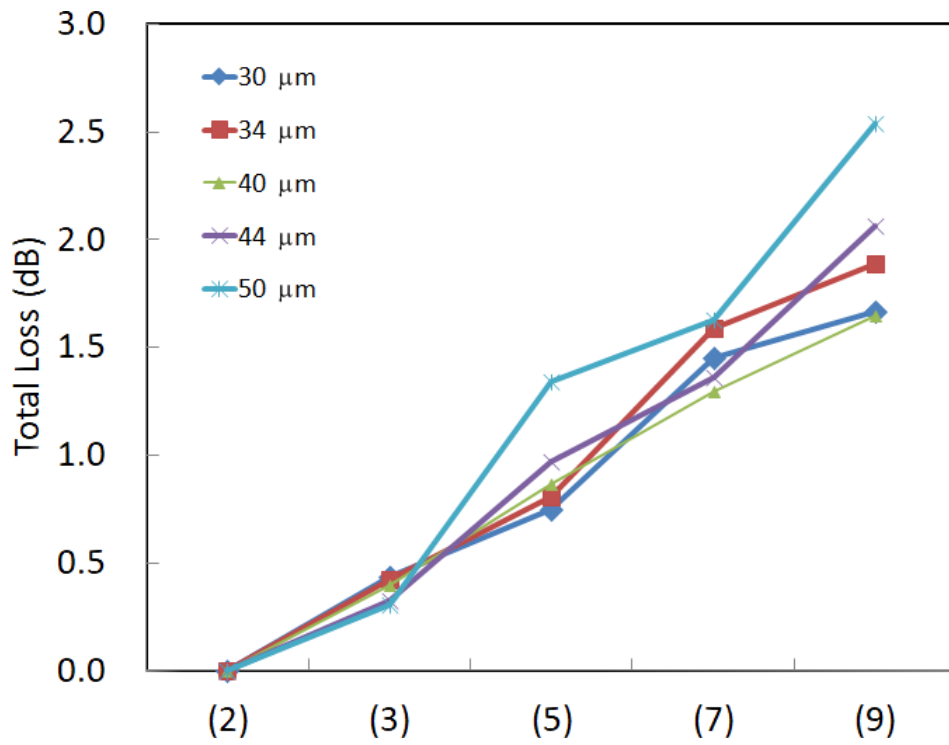
(b)

Fig. 4.52 The total loss for corresponding core size of (a) SI and (b) GI waveguide based optical link. The NA is 0.21 here. The meaning of ends (2), (3), (5), (7), and (9) in abscissa refer to Fig. 4.41.

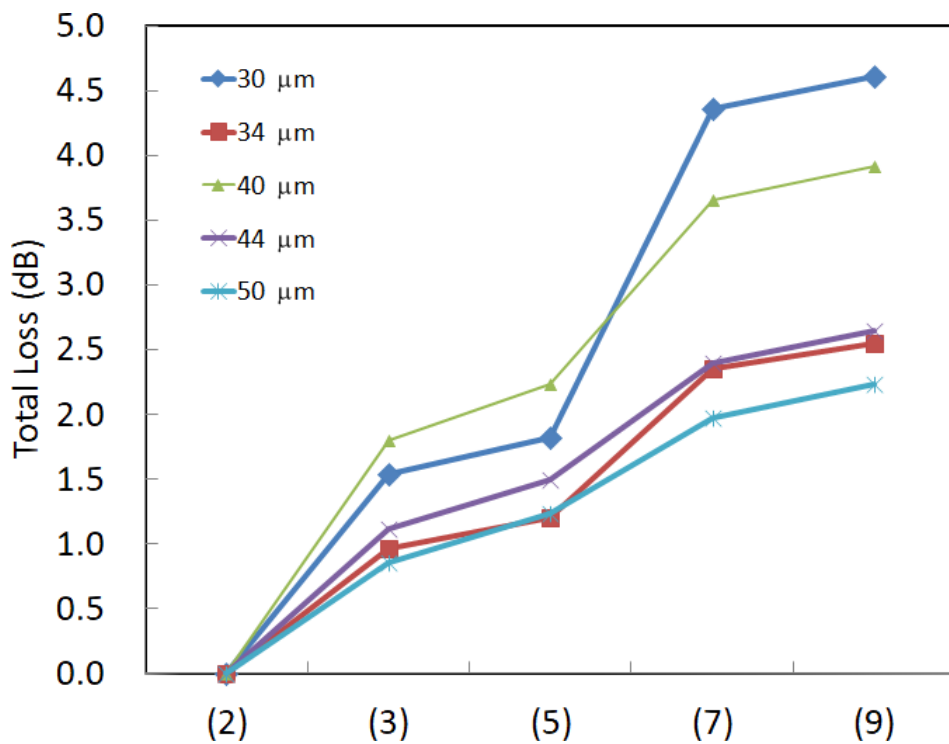
4.5.4 Connection losses with imperfections within cores

In above conditions, no imperfections in core area are considered. In the case of real PPOWs as discussed in Sec. 4.1, the scattering effect is inevitable and it results in mode conversion. According to the results shown in Sec. 4.5.3, the small enough (smaller than 40 μm here) cores in both SI and GI cores performs very similar and could maintain most of the power except for the loss due to Fresnel reflection. In this calculation, the same conditions of extra scattering are considered in SI- and GI- core waveguides. Here, although it is somehow unclear whether the same mechanism of scattering effect is involved in both cases, in order to reduce the influence of randomly generated scatters. Other parameters applied in this section are identical to those in Sec. 4.5.3, as listed in Table. 4.16.

Figure 4.53 shows the calculation results of total loss for different core sizes when scattering effect is involved. In this model, the level of scattering effect is much higher than the real conditions. In the case of SI cores, except for the 50- μm core case, which is slightly larger than that of GI-MMF, the relation between core size and total loss is not significant. Although the values of total loss is much higher than those in Sec. 4.5.3, the trends shown in Fig. 4.53(a) imply that the SI cores is not sensitive to scattering effect because the superimposed total modal intensity distribution of SI cores are uniform in the core area. Contrarily, the results of GI cases deliver a quite disappointed message: the modal fields are destroyed much more than these in SI cores. This is because once modes are scattered close to the core/cladding boundary, they may leak from the launched core easily. That is to say, the larger size cores can confine propagation modes more tightly than smaller ones. Although the amazing high losses somehow imply the model is not realistic enough, it still confirms the imperfection



(a)



(b)

Fig. 4.53 The total loss for corresponding core size of (a) SI and (b) GI waveguide based optical link. In this case scattering effect is involved. The meaning of ends (2), (3), (5), (7), and (9) in abscissa refer to Fig. 4.41.

sometimes could deteriorate the link performance significantly.

4.5.5 Conclusion

According to the results in Sec. 4.5.1 to 4.5.3, both SI and GI waveguides based optical link potentially perform very low link budget. In terms of core shape, the circular shape is the best for 50 μm core size, although there is almost no core-size dependence if GI cores are applied. Furthermore, as discussed in Sec. 4.5.2, the NAs of SI cores have no strong relation to the connection loss of the link, instead, smaller core sizes ($< 50 \mu\text{m}$) have a benefit in coupling between SI cores and other components under the RML condition. Particularly when the core size ranges from 30 to 40 μm , the total loss has no big difference for both SI and GI cores, as discussed in Sec. 4.5.3. Although the future development of waveguides on OPCB tends toward smaller core size and narrower pitch, which coincide to the calculation results, some practical issues still deteriorate the overall performance. For example, the smaller core size increases alignment tolerance degradation and narrower pitch induces stronger mode coupling to adjacent cores. Contrarily, GI waveguides perform more stable in most cases, and we believe they also will become the trend of high-end use in this field. Furthermore, as discussed in Sec. 4.5.4, the imperfections of core materials are one of the practical concerns. In this section, GI cores are still probably perform worse than the SI counterparts. It is required to find persuasive ways to model these imperfections and optimize other parameters.

REFERENCE

1. Y. Takeyoshi and T. Ishigure, "High-density 2×4 channel polymer optical waveguide with graded-index circular cores," J. Lightw. Technol., **27**(14), 2852-2861 (2009).
<http://ieeexplore.ieee.org/iel5/68/4351987/04367530.pdf?arnumber=4367530>
2. N. Bamiedakis, J. Beals, IV, R. V. Penty, I. H. White, J. V. DeGroot, Jr., and T. V. Clapp, "Cost-effective multimode polymer waveguides for high-speed on-board optical interconnects," J. Quant. Electron., **45**(4), 415-424 (2009).
<http://ieeexplore.ieee.org/stamp/stamp.jsp?tp=&arnumber=4803864>
3. H. H. Hsu and T. Ishigure, "Graded index core optical polymer parallel waveguide and its crosstalk analysis," presented at International Conference on Electronics Packaging, Sapporo, Japan, 12-14 May 2010.
4. T. Ishigure, S. Tanaka, E. Kobayashi, and Y. Koike, "Accurate refractive index profiling in a graded-index plastic optical fiber exceeding gigabit transmission rates," J. Lightw. Technol., **20**(8), 1449-1456 (2002).
<http://www.opticsinfobase.org/abstract.cfm?URI=jlt-20-8-1449>
5. T. Ishigure, E. Nihei, S. Yamazaki, K. Kobayashi, and Y. Koike, "Formation of the refractive index profile in the graded index polymer optical fiber for gigabit data transmission," J. Lightw. Technol., **15**(11), 2095-2100 (1997).
http://ieeexplore.ieee.org/xpls/abs_all.jsp?arnumber=641528&tag=1
6. C. A. Burrus and R. D. Standley, "Viewing Refractive-Index Profiles and Small Scale Inhomogeneities in Glass Optical Fibers Some Techniques," Appl. Opt., **13**(10), 235-2368 (1974).
<http://www.opticsinfobase.org/abstract.cfm?URI=ao-13-10-2365>
7. Y. Koike and T. Ishigure, "Bandwidth and transmission distance achieved by POF," IEICE Transaction on Electronics, E82-C, 1553-1561 (1999).
<http://www.ishigure.appi.keio.ac.jp/PDFs/IEICE.pdf> (2012.2.10)
8. T. Ishigure and Y. Takeyoshi, "Polymer waveguide with 4-channel graded-index circular cores for parallel optical interconnects," Opt. Express, **15**(9), 5843-5850 (2007).
<http://www.opticsinfobase.org/abstract.cfm?uri=oe-15-9-5843>
9. A. W. Snyder and J. D. Love, *Optical Waveguide Theory* (Chapman & Hall, 1983).
<http://goo.gl/VK07D> (2012.2.10)
10. K. Takahashi, T. Ishigure, and Y. Koike, "Index profile design for high-bandwidth W-shaped plastic optical fiber," J. Lightw. Technol., **24**, 2867 (2006).

<http://www.opticsinfobase.org/abstract.cfm?uri=JLT-24-7-2867>

11. T. Ishigure, H. Endo, K. Ohdoko, K. Takahashi, and Y. Koike, "Modal bandwidth enhancement in a plastic optical fiber by W-refractive index profile," J. Lightw. Technol., **23**(4), 1754-1762 (2005).

<http://www.opticsinfobase.org/abstract.cfm?uri=JLT-23-4-1754>

12. H. H. Hsu and T. Ishigure, "High-density channel alignment of graded index core polymer optical waveguide and its crosstalk analysis with ray tracing method," Opt. Express, **18**, 13368 (2010).

<http://www.opticsinfobase.org/abstract.cfm?uri=oe-18-13-13368>

13. Refractive index of FUSED SILICA [GLASSES] - RefractiveIndex.INFO

http://refractiveindex.info/?group=GLASSES&material=F_SILICA (2012.2.10)

14. James A. Lock, Susan Y. Wrbanek, and Kenneth E. Weiland, "Scattering of a tightly focused beam by an optically trapped particle," Appl. Opt., **45**(15), 3634-3645 (2006).

<http://www.opticsinfobase.org/ao/abstract.cfm?URI=ao-45-15-3634>

5

SUMMARY

Although most of the formulations introduced in chapters 2 and 3 are already well known, still some new ideas were inspired during the studies. Through the research for this dissertation, from the analysis was started from the eikonal equation and a series of formulations developed thirty years ago were introduced. After understanding how rays propagate in the core and cladding, some ideas for waveguide imperfections were tried to be involved. Under some physical assumptions, the potential of ray tracing method for our applications in the field of optical interconnections with PPOWs was recognized. Finally, it was tried to calculate the time elapse of the rays, by which calculation of eye diagram and BER are the ultimate goals. Unfortunately, although the ray optics can be regarded as an approximation of wave optics, the programming skill and consumption of calculation time are still big barriers, consequently exact solutions derived from wave optics drive us to think about some ideas beyond commercially available software.

Similarly, in chapter 3, formulations originated from Helmholtz equation were introduced, first. Under the rational assumptions such as weakly guiding and SVEA, the behavior of wave propagation could be modeled easily. Surely it was not necessarily perfect conditions were taken into account, and how to involve waveguide perturbations to the wave optics theory is remain as another issue. Moreover, in order to make the

statement more robust, the widely applied formulations for Mie scattering in optical tweezers applications (GLMT) were introduced. Fortunately, the calculation results for scattering effect showed similar trends between FD-BPM and GLMT, but some more advanced studies based on this should be continued.

After the above tools were created, these tools were applied to characterize multimode polymer optical waveguides (PPOWs) and optical links composed of the PPOWs. In this dissertation, much more attention was paid to the study of fundamental theory than the application. First in the single device regime, the ray tracing method was applied to simulate the fabricated PPOWs because the scattering effect essentially exists in polymer materials. With the randomly determined parameters, the calculation results looked closer to the measurement results. So far, we have enough knowledge to do advance modeling with wave optics for optical link systems. In the short range data communication, the inter-channel crosstalk is not a big concern. In this application, the coupling loss in an optical link was considered. The scattering effect was involved in our FD-BPM tool, and then, the importance of this factor was visually and numerically confirmed.

There are still lots of works upon the theoretical modeling for both active and passive photonic devices, using TD-BPM, FEM-BPM, FDTD, and modal expansion method (MEM). Most of them are already well built and commercialized. Of course our target is not to compete with the performance of the commercially available software. Always the practical conditions should be closer to real applications. Frankly speaking it is not really an easy work during these days; we believe the substantial fundamentals bring us to a higher level, and surely the central idea of this dissertation goes continuously.

APPENDIX

A

SAMPLE CODES FOR RAY TRAJECTORY IN A RECTANGULAR GI MEDIA

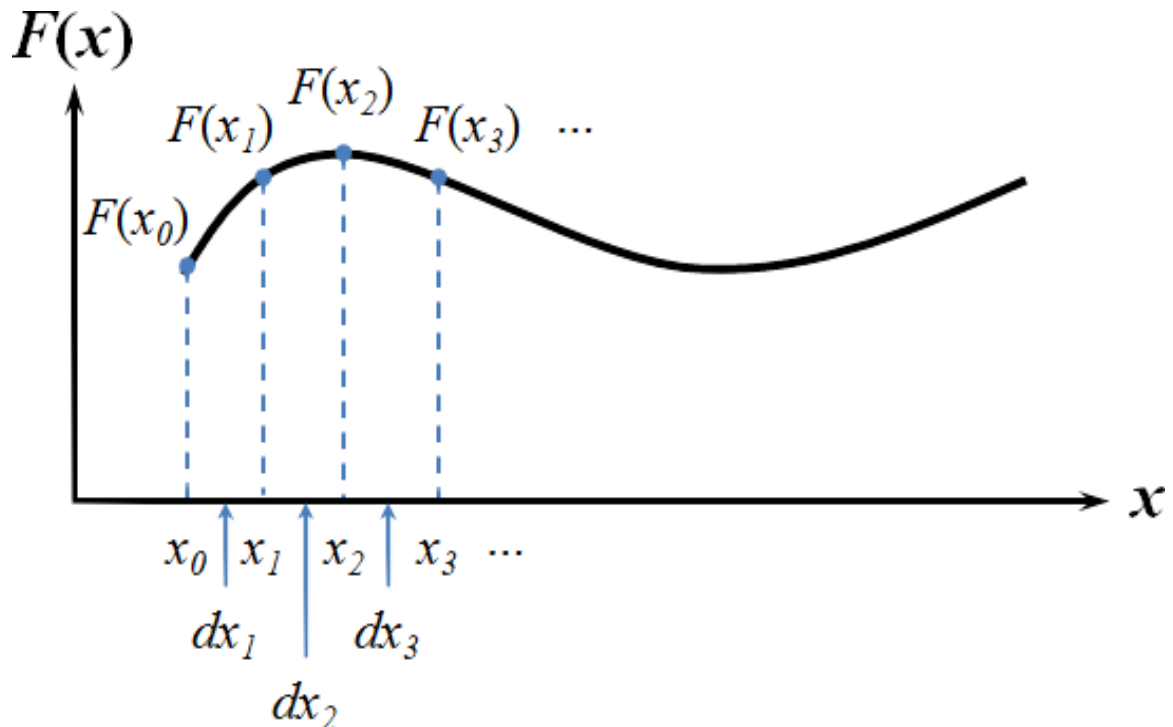


Fig. A.1 Schematic illustration of integration of Eq. (A-1)

The programming processes are introduced as follow. Here, we apply Eq. (2-16a) to an example and rearrange it as

$$z\Omega = \int F(x)dx \quad (\text{A-1})$$

First, the starting point $(x_0, y_0, 0)$, x_{tp} , and y_{tp} are pre-defined and then the ray invariant β can be calculated. Next, let z is an array which ranges from 1 to L with uniform N steps ($z_i - z_{i-1} = \Delta z$, $i = 1$ to N), where L is the length of media. We consider the relation shown in Fig. A.1, the integration of the continuous function $F(x)$ can be approximated by summation of rectangles with fine enough dx_i . Note that dx_i are not necessary mutually the same. According to Eq. (A-1), dx_1 can be expressed as:

$$dx_1 \cong \frac{z_1\Omega}{F(x_0)} \quad (\text{A-2})$$

and $x_1 = x_0 + dx_1$. For x_i with corresponding z_i can be calculated recursively with the following equation:

$$dx_i \cong \frac{z_i\Omega - \sum_{j=2}^i F(x_{j-2})dx_{j-1}}{F(x_{i-1})} \quad (\text{A-3})$$

where j is an integer from 2 to i . Similarly, coordinates of ray trajectory along y direction with corresponding z_i also can be calculated in the same way. Although it is intuitively recognized that the integration of Eq. (A-1) performs closer to real value by summing the trapezoids rather than rectangles, the $F(x_1)$ is not available without dx_1 calculated first. The fine enough Δz ($\sim 0.1 \mu\text{m}$) is certainly required however this increases the calculation time quite significantly.

```

=====
% "z" is an array with uniform interval. For example z=1:1:1000.
% "raydata" is a 1x12 array with following format:
% [x0 x1 y0 y1 z0 z1 I0 xtp ytp dirx diry t]
% "outputray" is a 1x1 structure.

function [x y z]=fun_noncir(z,raydata)

global ax ay nco ncl

x0=raydata(1);
y0=raydata(3);

```

```

z0=z;
x00=x0;
y00=y0;
xtp=raydata(8);
ytp=raydata(9);
dirx=raydata(10);
diry=raydata(11);
nhit=0;
delta=(nco^2-ncl^2)/(2*nco^2);

x1=[];
y1=[];
state=0;

while isempty(z)==0 || state==1

    nhit=nhit+1;
    clear Fx0 Fx FF x dx

    FF(1)=0;
    x=[];

    % x, dx
    for k=1:length(z)

        betabar=nco*sqrt(1-2*delta*(fx(xtp)+gy(ytp)));
        omega=nco*sqrt(2*delta)/betabar;
        Fx0=1./sqrt(fx(xtp)-fx(x0));
        Fx(1)=Fx0;

        if k==1
            dx(k)=omega*z(k)/Fx0;

            if dx(end)<1e-3;
                dx(end)=0;
            end

            x(k)=x0+dirx*dx(k);
        else
            dx(k)=(omega*z(k)-FF)/Fx(k-1);

            if dx(end)<1e-3;
                dx(end)=0;
            end

            x(k)=x(k-1)+dirx*dx(k);
        end

        if x(k)>xtp || x(k)>ax
            x(k)=[];
            dirx=-1;
            break
        elseif x(k)<-xtp || x(k)<-ax
            x(k)=[];
            dirx=1;
            break
        end
    end
end

```



```

% =====

if k==2
    FF(k)=Fx0*dx(1);
elseif k>2
    FF(k)=Fx(k-2)*dx(k-1);
end

FF=sum(FF);
Fx(k)=1./sqrt(fx(xtp)-fx(x(k)));
end

x1=cat(2,x1,x);
% =====

clear Gy0 Gy GG y dy
GG(1)=0;
y=[];

% y, dy
for v=1:length(x)

    betabar=nco*sqrt(1-2*delta*(fx(xtp)+gy(ytp)));
    omega=nco*sqrt(2*delta)/betabar;
    Gy0=1./sqrt(gy(ytp)-gy(y0));
    Gy(1)=Gy0;

    if v==1
        dy(v)=omega*z(v)/Gy0;

        if dy(end)<1e-3;
            dy(end)=0;
        end

        y(v)=y0+diry*dy(v);
    else
        dy(v)=(omega*z(v)-GG)/Gy(v-1);

        if dy(end)<1e-3;
            dy(end)=0;
        end

        y(v)=y(v-1)+diry*dy(v);
    end

    if y(v)>ytp || y(v)>ay
        y(v)=[];
        diry=-1;
        break
    elseif y(v)<-ytp || y(v)<-ay
        y(v)=[];
        diry=1;
        break
    end

% =====

if v==2

```

```

        GG(v)=Gy0*dy(1);
elseif v>2
        GG(v)=Gy(v-2)*dy(v-1);
end

GG=sum(GG);
Gy(v)=1./sqrt(gy(ytp)-gy(y(v)));
end

y1=cat(2,y1,y);
% =====

if isempty(y)==0
    zend=z(length(y));
    zp0(nhit)=zend;
    y0=y(end);
    x1=x1(1:length(y1));

    % x0 changes w.r.t y
    if length(x)>length(y)
        x0=x1(end);

        for kk=1:length(x1)

            if kk==length(x1)
                x=[];
                y=[];
                z=[];
                return
            end

            bb=x1(end-kk);

            if bb~=x1(end)
                break
            end
        end

        if bb<x1(end)
            dirx=1;
        else
            dirx=-1;
        end
    else
        x0=x(end);
    end

    z=z((length(y)+1):end)-zend;
end
end

x=cat(2,x00,x1);
y=cat(2,y00,y1);
z=cat(2,0,z0(1:length(y1)));
=====

```

AKNOWLEDGEMENT

Since the first replied e-mail from Ishigure Sensei, the wonderful feeling of affinity to this lab started. This is my great honor to enter Ishigure laboratory, and fortunately I got so many things out of my expectation. These days I was cheered and inspired by many discussions with Ishigure Sensei that this could be the most valuable and worth cherished experience in this laboratory. I am also much grateful to the MEBIOS program, which is the most decisive reason to contribute my life to this land. To my wife, Yi-Ching Chen, let's confront the next challenge.

Life is like a box of chocolate you never know what you will get next. Thanks to Mr. Sakurai, because of your unique style that I could escape from being a scientific freak. Thanks to GCOE program, because of so many formal requirements that I could join another better one. Therefore, I specially cherish the memory to be a student aboard in Keio University. Although the life here is not as bountiful as before, fortunately I met Yu-Yang Lee, Yu-Shiuan Cheng, and I-Te Lin. Getting along with you occupied most of my happy hours within the three years, and I hope all of you will become shiny stars in both career and personal life.

It is hard to make the decision to terminate the previous business life and then study abroad. Fortunately I met the right people in the right place, and now I can look more positively that all wishes may come true because of our endeavor. Although it is a cliché to say lots of grateful words at this moment, I still have to say thank you very much to those people who gave me so great help in Japan.

Yokohama, Feb. 2012
Hsu, Hsiang-Han,